

The University of Nottingham

UNITED KINGDOM · CHINA · MALAYSIA

Inorganic Synthesis inside Carbon Nanotubes

Craig T. Stoppiello, MSci.

Thesis submitted to the University of Nottingham for the degree of doctor of Philosophy

December 2016

Abstract

The use of single-walled carbon nanotubes (SWNTs) as test tubes for the encapsulation of metallic nanoparticles (MNPs) and the formation of inorganic nanomaterials has been advanced. A methodology to encapsulate the group 10 and 11 metals inside SWNTs to investigate their properties has been optimised. Each metal interacts with carbon differently at the atomic level, as shown by aberration-corrected high resolution transmission electron microscopy (AC-HRTEM), leading to the promotion of a plethora of different processes stimulated by MNPs under the electron beam. Additionally, interactions between SWNTs and small clusters of the group 10 metals have been examined, revealing marked differences between metal-carbon bonding for each metal. This has allowed for a useful insight into metal-carbon interactions on the atomic level which could have profound implications on the future development of new catalysts or nanoscale devices.

Following on from this, a series of chemical reactions with platinum compounds were carried out within SWNTs which have shown SWNTs to be both a very effective reaction vessel and template for the formation of low-dimensional PtX_2 (X = I, S) nanocrystals, materials that are difficult to create by traditional synthetic methods. The stepwise synthesis within SWNTs has enabled the formation of the platinum compounds to be monitored at each reaction stage by AC-HRTEM, verifying the atomic structures of the products and intermediates, and also by an innovative combination of fluorescence-detected X-ray absorption spectroscopy (FD-XAS) and Raman spectroscopy, monitoring the oxidation states of the platinum guest compounds within the nanotube and the vibrational properties of the host SWNT respectively. The stepwise synthesis has appeared to offer only limited preparative

potential because of the lack of stoichiometric control in the resultant inorganic nanomaterials. A new approach for nanoscale synthesis in nanotubes developed in this study utilises the versatile coordination chemistry of platinum which has enabled the insertion of the required chemical elements (*e.g.* metal, and halogens or chalcogens) into the nanoreactor in the correct proportions for the controlled formation of PtI_2 and PtS_2 with the exact stoichiometry and structure.

FD-XAS has also been used to probe the transformations of $Pt(acac)_2$@SWNT to Pt@SWNT, and $Cu(acac)_2$@SWNT to Cu_2O_x@SWNT (where $x > 1$). It was shown that the temperature of both transformations was significantly lower than required for the same reactions in the bulk, which demonstrates the ability of SWNTs to lower the activation energy by polarising encapsulated molecules.

Finally, a variety of novel MNPs and MO_x (M = Pt, Pd, Ni) materials were encapsulated within hollow graphitised carbon nanofibres (GNFs) and evaluated for the sensing of glucose. MO_x@GNFs were revealed to be more active sensors than their corresponding MNPs which can be attributed to the increase in Lewis acidity of the metal centres upon oxide formation. Furthermore, the effectiveness of each metal and their corresponding oxides for glucose detection was found to increase in the order Pt > Pd > Ni which can be attributed to both physical and chemical properties of the respective metals. Overall, this thesis demonstrates that nanotubes can be used effectively to not only investigate chemical transformations on the atomic level, but also act as nano-sized test tubes and templates for the formation of novel, low-dimensional inorganic materials with bespoke structure and composition.

Acknowledgements

Scientific research requires rigorous teamwork usually involving international collaborations, and I feel blessed to have met some fantastic individuals over the past few years, without whom this thesis would not have been possible. Firstly, I express my deepest gratitude to my supervisor, Prof. Andrei Khlobystov for his unwavering enthusiasm and support for this project. His deep adoration for science is truly inspiring, and I have gained a vast array of skills and knowledge thanks to his untiring encouragement.

I must also thank Dr Thomas Chamberlain for his guidance both in and out of the laboratory. He continues to be a fantastic mentor, and I especially look back fondly on our late night escapades working hard in the labs in France and Germany. His strong work ethic coupled with his determination to help others succeed is particularly moving and fully admirable; I warmly look forward to our collaborations in the future. Additionally, Dr Mike Fay has spent hours training me to use the TEM, and this is something which I am extremely grateful for, as it is a lifetime skill which will no doubt be very useful to me in years to come.

From the moment I joined the Nottingham Nanocarbon group I was piled with support, praise and encouragement; especially from Ákos Botos, whose work I followed on from and who helped me in the laboratory during the early months. Dr Robert McSweeney deserves much accolade for assisting me in performing the electrochemical procedures outlined in Chapter VI. His sound electrochemical advice and knowledge has been paramount in helping me understand the electrochemistry in that chapter. Electrochemistry aside, I am also incredibly grateful for all of the support Rob has provided to me both in and out of the lab, and I look forward to continuing

our friendship. The same has to be said for Maxwell Astle, who as well as performing TGA and PXRD on my samples has become a close friend over the past few years and is always there for a chat/tea break; I very much look forward to working with him in the future. All of the Raman spectroscopy presented in this thesis was performed by Dr Graham Rance, and I am very appreciative not only for this, but also for his help with detailed Raman analysis, and proof reading of some of the chapters.

I can't forget other members of the Nottingham Nanocarbon group, especially Bradley for our exhaustive political discussions (and his production of exquisite baked goods); Kate, Rhys, Mehtap, Julie, Kayleigh and Nityananda. They are all credits to the profession and I wish them the best of luck with their work. During the past few years I've been fortunate enough to supervise some excellent MSci. research students including Charles Collins, and I would like to thank him for laying the foundation for the small molecule sensing work.

All of the AC-HRTEM images which I present were produced by my colleagues at the University of Ulm; Ute Kaiser, Johannes Biskupek, Thilo Zoberbier and Kecheng Cao. I must thank them all for viewing the samples, their scientific analysis, and endless hospitality upon my trips to Germany. I especially thank Thilo and Johannes for their help with interpreting data and providing processed images from the group 10 metals in SWNTs.

Additionally, I thank Ziyou Li and Jun Yuan for performing AC-STEM and stimulating intellectual discussion; this thesis is much stronger as a result of it. Also, I would like to pay tribute to the other researchers and technicians I met during my visits to the ESRF in Grenoble; including Paul Thompson, German Castro, Richard Bourne, Richard Fogarty and Alastair Baker for their practical support and scientific

advice. I especially thank Dr Bourne for developing the Matlab programme used to smooth the FD-XAS. Also, Stephen Skowron very patiently taught me how to perform QSTEM simulations, and I am very grateful to him for this

The School of Chemistry at the University of Nottingham is a vibrant place to work, and I am thankful to my colleagues and friends around the School for all of their moral support, notably Harry, Beth and Helen. Additionally, I thank the technical and support staff, including Mark and Sue.

Finally, I would like to say thank you to my family; mum, dad, Laura, Joe and grandparents. I am especially grateful to my mum and dad for all of the sacrifices they've made to ensure that my siblings and I get the best out of life. Their constant love, support and general nagging helps to keep me going, and I appreciate everything they do for me.

Abbreviations and Symbols

Abbreviation	**Term**
@	Encapsulated within
Δ	heat
acac	Acetylacetonate , $((CH_3CO)_2CH)^-$
AC-HRTEM	Aberration-corrected high resolution transmission electron microscopy
AC-STEM	Aberration-corrected scanning transmission electron microscopy
c	Speed of light
ca.	Circa
CCD	Charge coupled device
CN	Carbon nanostructure
COD	Cyclo-octa-1,5-diene
C_s	Spherical aberration
CV	Cyclic voltammetry
CVD	Chemical vapour deposition
D band	Disorder band
d_{NT}	Nanotube diameter
DWNT	Double-walled carbon nanotube
e	Electron
E	energy
E_a	Activation energy
E_{coh}	Cohesive energy
e-beam	Electron beam

EDX	Energy dispersive X-ray spectroscopy
EELs	Electron energy loss spectroscopy
e.g.	*Exempli gratia,* for example
FD-XAS	Florescence-detected X-ray absorption spectroscopy
FFT	Fast Fourier transform
G band	Graphitic band
GCE	Glassy carbon electrode
GNF	Hollow graphitised carbon nanofibre
HAADF	High angle annular dark field
HFacac	Hexafluoroacetylacetonate, $((CF_3CO)_2CH)^-$
HR-TEM	High resolution transmission electron microscopy
hr	Hour(s)
i.e.	*Id est,* that is
IR	Infra-red
m_e	Mass of electron
M-C	Metal-carbon
min	Minute(s)
mbar	millibar
mM	$x10^{-3}$ moles per litre
MNP	Metallic nanoparticle
MOF	Metal organic framework
MWNT	Multi-walled carbon nanotube
NT	Nanotube
PTFE	Polytetrafluoroethylene

RBM	Radial breathing mode
RT	Room temperature
sat.	Saturated
S-GNR	Sulfur terminated graphitised nanoribbon
SWNT	Single-walled carbon nanotubes
TEM	Transmission electron microscopy
TGA	Thermogravimetric analysis
$T_{max}(M)$	Maximum kinetic energy transferred from the electron beam to a particular metal, M
TTF	Tetrathiafulvalene
w.r.t.	With respect to
XAS	X-ray absorption spectroscopy
XMNP	Nanoparticle(s) of a particular element, X
XRD	X-ray diffraction
Z	Atomic number

List of Publications

1. Botos A., Biskupek J., Chamberlain T. W., Rance G. A., **Stoppiello C. T.**, Sloan J., Lui Z., Suenaga K., Kaiser U. and Khlobystov A. N., ***J. Am. Chem. Soc***. 2016, **138**, 8175-8183.

2. Lebedeva M. A, Chamberlain T. W., Thomas A., Thomas B. E., **Stoppiello C. T**., Volkova E., Suyetin M., Khlobystov A. N., ***Nanoscale***, 2016, **8**, 11727-11737.

3. **Stoppiello C. T.**, Chamberlain T. W., Biskupek J., Li Z. Y., Rance G. A., Botos A., Fogarty R., Bourne R. A., Yuan J., Lovelock K. R. J., Thompson P., Fay M. W., Kaiser U., Khlobystov A. N., ***Chem. Sci.***, submitted.

4. Aygun M., **Stoppiello C. T.**, Lebedeva M. A., Gimenez-Lopez D. C., Chamberlain T. W. and Khlobystov A. N., ***Nano Res.***, submitted.

5. Cao K., Biskupek J., **Stoppiello C. T.**, McSweeney R. L., Chamberlain T. W., Lui Z., Suenaga K., Khlobystov A. N. and Kaiser U., ***Nature,*** submitted.

6. Kuganathan N., Calatayud, D. G., Mirabello V., Kasimuthu C., Da Como E., Jacobs R. M. J., Rees M., **Stoppiello C. T.**, Khlobystov A. N., Tyrrell R. M., and Pascu, S. I., ***ACS Nano,*** awaiting submission.

Table of Contents

Abstract *2*

Acknowledgements *4*

Abbreviations and Symbols *7*

List of Publications *10*

Chapter I: Inorganic Materials inside Single-Walled Carbon Nanotubes *14*

1.1 Introduction **14**

1.2 Characterisation Techniques **16**

1.2.1 Transmission Electron Microscopy 16

1.2.2 Energy Disperse X-ray Spectroscopy 19

1.2.3 Raman Spectroscopy 20

1.2.4 Fluorescence-Detected X-ray Absorption Spectroscopy 21

1.3 Methods of Nanotube Filling **24**

1.3.1 Oxides/Hydroxides in SWNTs 27

1.3.2 Halide Salts in SWNTS 32

1.3.2.1 Main Group Halides 33

1.3.2.2 Transition Metal Halides 37

1.3.2.3 Lanthanide Halides 45

1.3.3 Metal Chalcogenides 48

1.3.4 Reactions in SWNTs 51

1.4 Summary **53**

1.5 Aim and Objectives **54**

1.6 References **55**

Chapter II: The Encapsulation of Group 11 Metals into Single-Walled Carbon Nanotubes *61*

2. 1 Introduction **61**

2.2 Results **65**

2.2.1 Encapsulation 65

2.2.2 Copper 67

2.2.2.1 AC-HRTEM Analysis 68

2.2.2.2 Formation of Cu_2O_x 73

2.2.2.3 Electron Transfers in $Cu(acac)_2$@SWNT and Cu_2O_x@SWNT 74

2.2.3 Silver 80

2.2.4 Gold 84

2.3 Discussion **87**

2.4 Conclusion **92**

2.5 Experimental **93**

2.5 1 Encapsulation of Complexes 93

2.5.2 Formation of MNPs@SWNT 94

2.5.3 Electron Microscopy 94

2.5.4 EDX Spectroscopy 94

2.5.5 Raman Spectroscopy 95

2.5.6 Fluorescence-Detected X-ray Absorption Spectroscopy 95

2.5.7 Image Simulation 95

2.6 References 96

Chapter III: Investigations into the Behaviour of the Group 10 Metals when Confined inside Single-Walled Carbon Nanotubes 98

3.1 Introduction 98

3.2 Results 99

3.2.1 Materials Preparation 99

3.2.2 AC-HRTEM Analysis 101

3.2.2.1 Nickel 101

3.2.2.2 Palladium 105

3.2.2.3 Platinum 108

3.2.3 Electron Transfers within MNPs@SWNT 112

3.3 Discussion 116

3.4 Conclusion 119

3.5 Experimental 120

3.5.1 Encapsulation of Complexes 120

3.5.2 Formation of MNPs@SWNT 121

3.5.3 Electron Microscopy 121

3.5.4 EDX Spectroscopy 122

3.5.5 Raman Spectroscopy 122

3.5.6 Fluorescence-Detected X-ray Absorption Spectroscopy 122

3.6 References 123

Chapter IV: A One-Pot-One-Reactant Synthesis of Platinum Compounds at the Nanoscale 124

4.1 Introduction: 124

4.2 Results and Discussion: 127

4.2.1 Stepwise Synthesis 127

4.2.2 Encapsulation of Precursors 134

4.2.2.1 PtI_2@SWNT 138

4.2.2.2 PtS_2@SWNT 143

4.3 Conclusion 146

4.4 Experimental 147

4.4.1 Materials 147

4.4.1.1 PtI_2@SWNT 148

4.4.1.2PtS_2@SWNT 148

4.4.2 Electron Microscopy 149

4.4.3 EDX Spectroscopy 149

4.4.4 Raman Spectroscopy 149

4.4.5 Image Simulation 150

4.4.6 Fluorescence-Detected X-ray Absorption Spectroscopy (FD-XAS) 150

4.5 References 151

Chapter V: Monitoring Nanoscale Transformations using Fluorescence-Detected X-ray Absorption Spectroscopy 153

5.1 Introduction 153

5.2 Results and Discussion 156

5.2.1 *Ex-situ* Decomposition of $Cu(acac)_2$@SWNT to Cu_2O_x@SWNT 156
5.2.1.1 Attempted Monitoring of the Shift with *in-situ* Heating 161
5.2.2 Transformation of $Pt(acac)_2$@SWNT to Pt@SWNT 172
5.2.2.1 Attempted Monitoring of the Shift with *in-situ* Heating 177

5.3 Conclusion 181

5.4 Experimental 182
5.4.1 Fluorescence-Detected X-ray Absorption Spectroscopy (FD-XAS) 183
5.4.2 Electron Microscopy 183
5.4.3 Raman Spectroscopy 184

5.5 References 184

Chapter VI: Applications of Metal containing Carbon Nanostructures 187

6.1 Introduction 187

6.2 Results and Discussion 190
6.2.1 MNPs Encapsulated within GNFs 190
6.2.1.1 Materials Characterisation 191
6.2.1.2 Sensing Glucose 195
6.2.2 Metal Oxides Encapsulated within GNFs 201
6.2.2.1 Materials Characterisation 201
6.2.2.2 Glucose Sensing using MO_x@GNF 207

6.3 Conclusions 211

6.4 Experimental 212
6.4.1 Synthesis of MNPs@GNF 213
6.4.1.1 Synthesis of M_xO_y@GNF 213
6.4.2 HR-TEM Analysis 213
6.4.3 EDX Spectroscopy 214
6.4.4 Powder XRD Analysis 214
6.4.5 Thermogravimetric Analysis 214
6.4.6 Electrochemical Experiments 215

6.5 References 215

Concluding Remarks 217

7.1 References 222

Chapter I: Inorganic Materials inside Single-Walled Carbon Nanotubes

1.1 Introduction

In an ever changing world blighted by the overuse of natural resources fuelled by mass consumerism and an unsustainable population growth, it is becoming vital for humans to expand the boundaries of materials research to develop new, sustainable alternatives, and also refine current methods of material synthesis. In recent years a substantial amount of interest has been focussed on the potential use of nanomaterials as a saviour to the issues facing humanity, be it by using nanoparticles for energy storage,[1, 2] water purification,[3, 4] gene specific drugs,[5, 6] or sustainable food production.[7, 8] It is essential that the fabrication of such nanomaterials, and an atomic level understanding of their structures is fully understood. Confinement of a small number of atoms into a nanometre sized space is one of the most powerful methods for the construction of bespoke nanostructures, and nano-sized containers such as single-walled carbon nanotubes (SWNTs) can be effectively used for this purpose.

Since they were first positively identified by Sumio Iijima in 1991, SWNTs have received a significant amount of attention in the field of chemistry.[9] Technically a SWNT can be defined as a cylindrical species produced by rolling up a sheet of graphene along an arbitrary vector known as a chiral vector, and this forms a material with a hollow internal cavity. The chiral vector, which determines the structure of the nanotube, is defined by chiral indices (m,n), figure 1.1. These define the diameter of the nanotube and determine its helicity; when $m = n$, an armchair nanotube is formed, whereas when $n = 0$, a zig-zag nanotube is produced, and the electronic properties of the nanotube can be ascertained from these values. When $m - n = 3k$, where k is an

integer, the nanotube is metallic, but for all other values the nanotube is semiconducting, and the value of the bandgap is indirectly proportional to the diameter of the nanotube.[10]

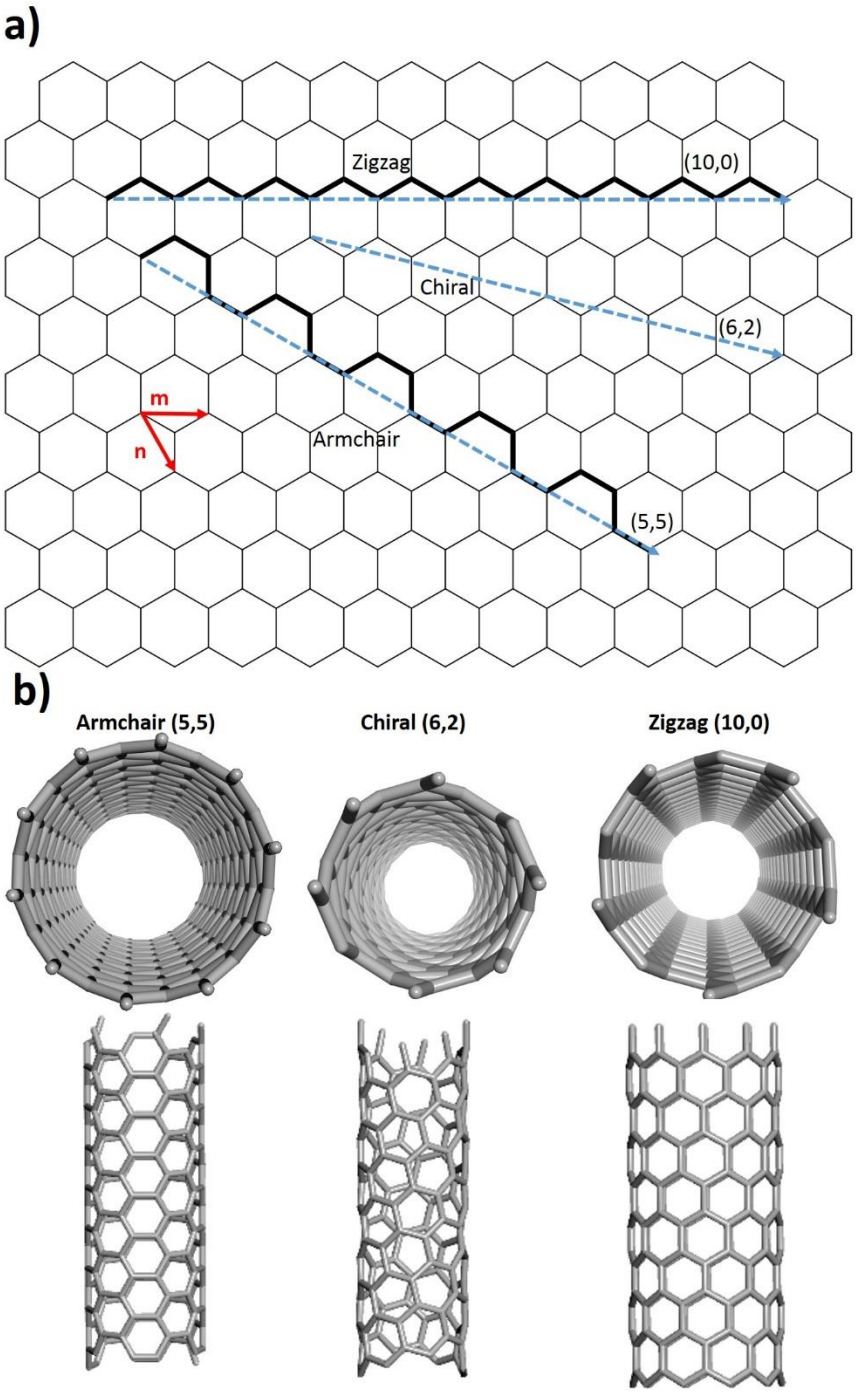


Figure 1.1: a) A schematic diagram showing how a sheet of graphene can be rolled along a rollup vector determined by chiral indices *m*,*n*. The value of such indices determines the structure of the nanotube, as shown by the examples (b).

With diameters between 0.7-2.0 nm and lengths up to the order of millimetres, they have an extremely high aspect ratio and can be treated as quasi-one-dimensional. As such they can be viewed as a bridge between the nanoscale and macroscale worlds.

Due to the network of covalent sp^2 bonds formed between each carbon atom, carbon nanotubes are one of the strongest materials known, with a Young's modulus of up to 3 TPa.[11] Moreover, they are excellent conductors of heat since they exhibit ballistic conduction along their entire length.[12] Additionally, they are extremely flexible and have high thermal stability; up to 800 ^{o}C in air,[13] and their chemically inert nature makes them ideal candidates for templates in nanomaterial formation. The hollow internal cavity of SWNTs allows other materials to be encapsulated within them, and the effect of confinement within the quasi-one-dimensional boundary of the nanotube determines the structure of the encapsulated species and can alter the physical and electronic properties of these systems.[14-18]

1.2 Characterisation Techniques

1.2.1 Transmission Electron Microscopy

It is possible to study encapsulated materials using high resolution transmission electron microscopy (HR-TEM) since SWNTs are only one layer of atoms thick and therefore appear almost transparent under the electron beam. Optical microscopes are limited in resolution to the wavelength of light, but with electrons as an imaging tool it is possible to achieve much higher resolution. Electrons are a form of ionising radiation, and upon contact with a specimen, a wide range of signals are generated which can be exploited as characterisation techniques (figure 1.2).[19] For example, elastically scattered electrons and electrons from the direct beam are responsible for

image generation in bright field TEM, whereas characteristic X-rays can be used for elemental composition confirmation (section 1.2.2).

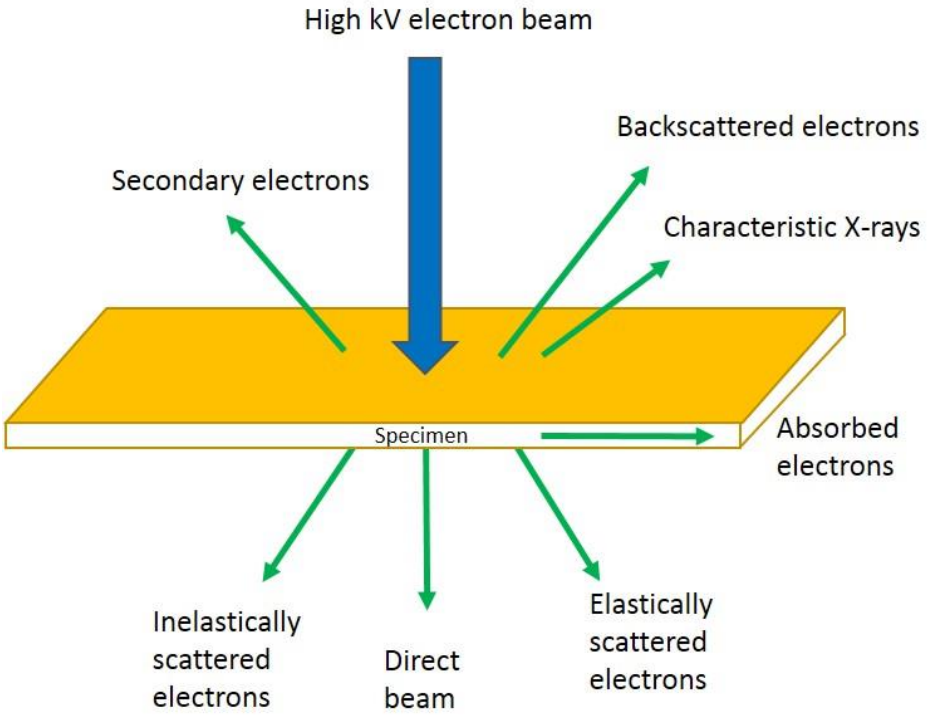


Figure 1.2: A schematic diagram showing the possible signals created upon a beam of high energy electrons interacting with a specimen.

Electrons are generated in an electron gun, accelerated towards an anode, and then using a condenser lens, focussed towards a specimen. Once electrons hit the specimen, they can interact with it in a variety of different ways, and it is elastically scattered electrons which create an image, after passing through a variety of different lenses and then reaching a detector (figure 1.3).

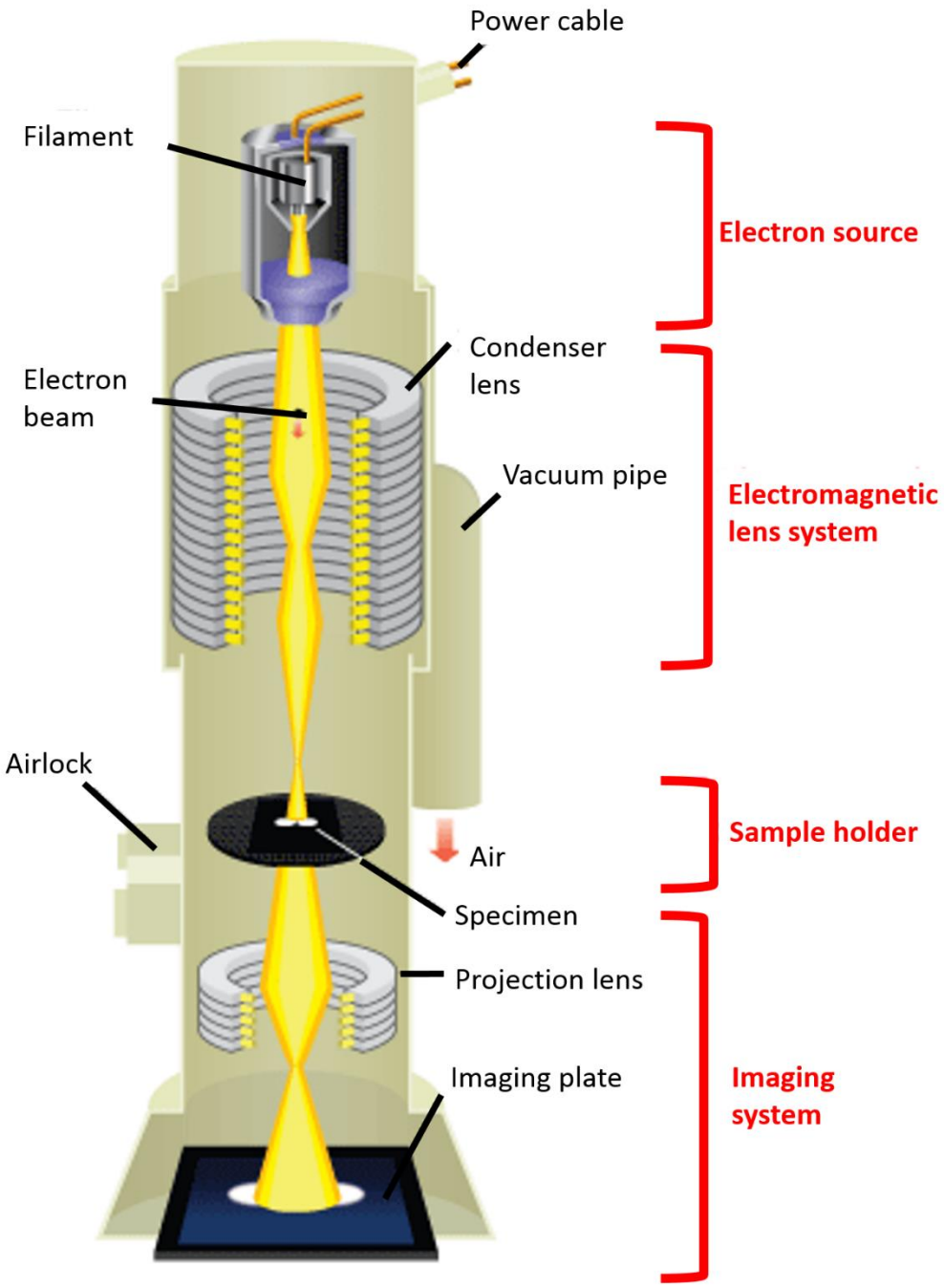


Figure 1.3: Schematic diagram showing how an image is created using TEM. Electrons leave a filament, pass through a condenser lens and interact with the sample. Following this, they pass through a series of lenses and reach a detector where an image is created.[20]

Theoretically, with an electron microscope operating at an accelerating voltage of 200 kV, it is possible to reach a resolution of 0.0025 nm.[19] In practice this is unachievable due to imperfections (aberrations) in the lenses, and typical resolutions of around 0.2

nm are possible. Recent developments in electron microscopy have allowed for such aberrations to be mitigated by making modifications to a particular microscope, and so it is conceivable now to achieve sub-angstrom resolution, making it possible to study materials with atomic precision.[21-23]

As well as imaging samples, is it possible to use energy from the electrons to initiate chemical reactions, and a variety of nanoscale transformations have been shown to occur using the energy of the electron beam. Petrik *et al.* have shown that single crystals of $NaNO_3$ can be altered by electron beam radiation, and it has been shown that diamond films can be fabricated on silicon substrates using the energy of the electron beam.[24, 25] Allen *et al.* have demonstrated the transformation of La@C_{82}@SWNT under electron beam irradiation to form an inner nanotube, which could provide an alternative route for the formation of double-walled carbon nanotubes, and more recently the formation of sulfur terminated graphitised nanoribbons (S-GNR) from encapsulated tetrathiafulvalene or the formation of fullerenes from a sheet of graphene have been demonstrated.[26-28]

1.2.2 Energy Disperse X-ray Spectroscopy

Energy Dispersive X-ray spectroscopy (EDX, also known as EDS) is a powerful analytical technique which allows for the determination of elemental composition of a sample. It can be used in conjunction with TEM, and involves exposing a sample to high energy electrons. The electrons interact with the sample, resulting in the ejection of a core electron and a hole in the inner shell (the K shell). This hole is then subsequently filled by an electron from a higher shell, and the excess energy is emitted as an X-ray. The energy of the X-ray is characteristic to a particular element, and so can be used to determine the presence of a certain element.

1.2.3 Raman Spectroscopy

In addition to microscopically analysing structures, it is also possible to exploit the electronic properties of SWNTs and explore them spectroscopically, including using Raman spectroscopy. While all allotropes of carbon are Raman active, the positions, widths and relative intensities of bands are different.[29, 30] A spectrum of pristine SWNTs (figure 1.4) contains a low frequency radial breathing mode (RBM) at frequencies below 200 cm^{-1} which is inversely proportional to diameter of nanotubes; a graphitic (G) band which is caused by planar vibrations of carbon atoms in the sp^2 carbon lattice and is sensitive to strain, curvature, symmetry and dopants, occurring around 1570-1590 cm^{-1}; and a D band at around 1300 cm^{-1} which is caused by disorder within the sp^2 lattice and is sensitive to defects such as atomic vacancies and sp^3 hybridised carbon atoms. Additionally, there is an overtone of this vibration, the G* band which usually appears between 2700-2900 cm^{-1}.[31-34] Upon encapsulation of guest species into the internal channel of SWNTs, the position of the G band can shift, and this can be used to give an indication as to whether electron density has been transferred between the SWNT and guest compound. A red shift is indicative of an electron transfer from the guest to the SWNT, whereas a blue shift is indicative of an electron transfer from the SWNT to guest, and this is caused by a contraction in the hexagonal rings of the SWNT as a result of transfer of π-electrons to the guest compound.[35]

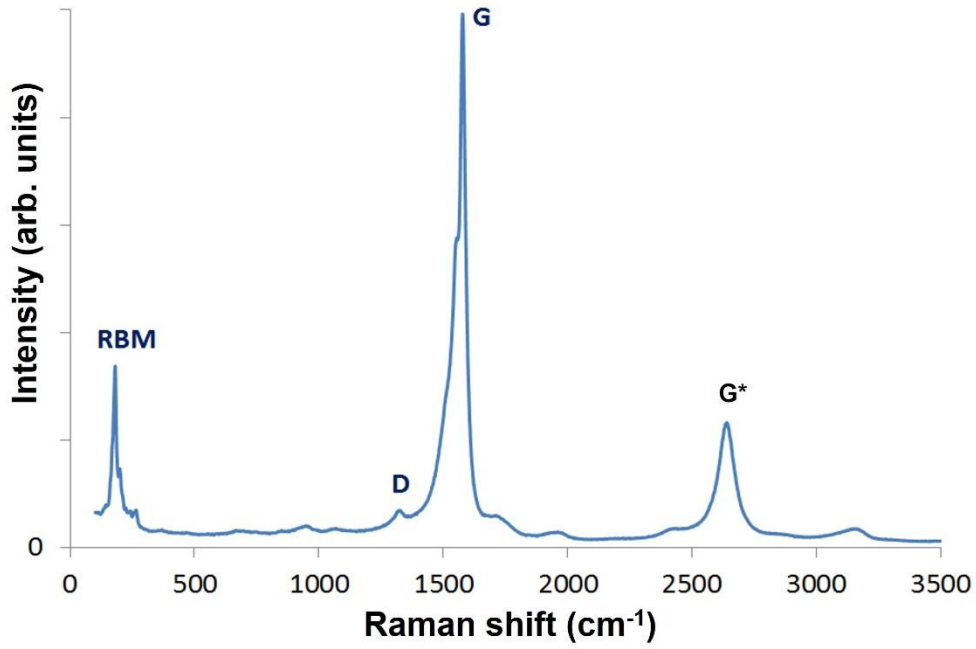


Figure 1.4: Raman spectrum of pristine SWNTs with the key features labelled.

1.2.4 Fluorescence-Detected X-ray Absorption Spectroscopy

X-ray absorption spectroscopy (XAS) and more specifically fluorescence-detected X-ray absorption spectroscopy (FD-XAS) can be used to probe the oxidation states of materials which have been encapsulated within SWNTs by detecting fluorescent X-rays as a function of X-ray energy. When a sample is exposed to X-rays, the electromagnetic radiation interacts with electrons in the atoms, and the X-rays can either be scattered, absorbed or excite the electrons (figure 1.5).

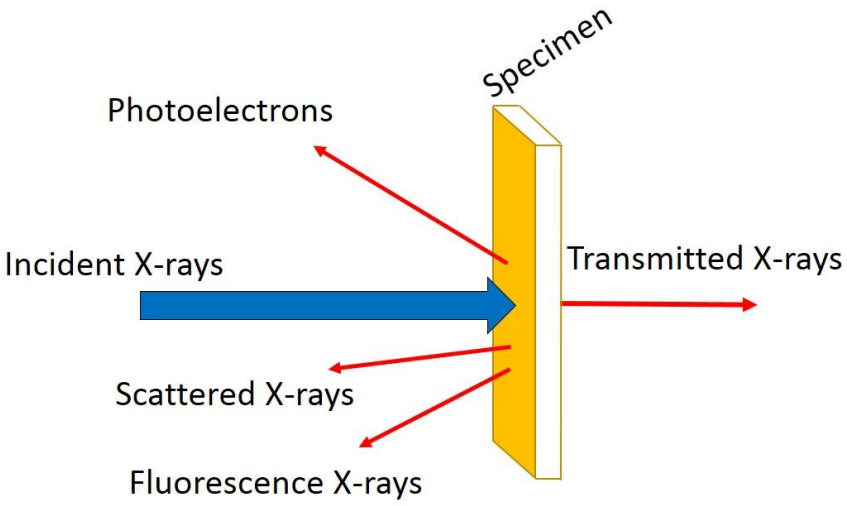


Figure 1.5: Schematic showing incident X-rays hitting a sample. X-rays can be transmitted through the sample or scattered back. In addition, photoelectrons and fluorescence X-rays can be detected from the sample.

At certain X-ray energies, the energy of incident X-rays is sufficient to result in excitation of a core electron to a continuum state, i.e. produce a photoelectron. This leads to an electron from a higher shell falling to occupy the position and due to conservation of momentum an Auger electron or fluorescent photon is emitted (figure 1.6), and this leads to a peak in fluorescence being detected.

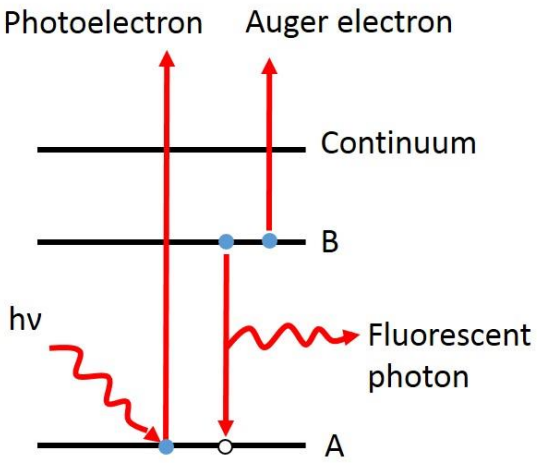


Figure 1.6: Schematic diagram showing a core electron (level A) being exposed to an incident X-ray. At a certain X-ray energy, absorption of an X-ray photon, hv, leads to excitation of the electron to a continuum state, and subsequently an electron from a higher shell (level B) falls. Due to conservation of momentum, an

Auger electron or X-ray fluorescence is produced, it is the X-ray fluorescence which is monitored.

The energies of the absorbed X-rays at these particular absorption peaks (edges) correspond to the binding energies of electrons in the K, L, M shells of the absorbing elements; *e.g.*, an absorption from the K shell is caused by excitation of an electron from the 1s orbital, whereas an excitation of electron from the L_{III} edge corresponds to excitation from one of the three 2p orbitals. Since electrons are more tightly held for compounds of a higher oxidation state, X-rays of a higher energy are required to remove electrons, and so the position of the edge correlates to the oxidation state of the compounds, and XAS has been used to discriminate between the oxidation states of various metal nanoparticles.[36-39]

A FD-XAS can be divided into 4 regions (figure 1.7). Firstly, the pre-edge which is caused by electronic transitions from the core to higher unfilled orbitals and can give information about the electronic structure of materials. Secondly, there is the X-ray absorption near edge structure (XANES) which is due to transitions of electrons to non-bound levels and the position of which is what can be used to determine oxidation state. At energies between 10-40 eV above the edge is the near-edge X-ray absorption fine structure (NEXAFS) region and energies over this form part of the extended X-ray absorption fine structure region (EXAFS). The final two regions can provide information on the coordination environment of the sample being probed as the resultant signal is caused by interference of outgoing electron waves by backscattered electrons from neighbouring atoms, and therefore can be used to probe the coordination environment and even bond lengths of materials, as demonstrated by Eliseev *et al.* for the encapsulation of nanomaterials in SWNTs, such as CuX (X = Cl, Br, I).[40]

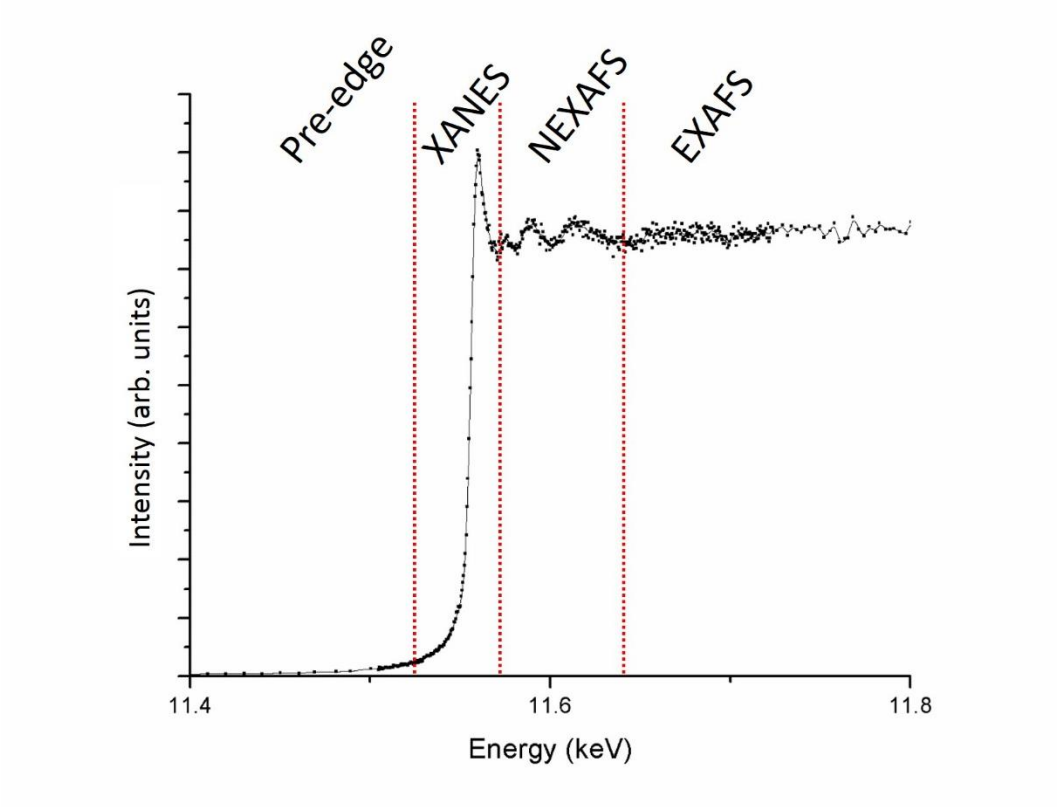


Figure 1.7: FD-XAS of Pt@SWNT with the four regions labelled. For the purpose of determining oxidation state of materials in SWNTs, the XANES region is monitored; however, useful information about coordination environment of the complex can also be obtained from the NEXAFS and EXAFS regions.

In summary, TEM can be used to structurally characterise materials at the atomic level, and the addition of EDX allows the atomic composition of the analysed materials to be determined. The electron transfers, and subsequently electronic properties of materials can be determined by employing a combination of both Raman spectroscopy and FD-XAS.

1.3 Methods of Nanotube Filling

Three general procedures for the filling of guest compounds into SWNTs can be used, and these depend on the nature of the guest. Before any compound can be inserted, the termini of the SWNTs must be opened, and this can be achieved by either oxidising the SWNTs by heating in air, which can be catalysed by silver

nanoparticles;[41, 42] treating with an oxidising agent such nitric acid,[43-45] or hydrogen peroxide in the liquid phase,[46] or by a mechanical method such as ball-milling,[47, 48] or diamond abrasion.[49] The efficiency of encapsulation depends on the relationship between the diameter of the guest compound and diameter of the nanotube, (d_{NT});[50] for the most effective interactions, the distance between the concave surface of nanotube and guest compound has to be close to the van der Waals gap of *ca.* 0.3 nm, as this provides optimum van der Waals interactions which hold the compound inside the SWNT securely. Using too large a nanotube, or too small a guest species can lead to less effective encapsulation and it is possible for the encapsulated species to subsequently leave the nanotubes.

When SWNTs are immersed in a liquid, and as long as the liquid has a surface tension no greater than 200 mN/m, it can spontaneous fill the nanotube.[51] Although this is often referred to as capillary filling, for SWNTs which have diameters of < 2 nm, the classical continuum approximation of liquids fails as the meniscus disappears and so technically capillary action is an approximation. Theoretical investigations of this method show that it has a stepwise mechanism where the anions and cations which are initially disordered in the liquid phase become ordered upon being confined in nanotubes, and is driven by the initial entry of cations which are under coordinated and so require anions which follow.[52] As long as the material being encapsulated has a low enough surface tension and melts without decomposition it can be inserted, and this ubiquitous method has been used to encapsulate a wide range of different metals and inorganic materials, as described later in this chapter.

For species that can be vapourised, sealing them in a container under vacuum with opened SWNTs and heating to above the sublimation temperature of the compound results in the vapours of the guest species penetrating the nanotube and becoming

trapped inside. This method has been used to encapsulate a variety of organic compounds,[53, 54] fullerenes,[28, 55, 56] and organometallic complexes[57-59] into SWNTs, as well as non-metallic elements such as I, S, Se, and Te.[60, 61] This is a stepwise mechanism which involves compounds adsorbing onto the outer surface on the nanotube, then diffusing into the nanotube channel and has been studied in detail for the encapsulation of C_{60} (figure 1.8).A small energy barrier, *ca.* 0.3 eV for C_{60}, needs to be overcome for compounds to enter the nanotube, but this is greatly compensated for upon encapsulation.[62, 63]

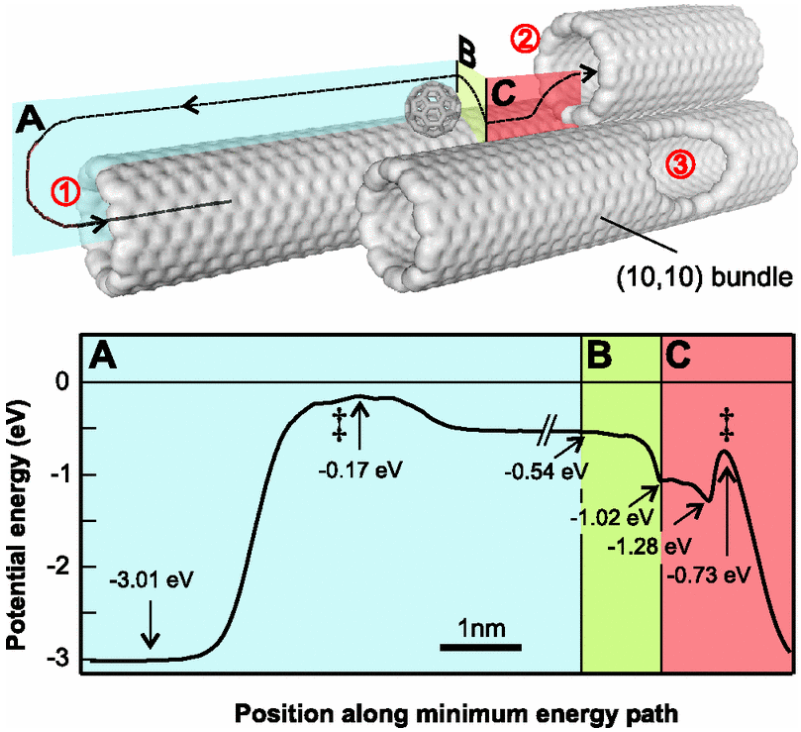


Figure 1.8: Model and energy profile showing how the energy of a fullerene changes as it becomes encapsulated inside a (10, 10) SWNT. There is a slight barrier (0.3 eV) to overcome in order for encapsulation to take place, but then once the compound is encapsulated the potential energy decreases. [20]

For moieties which cannot be melted or vapourised, it is possible to immerse SWNTs into solutions of these materials, but in order for an encapsulation to be successful, the interaction between the SWNT and guest compound must be stronger than solvent-nanotube interactions and solvent-guest interactions,[64] and this method is

relatively inefficient as the guest compound is usually surrounded by many solvent molecules, which can interfere with the filling process, but has been shown to encapsulate C_{60} using n-hexane as the solvent.[65] Additionally, guest compounds can be encapsulated using supercritical fluids, and this has been demonstrated with the encapsulation of fullerenes in super-critical CO_2.[66]

Herein is an overview of inorganic materials encapsulated into SWNTs, with emphasis being placed on how the materials change as a result of confinement into the SWNTs.

1.3.1 Oxides/Hydroxides in SWNTs

A small number of metal oxides/hydroxides have been encapsulated into SWNTs and these are summarised in table 1.1.

Table 1.1: A summary of metal oxides/hydroxides confined inside SWNTs, and the effect of confinement.

Material	Group	Effect of confinement	Ref.
MOH (M = K, Cs)	1	Reduction of Cs-Cs atomic distances observed. Washing with H_2O led to emptying of SWNTs.	67, 68
$Ba(OH)_2$	2	One-dimensional $Ba(OH)_2$ crystals formed.	68
CrO_3	6	CrO_3 shown to accept electron density from the SWNT.	69, 70
MoO_3	6	Reduction in Mo:O ratio.	71
Re_2O_7	7	Stoichiometry changes from $ReO_{3.5}$ to $ReO_{1.5}$.	72
PbO	14	Nanotubes become sensitive to light irradiation and decompose, leaving free PbO wires.	73
$UO_2(CH_3COO)_2$	III	Formation of UO_2. A slight contraction in U-U atomic distances was observed.	67, 68
$UO_2(NO_3)_2$	III	Dissociation of NO_3, and formation of UO_2	67

Initially, attempts to open the termini of SWNTs involved heating in the presence of metal hydroxides, which consequently led to the formation of MOH@SWNTs, and so the guest then had to be removed using water. The encapsulation of MOH (M = K, Cs) has been demonstrated by Thamavaranukup *et al*. using a molten filling method which led to formation of nanocrystals inside the SWNT.[67] HR-TEM was used to observe CsOH@SWNT and a slight contraction in the Cs-Cs interatomic distances were observed compared to bulk CsOH (figure 1.9). Treating both MOH@SWNT samples with water lead to the removal of both metal hydroxides (as confirmed by their absence in EDX spectra). This allowed the solution filling of both uranyl acetate and uranyl nitrate, which led to dissociation of the complexes and the formation of UO_2. Although the purpose of adding MOH (M = K, Cs) was only to open up the SWNTs allowing for subsequent filling, the formation of a low-dimensional material with atomic distances confined by the nanotube, as in the case of CsOH, was shown.

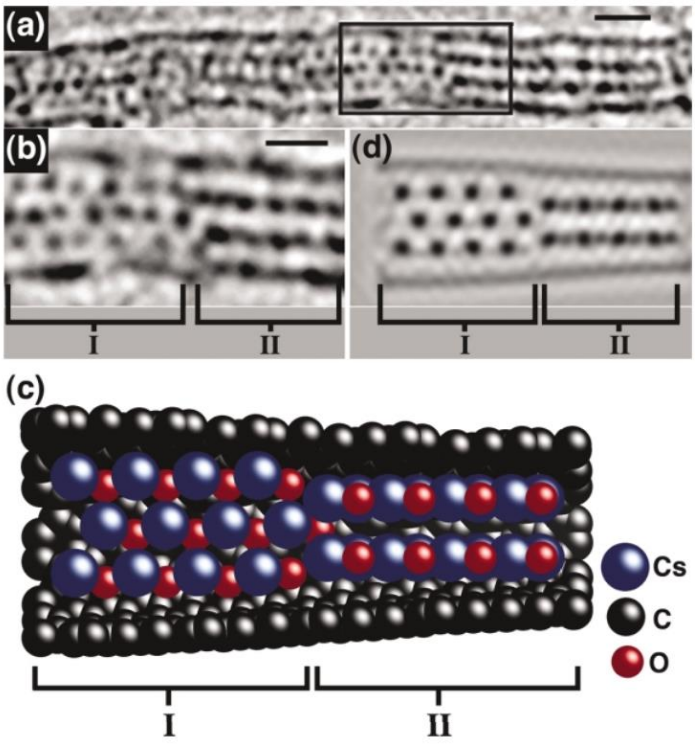


Figure 1.9: a) TEM image of CsOH@SWNT (the scale bar is 1.0 nm); b) Enlarged TEM image of CsOH@SWNT (the scale bar is 0.6 nm); c) Model of

the two projections of CsOH as present in b) I and II; d) Simulated TEM image based on c).[67]

Following on from the successful formation of UO_2 nanocrystals by pre-treating the nanotube with MOH (M = K, Cs), the treatment of SWNTs with of $Ba(OH)_2$ was carried out by Shao *et al.* in order to open the nanotube termini.[68] Again, the encapsulated hydroxide was removed by stirring in water, and both KI and $UO_2(CH_3COO)_2$ were subsequently encapsulated separately. The encapsulation of $UO_2(CH_3COO)_2$ then led to the formation of UO_2, which was removed *via* treatment with concentrated HCl, as confirmed by HR-TEM (figure 1.10).

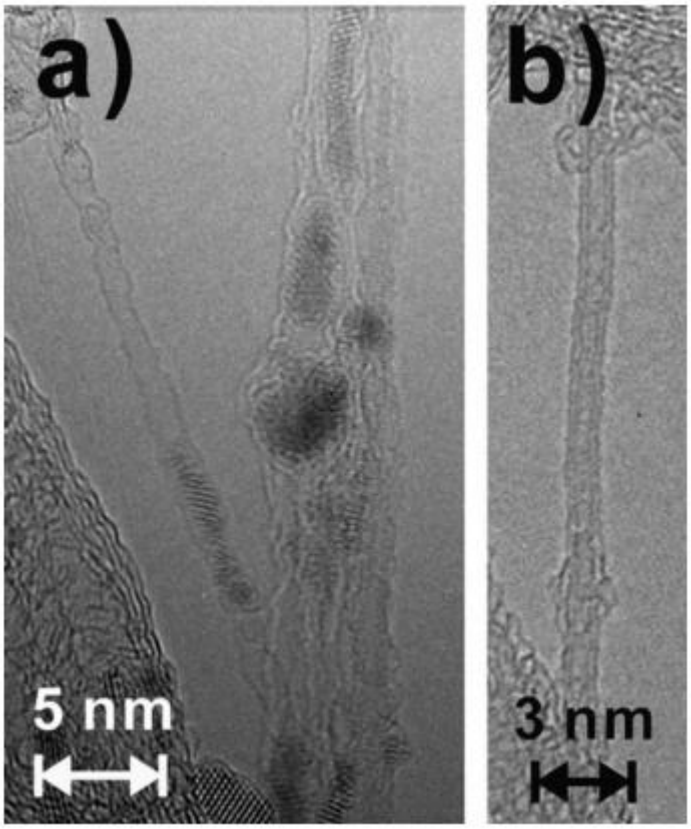


Figure 1.10: a) HR-TEM image of a uranium containing compound encapsulated inside SWNTs; b) HR-TEM image of an empty carbon nanotube after removal of the uranium compound by stirring in concentrated HCl.[68]

Many studies have been undertaken to investigate the charge transfer properties of guest compounds encapsulated into SWNTs. Curio *et al*. have shown that the encapsulation of CrO_3 leads to electron transfer from the SWNT to the guest species,[74]

and there is scope for such materials to be used as electrodes for supercapacitors.[70] However, the structure of CrO_3 within SWNTs was not studied, and it remains unknown whether confinement in nanotube affects the structure of the guest compound.

The addition of certain guest materials into SWNTs significantly alter the properties of the SWNT, as is the case with PbO. Hulman *et al*. demonstrated that encapsulating PbO into SWNTs leads to the formation of a low-dimensional PbO crystal (figure 1.11), but this results in the nanotubes becoming sensitive to laser radiation, and at high laser intensities oxidation of the nanotubes occurred, which does not occur for pristine SWNTs under the same conditions, and therefore the encapsulated material could be used as a catalyst for photoactive nanotube oxidation.[73]

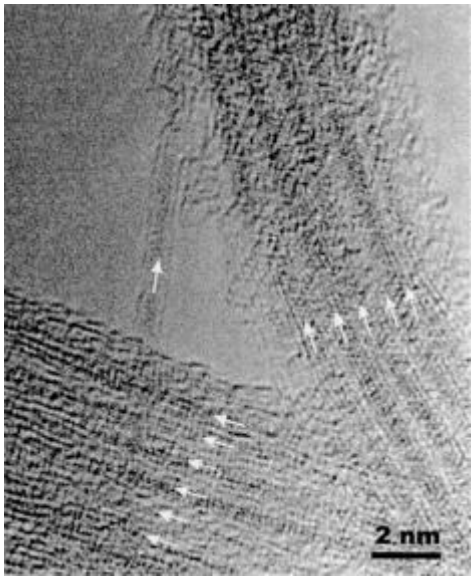


Figure 1.11: HR-TEM image of PbO@SWNT. The white arrows show the position of PbO inside the SWNTs.

In addition to the molten filling method to introduce metal oxides/hydroxides to SWNTs, the sublimation method has also been employed. Encapsulation of Re_2O_7 was successfully attempted by Costa *et al*., and led to the formation of Re_xO_y@SWNT, as confirmed by HR-TEM, and a slight contraction on Re-Re

interatomic distances is observed, compared to bulk Re_2O_7. The stoichiometry of the original complex has changed, and an oxygen deficient compound with a stoichiometry of $ReO_{1.5}$ is proposed, which is attributed to being caused by electron beam irradiation (operated at 300 kV) and confinement inside the SWNTs.[72] Bulk Re_2O_7 has a large unit cell, with dimensions *ca.* 12 Å x 15 Å x 5 Å, which is too sterically demanding to fit into SWNTs, and so it is not surprising that a new structure has formed.[75]

Reduction by H_2 at 200 ^oC led to the formation of Re metallic clusters, and this occurred at a much lower temperature than that required to reduce bulk Re_2O_7, which usually occurs above 400 ^oC (figure 1.12).[76]

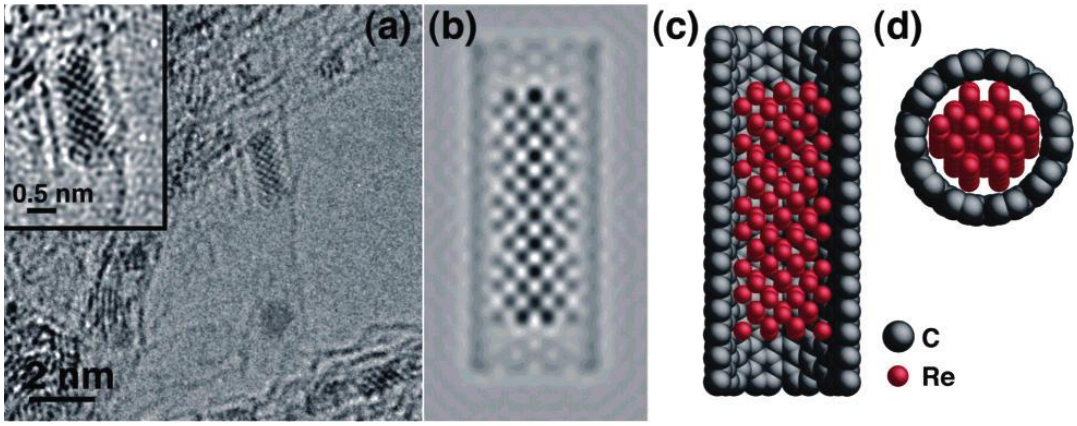


Figure 1.12: a) Image of a cluster of Re metal encapsulated in a 1.5 nm diameter SWNT. In the top left side the magnification shows the lattice structure of the cluster; b) Simulated image using the composite model in part c; c) Composite model of the SWNT plus the encapsulated Re cluster (side on view); d) Top end view of the model from part c.[76]

More recently, MoO_3 was encapsulated into SWNTs by Sagawa *et al*. using a molten filling method.[77] HR-TEM was employed to study the lattice structure of the encapsulated crystal and it was concluded that there was the formation of a new type of a MoO_x crystal, where the number of oxygen atoms have been reduced ($x < 3$). However, it is not clear whether this is as a result of confinement or electron beam

irradiation, although the energy of the electrons in this analysis were 100 kV, which is much lower than that used by Costa *et al.* for the analysis of Re_2O_7@SWNT, but still great enough to lead to changes in structure (see Chapters II and III). The unit cell of bulk MoO_3 is *ca.* 4 Å x 4 Å x 7 Å, which is small enough to fit inside a SWNT, and so it is possible that the species is being reduced under electron beam irradiation, or just that the new structure was more stable when confined inside the SWNT.[78]

Overall, only a small number of metal oxides and hydroxides have been investigated in carbon nanotubes, but there is a clear indication that the stoichiometry (MoO_x, Re_xO_y) and the dimensions of the crystal lattice of the guest compounds (Re_xO_y, CsOH) can be controlled by the confinement in nanotubes, which can potentially open new methodologies for synthesis of unusual inorganic structures. It is interesting that in both cases the observed changes in the crystal lattice parameter indicate reduction of interatomic distances in the nanotube, which is a result of the guest species altering its size to best fit inside the SWNTs. Furthermore, the electron transfer taking place between the host nanotube and the guest metal oxide (such as CrO_3) can have an effect on physicochemical properties of SWNT, as demonstrated for example for PbO@SWNT where the nanotubes showed high susceptibility to photo-induced oxidation.

1.3.2 Halide Salts in SWNTS

In addition to metal oxides and hydroxides, a plethora of halide salts have been encapsulated into SWNTs (see tables 1.2, 1.3 1.4), with most studies exclusively focussing on either the morphology of material formed using microscopy, or electronic transfers using spectroscopic techniques. Initial studies involved the addition of metal halides into SWNT followed by reduction to form metallic

nanoparticles (MNPs). Sloan *et al.* encapsulated $RuCl_3$ and $CoCl_2$ using a solution filling technique and exposed to H_2 to form MNPs@SWNT (M = Ru, Co).[79]

1.3.2.1 Main Group Halides

Early studies on halogen containing salts in SWNTs was dedicated to the encapsulation of alkali metal halides to form new one-dimensional crystals, but then this methodology was extended to include a variety of other main group and transition metal halides (table 1.2).

Table 1.2: A summary of main group metal halides that have been encapsulated into SWNTs.

Material	Group	Effect of confinement	Ref.
KI	1	The number of atomic layer in the crystal depends on the diameter of SWNTs, with a 4 % expansion in interatomic distances.	80, 81
MI (M= Na, Rb)	1	No effect, similar to bulk structure.	82
LiI	1	Lattice expansion of 25% compared to bulk LiI.	82
CsI	1	No effect, interatomic distances consistent with bulk CsI.	82
BaI_2	2	Reduction of coordination number of barium from 9 to 6.	83
$TlCl_3$	13	Electron density is transferred from the SWNT to $TlCl_3$.	84
PbI_2	14	Becomes amorphous in narrower SWNTs. The 2H polymorph forms preferentially in wider SWNTs.	85
SnF_2	14	One-dimensional crystal formed, with similar interatomic distances to that of bulk SnF_2.	86 87

Meyer *et al.* demonstrated the filling of KI into a 1.6 nm diameter SWNT using the molten filling technique, and this led to the formation of a one-dimensional KI crystal that was structurally characterised using HR-TEM (figure 1.13).[80] It was shown that the diameter of the nanotube directs how many layers of potassium and iodine atoms are present, as when a slightly narrower SWNT (d_{NT} = 1.4 nm) was used, only a bi-layer KI crystal was observed.[81] Both crystals exhibited slight contractions in atomic spacing which was attributed to confinement in the SWNTs. This is important as it demonstrates the use of SWNTs as templates to control development of nanocrystals, as the size of SWNTs clearly directs the size of the crystal formed.

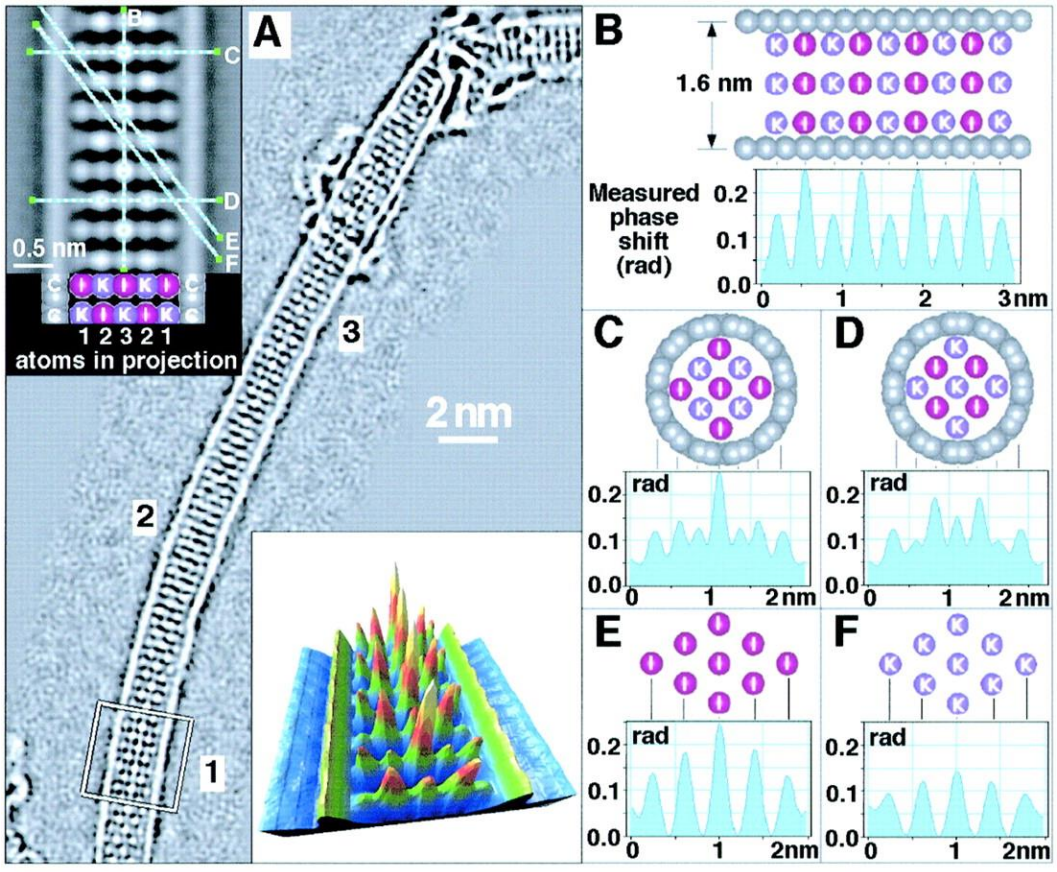


Figure 1.13: a) Phase image showing KI@SWNT, reconstructed from a focal series of 20 images. The upper left inset shows an enlargement of region 1 and a schematic illustration depicting alternating arrangement of I-2-3I-2K-I and K-2I-3K-2I-K (100) layers within the crystal. The lower right inset shows the surface plot of region 1. (b-f) Single-pixel line profiles from line traces marked b-f in the upper left inset in a).[80]

Following on from the successful encapsulation and characterisation of KI@SWNT, this methodology was extended by Sloan *et al.* to encapsulate the other alkali iodides (M = Li, Na, Rb and Cs).[82] It was shown that with the exception of encapsulated CsI which forms both body centred cubic and rock salt structure types, all other alkali metal iodides formed crystallised in rock salt structure form. Furthermore, the diameter of SWNTs was shown to directly influence the thickness of the nanocrystals, as all were shown to be between two and six atomic layers in thickness depending on the diameter of the nanotube. As an extension to this, HgI_2 was crystallised in ultra-narrow nanotubes (d_{NT} = 0.8 nm) and was shown to form chains only 1 and 2 atoms thick. Although this work was carried out in treble-walled carbon nanotubes, it clearly demonstrates the effect of confinement on atomic structures.

The filling of SWNTs with BaI_2 was undertaken by Sloan *et al*. and showed that upon encapsulation, the lattice of the guest dramatically changes. Confinement within the internal channel of SWNTs has led to a decrease in the coordination number of barium, from 9 in the bulk to 6, although it should be mentioned that due to the similarity in atomic masses of Ba (Z = 56) and I (Z = 53), their electron scattering power is similar and it is difficult to discriminate between them using only HR-TEM (figure 1.14),[83] and methods for how to discriminate between heavier elements using TEM will be discussed further in Chapter IV.

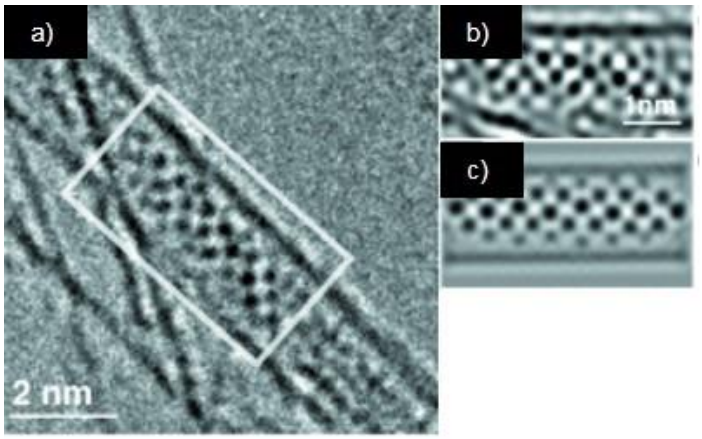


Figure 1.14: a) HR-TEM image of BaI_2@SWNT; b) Detail from boxed region in a); c) Simulated HR-TEM image. [83]

In addition to s-block metal halides salts inside SWNTs, the encapsulation of another main group iodide, PbI_2 has been successfully demonstrated by Flahaut *et al.*[85] Again it was found that the diameter of the nanotube has a profound influence on the structure of the filled material, with the coordination number of ions greatly reduced upon confinement. Bulk PbI_2 exhibits two crystal polymorphs, a 2H-type and 4H-type, with direct control on each polymorph being needed for the material to be a viable candidate for use in semiconductors, and confinement inside SWNT has been shown to lead to the 2H-type being preferentially formed. Additionally, although PbI_2 has many useful applications such as being a detector for nuclear radiation, it is highly toxic, and so confining it into a SWNT could alleviate such problems and allow it to be used more readily.[88]

PbI_2 is the only plumbous halide to be encapsulated into SWNTs, but another group 4 halide, SnF_2 has been encapsulated using a molten filling approach. Due to the small atomic number of the fluoride anion, it is not resolved in HR-TEM, but instead a highly ordered network of stannate cations are viewed.[87] A two-layer structure of SnF_2 has been proposed, and this is supported by TEM simulation.[86]

Finally, $TlCl_3$ was encapsulated into SWNTs using a molten filling method, and this led to large blue shift in the position of the G band of Raman spectroscopy showing electron transfer from the SWNT to guest compound. The magnitude of this transfer was compared to both a main group and lanthanide chalcogenides, and will be discussed later in this section, although no detailed structural analysis of $TlCl_3$-@SWNT carried out.[84]

In summary, a variety of different main group halide salts have been encapsulated into SWNTs, and the diameter of SWNTs has been shown to have a significant effect on directing the morphology of crystals formed, with narrower nanotubes leading to fewer crystal layers (as shown for the case of MI (M= Na, K, Rb, Cs), and selective formation of certain crystal polymorphs as with PbI_2. Only a handful of studies have investigated how encapsulated materials alter the electronic properties of SWNTs, with electron transfer shown to occur from the host nanotube to guest compound for both $TlCl_3$ and PbI_2.

1.3.2.2 Transition Metal Halides

A range of different transition metal halides, MX_Y (X = Cl, Br, I; Y = 1, 2) have been encapsulated into SWNTs, with either the metal of a particular period or group, or halide being systematically changed, and this has led to trends in crystallinity and electronic properties to be studied systematically (table 1.3).

Table 1.3: A summary of transition metal halides encapsulated within SWNTs.

Material	Group	Effect of confinement	Ref.
$MnCl_2$	7	Accepts electron density from SWNT, greater than $MnBr_2$ does.	89
$MnBr_2$	7	Accepts electron density from SWNT, but less effectively than $MnCl_2$.	89

$FeCl_2$	8	Two different Fe^{2+} environments found, which is caused by confinement.	90
$FeBr_2$	8	Electron transfer from the SWNT to $FeBr_2$.	90, 91
FeI_2	8	Encapsulated FeI_2 has slightly elongated interatomic distances relative to bulk FeI_2. Electron transfer from SWNT to FeI_2.	90
$CoBr_2$	9	Electron transfer from SWNT to $CoBr_2$.	91
CoI_2	9	Ovoid distortion of SWNT by CoI_2 crystal.	92
$NiBr_2$	10	Electron transfer from SWNT to $NiBr_2$, 5% reduction in interatomic distances upon encapsulation.	91, 93
$NiCl_2$	10	Electron transfer from SWNT to $NiCl_2$, 5% reduction in interatomic distances upon encapsulation.	93
CuI	11	Two different CuI crystals formed, depending on SWNT diameter.	40, 94-96
CuCl	11	Cu-C bonding has occurred upon encapsulation.	40
CuBr	11	Electron density transferred from SWNT to CuBr.	97 40, 96
AgCl	11	Remains non crystalline in SWNTs.	17
AgBr	11	Hexagonal crystal structure which is usually only present in the bulk at high pressure is observed.	96, 98
AgI	11	Slight contraction of interatomic distances.	17
HgI_2	12	One-dimensional chain of Hg and I atoms present.	82
ZnX_2 (X = Cl, Br, I)	12	All ZnX_2 compounds accept electron density from the SWNT.	82
CdX_2 (X = Cl, Br, I)	12	All ZnX_2 compounds accept electron density from the SWNT.	14

FeX_2 (X = Cl, Br, I) molecules have been encapsulated into SWNTs using a molten filling method, and although the encapsulation was highly successful and most of the

nanotubes were full as determined by HR-TEM, a detailed structural analysis of the crystals was not undertaken, but it is revealed that the encapsulation of FeI_2 has led to the formation of FeI_2 nanocrystals with slightly elongated interatomic distances compared to those of bulk FeI_2.[90] Furthermore, Raman spectroscopy was used to investigate charge transfers between the nanotube and guest material and a blue shift in the position of the G band was observed for all materials (typically + 10 cm^{-1}) which shows that charge is being transferred from the SWNTs to each guest structure. Additionally, XAS shows that there is a change in the work function of the SWNTs which is caused by encapsulation. For encapsulated $FeCl_2$, two different Fe^{2+} environments were found, and so whilst detailed structural analysis has not been undertaken, the effects of confinement are still observed.

More recently, Raman spectroscopy of $FeBr_2$@SWNT was studied alongside encapsulated $CoBr_2$ and $NiBr_2$ by Kharlamova, and the ability for the SWNT to transfer charge to the guest species was shown to increase in the order $NiBr_2 < CoBr_2 < FeBr_2$, which is possibly attributed to iron being the most electropositive of the three elements.[91] Clearly this is of interest as it demonstrates that the electronic modification of SWNTs can be tuned by systematically altering the guest species.

This relates well to previous work investigating NiX_2@SWNT (X = Cl, Br) where both materials were shown to accept electron density from the nanotubes, but no comparison as to which of the two accepts more was made.[93] It is noted that inter-atomic spacings in both structures decreased by about 5% upon encapsulation due to the effects of nanotube confinement, but the encapsulated layered structures still formed similar hexagonal structures to those of bulk Ni(II) halides. Additionally, the filling rate was higher for $NiBr_2$ than $NiCl_2$, and while a reason for this is not

discussed, it has also been discovered in other metal halide examples (see below) where it is attributed to the smaller ionic radius of the chloride anion.

In addition to $CoBr_2$, CoI_2 has been inserted using a molten filling method.[92] In this case an extended chain of nanocrystal has been created in the nanotube, with rotational symmetry clearly visible. Following on from previous examples (such as alkali metal halides) where the formed nanocrystals have slightly distorted lattices due to confinement, in this study it is shown that the SWNT also changes shape to accommodate the encapsulated crystal, with the usual circular cross section of the nanotube becoming ovoid in geometry (figure 1.15). This has been attributed to the strong interaction between SWNT and formed CoI_2, although no studies on electron transfers between either moiety have been undertaken here.

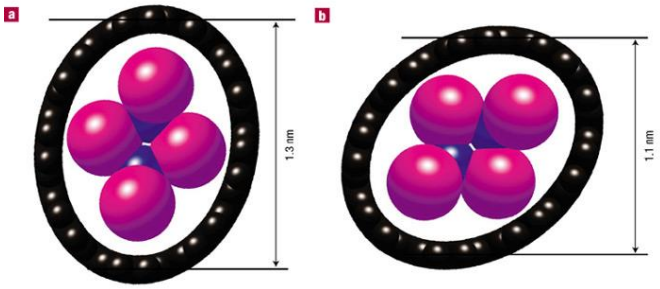


Figure 1.15: a,b) Cross-sections of CoI_2@SWNT showing ovoid distortion to the SWNT by the nanocrystal.[92]

Additionally, the encapsulation of group 11 halides has been thoroughly investigated, with HR-TEM has been used to study CuI@SWNT.[94, 95] Two different types of CuI crystals were formed depending on the diameter of SWNT used, which shows the templating effect of SWNTs to control the formation of different structures.[94] Due to advances in microscopy, more detailed images of CuI@SWNT have recently been obtained, and these continue to support the correlation between the structure formed in SWNTs and the nanotube diameter.[95] Moreover, the electronic properties have been studied using Raman spectroscopy, and a large blue shift in the G band of

SWNTs compared to pristine SWNTs is shown, demonstrating electron transfer from SWNT to CuI, which is in agreement with other metal halides encapsulated within SWNTs.

Furthermore the electronic properties of CuI along with other Cu(I) halides, CuX@SWNT (X = Cl, Br) has been extensively studied.[40] Optical absorption spectroscopy was used to show that although all halides accept charge from the nanotube, the amount of charge transferred from the SWNT increases in the sequence CuI < CuBr < CuCl which is attributed to the increased electron affinity of the three halides. Raman spectroscopy also shows charge transfer as a blue shift in the position of the G band of all materials is shown (figure 1.16), and this supports X-ray absorption data which shows a degree of Cu-C bonding as a result of encapsulation. Crystallinity was shown to be inversely proportional to the size of the anion, and this was attributed to both the larger iodide anions being able to form more effective van der Waals interactions with the interior of the nanotube sidewall, and also due to the electronegativity of the anions. A similar investigation into how the halides affects electron acceptor/donor properties of the nanotube has recently been carried out by Kharlamova for MnX_2 (X = Cl, Br,) where it was shown that $MnCl_2$ led to a stronger electron transfer from the SWNT than $MnBr_2$, which although not discussed, could be attributed to the greater electron affinity of Cl.[89]

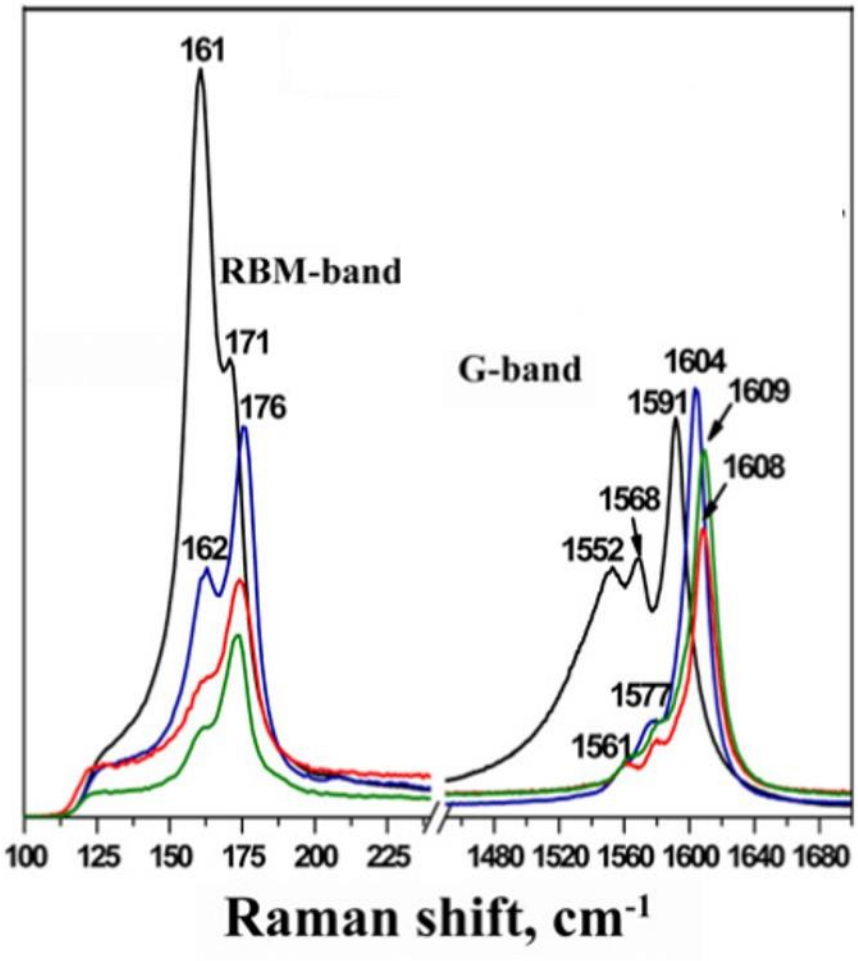


Figure 1.16: RBM and *G* bands of the Raman spectra of empty SWNTs (black line), CuCl@SWNT (red line), CuBr@SWNT (green line) and CuI@SWNT (blue line). Encapsulation of CuX (X = Cl, Br, I) leads to shift in the position of both the RBM and G bands.[40]

As an extension, a detailed HR-TEM analysis of CuBr and CuI has been undertaken along with AgBr,[96] and it was found that for all the encapsulated crystals, phase transition between cubic and hexagonal structures can occur as a result of electron beam irradiation, which in this case occurred with a TEM operating at 80 kV. This is interesting as it shows one effect of both confinement and electron beam irradiation on nanomaterials to form structures otherwise not known for bulk crystals. For AgBr, a hexagonal structure is observed, which in the bulk is only possible at high pressures,[99] and so the internal cavity of the SWNT is suggested to emulate a high

pressure system by acting to increase the local concentration of particular atoms, in a similar way to how a high pressure reaction vessel would.

The trend that heavier halides for a particular metal halide salt have less of an effect on charge acceptor behaviour is present for the AgX (X = Cl, Br, I) salts which have been encapsulated within SWNTs, and correlated with the same trend observed for CuX@SWNT (X = Cl, Br, I).[98] Quite interestingly, HR-TEM shows that upon encapsulation AgCl does not crystallise out in SWNTs, and that although AgX (X = Br, I) both form hexagonal closed pack structures upon encapsulation, the crystallinity is higher for the iodide containing moiety (figure 1.17). This is attributed to the unit cell of AgI being a more ideal size to complimentarily fit into SWNTs, and a slight contraction in interatomic atomic distances for both AgX (X = Br, I) was also observed. [100-102]

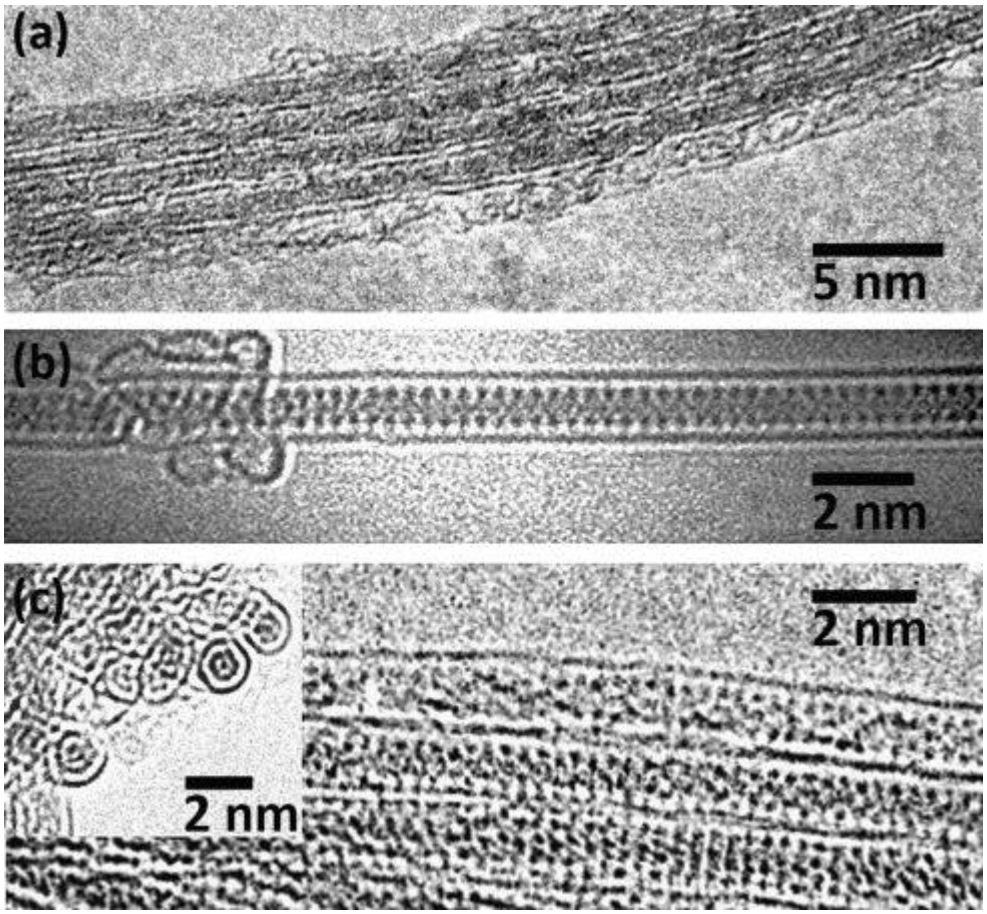


Figure 1.17: HR-TEM images of AgCl@SWNT a); AgBr@SWNT b); and AgI@SWNT c). Inset on c) illustrates cross-sectional view of AgI@SWNT hybrid bundle. [98]

Finally, halides of the group 12 metals (MX_2, M = Cd[13], Zn[82]; X = Cl, Br, I) have all been encapsulated using a molten filling method. Again, crystallinity was shown to be greater for each of the iodide containing salts in both series, and all halides showed charge transfer from the nanotube, but no detailed structural characterisation to determine whether the SWNT had an effect on the morphology of the encapsulated material was undertaken

To summarise the transition metal halides, all accept electron density from nanotube, and all show differences in their crystal structures upon confinement, with the majority exhibiting distortions in their interatomic distances. For some materials such as $NiBr_2$ this was in the form of a slight change of interatomic spacings, but for other

salts such as $FeCl_2$ and CuI completely different crystal structures were found inside SWNTs, as compared to those in the bulk at ambient pressure.

1.3.2.3 Lanthanide Halides

Many lanthanide halides have been encapsulated into SWNTs (table 1.4) Although lanthanide salts have many potential applications, such as in spintronic devices,[103] they are highly air sensitive, and so encapsulation into SWNTs should protect them from hydrolysis by atmospheric moisture. Moreover they have a high atomic number, therefore are very easily resolved using HR-TEM, and so are easily visualised in SWNTs.

Table 1.4: A summary of lanthanide metal halides encapsulated within SWNTs.

Material	Effect of confinement	Ref.
$LnCl_3$ (Ln = La, Nd, Sm, Er, Gd, Yb)	Stoichiometry is retained for all encapsulated $LnCl_3$ species but structural changes occur depending on the nanotube diameter.	104
LaI_3	Formation of LaI_2 only, due to large unit cell of LaI_3.	105
$TbCl_3$	Electron transfer from SWNTs to guest compound.	84, 104
$TbBr_3$	Gradually decreasing the diameter of SWNTs leads to a systematic reduction in the ratio of Br:Tb.	106
$PrCl_3$	Electron transfer from SWNTs to guest compound.	84, 107
$TmCl_3$	Electron transfer from SWNTs to guest compound.	108

Consequently, a variety of lanthanide chlorides, $LnCl_3$ (Ln = La, Nd, Sm, Er, Gd, Tb, Yb) have been encapsulated by Sloan *et al.*[104] It was determined that the dimensions of the crystal lattice of the encapsulated species varied depending on the size of the nanotube (figure 1.18). This is of contrast to work completed by Friedrichs *et al.* which determined that the encapsulation of LaI_3 inside a narrow nanotube (d_{NT} = 1.5 nm) only led to the formation of LaI_2 due to the steric confinement caused by the

dimensions of the nanotubes.[105] This is interesting as a change in the stoichiometry is necessary for encapsulation and is directed by the size of the unit cell of the guest compound. The dimensions of the unit cell of LaI_3 are *ca.* 14 Å x 10 Å x 4 Å, which is too large to fit into a SWNTs, whereas the dimensions of the unit cell of LaI_2 are only 14 Å x 3 Å x 3 Å.[109]

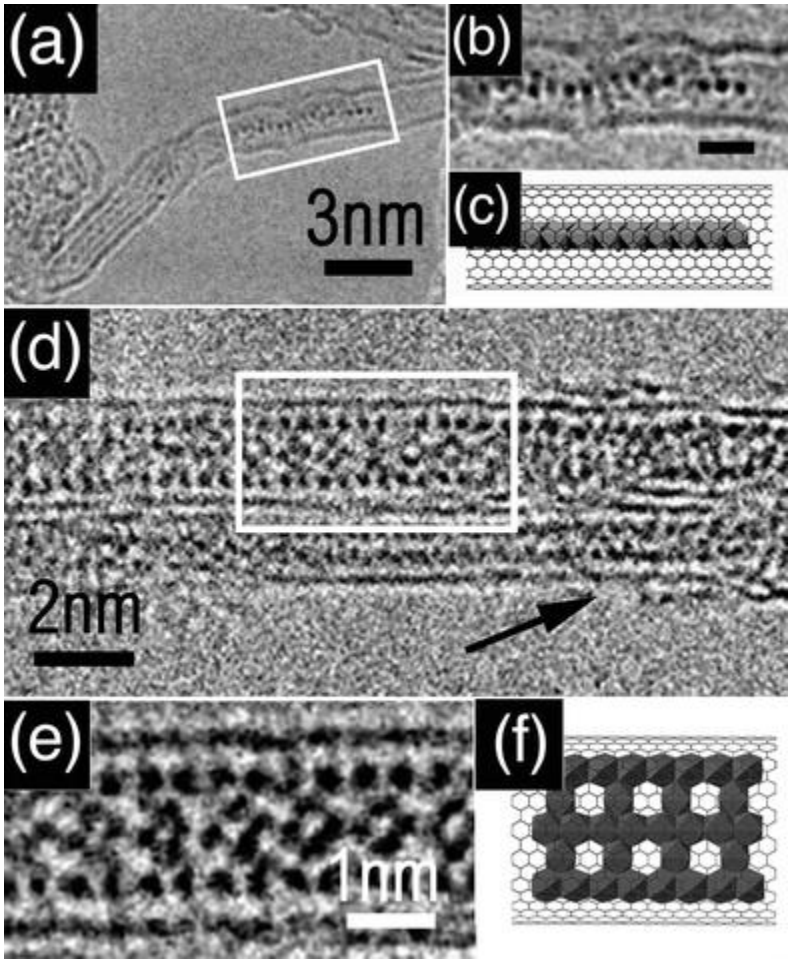


Figure 1.18: a) HR-TEM micrograph showing $GdCl_3$@SWNT; b) Enlargement of boxed region from a) showing a linear array of dark spots which terminates towards the right of the micrograph (scale bar = 1 nm); c) Structural representation of b); d) $NdCl_3$@SWNT; e) Enlargement of the boxed region in d) showing the unusual microstructure of $NdCl_3$@SWNT; f) Suggested structural model for e). [104]

In addition to the morphology of lanthanide halides inside SWNTS being studied, the effect of electron density transfer between the guests and SWNTs has been

investigated.[110] It has been shown that when compared to encapsulated MCl_2 (M = Cd, Zn), $TbCl_3$ accepts more electron density from SWNTs, and this represented the first time incorporated 3d-, 4d- 4f- metal chlorides were compared. $TlCl_3$ accepts more electron density from the nanotube than $TbCl_3$ but less than $PrCl_3$, and no structural comparison was undertaken. [84] The trend in electron transfer properties was attributed to both the chemical nature of the metal present in each salt, and also to the filling rate of the nanotubes.[84]

In addition to investigations into electronic properties, it has been shown that altering the diameter of SWNTs has a significant effect on the crystal structure encapsulated lanthanide salts. $TbBr_3$ has been encapsulated using a molten filling method, and systematically reducing the diameter of the host SWNTs has been shown to gradually remove bromide anions, thus altering the stoichiometry.[106] Again, this can be attributed to a reduction of the size of unit cell upon the removal of bromide anions.

Overall, the large unit cell dimensions of lanthanide halides compared to halides of the transition metals and main group elements results in there being a more noticeable dependence on the diameter of the SWNT. This is seen for salts with large unit cells such as LaI_3 which has to reduce its stoichiometry in order to become encapsulated, and once again demonstrates that SWNTs can be used to control the morphology of nanomaterials.

1.3.3 Metal Chalcogenides

As well as inorganic oxides, hydroxides, and halides, a number of chalcogenide containing compounds salts have been encapsulated into SWNTs (table 1.5).

Table 1.5: A summary of metal chalcogenides encapsulated within SWNTs.

Material	Group	Effect of confinement	Ref.
$MnTe_2$	7	Photoluminescence studies show modification of electronic properties of $MnTe_2$.	111
HgTe	12	Bandgap increases from 0.28 eV to 1.35 eV.	112 113, 114
GaSe	13	Electron transfer is observed from SWNT to guest, and is stronger than the transfer observed from SWNTs to $TmCl_3$.	108 115
GaTe	13	Electron transfer from SWNT to GaTe observed.	116
SnS	14	No electron transfer observed.	116
SnSe	14	Crystals which are two atoms thick are observed when SWNT diameters are less than 1.4 nm.	117
SnTe	14	No noticeable charge transfers between SWNTs and SnTe.	118
Bi_2Se_3	15	No charge transfer observed.	116

The encapsulation of HgTe by a molten filling method leads to the formation of a new type of low-dimensional HgTe crystal structure not seen in the bulk.[112, 113] Whilst the Hg-Te bond lengths are the same as in the bulk, the angles have deviated from the usual tetrahedral structure, and so this shows that confinement in a nanotube not only alters bond lengths but also the geometry of atoms. In this example, it is noted that the morphology of the nanotube remains constant, and so unlike previous examples

where the nanotube cross section has adopted an ovoid geometry, here it remains circular which suggests the absence of a strong interaction between the SWNT and HgTe crystal (figure 1.19). More recent studies have focussed on investigating the band gap of HgTe confined to the nanoscale, and it was found that a band gap of 1.35 eV was present,[114] which is significantly larger than the band gap of bulk HgTe (0.28 eV), and demonstrates that not only does confinement into SWNTs affect structure, it also alters the electronic properties of the guest species.[119]

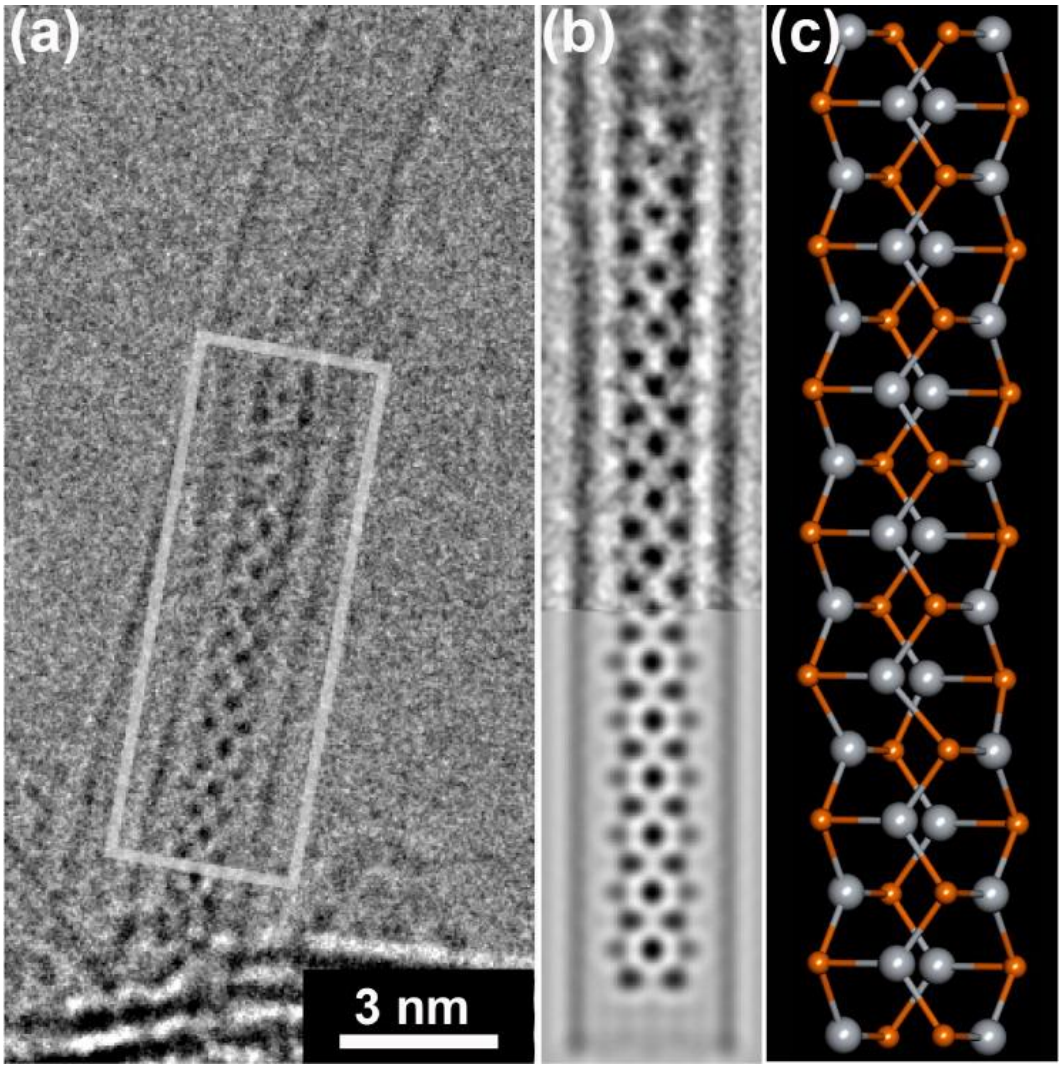


Figure 1.19: a) AC-HRTEM image of HgTe@SWNT; b) Enlarged image from the area indicated in a), with a TEM simulation; c) a model of HgTe corresponding to the images in a) and b).[114]

The encapsulation of SnTe into SWNTs led to the formation of one-dimensional SnTe crystals inside the SWNT, and again, a contraction is observed compared to bulk SnTe which possesses a rock salt structure.[118] Similarly, the encapsulation of SnSe leads to a highly ordered two atomic layered nanocrystal and upon encapsulation, the electronic bandgap of SnSe expands slightly which shows that confinement to the nanoscale is affecting the electronic properties of the strucuture.[117]

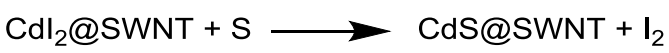
Kharlamova recently compared the electronic properties of SnS, GaTe and Bi_2Se_3 and although no detailed structural characterisation was performed, is was shown that the encapsulation of SnS or Bi_2Se_3 does not result in any electron transfer between the SWNT and either guest, whereas the encapsulation of GaTe leads it to accepting electron density from the nanotube.[116] This variance can be attributed to the different work functions of each of the metal dichalcogenides in the bulk states, and similarly bulk GaTe has a larger bandgap (1.7 eV)[120] than SnS (1.3 eV)[121] and Bi_2Se_3 (0.3 eV),[122] although the bandgap of these structures confined to the nanoscale has not been studied, and as seen previously, the bandgap of structures can vary upon confinement to the nanoscale.

To summarise, a small number of chalcogenide containing materials have been encapsulated into SWNTs, and similarly to the encapsulation of other salts, structural changes are present upon confinement. While electron density was shown to transfer from SWNTs to all metal halides where monitored, only some materials such as GaSe gain electron density from the SWNT, whereas others such as SnS and Bi_2Se_3 gain no electron density upon encapsulation, and so electron transfer depends not only on the SWNT, but also the intrinsic properties of the material being encapsulated.

1.3.4 Reactions in SWNTs

In the bulk, transition metal dichalcogenides are quasi-two-dimensional and form layered structures, analogous to graphene.[123, 124] Additionally, many possess a bandgap, and since studies have shown that the band gap of a material can vary as a function of diameter, SWNTs can be used to template a variety of material dimensions, and thus allow for the creation of structures with tuneable band gaps, such as with S-GNRs.[26, 125] However, the high melting points and the fact that many decompose upon melting, such as MoS_2 which melts at 1185 ^oC, [126] means that filling these materials into SWNTs by a molten method isn't suitable, and $MnTe_2$ remains the only transition metal dichalcogenide to be encapsulated into SWNTs using this methodology.[111]

Therefore a different technique whereby a precursor is encapsulated, followed by a chemical reaction, can be used to create a material that cannot be added using a previously discussed encapsulation method. CdS@SWNT was formed by Eliseev *et al.* by taking CdI_2@SWNT and reacting with elemental sulfur, scheme 1.1.[127]



Scheme 1.1: The formation of CdS@SWNT from CdI_2@SWNT.

This is significant as bulk CdS melts at 1750 ^oC at 100 bar, and so it cannot be encapsulated using a molten filling method. The formation of CdS@SWNT (figure 1.20) from CdI_2@SWNT has been attributed to higher chemical affinity of SWNTs to electron acceptors than donors, but Raman spectroscopy suggests that encapsulated CdI_2 accepts more electron density from the nanotube than CdS does, and so a more rigorous analysis of this system is needed.

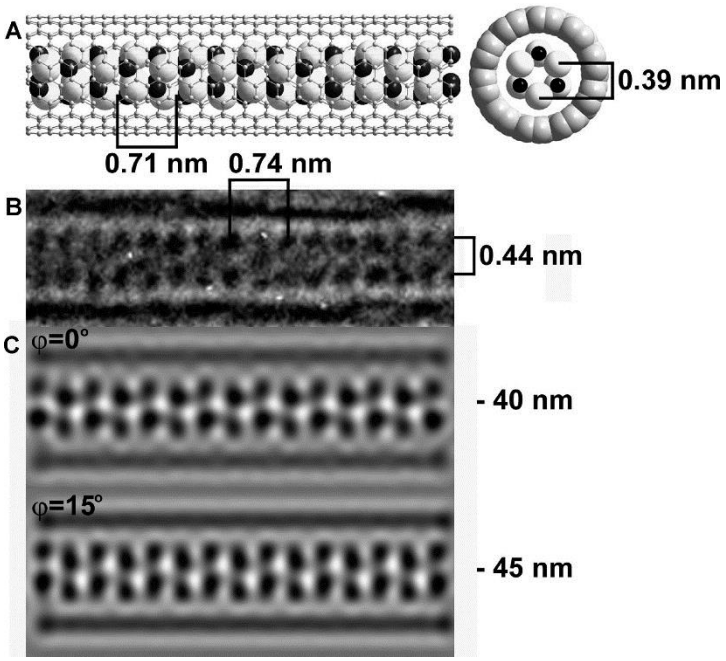


Figure 1.20: a) Structural model of CdS@SWNT (black spheres, cadmium atoms; light grey spheres, sulfur atoms; small grey spheres, carbon atoms); b) HR-TEM image of CdS@SWNT, and c) simulated images for the proposed model. [127]

Additionally, this methodology has been extended to form a variety metal chalcogenides (MX, M = Cd, Zn, Pb; X = S, Se, Te) from the corresponding diiodide of each metal. [127]

Similarly, the formation of low-dimensional MS_2 (M = W, [18] Mo[16]) in multi-walled carbon nanotubes has been demonstrated by Wang *et al. via* encapsulation of molecular precursors and then subsequent thermal treating with H_2S and H_2. Although both MS_2 transition metal dichalcogenide are non-metallic semiconductors in the bulk, it has been found previously that reducing the dimensions alters the electronic properties of both materials, and so by forming both materials in a manageable way whereby their dimensions can be tuned using the special limitations of a MWNT, the electronic properties can be readily altered and this proficiently avoids the problem that both MS_2 materials melt at an extremely high temperature.[15, 17, 128]

More recently, Botos *et al*. have demonstrated that MS_2 (M = Mo, W) nanoribbons can be formed in SWNTs from $M(CO)_6$ *via* a metal-iodide intermediate, and it has been shown that the SWNT acts not only as a template to restrict the morphology of the MS_2, but also as a reservoir of electrons to stabilise the intermediate.[129]

1.4 Summary

A plethora of inorganic salts have been encapsulated within the hollow channel of SWNTs. The confinement of such can lead to the formation of low-dimensional nanocrystals, but the degree of success depends on the size of the material being encapsulated, since AgCl does not crystallise out inside SWNTs but AgI will. In some cases, the material that is encapsulated retains the same crystal structure observed in the bulk, but with a slight distortion to the interatomic distances within the material, and this can lead to a slight contraction of atomic distances compared to the bulk, as in CsI, or an expansion as for LiI. For other salts, such as lanthanide iodides, the unit cell is too large to fit into the channel of a SWNT and a more drastic transformation takes place, which could lead to a change in stoichiometry of the encapsulated material, as is the case for LaI_3. In other cases such as MoO_3, the stoichiometry alters, but it is not clear whether this is only caused by confinement, or as a result of electron beam irradiation, and this emphasises the need for multiple characterisation techniques, both microscopically and spectroscopically. A combination of HR-TEM imaging with XAS and Raman spectroscopy proves to be a useful tool to correlate structural features of compounds encapsulated in SWNTs with the electron transfer between the guest compound and host nanotube being monitored.

Charge transfers have been observed between the SWNTs and most of the metal oxides and halides where monitored, and also for a selection of chalcogenide

containing complexes. This has led to changes in the electronic properties of both the guest and host SWNT, and since the degree of transfer can be quantified and compared by methodically altering both metal and non-metal components separately, the electronic properties of the SWNT and guest can be systematically altered.

The use of SWNTs as reaction vessels for the formation new low-dimensional inorganic structure has been briefly studied; however, very little analysis is given into the formation of these materials and so an all-encompassing system of synthesising, characterising and stipulating formation mechanisms of inorganic compounds in SWNTs is urgently required.

1.5 Aim and Objectives

The aim of this project is to advance the use of SWNTs as reaction vessels for the formation of inorganic materials at the nanoscale, and will involve:

- The encapsulation of group 11 metals into SWNTs to study how metal-carbon (M-C) interactions and bonding vary down a group, on the atomic level;
- A systematic appraisal of M-C bonding for metals important in catalysis (M = Ni, Pd, Pt) to ascertain trends in the group;
- Developing methodologies for inorganic synthesis in SWNTs, enabling the control of dimensions and stoichiometry of the confined nanomaterials;
- Monitoring transformations of inorganic compounds in SWNTs both microscopically and spectroscopically;
- Testing basic electrochemical properties of selected inorganic materials in carbon nanostructures and evaluating their use for sensing applications.

A comprehensive understanding of how metals bond and interact with carbon on an atomic level may lead to the development of new catalytic processes, electronic devices, sensors, detectors and many other applications. Furthermore studying methods of inorganic material formation and probing reaction mechanisms will allow for the intelligent design of a wide range of new nanomaterials, where the structure and properties are controlled by confinement in nanotubes.

1.6 References

1. Z. S. Wu, W. C. Ren, L. Wen, L. B. Gao, J. P. Zhao, Z. P. Chen, G. M. Zhou, F. Li and H. M. Cheng, *ACS Nano*, 2010, **4**, 3187.
2. M. J. Zhi, C. C. Xiang, J. T. Li, M. Li and N. Q. Wu, *Nanoscale*, 2013, **5**, 72.
3. L. Liu, J. C. Liu and D. D. Sun, *Catal. Sci. Tech.*, 2012, **2**, 2525.
4. J. Yin, E. S. Kim, J. Yang and B. L. Deng, *J. Membr. Sci.*, 2012, **423**, 238.
5. J. Panyam and V. Labhasetwar, *Adv. Drug Deliv. Rev.*, 2003, **55**, 329.
6. O. Veiseh, J. W. Gunn and M. Q. Zhang, *Adv. Drug Deliv. Rev.*, 2010, **62**, 284.
7. B. A. Magnuson, T. S. Jonaitis and J. W. Card, *J. Food Sci.*, 2011, **76**, R126.
8. L. R. Khot, S. Sankaran, J. M. Maja, R. Ehsani and E. W. Schuster, *Crop Prot.*, 2012, **35**, 64.
9. S. Iijima, *Nature*, 1991, **354**, 56.
10. R. A. Bell, in *Conduction in Carbon Nanotube Networks: Large-Scale Theoretical Simulations*, 2015, pp. 9.
11. J. P. Salvetat, J. M. Bonard, N. H. Thomson, A. J. Kulik, L. Forro, W. Benoit and L. Zuppiroli, *Appl. Phys. A-Mater. Sci. Process.*, 1999, **69**, 255.
12. M. S. Fuhrer, M. Forero, A. Zettl and P. L. McEuen, in *Electronic Properties of Molecular Nanostructures*, eds. H. Kuzmany, J. Fink, M. Mehring and S. Roth, 2001, vol. 591, pp. 401.
13. K. M. Liew, C. H. Wong, X. Q. He and M. J. Tan, *Phys. Rev. B*, 2005, **71**.
14. M. V. Kharlamova, L. V. Yashina and A. V. Lukashin, *J. Mater. Sci.*, 2013, **48**, 8412.
15. M. V. Bollinger, K. W. Jacobsen and J. K. Norskov, *Phys. Rev. B*, 2003, **67**.
16. Z. Wang, H. Li, Z. Liu, Z. Shi, J. Lu, K. Suenaga, S.-K. Joung, T. Okazaki, Z. Gu, J. Zhou, Z. Gao, G. Li, S. Sanvito, E. Wang and S. Iijima, *J. Am. Chem. Soc.*, 2010, **132**, 13840.
17. M. Remskar, Z. Skraba, M. Regula, C. Ballif, R. Sanjines and F. Levy, *Adv. Mater.*, 1998, **10**, 246.
18. Z. Wang, K. Zhao, H. Li, Z. Liu, Z. Shi, J. Lu, K. Suenaga, S.-K. Joung, T. Okazaki, Z. Jin, Z. Gu, Z. Gao and S. Iijima, *J. Mater. Chem.*, 2011, **21**, 171.
19. D. B. Williams; and C. B. Carter, *Transmission Electron Microscopy* Springer Science New York, 2009.
20. Physics world http://www.hk-phy.org/atomic_world/tem/tem02_e.html, (accessed 30th November, 2016).
21. H. H. Rose, *Sci. Technol. Adv. Mater.*, 2008, **9**, 30.

22. N. Tanaka, *Sci. Technol. Adv. Mater.*, 2008, **9**, 14111.
23. L. H. Guan, K. Suenaga and S. Iijima, *Nano Lett.*, 2008, **8**, 459.
24. N. G. Petrik, K. Knutsen, E. Paparazzo, S. Lea, D. M. Camaioni and T. M. Orlando, *The Journal of Physical Chemistry B*, 2000, **104**, 1563.
25. S. Kiyohara, H. Takamatsu and K. Mori, *Semicond. Sci. Technol.*, 2002, **17**, 1096.
26. A. Chuvilin, E. Bichoutskaia, M. C. Gimenez-Lopez, T. W. Chamberlain, G. A. Rance, N. Kuganathan, J. Biskupek, U. Kaiser and A. N. Khlobystov, *Nat. Mater.*, 2011, **10**, 687.
27. A. Chuvilin, U. Kaiser, E. Bichoutskaia, N. A. Besley and A. N. Khlobystov, *Nat Chem*, 2010, **2**, 450.
28. C. S. Allen, Y. Ito, A. W. Robertson, H. Shinohara and J. H. Warner, *ACS Nano*, 2011, **5**, 10084.
29. A. C. Ferrari and J. Robertson, *Phys. Rev. B*, 2000, **61**, 14095.
30. V. G. Hadjiev, S. Arepalli, P. Nikolaev, S. Jandl and L. Yowell, *Nanotechnology*, 2004, **15**, 562.
31. M. S. Dresselhaus, G. Dresselhaus, A. Jorio, A. G. Souza, M. A. Pimenta and R. Saito, *Acc. Chem. Res.*, 2002, **35**, 1070.
32. A. Jorio, C. Fantini, M. S. S. Dantas, M. A. Pimenta, A. G. Souza Filho, G. G. Samsonidze, V. W. Brar, G. Dresselhaus, M. S. Dresselhaus, A. K. Swan, M. S. Ünlü, B. B. Goldberg and R. Saito, *Phys. Rev. B*, 2002, **66**, 115411.
33. A. Jorio, M. A. Pimenta, A. G. Souza, R. Saito, G. Dresselhaus and M. S. Dresselhaus, *New J. Phys.*, 2003, **5**.
34. M. S. Dresselhaus, A. Jorio, M. Hofmann, G. Dresselhaus and R. Saito, *Nano Lett.*, 2010, **10**, 751.
35. L. Grigorian, K. A. Williams, S. Fang, G. U. Sumanasekera, A. L. Loper, E. C. Dickey, S. J. Pennycook and P. C. Eklund, *Phys. Rev. Lett.*, 1998, **80**, 5560.
36. Y. M. Li, J. H. C. Liu, C. A. Witham, W. Y. Huang, M. A. Marcus, S. C. Fakra, P. Alayoglu, Z. W. Zhu, C. M. Thompson, A. Arjun, K. Lee, E. Gross, F. D. Toste and G. A. Somorjai, *J. Am. Chem. Soc.*, 2011, **133**, 13527.
37. P. Zhang and T. K. Sham, *Phys. Rev. Lett.*, 2003, **90**, 245502.
38. D. Friebel, V. Viswanathan, D. J. Miller, T. Anniyev, H. Ogasawara, A. H. Larsen, C. P. O'Grady, J. K. Norskov and A. Nilsson, *J. Am. Chem. Soc.*, 2012, **134**, 9664.
39. F. Zhang, F. Jiao, X. L. Pan, K. Gao, J. P. Xiao, S. Zhang and X. H. Bao, *ACS Catal.*, 2015, **5**, 1381.
40. A. A. Eliseev, L. V. Yashina, N. I. Verbitskiy, M. M. Brzhezinskaya, M. V. Kharlamova, M. V. Chernysheva, A. V. Lukashin, N. A. Kiselev, A. S. Kumskov, B. Freitag, A. V. Generalov, A. S. Vinogradov, Y. V. Zubavichus, E. Kleimenov and M. Nachtegaal, *Carbon*, 2012, **50**, 4021.
41. C. F. Wang, S. J. Guo, X. L. Pan, W. Chen and X. H. Bao, *J. Mater. Chem.*, 2008, **18**, 5782.
42. A. La Torre, G. A. Rance, J. El Harfi, J. N. Li, D. J. Irvine, P. D. Brown and A. N. Khlobystov, *Nanoscale*, 2010, **2**, 1006.
43. A. G. Rinzler, J. Liu, H. Dai, P. Nikolaev, C. B. Huffman, F. J. Rodriguez-Macias, P. J. Boul, A. H. Lu, D. Heymann, D. T. Colbert, R. S. Lee, J. E. Fischer, A. M. Rao, P. C. Eklund and R. E. Smalley, *Appl. Phys. A-Mater. Sci. Process.*, 1998, **67**, 29.
44. S. C. Tsang, Y. K. Chen, P. J. F. Harris and M. L. H. Green, *Nature*, 1994, **372**, 159.

45. K. C. Park, T. Hayashi, H. Tomiyasu, M. Endo and M. S. Dresselhaus, *J. Mater. Chem.*, 2005, **15**, 407.
46. K. J. Ziegler, Z. N. Gu, H. Q. Peng, E. L. Flor, R. H. Hauge and R. E. Smalley, *J. Am. Chem. Soc.*, 2005, **127**, 1541.
47. N. Pierard, A. Fonseca, Z. Konya, I. Willems, G. Van Tendeloo and J. B. Nagy, *Chem. Phys. Lett.*, 2001, **335**, 1.
48. A. Kukovecz, T. Kanyo, Z. Konya and I. Kiricsi, *Carbon*, 2005, **43**, 994.
49. I. Stepanek, G. Maurin, P. Bernier, J. Gavillet, A. Loiseau, R. Edwards and O. Jaschinski, *Chem. Phys. Lett.*, 2000, **331**, 125.
50. D. A. Britz and A. N. Khlobystov, *Chem. Soc. Rev.*, 2006, **35**, 637.
51. D. Mattia and Y. Gogotsi, *Microfluid. Nanofluidics*, 2008, **5**, 289.
52. M. Wilson and S. Friedrichs, *Acta Crystallogr. Sect. A*, 2006, **62**, 287.
53. K. Yanagi, Y. Miyata and H. Kataura, *Adv. Mater.*, 2006, **18**, 437.
54. Y. Ren and G. Pastorin, *Adv. Mater.*, 2008, **20**, 2031.
55. K. Suenaga, T. Okazaki, C. R. Wang, S. Bandow, H. Shinohara and S. Iijima, *Phys. Rev. Lett.*, 2003, **90**, 55506.
56. S. Toth, D. Quintavalle, B. Nafradi, L. Korecz, L. Forro and F. Simon, *Phys. Rev. B*, 2008, **77**, 214409.
57. R. L. McSweeney, T. W. Chamberlain, E. S. Davies and A. N. Khlobystov, *Chem. Commun.*, 2014, **50**, 14338.
58. L. H. Guan, Z. J. Shi, M. X. Li and Z. N. Gu, *Carbon*, 2005, **43**, 2780.
59. L. J. Li, A. N. Khlobystov, J. G. Wiltshire, G. A. D. Briggs and R. J. Nicholas, *Nat. Mater.*, 2005, **4**, 481.
60. L. H. Guan, K. Suenaga, Z. J. Shi, Z. N. Gu and S. Iijima, *Nano Lett.*, 2007, **7**, 1532.
61. M. V. Chernysheva, E. A. Kiseleva, N. I. Verbitskii, A. A. Eliseev, A. V. Lukashin, Y. D. Tretyakov, S. V. Savilov, N. A. Kiselev, O. M. Zhigalina, A. S. Kumskov, A. V. Krestinin and J. L. Hutchison, *Physica E Low Dimens. Syst. Nanostruct.*, 2008, **40**, 2283.
62. H. Ulbricht, G. Moos and T. Hertel, *Phys. Rev. Lett.*, 2003, **90**.
63. L. A. Girifalco and M. Hodak, *Phys. Rev. B*, 2002, **65**, 125404.
64. M. Yudasaka, K. Ajima, K. Suenaga, T. Ichihashi, A. Hashimoto and S. Iijima, *Chem. Phys. Lett.*, 2003, **380**, 42.
65. T. W. Chamberlain, A. M. Popov, A. A. Knizhnik, G. E. Samoilov and A. N. Khlobystov, *ACS Nano*, 2010, **4**, 5203.
66. A. N. Khlobystov, D. A. Britz, J. W. Wang, S. A. O'Neil, M. Poliakoff and G. A. D. Briggs, *J. Mater. Chem.*, 2004, **14**, 2852.
67. N. Thamavaranukup, H. A. Hoppe, L. Ruiz-Gonzalez, P. Costa, J. Sloan, A. Kirkland and M. L. H. Green, *Chem. Commun.*, 2004, 1686.
68. L. Shao, G. Tobias, Y. Huh and M. L. H. Green, *Carbon*, 2006, **44**, 2855.
69. P. Corio, A. P. Santos, P. S. Santos, M. L. A. Temperini, V. W. Brar, M. A. Pimenta and M. S. Dresselhaus, *Chem. Phys. Lett.*, 2004, **383**, 475.
70. G. Lota, E. Frackowiak, J. Mittal and M. Monthioux, *Chem. Phys. Lett.*, 2007, **434**, 73.
71. R. Sagawa, W. Togashi, T. Akita and Y. Takai, *Microscopy*, 2013, **62**, 271.
72. P. Costa, J. Sloan, T. Rutherford and M. L. H. Green, *Chem. Mater.*, 2005, **17**, 6579.
73. M. Hulman, H. Kuzmany, P. M. F. J. Costa, S. Friedrichs and M. L. H. Green, *Appl. Phys. Lett.*, 2004, **85**, 2068.

74. P. Corio, A. P. Santos, P. S. Santos, M. L. A. Temperini, V. W. Brar, M. A. Pimenta and M. S. Dresselhaus, *Chem. Phys. Lett.*, 2004, **383**, 475.
75. B. Krebs, A. Mueller and H. H. Beyer, *Inorg. Chem.*, 1969, **8**, 436.
76. S. Tribalat, *Rhenium et Technetium* Gauthier-Villars, Paris 1957.
77. R. Sagawa, W. Togashi, T. Akita and Y. Takai, *Surf. Interface Anal.*, 2012, **44**, 797.
78. E. M. McCarron and J. C. Calabrese, *J. Solid State Chem.*, 1991, **91**, 121.
79. J. Sloan, J. Hammer, M. Zwiefka-Sibley and M. L. H. Green, *Chem. Commun.*, 1998, 347.
80. R. R. Meyer, J. Sloan, R. E. Dunin-Borkowski, A. I. Kirkland, M. C. Novotny, S. R. Bailey, J. L. Hutchison and M. L. H. Green, *Science*, 2000, **289**, 1324.
81. J. Sloan, M. C. Novotny, S. R. Bailey, G. Brown, C. Xu, V. C. Williams, S. Friedrichs, E. Flahaut, R. L. Callender, A. P. E. York, K. S. Coleman, M. L. H. Green, R. E. Dunin-Borkowski and J. L. Hutchison, *Chem. Phys. Lett.*, 2000, **329**, 61.
82. J. Sloan, A. I. Kirkland, J. L. Hutchison and M. L. H. Green, *C. R. Phys.*, 2003, **4**, 1063.
83. J. Sloan, S. J. Grosvenor, S. Friedrichs, A. I. Kirkland, J. L. Hutchison and M. L. H. Green, *Angew. Chem.-Int. Edit.*, 2002, **41**, 1156.
84. M. V. Kharlamova, *Appl. Phys. A-Mater. Sci. Process.*, 2015, **118**, 27.
85. E. Flahaut, J. Sloan, S. Friedrichs, A. I. Kirkland, K. S. Coleman, V. C. Williams, N. Hanson, J. L. Hutchison and M. L. H. Green, *Chem. Mater.*, 2006, **18**, 2059.
86. R. M. Zakalyukin, L. N. Demyanets and N. A. Kiselev, *Crystallogr. Rep.*, 2010, **55**, 688.
87. R. M. Zakalyukin, L. N. Demyanets, N. A. Kiselev, A. S. Kumskov, M. B. Kislov, A. V. Krestinin and J. L. Hutchison, *Crystallogr. Rep.*, 2010, **55**, 507.
88. J. C. Lund, K. S. Shah, M. R. Squillante, L. P. Moy, F. Sinclair and G. Entine, *Nuclear Instruments & Methods in Physics Research Section a-Accelerators Spectrometers Detectors and Associated Equipment*, 1989, **283**, 299.
89. M. V. Kharlamova, *Appl. Phys. A-Mater. Sci. Process.*, 2016, **122**, 8.
90. M. V. Kharlamova, M. M. Brzhezinskay, A. S. Vinogradov, I. P. Suzdalev, Y. V. Maksimov, V. K. Imshennik, S. V. Novichikhin, A. V. Krestinin, L. V. Yashina, A. V. Lukashin, Y. D. Tret'yakov and A. A. Eliseev, *Nanotechnol. Russ.*, 2009, **4**, 634.
91. M. V. Kharlamova, *J. Spectrosc.*, 2015, 653848.
92. E. Philp, J. Sloan, A. I. Kirkland, R. R. Meyer, S. Friedrichs, J. L. Hutchison and M. L. H. Green, *Nat. Mater.*, 2003, **2**, 788.
93. M. V. Kharlamova, L. V. Yashina, A. A. Eliseev, A. A. Volykhov, V. S. Neudachina, M. M. Brzhezinskaya, T. S. Zyubina, A. V. Lukashin and Y. D. Tretyakov, *physica status solidi (b)*, 2012, **249**, 2328.
94. N. A. Kiselev, R. M. Zakalyukin, O. M. Zhigalina, N. Grobert, A. S. Kumskov, Y. V. Grigoriev, M. V. Chernysheva, A. A. Eliseev, A. V. Krestinin, Y. D. Tretyakov, B. Freitag and J. L. Hutchison, *J. Microsc.*, 2008, **232**, 335.
95. A. S. Kumskov, V. G. Zhigalina, A. L. Chuvilin, N. I. Verbitskiy, A. G. Ryabenko, D. D. Zaytsev, A. A. Eliseev and N. A. Kiselev, *Carbon*, 2012, **50**, 4696.

96. N. A. Kiselev, A. S. Kumskov, R. M. Zakalyukin, A. L. Vasiliev, M. V. Chernisheva, A. A. Eliseev, A. V. Krestinin, B. Freitag and J. L. Hutchison, *J. Microsc.*, 2012, **246**, 309.
97. A. A. Zhukov, M. V. Chernysheva and A. A. Eliseev, *J. Exp. Theor. Phys.*, 2016, **123**, 143.
98. A. A. Eliseev, L. V. Yashina, M. M. Brzhezinskaya, M. V. Chernysheva, M. V. Kharlamova, N. I. Verbitsky, A. V. Lukashin, N. A. Kiselev, A. S. Kumskov, R. M. Zakalyuhin, J. L. Hutchison, B. Freitag and A. S. Vinogradov, *Carbon*, 2010, **48**, 2708.
99. S. Hull and D. A. Keen, *Phys. Rev. B*, 1999, **59**, 750.
100. H. Takahashi, S. Tamaki and S. Sato, *J. Phys. Soc. Jpn.*, 1987, **56**, 3593.
101. *Nature*, 1955, **176**, 147.
102. R. J. Cava, F. Reidinger and B. J. Wuensch, *Solid State Commun.*, 1977, **24**, 411.
103. G. Caroena, W. V. M. Machado, J. F. Justo and L. V. C. Assali, *Appl. Phys. Lett.*, 2013, **102**, 062101.
104. C. G. Xu, J. Sloan, G. Brown, S. Bailey, V. C. Williams, S. Friedrichs, K. S. Coleman, E. Flahaut, J. L. Hutchison, R. E. Dunin-Borkowski and M. L. H. Green, *Chem. Commun.*, 2000, 2427.
105. S. Friedrichs, A. I. Kirkland, R. R. Meyer, J. Sloan and M. L. H. Green, *Microsc. Microanal.*, 2005, **11**, 421.
106. N. A. Kiselev, A. S. Kumskov, V. G. Zhigalina, A. L. Vasiliev, J. Sloan, N. S. Falaleev, N. I. Verbitskiy and A. A. Eliseev, *J. Microsc.*, 2016, **262**, 92.
107. M. V. Kharlamova, A. A. Volykhov, L. V. Yashina, A. V. Egorov and A. V. Lukashin, *J. Mater. Sci.*, 2015, **50**, 5419.
108. M. V. Kharlamova, L. V. Yashina and A. V. Lukashin, *Appl. Phys. A-Mater. Sci. Process.*, 2013, **112**, 297.
109. W. H. Zachariasen, *Acta Crystallogr.*, 1948, **1**, 265.
110. M. V. Kharlamova, *Appl. Phys. A-Mater. Sci. Process.*, 2013, **111**, 725.
111. L.-J. Li, T.-W. Lin, J. Doig, I. B. Mortimer, J. G. Wiltshire, R. A. Taylor, J. Sloan, M. L. H. Green and R. J. Nicholas, *Phys. Rev. B*, 2006, **74**.
112. R. Carter, J. Sloan, A. I. Kirkland, R. R. Meyer, P. J. D. Lindan, G. Lin, M. L. H. Green, A. Vlandas, J. L. Hutchison and J. Harding, *Phys. Rev. Lett.*, 2006, **96**, 215501.
113. J. Sloan, R. Carter, R. R. Meyer, A. Vlandas, A. I. Kirkland, P. J. D. Lindan, G. Lin, J. Harding and J. L. Hutchison, *Phys. Status Solidi B*, 2006, **243**, 3257.
114. J. H. Spencer, J. M. Nesbitt, H. Trewhitt, R. J. Kashtiban, G. Bell, V. G. Ivanov, E. Faulques, J. Sloan and D. C. Smith, *ACS Nano*, 2014, **8**, 9044.
115. M. V. Kharlamova, *Jetp Lett.*, 2013, **98**, 272.
116. M. V. Kharlamova, *J. Mater. Sci.*, 2014, **49**, 8402.
117. R. Carter, M. Suyetin, S. Lister, M. A. Dyson, H. Trewhitt, S. Goel, Z. Liu, K. Suenaga, C. Giusca, R. J. Kashtiban, J. L. Hutchison, J. C. Dore, G. R. Bell, E. Bichoutskaia and J. Sloan, *Dalton Trans.*, 2014, **43**, 7391.
118. L. V. Yashina, A. A. Eliseev, M. V. Kharlamova, A. A. Volykhov, A. V. Egorov, S. V. Savilov, A. V. Lukashin, R. Puttner and A. I. Belogorokhov, *J. Phys. Chem. C*, 2011, **115**, 3578.
119. J. Chu, in *New Data and Updates for III-V, II-VI and I-VII Compounds*, ed. U. Rössler, Springer Berlin Heidelberg, Berlin, Heidelberg, 2010, pp. 403.
120. U. Giorgianni, G. Mondio, P. Perillo, G. Saitta and G. Vermiglio, *J. Phys. France*, 1977, **38**, 1293.

121. M. Ichimura, K. Takeuchi, Y. Ono and E. Arai, *Thin Solid Films*, 2000, **361–362**, 98.
122. O. V. Yazyev, E. Kioupakis, J. E. Moore and S. G. Louie, *Phys. Rev. B*, 2012, **85**, 161101.
123. A. K. Geim and I. V. Grigorieva, *Nature*, 2013, **499**, 419.
124. F. Jellinek, *React. Solid.*, 1988, **5**, 323.
125. T. W. Chamberlain, J. Biskupek, G. A. Rance, A. Chuvilin, T. J. Alexander, E. Bichoutskaia, U. Kaiser and A. N. Khlobystov, *ACS Nano*, 2012, **6**, 3943.
126. R. Cusak, *Proc. Roy. Irish. Acad.*, 1897, **4**, 399.
127. A. A. Eliseev, M. V. Chernysheva, N. I. Verbitskii, E. A. Kiseleva, A. V. Lukashin, Y. D. Tretyakov, N. A. Kiselev, O. M. Zhigalina, R. M. Zakalyukin, A. L. Vasiliev, A. V. Krestinin, J. L. Hutchison and B. Freitag, *Chem. Mater.*, 2009, **21**, 5001.
128. X. Li and H. Zhu, *J. Materiomics*, 2015, **1**, 33.
129. A. Botos, J. Biskupek, T. W. Chamberlain, G. A. Rance, C. T. Stoppiello, J. Sloan, Z. Liu, K. Suenaga, U. Kaiser and A. N. Khlobystov, *J. Am. Chem. Soc.*, 2016, **138**, 8175.

Chapter II: The Encapsulation of Group 11 Metals into Single-Walled Carbon Nanotubes

2. 1 Introduction

It is vitally important to investigate the interactions between metals and carbon nanostructures for many different reasons, one of them being that nanostructures such as single-walled carbon nanotubes (SWNTs) are formed using transition metal catalysts and so it is essential that these processes are rigorously controlled, to effectively make new nanostructures. Moreover, an all-encompassing understanding of metal-carbon (M-C) bonds is key to fully appreciating how fundamental chemical reactions and catalytic process take place, although current knowledge of M-C bonding is disjointed, and only available for small select areas of the periodic table. Since many organometallic compounds are highly air and moisture sensitive, and contain spectator ligands which can hinder particular studies of M-C bonding, the investigation of individual metals and their interaction with carbon is rather sparse, therefore a method of examining a small amount of metal atoms and their interactions with carbon in a confined environment is required, and SWNTs can be a candidate for this.[1]

As seen in Chapter I, SWNTs are hollow tubes of sp^2 hybridised carbon atoms. With diameters between 0.7 and 2 nm and lengths up to the order of mm, they possess internal hollow channels which allows for the encapsulation of small clusters of metal nanoparticles (MNPs), to study their properties.[2, 3] Since they are incredibly thermally, mechanically and chemically robust, SWNTs can usually act as suitable

containers for small clusters of atoms, and a wide variety of metal complexes, organic molecules and inorganic salts have been encapsulated within their hollow channel.[4]

Many theoretical studies have been undertaken to predict the bonding interactions between metals, the π-electronic systems of graphene and both the convex and concave surfaces of SWNTs.[5-8] Such interactions are expected to have energies of between 0-2 eV but this is affected by the nature of the metal and the curvature of the nanostructure. A theoretical study on metal atoms on the surface of carbon nanostructures was undertaken by Valencia *et al.*, and it was predicted that copper and nickel prefer to adsorb above a C-C bond whereas all other 3d transition metals prefer to adsorb over hollow sites in between the bonds.[5] Furthermore, a theoretical comparison of different transition metals has shown that for period 3 metals, there is a non-uniform dependence of π-bonding energy on the atomic number, with a double maxima being shown along the period.[9]

Despite the best efforts of the nanotube synthesis industry, and in spite of new technologies constantly being introduced to improve the quality of nanotubes, not all nanotubes are in pristine condition, and many contain defects (figure 2.1). The absence of carbon atoms from the lattice of the nanotube wall, a mono-vacancy (figure 2.1 b), results in the introduction of radical carbon atoms to the nanotube structure, and so in addition to metal atoms being able to π-bond to the wall of SWNTs, σ-bonding can occur between metal atoms and these radical carbon atoms to stabilise them. Furthermore, the absence of two carbon atoms leads to the formation of a di-vacancy (figure 2.1 c), and similarly, metal atoms can also enter these and σ –bond to the radical carbon atoms.

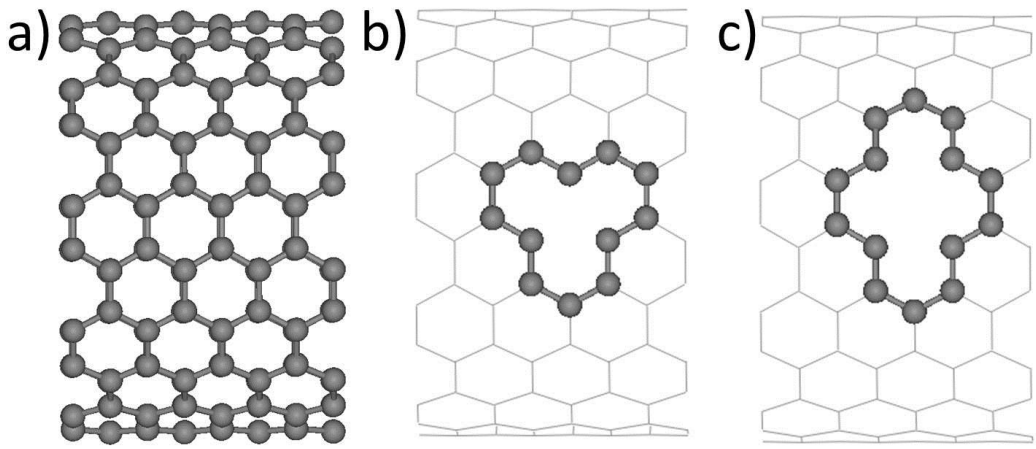


Figure 2.1: a) The sidewall of a pristine defect-free (10,10) SWNT. A mono-vacancy can occur if one carbon atom is missing (b), or if two are absent, a di-vacancy (c) occurs. Metal atoms are able to bond to the radicals formed around the vacancies to stabilise the structure.

In addition to theoretical studies, advancement in aberration-corrected high resolution transmission electron microscopy (AC-HRTEM) has allowed for interactions between metals and carbon nanotubes to be studied practically in direct space and real time. For example, the interaction of SWNTs with small clusters of nickel atoms has been observed by Lebedeva *et al.* and it was shown that the nickel atoms readily catalyse the cutting of SWNTs.[10]

An investigation into the behaviours of tungsten, rhenium and osmium encapsulated within SWNTs demonstrated the first instance metals from a particular period were confined into a SWNT and their properties investigated using AC-HRTEM.[11] Although the three elements are adjacent in the periodic table they display marked differences when a small number (*ca.* 50-60 atoms) of each are encapsulated and studied at the nanoscale. Osmium readily catalyses the cutting of SWNTs whereas rhenium and tungsten are much less reactive, and the data obtained from AC-HRTEM fully supports the trend which was predicted by density functional theory calculations.

Zoberbier *et al.* recently probed interactions between carbon and the group VIII metals on the atomic scale, and this represents the first time that interactions have been studied on metals of a particular group in the table.[12] Trends between both metal-carbon σ and π-bonding are observed, with osmium shown to form the strongest σ-bonds with carbon, whereas ruthenium was shown to form the strongest π-bonds (figure 2.2).

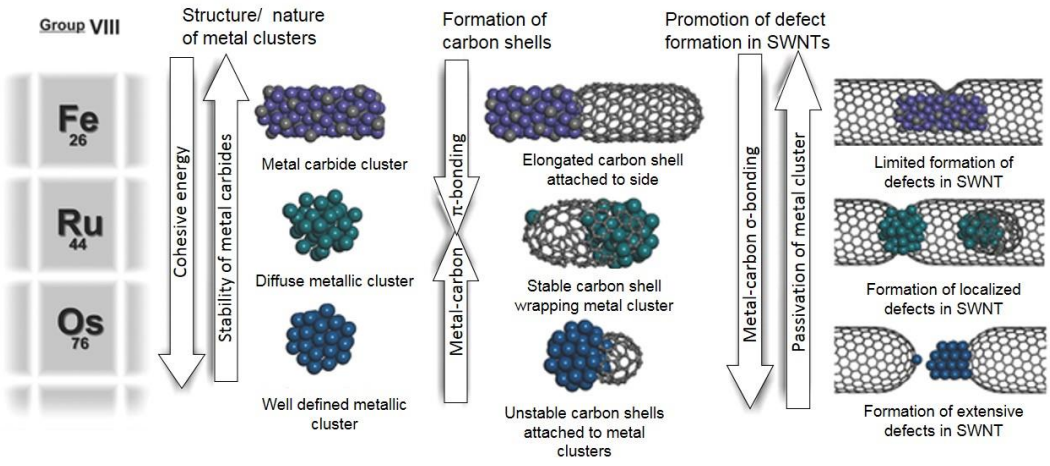


Figure 2.2: Schematic representation of the trends observed by 80 keV AC-HRTEM for the group VIII metals inside SWNTs.[12]

The group 11 metals, also known as the coinage metals, comprising of copper, silver and gold are an important group of metals as they have many industrial and chemical applications, such as gold nanoparticles (AuNPs) being used as oxidation catalysts;[13] silver nanoparticles (AgNPs) for cutting nanotubes;[14] and copper nanoparticles (CuNPs) as catalysts in the water-gas-shift reacton.[15] In the literature, there are examples of the coinage metals being encapsulated into SWNTs using solution filling methods, usually as a decomposition product of a metal halide precursor,[16, 17] although no studies on their bonding with carbon has been reported. A theoretical study on the interactions between the group 11 metals and carbon nanostructures has been undertaken by Inntam *et al.* who were able to predict that copper would interact the strongest with the SWNT wall, followed by gold and then silver.[6] Furthermore, the

same trend was shown by Reckein *et al.* who theoretically investigated the adsorption of benzene onto the coinage metals.[18]

Herein the encapsulation of the group 11 metals into the internal channel of SWNTs using a sublimation filling technique is reported, and an investigation into their interactions with both the carbon wall of the SWNTs, and excess (adventitious) carbon already encapsulated within the SWNTs is described. Structural determination of the MNPs and resultant products formed upon their interactions with carbon have been analysed with atomic precision using AC-HRTEM.

2.2 Results

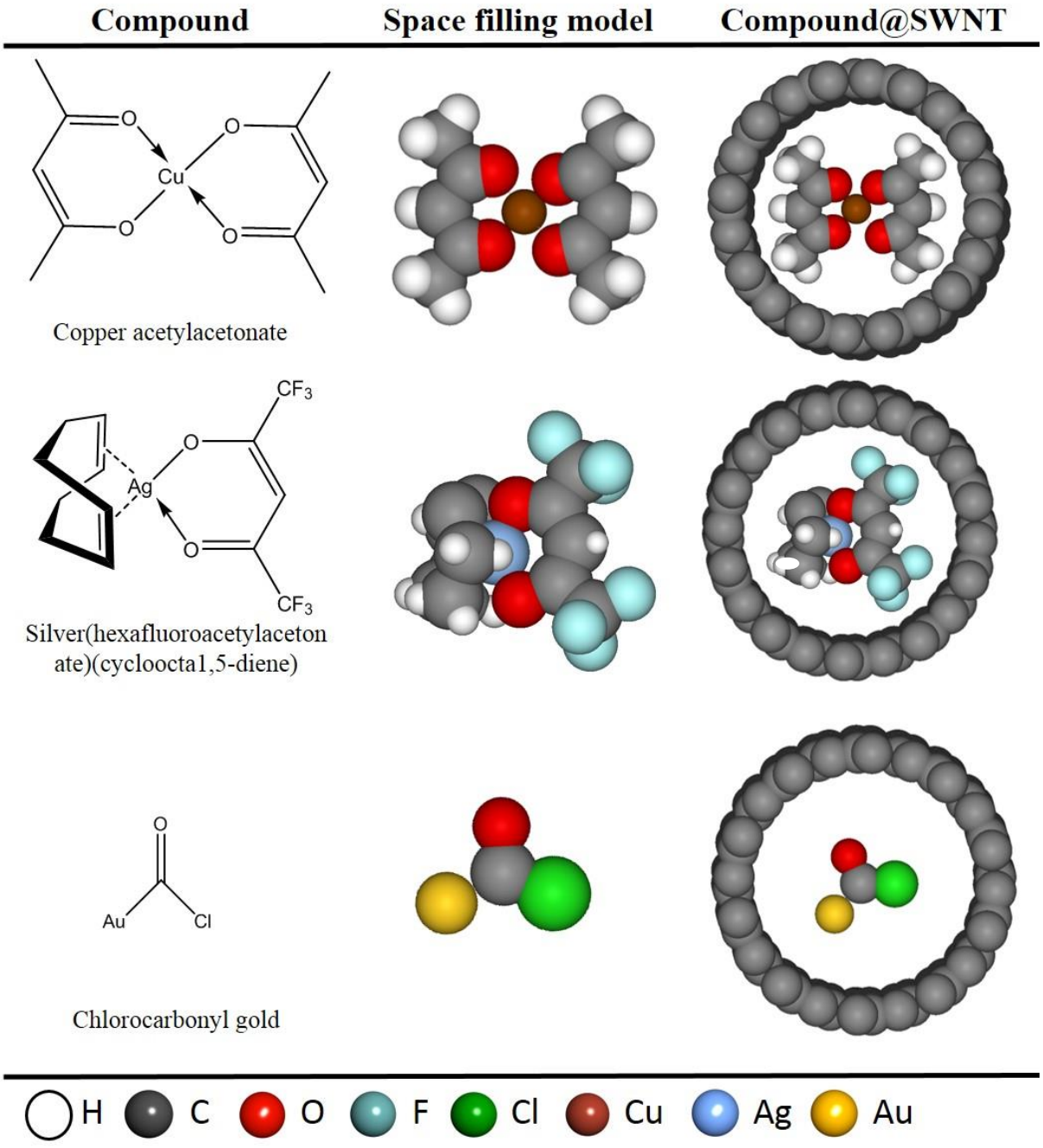
2.2.1 Encapsulation

Encapsulation of materials into the hollow channel of SWNTs relies on a process of self-assembly which is driven by the affinity for a molecule to be inside the hollow channel.[19] Due to the large contact area between the internal surface of nanotubes and guest species, there is an increase in van der Waals interactions when a guest is encapsulated, relative to it being on the outside, and so encapsulation is preferable to adsorption.[20]

As described in Chapter I, materials must be in the liquid or gas phase in order for them to become encapsulated into a SWNT, and for the encapsulation of metallic clusters inside SWNTs it is necessary to capture a precursor which contains the metal, and then remove the ligands to leave solely the metal atoms which consequently cluster together to form MNPs inside SWNTs. Vapour phase filling has many advantages over liquid phase filling and can provide a simple, clean and reproducible method for encapsulating molecules in nanotubes, with the only prerequisites being that the molecule sublimes without decomposition and that the molecule is able to fit

into the internal channel of a SWNT.[21] Table 2.1 shows the three compounds employed for the encapsulation of the coinage metals into SWNTs. It is important to note than all complexes are sufficiently small enough to fit inside the internal channel of a (10,10) SWNT, which has an internal diameter of *ca.* 1.4 nm.

Table 2.1: The three compounds used to insert copper, silver and gold into the internal channel of SWNTs. Also shown is a schematic model of each molecule and how the molecules are able to fit into the internal channel of a (10,10) SWNT.



2.2.2 Copper

Copper acetylacetonate ($Cu(acac)_2$) was chosen as a suitable precursor for the introduction of copper into the nanotube. Whilst it melts at 279-283 ^oC,[22] when sealed in a Pyrex ampoule under vacuum (10^{-5} mbar), it was found to sublime without

decomposition at 110 ^{o}C and so heating $Cu(acac)_2$ and SWNTs at slightly above this temperature under vacuum allowed the molecules to penetrate the nanotubes. After heating for three days, the mixture of SWNTs and complex was rapidly cooled leading to the formation of a copper containing species in SWNTs. The presence of copper clusters formed inside the SWNTs are confirmed by energy-dispersive X-ray (EDX) spectroscopy using a focussed 100 keV electron beam to irradiate a small bundle of SWNTs (figure 2.3).

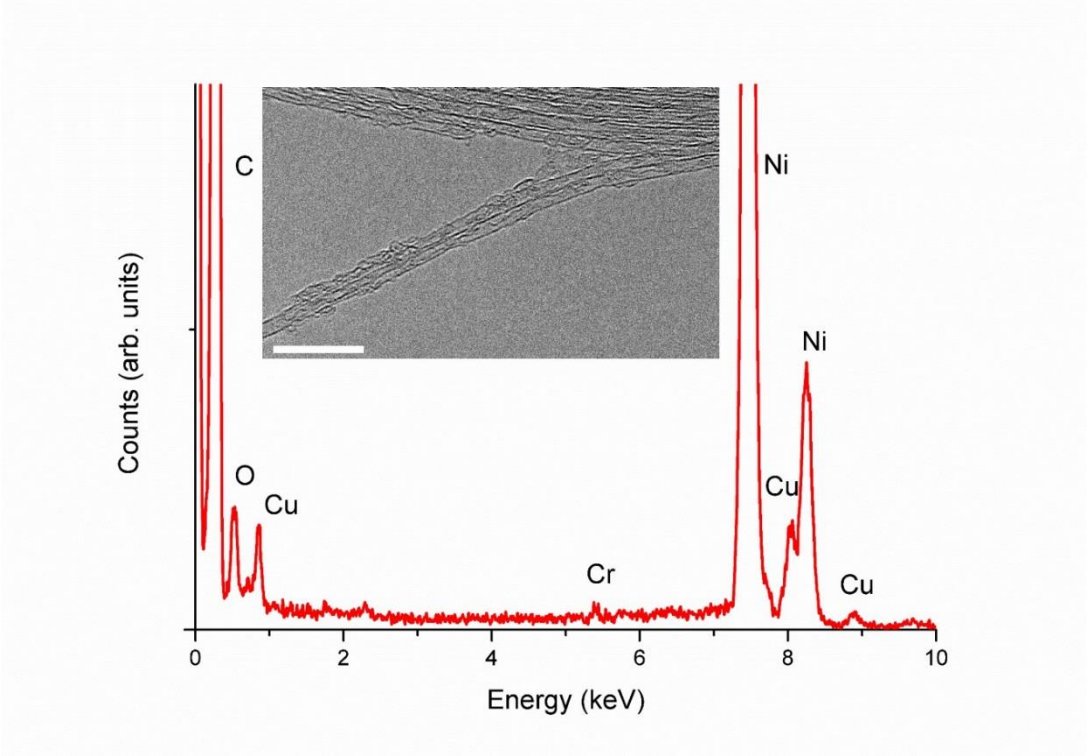


Figure 2.3: EDX spectrum recorded at 100 keV primary electron energy and integrated over a small bundle of nanotubes confirms the presence of copper inside the nanotube. Nickel and chromium peaks are due to the specimen holder of the sample. A HR-TEM image (inset) of the area over which the EDX spectrum was taken. The scale bar is 10 nm.

2.2.2.1 AC-HRTEM Analysis

AC-HRTEM revealed the presence of small clusters of copper atoms within the internal channel of the SWNTs (figure 2.4 a). Under the electron beam (80 kV in this case), the complex starts to decompose leading to the formation of CuNPs and a

mixture of volatile organic compounds. Nasibulin *et al.* have shown that the decomposition of $Cu(acac)_2$ can lead to the formation of small volatile organic molecules such as acetone, 2-propenal, carbon dioxide and 2-butanone, which are removed easily in the vacuum of TEM.[23]

It is possible to compare the structure of the encapsulated CuNP to that of bulk copper (figure 2.4 b). Although the cluster of copper atoms appear to move quite fast under the electron beam, it is still possible to obtain structural information from the time series. Slow rotational motion allows for clear visualisation of the hexagonal lattice which is consistent with the space group of the bulk metal, *Fm-3m*. There is a slight discrepancy between the interatomic distances of the copper atoms in the nanotube compared to those of bulk copper. This is due to encapsulated nanocrystal changing its morphology in order to best increase contact with the nanotube wall and therefore increase van der Waals interactions.

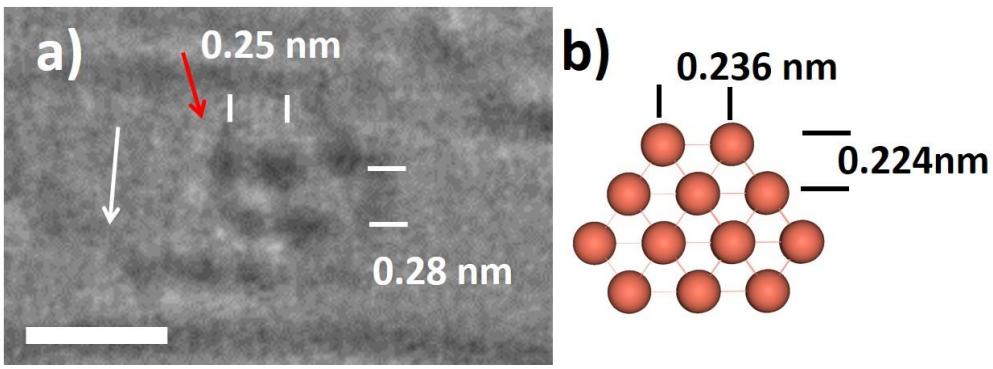


Figure 2.4: a) AC-HRTEM image (performed at 80 kV) showing $Cu(acac)_2$@SWNT. Under the electron beam, the volatile acetylacetonate ligands have been removed, with the copper atoms forming a cluster with hexangonal packing (red arrow). Adventitious carbon is also present in the nanotube (white arrow); b) a projection of the (110) plane of bulk copper is shown, and the atomic distances are comparable to that of the CuNPs in (a). The scale bar is 1 nm.

Initially, the atoms are together in a discrete cluster (figure 2.5 a), but over time the cluster appears to bond to the end of a chain of carbon atoms (figure 2.5 b), which is

adventitious carbon residue in the SWNTs. Subsequently, the carbon forms a shell around the CuNP cluster (figure 2.5 c), until eventually a spherical carbon shell forms around the whole cluster (figure 2.5 d). During this time the encapsulated particle stays detached from the side wall of the nanotube and does not create defects in the nanotube. Eventually the carbon shell begins to extrude from the CuNPs but not to a significant extent and the copper cluster still remains inside the carbon shell (figure 2.5 e).

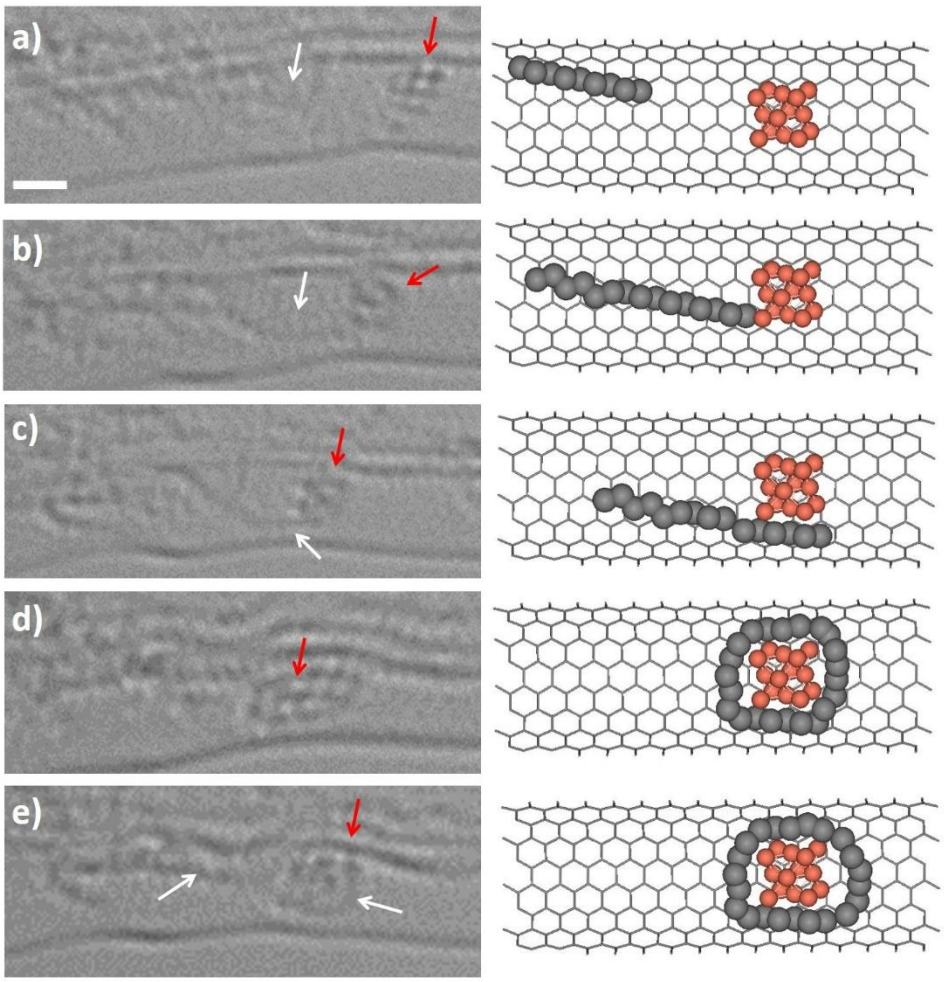
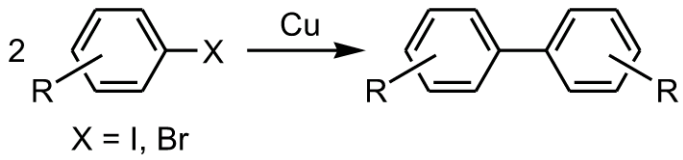


Figure 2.5: Sequential AC-HRTEM images (left hand side) showing how a cluster of copper atoms (red arrows) interacts with a carbon chain (white arrows), coupled with a structural model at each stage (right hand side). Initially the CuNPs and carbon chain are discrete units (a), the CuNP comes into contact with the end of the carbon chain (b), and starts to form a shell around the cluster (c). Eventually a carbon shell encases the whole particle (d) and finally an extended carbon shell starts to extrude from the particle (e). The images were

taken over 120 seconds with a total dose of *ca.* 3 x 10^9 e^-/nm^2. The scale bar is 1 nm.

Previous studies have shown that under the electron beam it is possible to remove carbon atoms from SWNTs and the type of interaction between the MNPs and SWNT depend on the nature of the metal present.[11, 12] In the case of copper, it is observed that individual atoms of copper from the cluster and can enter the sidewall of the SWNT (figure 2.6). If there is a breakage in the sidewall of the SWNT (as shown in figure 2.6 a) copper atoms are able to enter this vacant site (figures 2.6 b,c) to encourage the restructuring of the sidewalls of the SWNT (figure 2.6 d). This is similar to an Ullmann coupling reaction, where a C-C bond can form between two aryls when catalysed by copper (Scheme 2.1).[24]



Scheme 2.1: An Ullman coupling of aryl halides catalysed by copper. A modified version of this reaction has been proposed to take place on the nanotube sidewall.

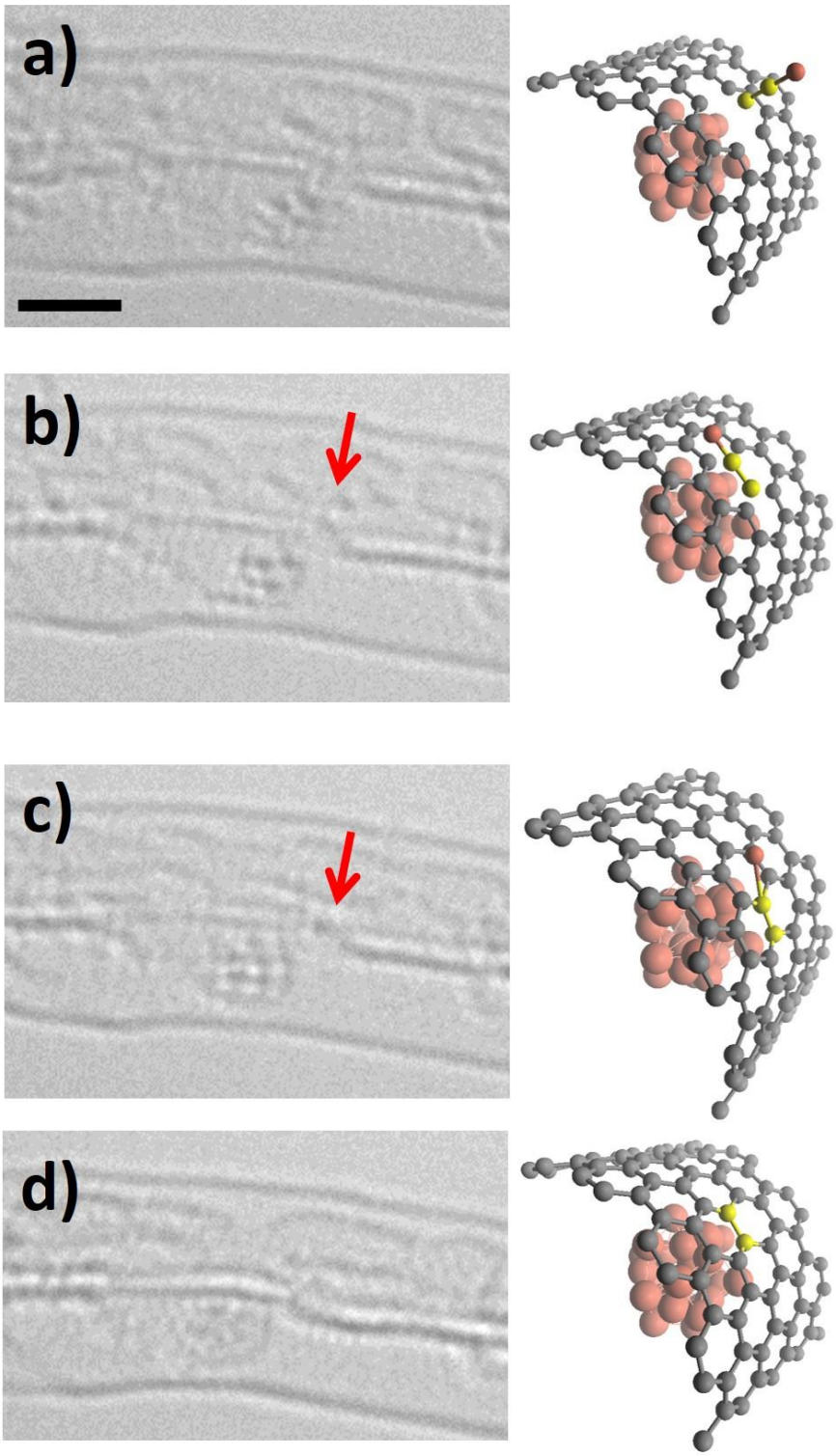


Figure 2.6: AC-HRTEM time series (left hand panel) showing how a breakage in the SWNT wall (a) can be restored with the addition of a copper atom (red arrow, (b)). The copper atom can enter the vacant site (c) and this leads to the healing of the SWNT (d). A corresponding geometry optimised model is shown at each stage (right hand panel). The yellow spheres represent new carbon atoms which have healed the sidewall of the SWNT. The images were taken over 60 seconds with a total dose of *ca.* 1.5 x 10^9 e^-/nm^2. The scale bar is 1 nm.

2.2.2.2 Formation of Cu_2O_x

Since bulk $Cu(acac)_2$ decomposes upon melting at 279-283 ^oC, the sample was heated above this temperature to investigate what changes, if any occurred to the sample. Heating $Cu(acac)_2$@SWNT at 500 ^oC for 1 hr in argon leads to the complete loss of the volatile acetylacetonate ligands and the formation of what appears to be Cu_2O@SWNT (figure 2.7).

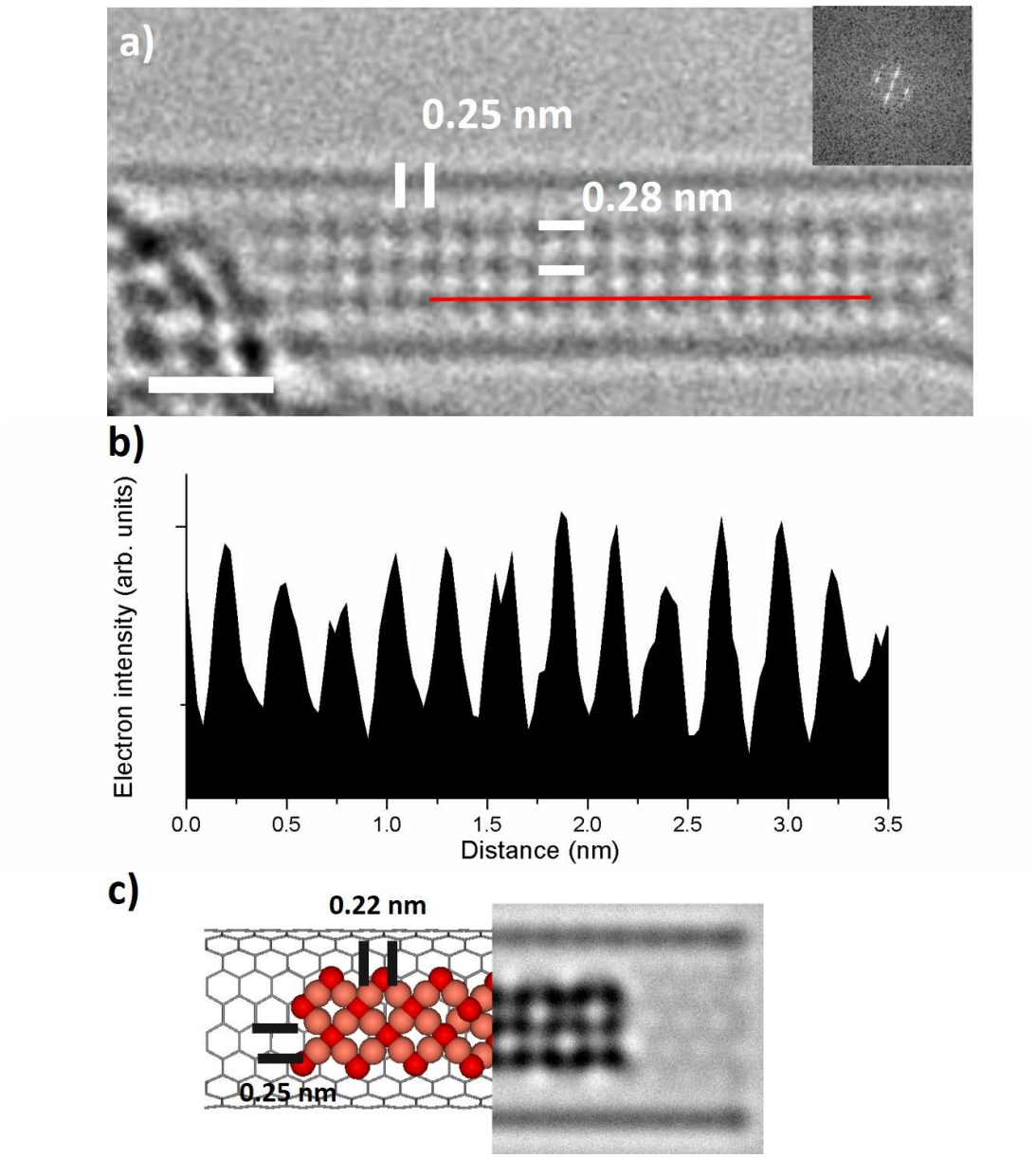


Figure 2.7: a) AC-HRTEM image (80 kV) showing Cu_2O@SWNT, formed after the thermal treatment of $Cu(acac)_2$@SWNT. Inset is a fast Fourier transform (FFT) of the micrograph showing crystallinity, and the red line shows the area from which the electron intensity profile (b) was taken, to show periodicity and

determine atomic spacings; c) a geometry optimised model of how a portion of the structure of bulk Cu_2O@SWNT could fit into a (10,10) SWNT, coupled with a Scherzer-focussed QSTEM simulation of the model at 80 kV. The scale bar is 0.8 nm.

The rendered model shows that the ratio of Cu:O atoms is slightly less that 2:1, i.e. there are more oxygen atoms than in bulk Cu_2O, which is caused by the material deviating from bulk stoichiometry to create the best fit inside the nanotube, and so henceforth the material will be referred to Cu_2O_x, where $x > 1$. The encapsulated Cu_2O_x species adopts a highly crystalline cubic structure similar to that of bulk Cu_2O. The QSTEM image simulation (figure 2.7 c) confirms that only copper atoms are visible, and the Cu-Cu bond distance has increased slightly upon encapsulation. This is due to it trying to maximise interactions with the nanotube sidewall.

2.2.2.3 Electron Transfers in $Cu(acac)_2$@SWNT and Cu_2O_x@SWNT

In order fully characterise the materials and to help to discover future applications for these nanomaterials, it is important to comprehensively understand the electronic properties of the systems. Raman spectroscopy has been employed to investigate whether any electron transfers take place between the nanotube and guest materials, (figure 2.8). The spectra of $Cu(acac)_2$@SWNT and Cu_2O_x@SWNT have similar features to that of an empty pristine SWNT with a variety of characteristic features such as peaks corresponding to the RBM, D, G and G* bands.

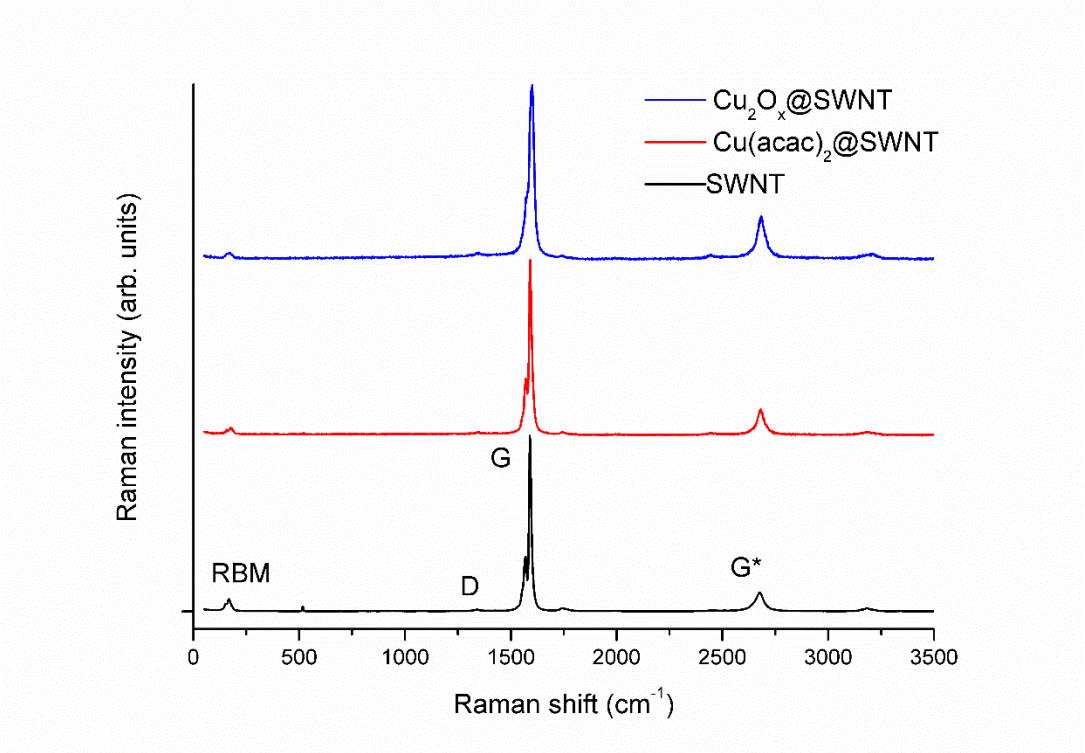


Figure 2.8: Normalised Raman spectra of an empty SWNT (black), $Cu(acac)_2$@SWNT (red) and Cu_2O_x@SWNT (blue). Shown on the spectrum of empty SWNTs are the key features indicative of a SWNT, the RBM, D, G and G* bands.

The G band of empty SWNTs occurs at 1590 cm^{-1}, however upon encapsulation of $Cu(acac)_2$@SWNT, there is a slight blue shift to 1591 cm^{-1} (table 2.2) which is negligible, and within the error of the instrument. After the thermal treatment of $Cu(acac)_2$@SWNT under argon, Cu_2O_x@SWNT is formed, and this leads to a significant blue shift in the G band of the SWNT to 1601 cm^{-1} (an increase of 11 cm^{-1} from pristine SWNTs, figure 2.9). This is indicative of an electron transfer from the nanotube to the guest molecule which results in a contraction of the hexagonal rings along the cylindrical wall of the nanotube.[25] This is attributed to the new Cu_2O_x species having a slight negative charge due to the excess oxygen atoms, and so the nanotube becomes electropositive to stabilise this species.[26] Therefore Cu_2O_x can be considered as a cuprate species $[Cu_2O_x]^{((x-1).2)-}$@$SWNT^{((x-1).2)+}$.

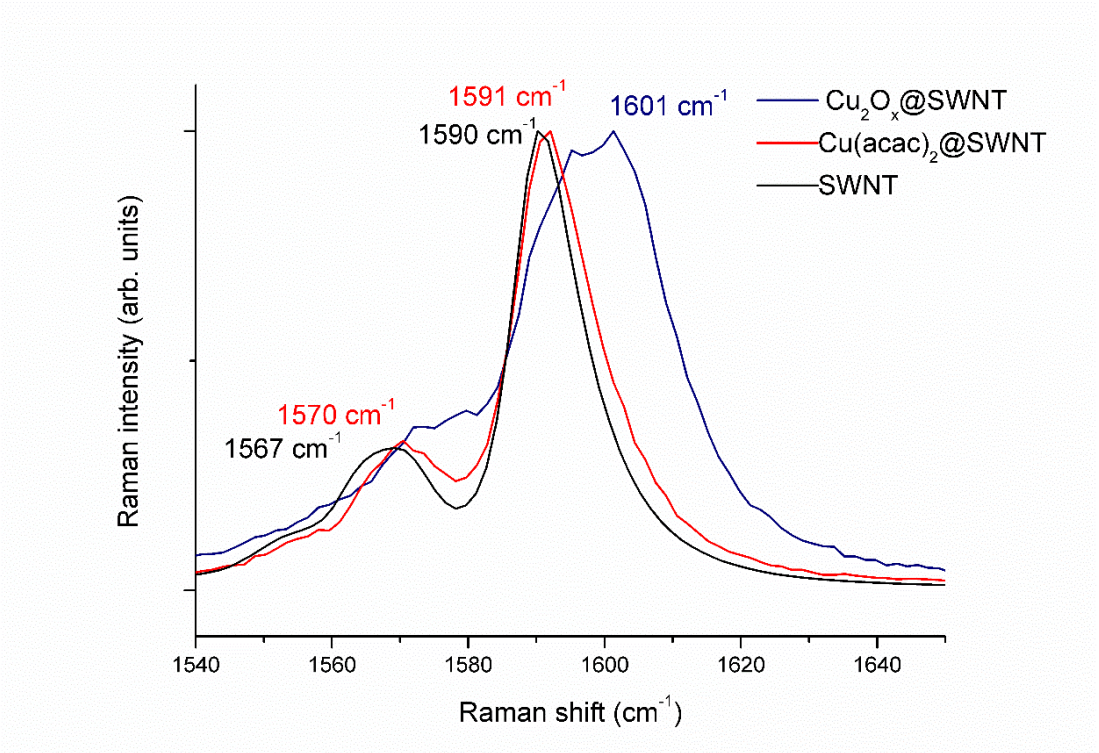


Figure 2.9: Normalised Raman spectra showing the G band of an empty SWNT (black, 1590 cm^{-1}), $Cu(acac)_2$@SWNT (red, 1591 cm^{-1}) and Cu_2O_x@SWNT (blue, 1601 cm^{-1}). A shift of 11 cm^{-1} is caused by the formation of Cu_2O_x@SWNT indicating electron transfer from the nanotube to the guest species.

Fluorescence-detected X-ray absorption spectroscopy (FD-XAS) can be used in conjunction with Raman spectroscopy to monitor electron transfers between SWNTs and the guest species by observing how the position of the absorption edge of the metal changes, and so although Raman spectroscopy explores electron transfers by monitoring changes on the nanotube, FD-XAS allows analysis of electron transfers from the perspective of the encapsulated material.

The FD-XAS of $Cu(acac)_2$@SWNT shows that the energy of the copper K edge has increased slightly relative to $Cu(acac)_2$, suggesting that electrons have been transferred from the copper atoms (figure 2.10). As seen previously, there is no change in the Raman spectrum of $Cu(acac)_2$@SWNT relative to pristine SWNTs, and so electron transfers taking place are therefore confined to the $Cu(acac)_2$ molecule.

The Cu-O bonds are being polarised by the nanotube, and this phenomenon is discussed in more detail in Chapter V. Upon transformation of $Cu(acac)_2$@SWNT to Cu_2O_x@SWNT, the energy of the copper K edge has decreased significantly (6.34 eV) which is consistent with the reduction of oxidation state of the copper, and is in better agreement with the edge energy of a known Cu(I) complex, although is slightly lower due to electron density being transferred to it from the SWNT (table 2.2) which was confirmed using Raman spectroscopy.

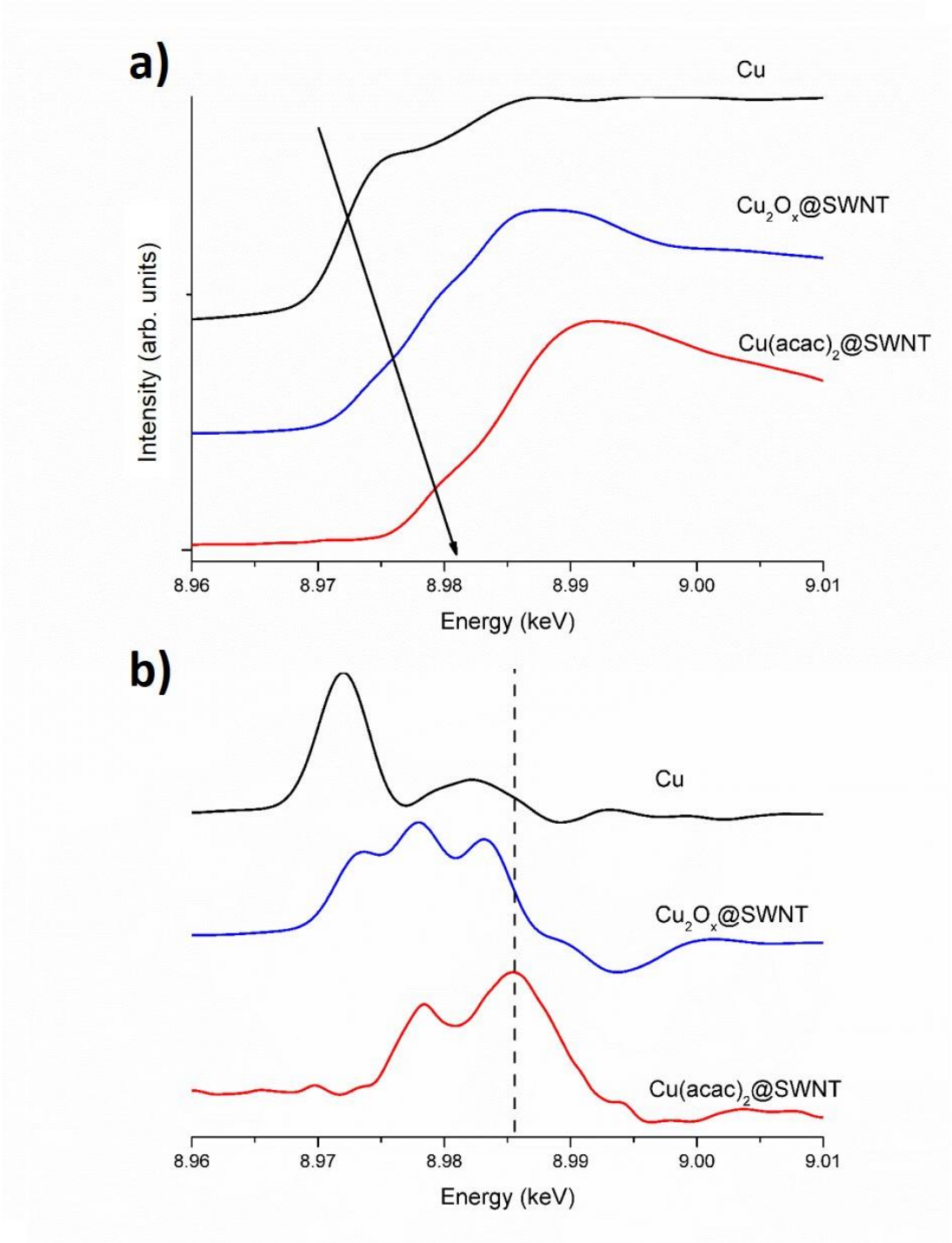


Figure 2.10: a) Normalised FD-XAS showing the copper K edges of Cu_2O_x@SWNT and $Cu(acac)_2$@SWNT compared to that of elemental Cu; b) the first derivative of each spectra is shown to determine the precise excitation energy.

Table 2.2: A summary of the electron transfers taking place in the materials produced. The energy of the copper K edge of the materials produced is compared to known standards, and shown with respect to (w.r.t.) the energy of the copper K edge of Cu(0). Where applicable the shift in G band of the SWNT is listed, and the direciton of charge transfer taking place within each material is summarised.

Material	Cu K edge/eV (shift w.r.t Cu 0)	G band position (cm^{-1}) (shift w. r. t. pristine SWNTs)	Direction of electron transfer
Cu	8975.53 ± 0.079 (0)	-	-
Cu_2O_x@SWNT	8980.42 ± 0.037 (4.89)	1601 (+11)	SWNT → Cu
$Cu(CO_2CH_3)$	8982.18 ±0.061 (6.65)	-	-
$CuBr_2$	8983.24 ± 0.083 (7.71)	-	-
$Cu(acac)_2$	8984.76 ± 0.37 (9.23)	-	-
$Cu(acac)_2$@SWNT	8986.76 ± 0.093 (11.23)	1591 (+1)	Cu →O
SWNT	-	1590 (0)	-

2.2.3 Silver

The encapsulation of silver into the internal channel of SWNTs was achieved by utilising the organometallic complex silver (hexafluoroacetylacetonate) (cycloocta1,5-diene), Ag(HFacac)(COD), (HFacac = $((CF_3CO)_2CH)^-$). In a similar procedure to the formation of a copper containing species inside SWNTs, the silver complex was sealed in a glass ampoule under vacuum with the SWNTs, and heated at slightly above the sublimation point of the complex (which was determined to be 110 ^oC using a similar sublimation procedure as for the copper complex) for three days to form Ag(HFacac)(COD)@SWNT (figure 2.11).

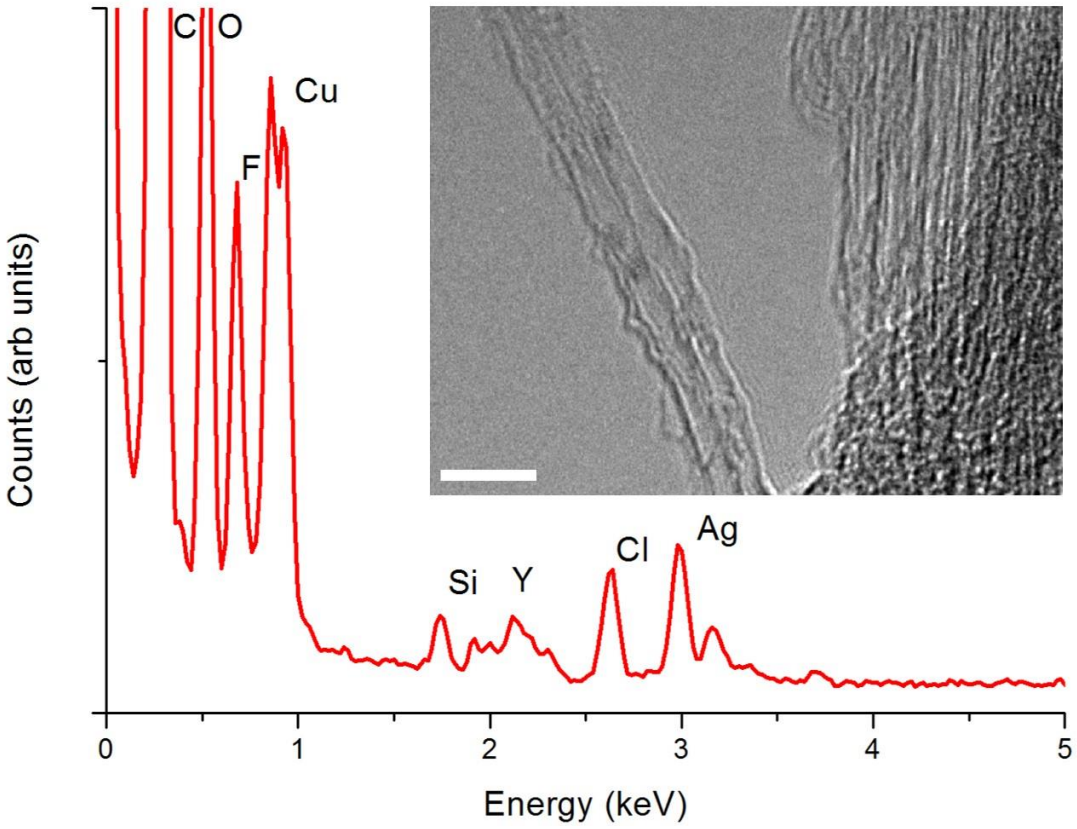


Figure 2.11: EDX spectrum recorded at 100 keV primary electron energy and integrated over a small bundle of nanotubes confirms the presence of silver inside the nanotube. Copper and silicon peaks are due the TEM grid, and yttrium is due to the catalyst of SWNT formation. A HR-TEM image (inset) of the area over which the EDX spectrum was taken. The scale bar is 5 nm.

In a similar fashion to the decomposition of $Cu(acac)_2$@SWNT, the silver complex has also decomposed under the electron beam leading to the aggregation of AgNPs. In contrast to the encapsulated nanoparticles of copper, silver atoms appear to have formed a compact face centred cubic cluster and the material appears darker in contrast to that of copper which is due to the fact that elements with a higher atomic number have a much higher contrast in TEM (figure 2.12 a).[27] The structure of AgNPs is comparable to the face centred cubic bulk structure of silver (figure 2.12 b) and the atomic spacings are shown with a line profile electron intensity map (2.12 c).

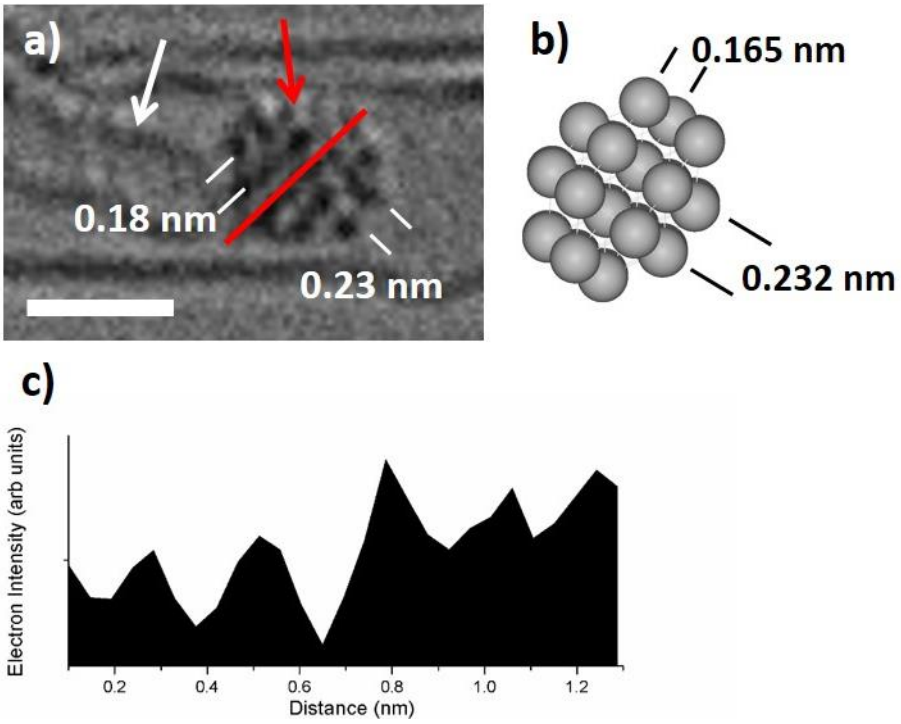


Figure 2.12: a) AC-HRTEM image (80 kV) showing silver inside a SWNT. The silver atoms (red arrow) have clustered together in a close cubic arrangement, and residue carbon from the ligands are also shown to have formed an extended carbon cylinder (white arrow); b) the (110) plane of the Ag crystal lattice for comparison; c the electron intensity profile generated from the red line in (a) showing the interatomic spacings for the atoms.

The AC-HRTEM image shows a large amount of adventitious carbon adjacent to the silver cluster, but in contrast to the previous example with copper, here the carbon cylinder (figure 2.13 a, white arrow) doesn't interact at all with the metallic cluster.

A higher electron dose was applied to stimulate interactions, however no changes between the metal cluster and residue carbon were observed.

In another example, a hemispherical carbon bubble has initially formed around the cluster of silver atoms, and over time (120 seconds) the silver cluster appears to promote the formation of another carbon nanotube within the SWNT (figure 2.13). The process occurs in a SWNT with a very defective sidewall (figure 2.13 a) and over time this appears to become more ordered (figure 2.13 b, c), and so under the electron beam, carbon atoms from the wall are being restructured and forming another nanotube inside the SWNT (figure 2.13 d).

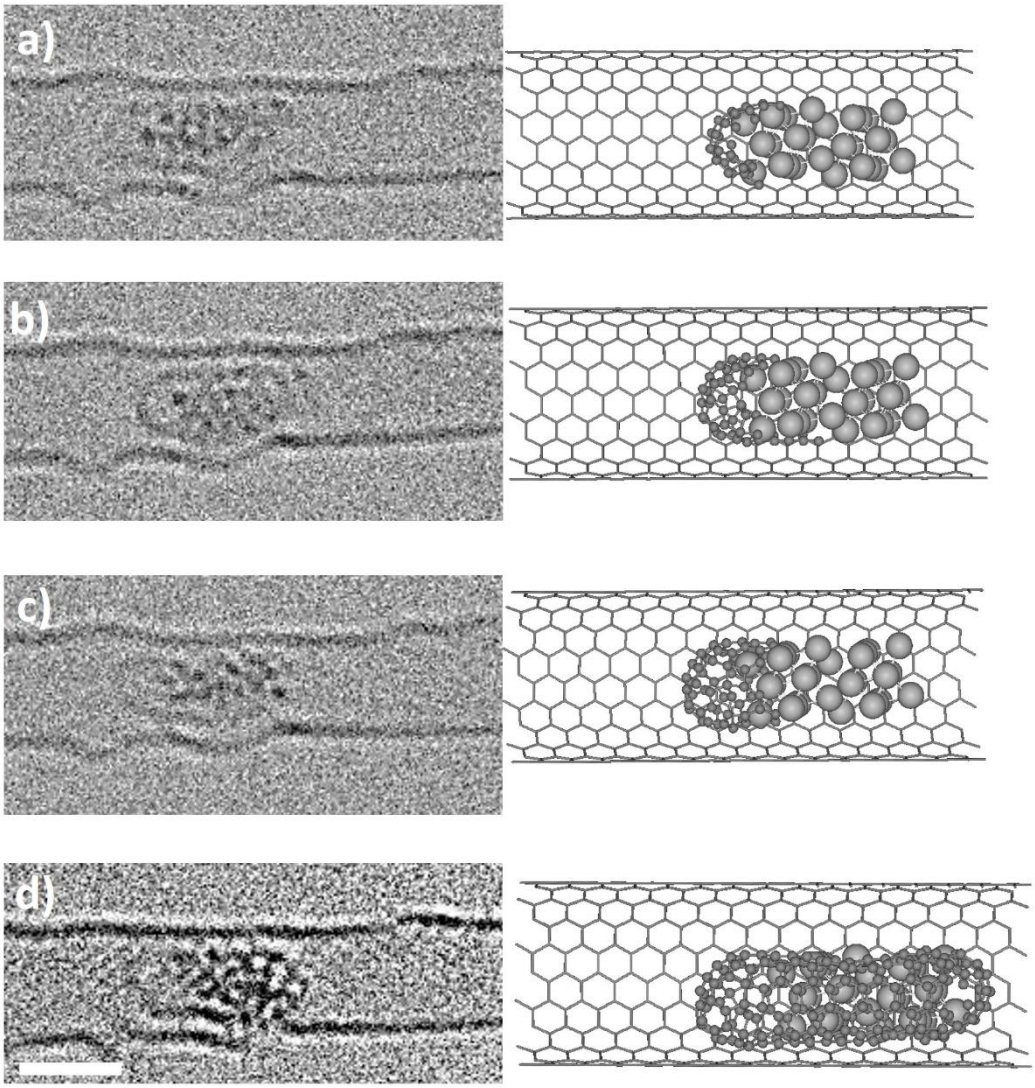


Figure 2.13: AC-HRTEM time series (left panel) showing how a SWNT can start to form from a cluster of silver atoms. Initially, there is an elongated hemisphere of amorphous carbon surrounding the AgNPs (a), and over time this extends (b-d). In addition to the formation of the extended carbon structure, the walls of the SWNT are becoming more ordered. The right panel depicts an atomic model of the process at each stage. The total electron dose is *ca.* 5 x 10^9 e^-/nm^2.

The encapsulated silver complex was also heated up under argon at 500 ^oC for 1 hr; however, no significant changes to the morphology of the sample were observed, and it remained as a metallic cluster.

2.2.4 Gold

The encapsulation of gold into the internal channels of SWNTs was achieved by utilising the precursor chlorocarbonyl gold, AuCOCl. In a similar procedure to the formation of the encapsulated copper and silver containing species, AuCOCl was sealed in a glass ampoule with the SWNTs, and heated at slightly above the sublimation point of the complex (determined experimentally to be 110 ^{o}C) for three days to form AgCOCl@SWNT (figure 2.14). EDX confirms the presence of gold.

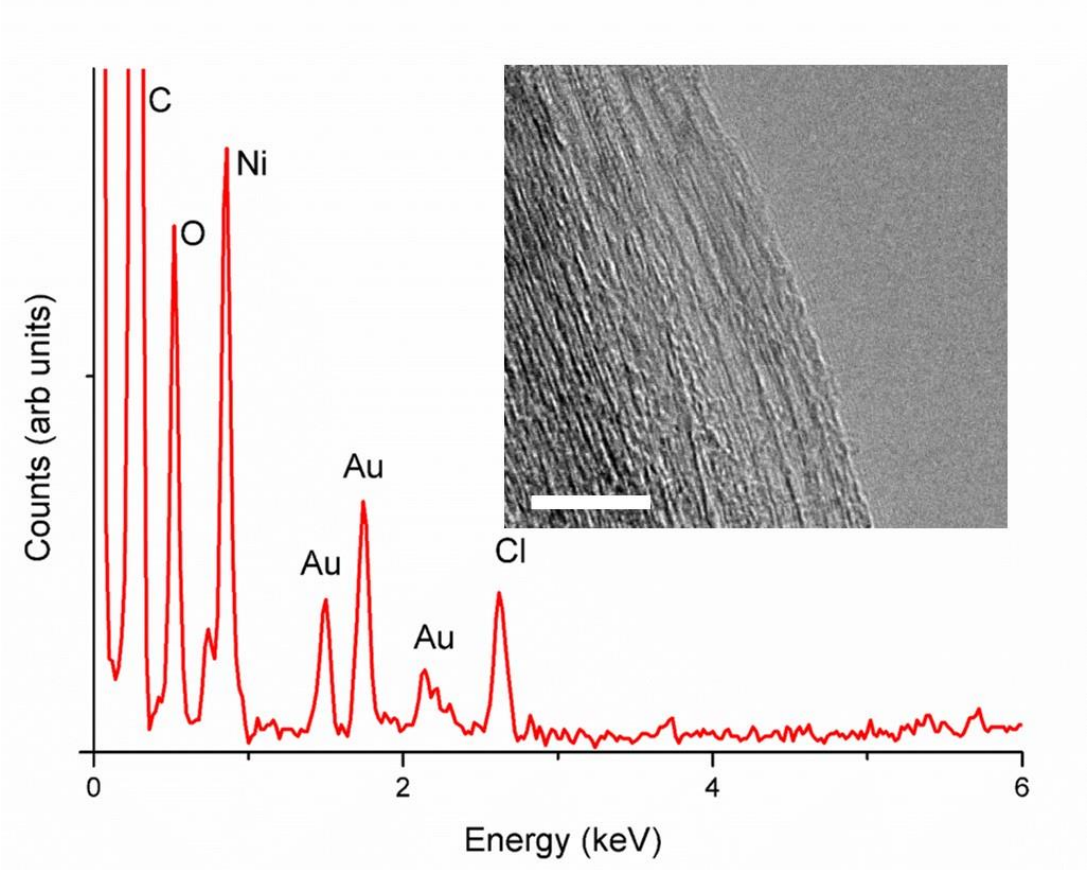


Figure 2.14: EDX spectrum recorded at 100 keV primary electron energy and integrated over a small bundle of nanotubes confirms the presence of gold inside the nanotube. The nickel peak is due to the specimen holder of the sample. A HR-TEM image (inset) of the area over which the EDX spectrum was taken. The scale bar is 5 nm.

Similar to the encapsulation of Ag@SWNT, the gold atoms have formed a close packed face centred cubic structure (figure 2.15 a), analogous to the (111) surface of the crystal lattice of bulk gold (figure 2.15 b).

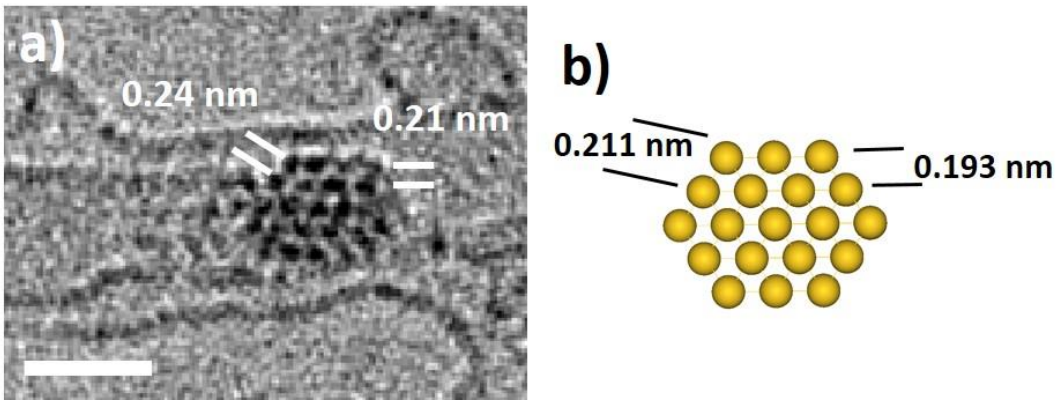


Figure 2.15: a) AC-HRTEM image (performed at 80 kV) showing AuCOCl@SWNT. Under the electron beam, the volatile ligands have been removed, leaving only gold. b) The unit cell of bulk gold for comparison reveals a slight increase in the spacing between the gold atoms in the SWNT. The scale bar is 0.5 nm

Although the gold cluster doesn't appear to interact with carbon from the sidewall of the SWNT, it is in contact with adventitious carbon from the SWNT interior and appears to form gold carbide in the TEM beam, as shown by the regular cubic structure and spacings similar to those in the literature (figure 2.16).[28]

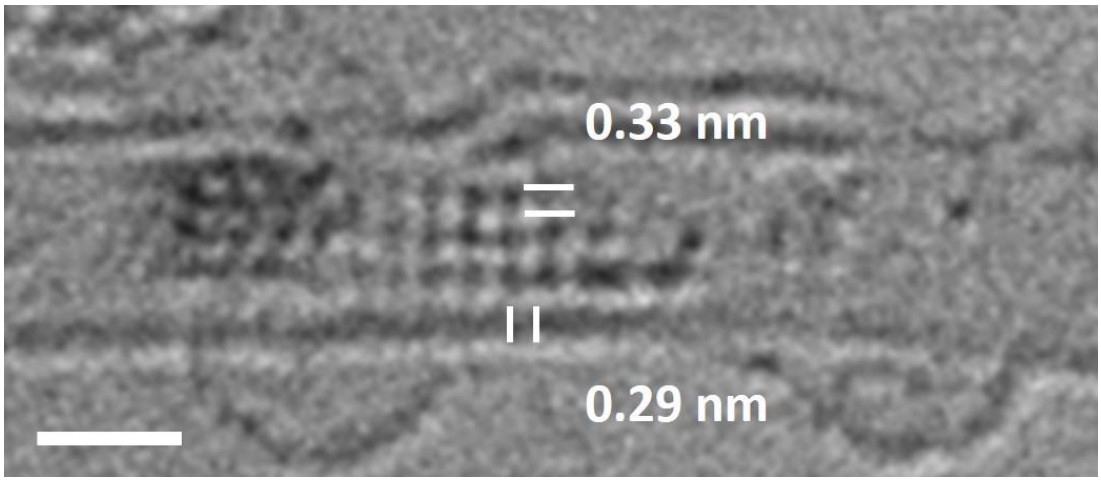


Figure 2.16: AC-HRTEM image (performed at 80 kV) showing what appears to be gold carbide next to a cluster of gold atoms. The gold carbide structure has a

regular cubic spacing similar to that reported in the literature.[28] The scale bar is 1 nm.

Subsequently, AuCOCl@SWNT was also heated under argon for 1 hr, and this also showed the formation of Au@SWNT. No materials consistent with the structure of gold carbide were present, only AuNPs (figure 2.17).

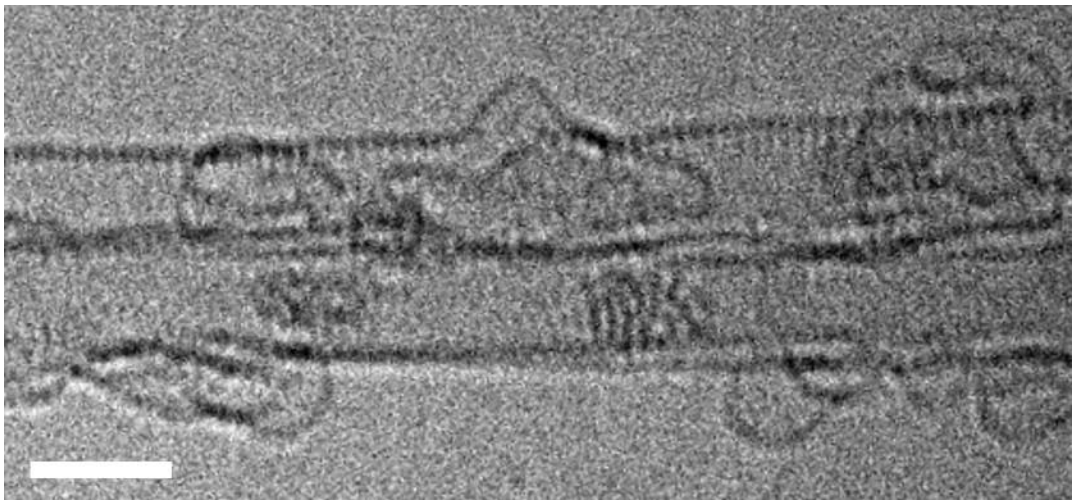
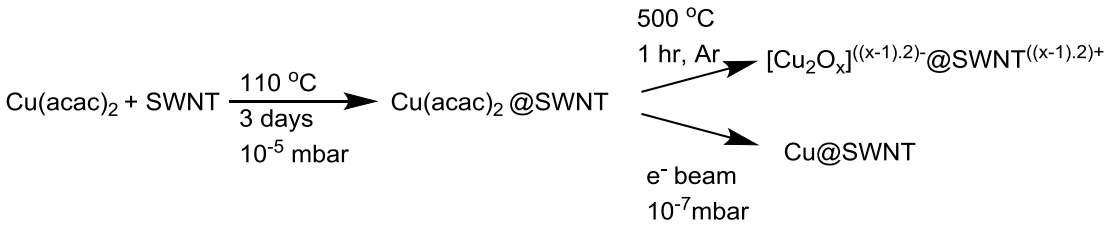


Figure 2.17: AC-HRTEM image showing clusters of Au@SWNT after heating in argon at 500 ºC. The scale bar is 1 nm.

2.3 Discussion

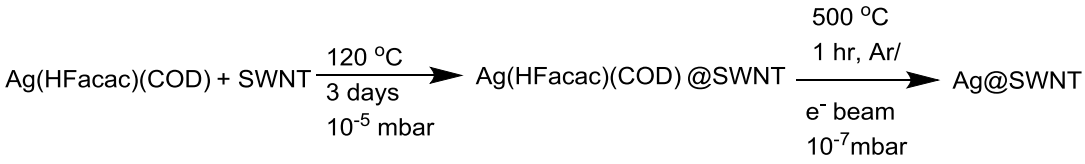
The process of forming nanoparticles of both copper and copper oxides has been discussed in depth in the literature.[23] Nasibulin *et al.* have shown that the products formed by the decomposition of $Cu(acac)_2$ depend on both the experimental conditions and presence of various reagents such as H_2, H_2O and CO_2.[23] When bulk $Cu(acac)_2$ was heated in an inert (nitrogen) atmosphere at temperatures below 700 ^oC, only CuNPs formed, but over this temperature Cu_2O was synthesised and it was shown that the addition of H_2 during the heating of $Cu(acac)_2$@SWNT lowered the temperature at which Cu_2O formed. The electron beam has been shown to produce only metallic copper, and there is no evidence of oxide formation; however, taking the same sample and heating it in an argon atmosphere has led to the formation of Cu_2O_x@SWNT (scheme 2.2).



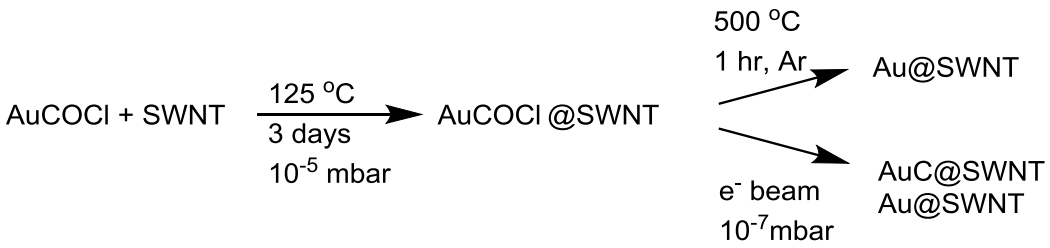
Scheme 2.2: The formation of both CuNPs and Cu_2O_x from $Cu(acac)_2$ encapsulated into a SWNT.

In the bulk, Cu_2O is formed by a mechanism which includes the reaction of copper dimers with oxygen containing organic groups formed *via* the decomposition of $Cu(acac)_2$. Heating $Cu(acac)_2$@SWNT at 500 ^oC was sufficient to lead to the formation of Cu_2O, which clearly is a much lower temperature than what is required for bulk $Cu(acac)_2$. This shows that encapsulation within nanotubes lowers the energy required for transformation to occur and is caused by the polarisation of the complex

within a nanotube which is shown by the increase in copper K edge energy of the FD-XAS. This transformation is of interest and will be discussed further in Chapter V. Conversely, heating both the encapsulated gold and silver complexes at 500 ^{o}C only led to decomposition of the complexes into MNPs, and the electron beam facilitated the formation of AuC from AuCOCl@SWNT, (schemes 2.3, 2.4).



Scheme 2.3: The formation of Ag@SWNT from a silver containing precursor.



Scheme 2.4: The formation of AuC@SWNT and Au@SWNT from a gold containing precursor.

While the electron beam serves as an imaging technique, it is a high energy instrument and so can also be used as a source of energy to promote chemical and physical transformations in the selected area of the sample. Furthermore, the maximum kinetic energy (T_{max}), transferred from the incident electron to an atom (M) and can be expressed as:

$$T_{max} = \frac{2 \cdot M \cdot E(E + 2m_e \cdot c^2)}{(M + m_e)^2 \cdot c^2 + 2M \cdot E}$$

Equation 2.1

Where M – mass of atoms, m_e – mass of electron, E – energy of the electron beam, and c – speed of light.

Using Equation 2.1, the maximum energy transferred due to a collision from an electron of the 80 kV beam to an atom of carbon, $T_{max}(C) = 15.8$ eV, and while this is below the threshold energy required for an ejection of a carbon atoms (approximately 17 eV), with the presence of MNPs acting catalytically, it is possible to reduce the energy required for noticeable electron beam changes.[29] This is supported by TEM imaging of pristine defect free SWNTs which show no sign of structural transformations taking place.

Typically, the maximum kinetic energy transferred to transition metals atoms, $T_{max}(M)$ at 80 kV is in the range 1-4 eV, which is much lower than that transferred to carbon. The maximum energy transferred is inversely proportional to atomic mass which implies that lighter elements behave more dynamically under the electron beam, and decreases rapidly down a group; however, this isn't necessarily the case as the trends observed here rely on more than just a dependence of $T_{max}(M)$ on the atomic mass.

The energy transferred to an atom from an incident electron should be similar to the interatomic bonding energy (cohesive energy) in the cluster if measurable structural transformations are to occur. The bulk cohesive energy (E_{coh}) for the three metals is in the range of 2.95 eV– 3.81 eV, which is much greater than the corresponding $T_{max}(M)$ values, although it is expected that the interatomic bonding for atoms near the surface of small clusters is much smaller relative to that of the atoms in the bulk. With this in mind, the metal clusters reported in this study could still be significantly affected by the electron beam even though the $T_{max}(M)$ is lower than E_{coh} for each metal, and indeed this is demonstrated with these AC-HRTEM measurements.

In order to qualitatively demonstrate how much kinetic energy an atom receives, the ratio $T_{max}(M)$ to $E_{coh}(M)$ can act as a guide. Employing this parameter, copper atoms are shown to receive up to 85% of energy required for their ejection from the bulk, silver up to 59% and gold only a maximum of 25%, and so it is predicted that copper atoms should act more dynamically in the presence of the electron beam as they are receiving more energy. This can explain why CuNPs appear more diffuse than silver and gold clusters (table 2.3).

Table 2.3: Cohesive energy of metals (E_{coh}) and maximum transferred energy ($T_{max}(M)$) from the 80 kV electron beam for the group 11 metal atoms. The ratio $T_{max}(M)/E_{coh}$ represents the energy received from the electron beam as a percentage of metal cohesive energy.

Metal	$T_{max}(M)$ (eV)	Cohesive energy, E_{coh} (eV/atom)	$[T_{max}(M)/E_{coh}] \times 100$ (%)
Copper	2.97	3.49	85
Silver	1.75	2.95	59
Gold	0.96	3.81	25

In a defect free, pristine SWNT, the d-orbitals of the encapsulated metal clusters are able to interact with the π-electron system of the SWNT, with the transition metal withdrawing electrons from the bonding orbital but donating electrons to the antibonding orbital of the C=C double bond, (figure 2.18 a, b), which is analogous to the Dewar-Chatt-Duncanson model describing bonding of an alkene to a metal atom.[30] When the metals are involved in bonding with the nanotube wall, the C-C bonds are weakened which make them easier to break. On the other hand, when one or more carbon atoms are missing from the sidewall of the SWNT (a vacancy-type defect, figure 2.18 c and figure 2.1) the metal atoms are able to σ-bond with the carbon atoms. Furthermore, theoretical studies have shown copper absorbed into a vacancy site is more stable than silver or gold, which is why only copper atoms are observed

in the wall of the nanotube in this study, and no silver or gold.[6] The effectiveness of M-C σ-bonds can determine the thermodynamic stability of the defects in SWNTs, as a strong M-C bond can stabilise dangling bonds of carbon atoms which lowers the activation barrier of C-C bond reformation.

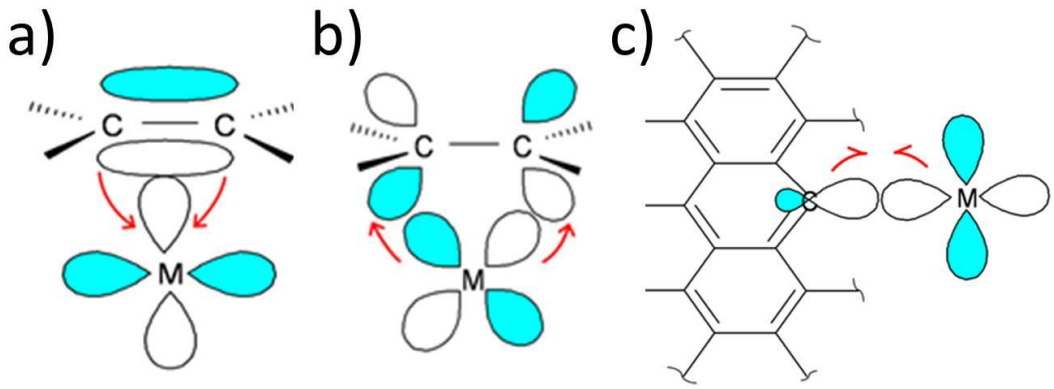


Figure 2.18: Schematic diagrams showing how the overlap of orbitals from a defect free nanotube can interact with those of a transition metal atom leading to M-C π-bonding (a, b). If a defect is present in the nanotube sidewall (c), the dangling bonds of carbon atoms can engage in M-C σ-bonding.

Theoretical simulations have been used to investigate the extent of the interaction between coinage metals and the exterior of the nanotube wall. It has been shown that copper and silver atoms adsorb over a C-C bond, whereas gold atoms adsorb above a carbon atom. Furthermore, the M-C bond distance has been predicted to decrease from Au > Ag > Cu implying that copper atoms interact more strongly with the carbon relative to silver or gold, and this is in agreement with the stability of coinage metal-olefin complexes in the bulk.[6, 31]

These direct space real-time observations of the coinage metals in SWNTs confirm the extent of π-bonding between the metal cluster and side wall and agree with the trend observed theoretically for metal clusters on the outside of the SWNT wall.

Once particles of transition metals become embedded within the wall of a SWNT, carbon atoms can become dislodged to a particular metallic element specific degree

(see equation 2.1) and undergo a process of electron beam induced ejection, or alternatively the dislodged carbon atoms can stay within the SWNT, and engage with the MNP to take part in a process of electron beam induced restructuring to form new carbon nanostructures.[12] Despite there being evidence in the literature of examples of all group 11 MNPs catalysing the formation of SWNTs on substrates, it appears that in a nanotube, only the encapsulation of silver leads to the extension of the carbon structure to form a nanotube within the nanotube.[32-34] It has been shown that encapsulation of copper leads to the formation of a fullerene type structure, whereas gold leads to the formation of gold carbide. This implies that copper promotes the ejection of carbon atoms more so than silver and gold as clearly less carbon is needed to form a fullerene, and therefore it can be proposed that copper forms a stronger bond with carbon than gold or silver. In order for a metal to successfully catalyse the formation of a new carbon structure, it needs to be able to bond with carbon atoms but then readily dissociate. Given the high throughput of carbon atoms from AgNPs required to form an extended carbon cylinder, silver therefore is shown to form weaker bonds with carbon than copper. On the other hand, the formation of what appears to be a stable gold carbide structure implies that bonding between silver and carbon is strong.

2.4 Conclusion

Copper, silver and gold have been systematically studied inside SWNTs by the encapsulation and subsequent decomposition of molecular precursors. Time-resolved transformations and the visualisation of nanostructures have been carried out using AC-HRTEM, and by careful comparison of the bonding of the coinage metals with carbon, it has been shown that the metals engage in different processes depending on their position in the periodic table. The electron beam can be used not only as an

imaging tool, but also as a chemical initiator, leading to the creation of different carbon nanostructures, and the formation of a copper-oxygen containing structure, Cu_2O_x ($x > 1$) has been shown.

This demonstrates the first instance in which metal atoms from all of the coinage group elements have been systematically encapsulated into SWNTs and as well as introducing the concept of using nanotubes as test tubes for the investigation of nanoscale reactions, it has great implications for future work involving metal catalysed transformations in carbon nanotubes.

2.5 Experimental

SWNTs (P2, arc discharge, Carbon Solutions, USA) were annealed at 600 ^oC for 15 min to open their termini and remove any residual amorphous carbon from their internal cavities resulting in a 50% mass loss being observed. The metallic precursors, $Cu(acac)_2$, Ag(HFacac)(COD) and AuCOCl were used as supplied (Sigma Aldrich).

2.5 1 Encapsulation of Complexes

Each metal precursor (10 mg) was sealed under vacuum (10^{-6} bar) in a Pyrex ampoule with freshly opened SWNTs (5 mg) and heated at slightly above their sublimation temperature for 3 days to ensure penetration of the SWNT by the complexes (table 2.4 below). The samples were cooled rapidly, washed repetitively with dichloromethane (4 x 25 mL), and filtered on PTFE membranes to remove any excess material from the exterior of the SWNTs.

Table 2.4: A summary of conditions required to form each encapsulated metal species.

Initial compound	Amount of compound (mmol)	Sublimation temperature (^oC)

$Cu(acac)_2$	3.82×10^{-2}	110
Ag(HFacac)(COD)	2.36×10^{-2}	120
AuCOCl	3.85×10^{-5}	125

2.5.2 Formation of MNPs@SWNT

Under atmospheres of argon, $Cu(acac)_2$@SWNT (5 mg), Ag(HFacac)(COD)@SWNT (5 mg) and AuCOCl@SWNT (5 mg) were each heated in Pyrex tubes at 500 ^oC for 1 hr and allowed to cool down slowly.

2.5.3 Electron Microscopy

SWNTs filled with the encapsulated materials were dispersed in propan-2-ol using an ultrasonic bath and drop cast onto lacey carbon-coated copper, or nickel in the case of copper containing samples. TEM grids (Agar). HR-TEM imaging and electron beam irradiation was carried out on a JEOL 2100 FEG-TEM microscope operated at 100 kV. AC-HRTEM was performed at the University of Ulm on a C_s corrected FEI Titan 80-300 TEM operated at 80 kV with information limit enhancement by reduced extraction voltage. All images were processed using Gatan Digital Micrograph, and the quoted distances were measured by drawing a line profile and measuring the electron intensity.

2.5.4 EDX Spectroscopy

Local EDX spectra were acquired for samples mounted on copper TEM grids (nickel grids were used for copper containing samples) using an Oxford Instruments INCA X-ray microanalysis system. The electron beam was condensed onto areas of specimens suspended over holes of the amorphous carbon film.

2.5.5 Raman Spectroscopy

The samples were separately dispersed in propan-2-ol, drop-cast onto Si(100) supports. Raman spectroscopy was performed using a HORIBA Jobin Yvon LabRAM HR spectrometer equipped with an automated *xyz* stage (Märzhäuser). Spectra were acquired using a 532 nm laser at 0.2mW power, in the range 50 to 4000 cm^{-1}, with 5 seconds and 8 accumulations per spectral window, using a 50× objective and a 300 μm confocal pinhole. To simultaneously scan a range of Raman shifts, a 600 lines/mm rotatable diffraction grating along a path length of 800 mm was employed. Spectra were detected using a SYNAPSE CCD detector (1024 pixels) thermoelectrically cooled to −60 °C. Before the spectra collection, the instrument was calibrated using the Rayleigh line at 0 cm^{-1} and a standard Si(100) reference band at 520.7 cm^{-1}.

2.5.6 Fluorescence-Detected X-ray Absorption Spectroscopy

All FD-XAS measurements were carried out on the XMaS beamline (BM28) at the ESRF in Grenoble. Samples were deposited onto carbon tape, which was then mounted onto a stainless steel sample holder. FD-XAS edge inflection points were obtained by fitting a smoothing spline to the measured spectrum, and taking the first derivative of the fitted spectrum.

2.5.7 Image Simulation

TEM image simulation was carried out using the multislice program QSTEM. QSTEM uses the Dirac-Fock scattering potential of Rez *et al*.[35] A fixed number of 20 slices per nanotube was chosen and images were calculated with a sampling of 0.05 nm per pixel. The aberration coefficients and defocus parameters *df*, *CS*, *A1*, and *B2* were set according to the imaging conditions in the specific experiment. The

convergence angle was fixed at 0.5 mrad. The effect of limited electron dose was emulated by applying noise to the calculated images using a custom-made Monte-Carlo program exploiting the Poisson statistics of electrons. Atomic models of SWNTs were built using a custom-made program taking into account different nanotube chiralities, if determinable in the experimental images. The structural models of the inorganic nanomaterials are based on scaled bulk structures and the model of Cu_2O_x@SWNT was rendered and iteratively fitted to the experimental results.

2.6 References

1. J. A. M. Simoes and J. L. Beauchamp, *Chem. Rev.*, 1990, **90**, 629.
2. D. A. Britz, A. N. Khlobystov, K. Porfyrakis, A. Ardavan and G. A. D. Briggs, *Chem. Commun.*, 2005, 37.
3. A. N. Khlobystov, *ACS Nano*, 2011, **5**, 9306.
4. J. Sloan and M. Monthioux, in *Carbon Meta-Nanotubes*, John Wiley & Sons, Ltd, 2011, pp. 225.
5. H. Valencia, A. Gil and G. Frapper, *J. Phys. Chem. C*, 2010, **114**, 14141.
6. C. Inntam and J. Limtrakul, *J. Phys. Chem. C*, 2010, **114**, 21327.
7. K. T. Chan, J. B. Neaton and M. L. Cohen, *Phys. Rev. B*, 2008, **77**, 12.
8. K. J. Kong, Y. M. Choi, B. H. Ryu, J. O. Lee and H. J. Chang, *Mater. Sci. Eng. C-Biomimetic Supramol. Syst.*, 2006, **26**, 1207.
9. Y. C. Ma, P. O. Lehtinen, A. S. Foster and R. M. Nieminen, *New J. Phys.*, 2004, **6**, 15.
10. I. V. Lebedeva, T. W. Chamberlain, A. M. Popov, A. A. Knizhnik, T. Zoberbier, J. Biskupek, U. Kaiser and A. N. Khlobystov, *Nanoscale*, 2014, **6**, 14877.
11. T. Zoberbier, T. W. Chamberlain, J. Biskupek, N. Kuganathan, S. Eyhusen, E. Bichoutskaia, U. Kaiser and A. N. Khlobystov, *J. Am. Chem. Soc.*, 2012, **134**, 3073.
12. T. Zoberbier, T. W. Chamberlain, J. Biskupek, M. Suyetin, A. G. Majouga, E. Besley, U. Kaiser and A. N. Khlobystov, *Small*, 2016, **12**, 1649.
13. G. L. Hallett-Tapley, M. J. Silvero, C. J. Bueno-Alejo, M. González-Béjar, C. D. McTiernan, M. Grenier, J. C. Netto-Ferreira and J. C. Scaiano, *J. Phys. Chem. C*, 2013, **117**, 12279.
14. S. A. Miners, G. A. Rance, A. La Torre, S. M. Kenny and A. N. Khlobystov, *J. Mater. Chem. C*, 2014, **2**, 8357.
15. P. Liu and J. A. Rodriguez, *J. Chem. Phys.*, 2007, **126**, 164705.
16. J. Sloan, J. Hammer, M. Zwiefka-Sibley and M. L. H. Green, *Chem. Commun.*, 1998, 347.
17. A. Eliseev, L. Yashina, M. Kharlamova and N. Kiselev, *Electronic Properties of Carbon Nanotubes*, 2011, 127.

18. W. Reckien, M. Eggers and T. Bredow, *Beilstein J. Org. Chem.*, 2014, **10**, 1775.
19. A. N. Khlobystov, D. A. Britz and G. A. D. Briggs, *Acc. Chem. Res.*, 2005, **38**, 901.
20. H. Ulbricht, G. Moos and T. Hertel, *Phys. Rev. Lett.*, 2003, **90**, 095501.
21. T. W. Chamberlain, T. Zoberbier, J. Biskupek, A. Botos, U. Kaiser and A. N. Khlobystov, *Chem. Sci.*, 2012, **3**, 1919.
22. M. V. Buzaeva, V. V. Dubrovina, O. A. Davydova and E. S. Klimov, *Russ. J. Appl. Chem.*, 2011, **84**, 892.
23. A. G. Nasibulin, P. P. Ahonen, O. Richard, E. I. Kauppinen and I. S. Altman, *J. Nanopart. Res.*, 2001, **3**, 385.
24. P. E. Fanta, *Chem. Rev.*, 1946, **38**, 139.
25. L. Grigorian, K. A. Williams, S. Fang, G. U. Sumanasekera, A. L. Loper, E. C. Dickey, S. J. Pennycook and P. C. Eklund, *Phys. Rev. Lett.*, 1998, **80**, 5560.
26. A. Botos, J. Biskupek, T. W. Chamberlain, G. A. Rance, C. T. Stoppiello, J. Sloan, Z. Liu, K. Suenaga, U. Kaiser and A. N. Khlobystov, *J. Am. Chem. Soc.*, 2016, **138**, 8175.
27. K. W. Urban, *Science*, 2008, **321**, 506.
28. B. Westenfelder, J. Biskupek, J. C. Meyer, S. Kurasch, X. H. Lin, F. Scholz, A. Gross and U. Kaiser, *Sci. Rep.*, 2015, **5**.
29. F. Banhart, J. Kotakoski and A. V. Krasheninnikov, *ACS Nano*, 2011, **5**, 26.
30. M. J. S. Dewar, *Bull. Soc. Chim. Fr.*, 1951, **18**, C71.
31. J. M. Mays, *International Review of Science. Inorganic Chemistry. Series 1. Volume 6. Transition Metals part 2.*, Butterworths, London, 1 edn., 1972.
32. W. Zhou, Z. Han, J. Wang, Y. Zhang, Z. Jin, X. Sun, Y. Zhang, C. Yan and Y. Li, *Nano Lett.*, 2006, **6**, 2987.
33. D. Hu, X. He, L. Sun, G. Xu, L. Jiao and L. Zhao, *Sci. Bull*, 2016, **61**, 917.
34. S. Bhaviripudi, E. Mile, S. A. Steiner, A. T. Zare, M. S. Dresselhaus, A. M. Belcher and J. Kong, *J. Am. Chem. Soc.*, 2007, **129**, 1516.
35. D. Rez, P. Rez and I. Grant, *Acta Crystallogr. Sect. A*, 1994, **50**, 481.

Chapter III: Investigations into the Behaviour of the Group 10 Metals when Confined inside Single-Walled Carbon Nanotubes

3.1 Introduction

The group 10 elements, consisting of platinum, palladium, and nickel are crucially important for many industrial catalytic applications.[1-5] However, very little is known about their interactions with carbon at the atomic scale, and this is essential to allow for a fundamental understanding of organometallic bonding, which is crucial for catalysis and sensing purposes.

In addition to the formation of encapsulated metallic nanoparticles (MNPs) to allow for the study of metal carbon interactions, it is also essential to find applications for the materials produced, as nanoparticles have different properties to their bulk analogues due to a high surface area to volume ratio.[6, 7] Furthermore, nanoparticles of group 10 metals, and indeed controlled methods to make these materials are necessary as they have potential use in a wide range of applications, such as nickel nanoparticles (NiNPs) for the hydration of CO_2; palladium nanoparticles (PdNPs) for selective drug delivery; and platinum nanoparticles (PtNPs) for small molecule sensing.[4, 8-12]

As shown in Chapter II, single-walled carbon nanotubes (SWNTs) can act as excellent containers for small amounts of metallic atoms and can successfully be employed to study properties of metals at the nanoscale. In this chapter, the method is going to be reproduced to study the group 10 metals. Atomic precursors containing the three metals will be inserted into SWNTs, decomposed to form MNPs and studied using

aberration-corrected high resolution transmission electron microscopy (AC-HRTEM). Herein the interactions between the group 10 elements and SWNTs has been discussed, with noticeable trends in terms of morphology, catalytic properties towards C-C bond formation, and metal-carbon (M-C) bonding observed.

3.2 Results

3.2.1 Materials Preparation

The transition metals palladium and platinum were encapsulated into SWNTs in the form of metal acteylacetonates ($M(acac)_2$), (M = Pt, Pd); and nickel in the form of nickel hexafluoroacetylacetonate, $Ni(HFacac)_2$, (HFacac = $((CF_3CO)_2CH)^-$) which were all easily be broken down into pure metal and volatile organic ligand (figure 3.1). The chosen complexes sublime without decomposition when heated under vacuum (10^{-5} mbar), and so heating them at slightly above their sublimation temperature in a sealed ampoule with SWNTs led to their encapsulation. Excess complex remained on the outside of the SWNTs, and this was removed using dichloromethane, which selectively removes complexes from the exterior of SWNTs.[13]

Heating the encapsulated complexes at 500 ^oC under argon for 1 hr led to the volatile ligands being expelled from the SWNTs, and the metal atoms aggregated into clusters of *ca.* 50-60 atoms inside the internal channel of the SWNTs (figure 3.1 a). The encapsulation of the metal clusters formed inside the nanotubes was successfully confirmed by HR-TEM and EDX spectroscopy using a focussed 100 keV electron beam irradiating a small sample of *ca.* 5-10 filled SWNTs (figure 3.1, b-d).

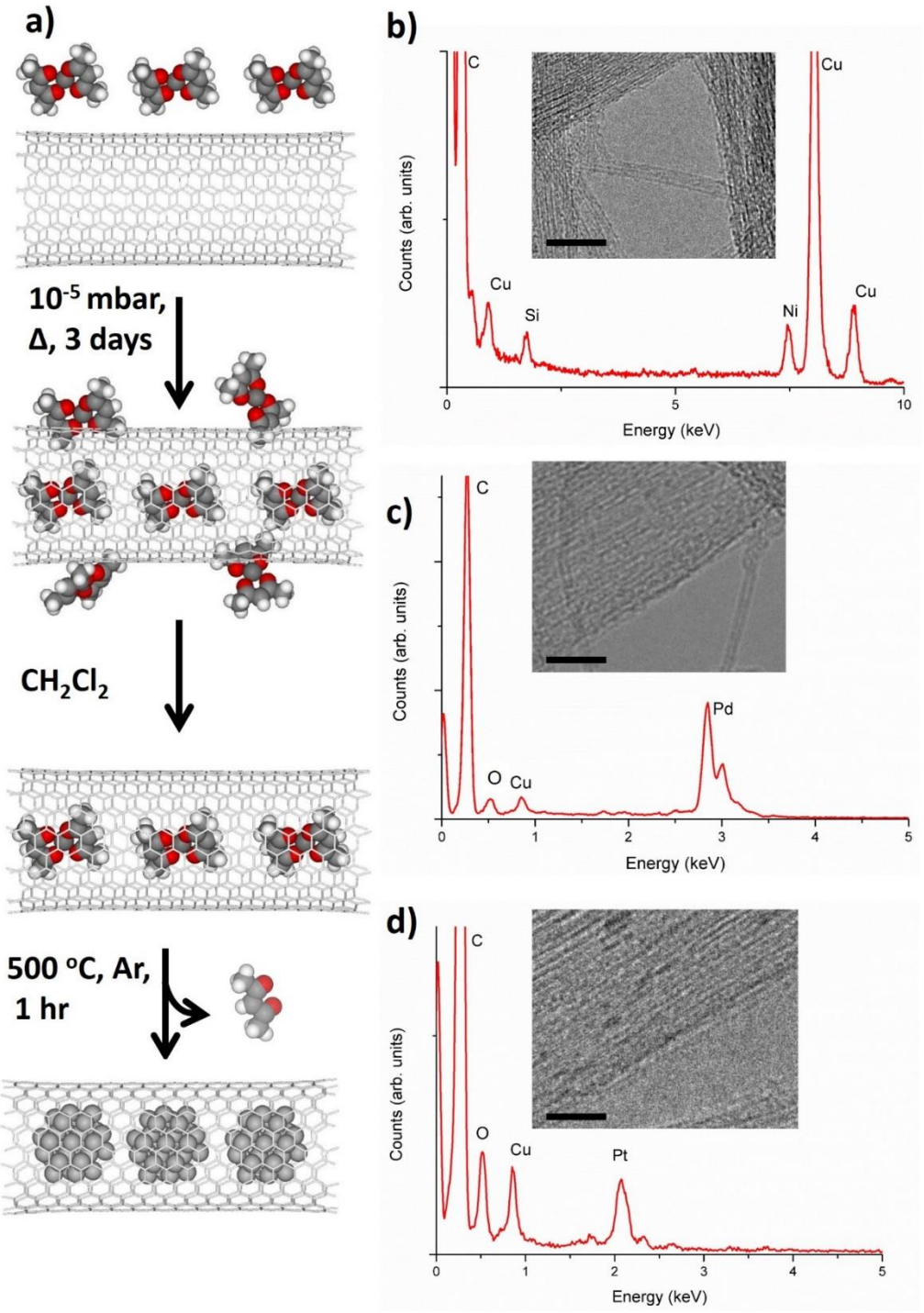


Figure 3.1: a) A schematic representation showing how MNPs of the group 10 elements were synthesised in SWNTs. An appropriate precursor is sealed under vacuum with SWNTs and heated slightly above its sublimation temperature for 3 days. The SWNTs are then washed with CH_2Cl_2 to remove unencapsulated material, followed by heating at 500 °C under argon to form the MNPs; b-d) EDX spectra recorded at 100 keV primary electron energy and integrated over a small bundle of nanotubes confirm the presence of the different group 10 metals inside SWNTs: b) nickel, c) palladium and d) platinum. Copper and silicon peaks are due to the specimen TEM grid. Inset of each EDX spectrum is

a low-magnification micrograph showing bundles of nanotubes filled with each metal. The scale bars are all 10 nm.

3.2.2 AC-HRTEM Analysis

AC-HRTEM has been used to investigate the materials formed, firstly as an imaging technique to view the distances between atoms in each sample, but also as a high energy experimental technique. Each material was irradiated with a constant electron dose rate of *ca.* 2 x 10^7 $e^-nm^{-2}s^{-2}$ and their resultant interactions with carbon nanostructures monitored.

3.2.2.1 Nickel

Relative to the heavier group 10 elements platinum and palladium, nickel atoms appear as a light contrast material, similar to carbon atoms. AC-HRTEM observations at 80 kV reveal the nickel clusters as cubic and compact (figure 3.2 a). Slow rotational motion allows for clear visualisation of the cubic lattice, which is consistent with the space group of bulk nickel, Fm-3m. The (100) plane of the nickel cluster is present, and the atoms appear to be spaced very similarly to that of bulk nickel (figure 3.2 b).

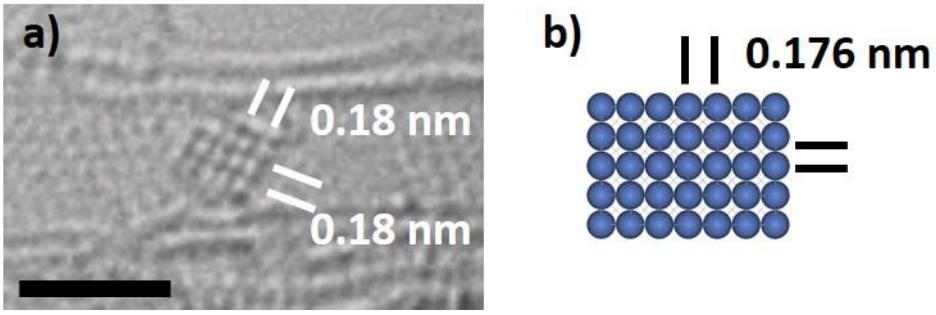


Figure 3.2: a) AC-HRTEM image showing nickel encapsulated within a SWNT. The NiNP has formed a close pack cubic structure which is similar to the structure of bulk nickel. The scale bar is 1 nm; b) The (100) crystal plane of bulk nickel for comparison.

Nickel clusters adopt a variety of different sizes, and their size seems to influence their behaviour. For example, when clusters of nickel atoms are relatively large, there

appears to be a significantly stronger interaction with the nanotube sidewall which rapidly leads to the breakage of SWNTs (figure 3.3).

As soon as nickel has interacted with the wall of the SWNT it promptly causes a large vacancy in the SWNT wall, which is of comparable size to the nickel cluster itself and the cluster is then ejected by the SWNT. In this example, prior to breaking the nanotube, the nickel cluster is attached to a long chain of adventitious carbon which is also present inside the SWNT, however this long chain is quickly repelled once contact is made with the sidewall, which shows a preference for the nickel cluster to bond to the nanotube itself, and similar behaviour has been observed previously by Lebedeva *et al.*[14]

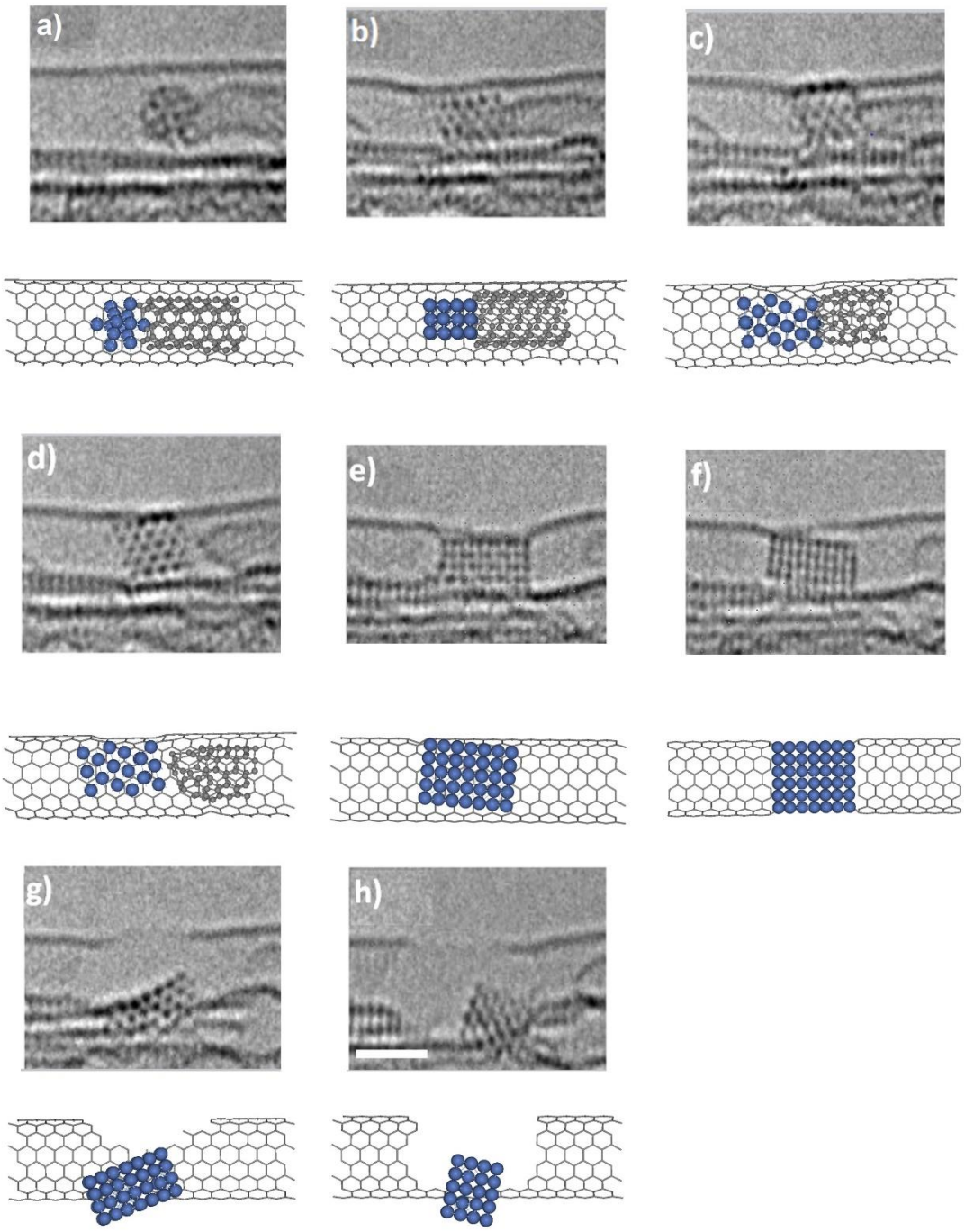


Figure 3.3: Sequential AC-HRTEM images showing how a large cluster of encapsulated nickel interacts with the sidewall of a SWNT. Here, a NiNP cluster attached to a carbon cylinder rapidly changes morphology (a, b) and makes contact with the SWNT sidewall (c). The carbon cylinder previously attached to the NiNP dissociates (d-f) during which time the NiNP cluster strongly establishes itself as part of the sidewall. The NiNP cluster then detaches from the sidewall (g-h). The scale bar is 1 nm. The images were taken over 60 seconds.

This cluster is relatively large and has an ordered cubic structure which appears to facilitate the breakage of the SWNT in an efficient manner and is very similar to

nickel cutting a nanotube, as shown previously by Lebedeva *et al*. However, the size and shape of the cluster can be shown to directly influence the strength of interaction between the nanotube and the sidewall. Sinitsa et al have shown that when a smaller cluster of nickel atoms is present, the interaction between the cluster and the wall is reduced which instead of breakage leads to the formation of a new carbon structure (figure 3.4).[15] Here a small cluster of NiNPs attached to the sidewall of a SWNT, but instead of ejecting atoms of carbon from the nanotube wall, restructuring takes place. Carbon atoms are removed from the wall of the nanotube but the NiNP facilitates the formation of a new hemispherical carbon shell.

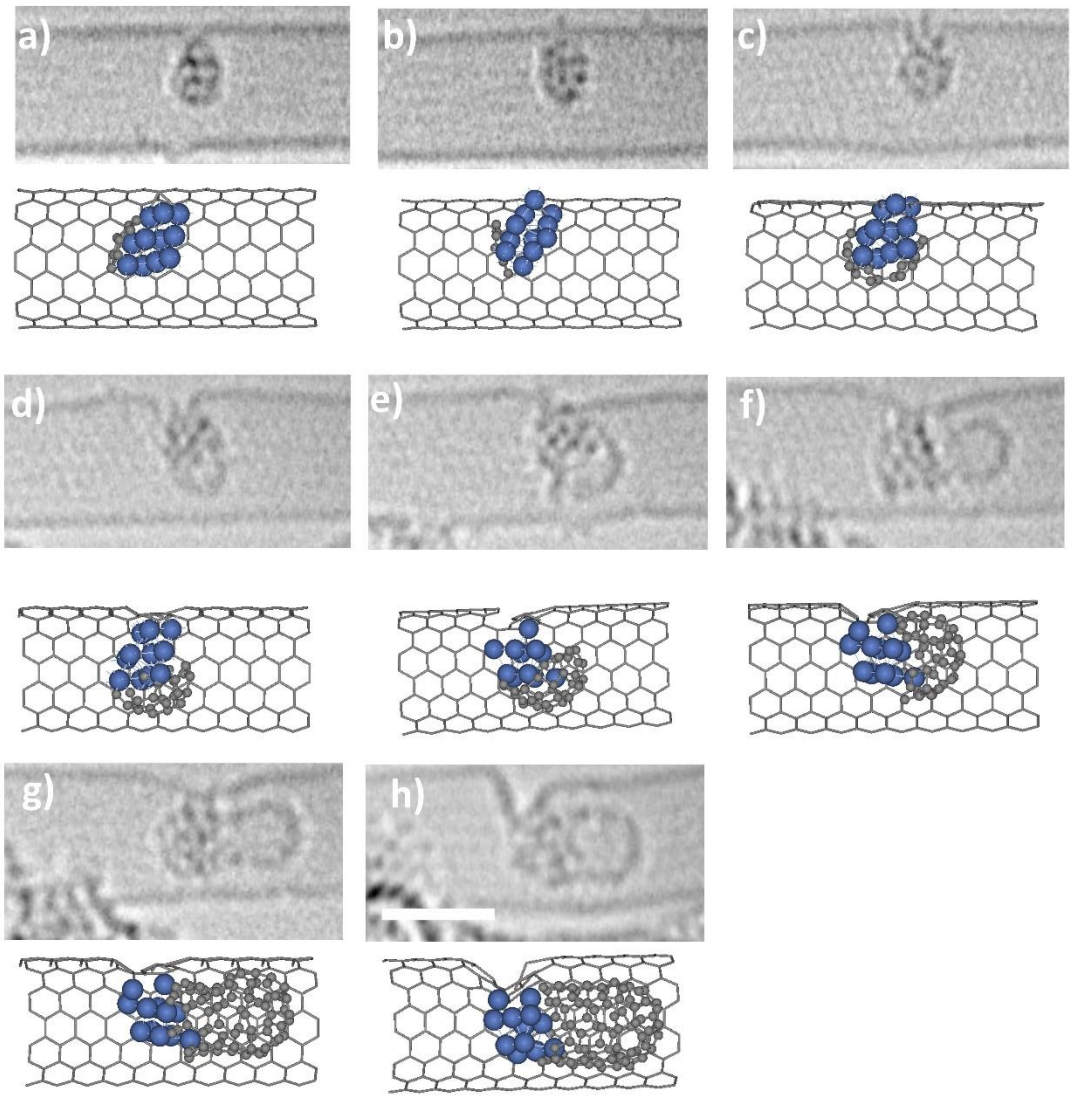


Figure 3.4: Sequential AC-HRTEM images showing how a small cluster of nickel interacts with the wall of a SWNT in real time. The NiNP makes contact with the side of the SWNT (a) and withdraws carbon atoms from the wall (b-d). The removed carbon atoms are reorganised in the form of a small carbon nanotube which extrudes from the NiNP (e-h). The scale bar is 1 nm, and images were taken over 80 seconds.

Initially there is a cluster of around 40 nickel atoms which is surrounded by a carbon shell. This group of atoms then attaches to the SWNT sidewall which leads to carbon from the wall being extracted by the small nickel cluster and using the energy of the electron beam, this leads to the formation of a protrusion of carbon atoms, about 2 nm long. In spite of the best efforts of the electron beam to damage the nanotube completely, there is no evidence of nanotube breakage, just a large defect where carbon atoms have been recycled from the wall into a cylinder (figure 3.4 h).

3.2.2.2 Palladium

Palladium atoms appear as a dark contrast material, and shown below is the (111) plane of the palladium crystal which is in agreement with the crystal structure of bulk palladium (figure 3.5).

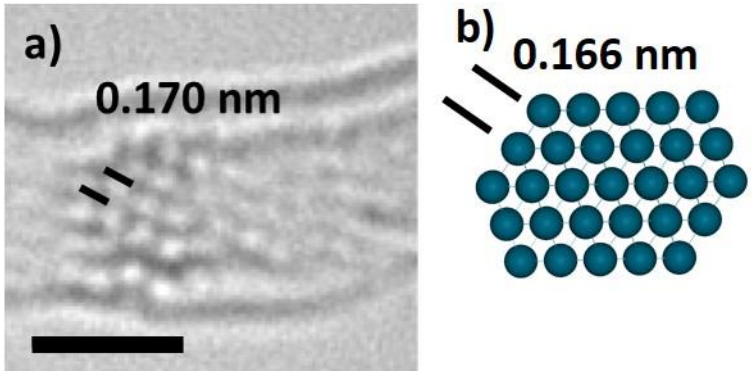


Figure 3.5: a) AC-HRTEM image showing PdNPs encapsulated within a SWNT. The PdNP has formed a hexagonal structure which is similar to the structure of bulk palladium; (b) The (111) crystal plane of bulk palladium for comparison, the scale bar is 1 nm.

Palladium appears to reorganise carbon structures; however, it doesn't appear to interact with the side wall of the SWNT which is very different to how nickel behaves,

and no vacancy defects are promoted. There are no persistent interactions between the metal and the nanotube sidewall, and on the contrary as the PdNP approaches the wall, it is actively repelled by the SWNT (figure 3.6).

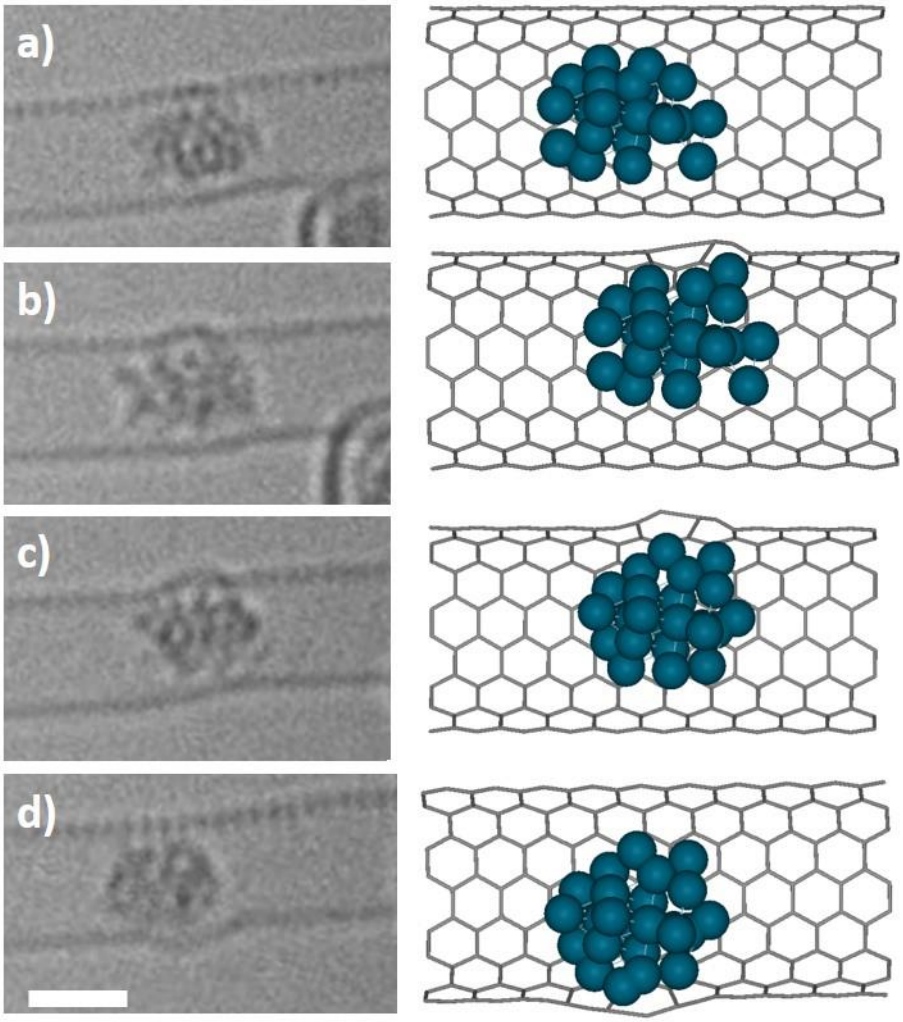


Figure 3.6: Sequential AC-HRTEM images (left hand side) showing how PdNPs interact with the sidewall of a SWNT in real time. The cluster of palladium atoms originates in the centre of the hollow cavity (a) and approaches the side which causes a slight distortion in the wall of the nanotube (b). The PdNP changes morphology to become spherical (c) and then moves back into the centre of the nanotube which subsequently causes a distortion for the other side of the nanotube wall (d). The scale bar is 1 nm. A corresponding model is shown to the right hand side of each micrograph. The images were recorded over 200 seconds.

In addition to differences in the interactions between nickel and palladium with the nanotube sidewall, there are significant changes when observing how palladium interacts with adventitious carbon in the nanotube. When palladium is attached to a

carbon bubble, there is an extraction of carbon atoms from one face of the cluster and a growth of a carbon containing cylinder on the other side. A cluster of encapsulated palladium atoms is interacting with amorphous carbon (figure 3.7 a), during this time, the palladium cluster appears to change morphology brings it closer to the SWNT sidewall. However, as similarly shown in the previous palladium example (figure 3.6) the palladium atoms do not come into contact with the side wall (figure 3.7 b), and there is a slight distortion in the sidewall to accommodate the PdNP. Eventually a carbon cylinder begins to extrude from the PdNP (figure 3.7 c) until there is only contact with carbon on one face of the PdNP (figure 3.7 d)

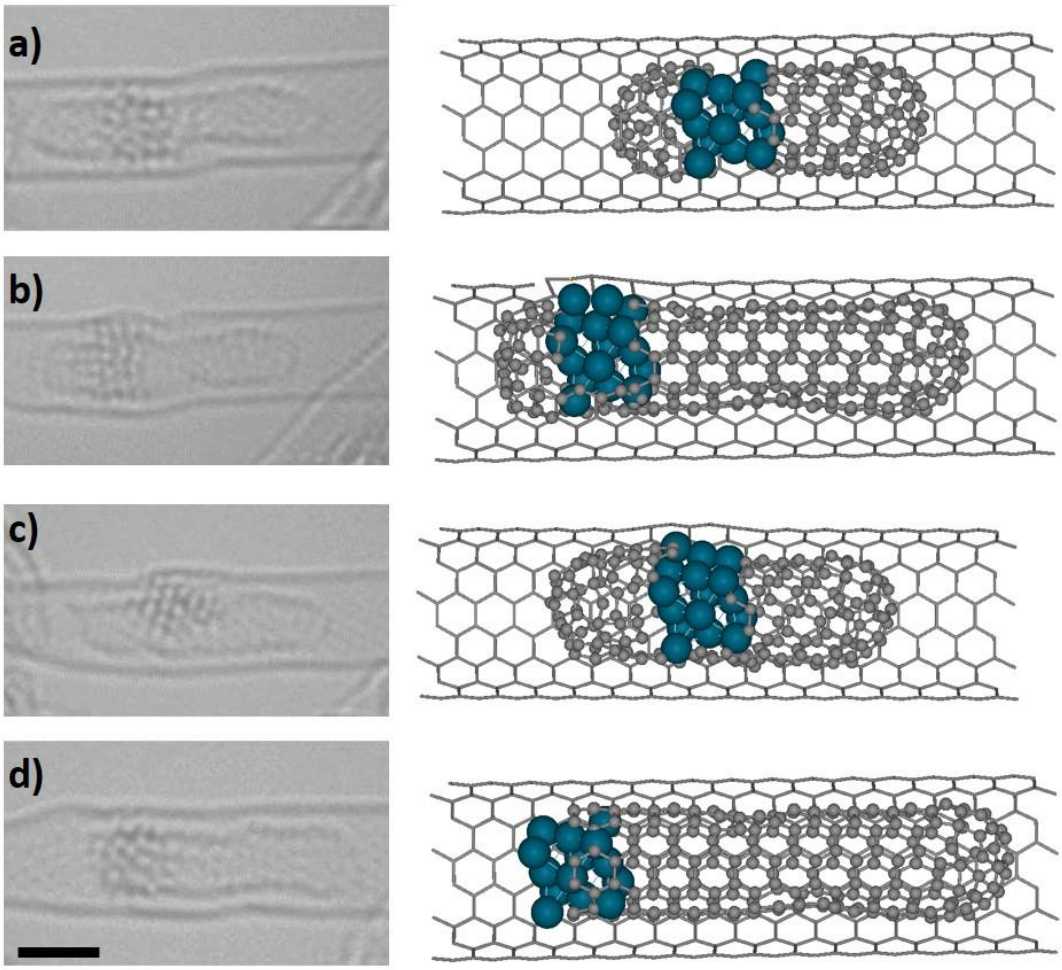


Figure 3.7: Sequential AC-HRTEM series (left hand side) showing the interactions between PdNPs and a chain of amorphous carbon in real-time. Originally there appears to be a chain of carbon atoms either side of the PdNP (a). Subsequently, the PdNP appear to migrate towards the wall of the SWNT

(b) and amorphous carbon is moved from the left hand side of the PdNP to the right hand side (c) where the carbon chain appears to extend. A corresponding model is shown to the right hand side of each micrograph. The scale bar is 1 nm and images were recorded over 300 seconds.

3.2.2.3 Platinum

Platinum appears in the SWNT as a very dark contrast crystalline material (figure 3.8 a), which correlates with the (111) crystal plane of bulk platinum (figure 3.8 b).

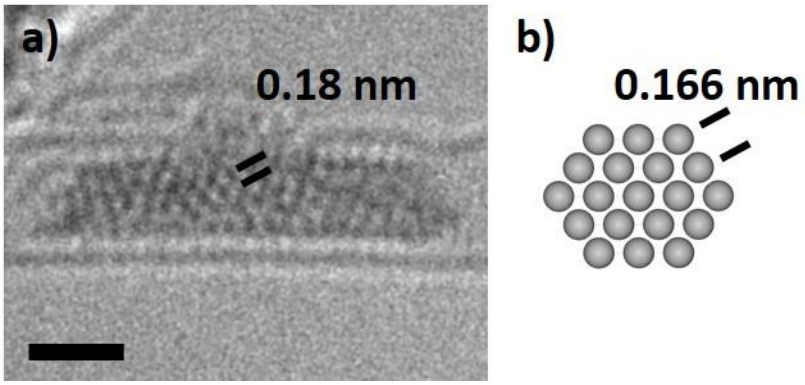


Figure 3.8: a) AC-HRTEM image showing PtNPs encapsulated within a SWNT. The PtNP has formed a hexagonal structure which is similar to the structure of bulk platinum; (b) The (111) crystal plane of bulk platinum for comparison. The scale bar is 1 nm.

Unlike the previous examples where nickel readily cut open the nanotube wall, and palladium evaded it, the platinum atoms readily attach to the sidewall of the nanotube, but there is no breakage of the SWNT sidewall; rather the PtNPs remain as part of the sidewall (figure 3.9). When a PtNP is attached to a hemispherical carbon bubble (figure 3.9 a), it begins to migrate towards the wall of the SWNT, and originally the PtNP appears to repel the wall, (figure 3.9 b) in a similar process to palladium (figure 3.6 b). Eventually platinum atoms engage in bonding with the nanotube sidewall (figure 3.9 c) but in contrast to the nickel which rapidly weakens the C-C bonding causing the nanotube to break, platinum readily attaches and dissociates with the nanotube wall (figure 3.9 d, e, f). During this time, the carbon structure around the

platinum cluster shrinks, and so there is no evidence of platinum promoting the growth of small nanotubes.

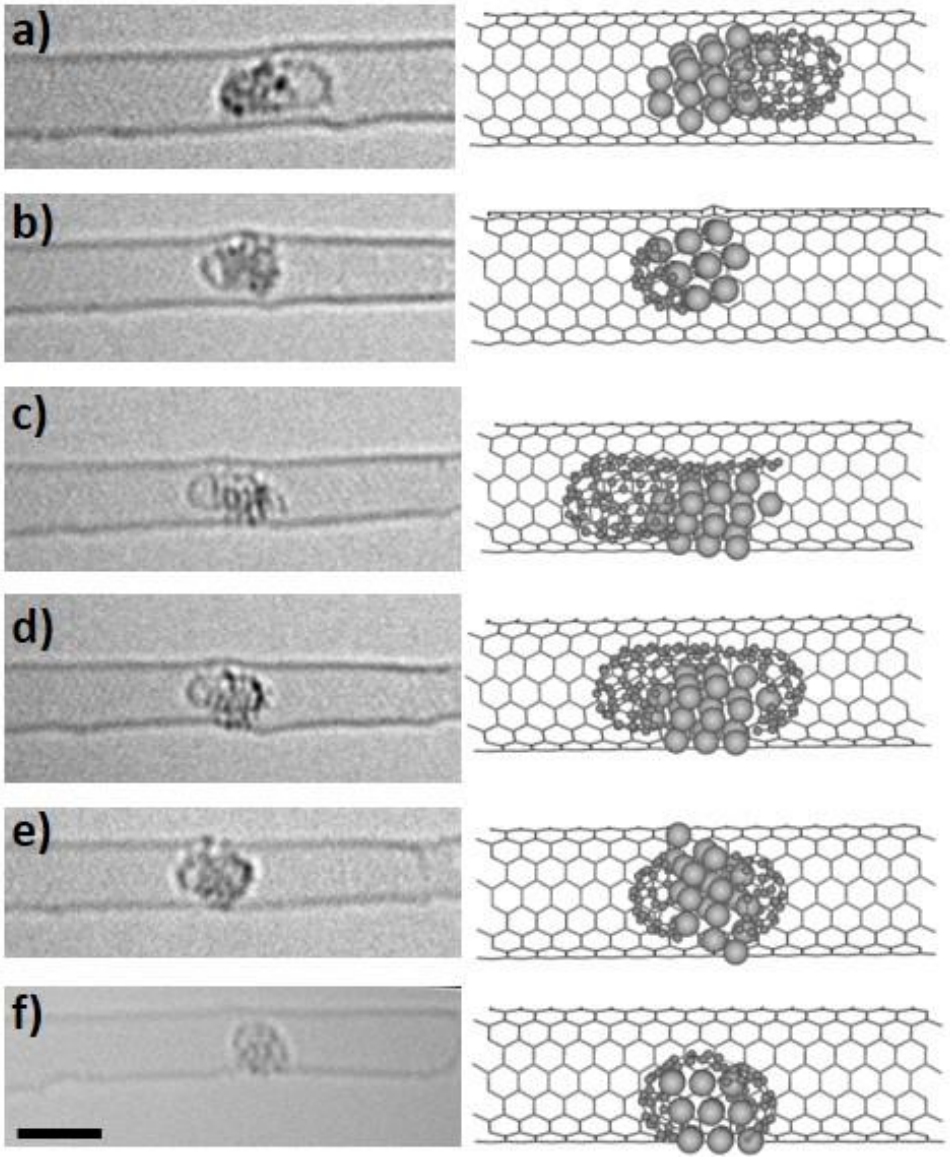


Figure 3.9: Sequential AC-HRTEM images showing how a small cluster of encapsulated platinum atoms interacts with the sidewall of a SWNT and adventitious carbon. Initially, a PtNP attached to a hemispherical carbon bubble (a) makes contact with the sidewalls of the SWNT (b,c). The hemispherical carbon shell around the PtNP cluster shrinks as the electron beam ejects carbon atoms from the structure (d-f). The scale bar is 1 nm and images were taken over *ca.* 250 seconds.

Similarly to nickel, but unlike palladium, a large size distribution of the nanoparticles formed was observed, and PtNPs are also present in the form of a large rod, which contains approximately 200-300 atoms of platinum.

When Pt nanoparticles are present as a large rod, (figure 3.10), they begin to migrate towards a defect in the wall of the SWNT (figure 3.10 b), and single platinum atoms engage in a process of bonding with the SWNT wall (figure 3.10 c). Over time, it appears that the platinum cluster is beginning to vacate the nanotube (figure 3.10 d); however, this doesn't occur, and the platinum cluster changes morphology to become a sphere which is the configuration with the least amount of surface energy (figure 3.10 e). Following this morphological transition, a process of rebuilding the wall of the SWNT begins (figure 3.10 f), and excess carbon, some of which is inside the nanotube, is used to anneal the sidewall (figure 3.10 g) until eventually the SWNT has been fully healed, and a nanoprotrusion, similar to ones previously observed with encapsulated osmium and ruthenium is formed.[16, 17]

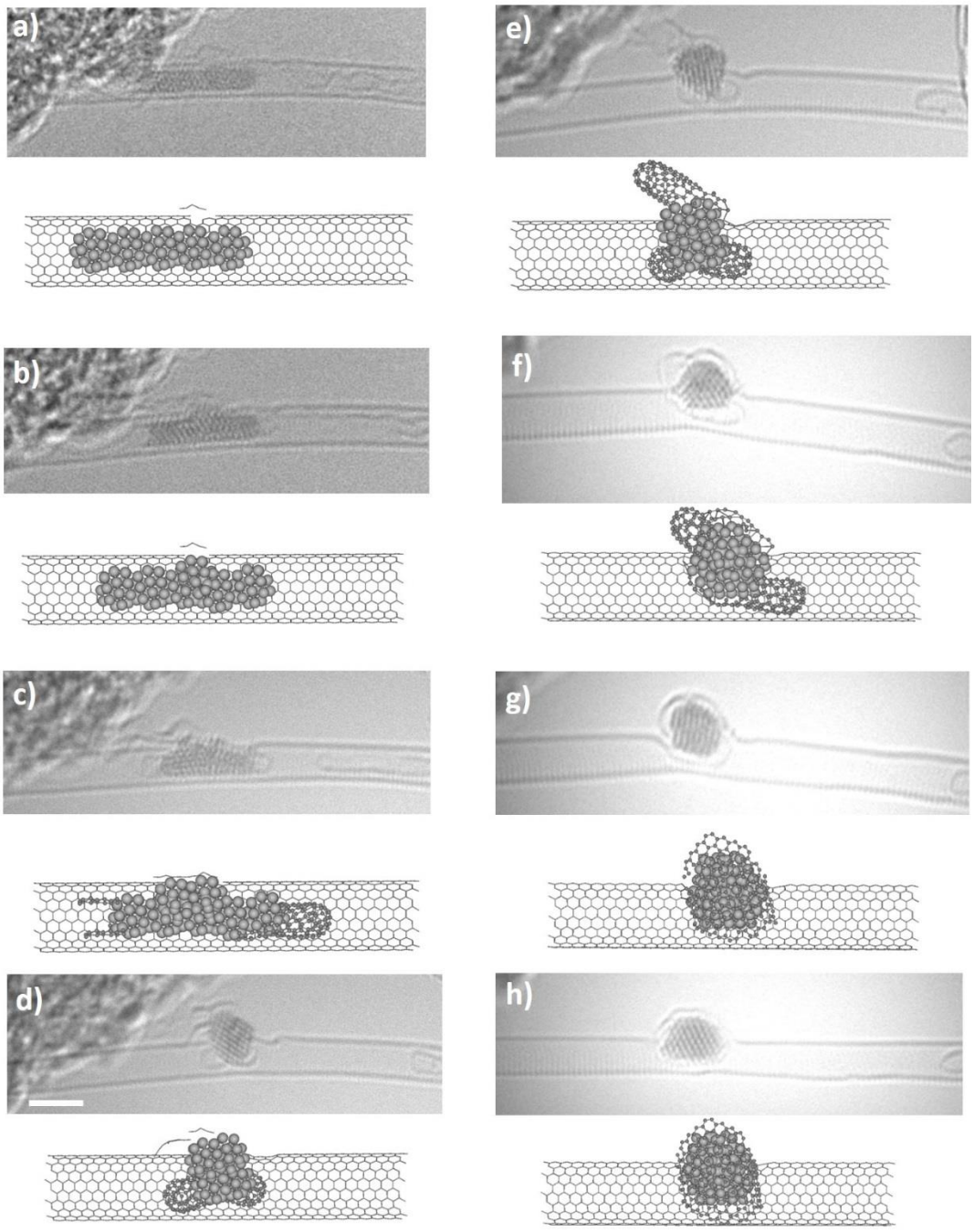


Figure 3.10: Sequential AC-HRTEM images showing how a large cluster of platinum atoms interacts with the SWNT. The PtNPs migrate towards a defect in the nanotube wall (b), platinum atoms insert into this defect (c) and the PtNP starts a process of annealing the nanotube wall (d). Over time, the large cluster of platinum atoms adopts the configuration which minimises its surface area, and a large spherical carbon shell forms around it (e-h). The scale bar is 1 nm. The images were recorded over 1000 seconds. Below each AC-HRTEM image is a corresponding model.

3.2.3 Electron Transfers within MNPs@SWNT

Cross correlating fluorescence-detected X-ray absorption spectroscopy (FD-XAS) with Raman spectroscopy allows for the determination of both the oxidation state of the material present inside the nanotube, and the vibrational characteristics of the host nanotube respectively, thus allowing for a systematic understanding of the electron transfer between the nanotube and encapsulated compound (table 3.1). The systematic study of the excitation edge energy of each material, grouped together by their atomic composition, and compared to the edge energy of known standards enables the monitoring of oxidation state of the metal present in each material.

Upon encapsulation of $Ni(HFacac)_2$@SWNT, the energy of the nickel K edge decreases by 1.24 eV which indicates a slight increase of electron density on the nickel centre upon encapsulation (figure 3.11 a,b; table 3.1), but the energy is still higher than that of a Ni(II) standard, $NiCl_2$. Upon decomposition to Ni@SWNT, the energy of the nickel K edge decreases much further (an additional 12.12 eV) which is characteristic of a neutral nickel species, and indeed this energy is only 0.88 eV greater than that of bulk nickel

The position of the G band of the Raman spectra of the filled nanotubes can be compared to that of an empty nanotube, but both are negligible suggesting there is no charge transfer between the guests and their respective nanotubes upon encapsulation (table 3.1).

For palladium containing species in SWNTs, the encapsulation of $Pd(acac)_2$ leads to a large decrease in the palladium L_{III} edge position compared to that of bulk $Pd(acac)_2$. There is a decrease of just over 1 eV, which although is smaller than the decrease in the nickel K edge energy for the encapsulation of $Ni(HFacac)_2$, is similar to the energy

of the edge in Pd(0), suggesting that negative charge is being transferred to the palladium (figure 3.11 c,d). The Raman spectrum of $Pd(acac)_2$@SWNT compliments this finding as an increase in the position of the G band (+4 cm^{-1}) is present which suggests electron transfer from the nanotube to the guest (table 3.1). Thermal decomposition of $Pd(acac)_2$@SWNT results in the formation of Pd@SWNT, and the position of the L_{III} edge of encapsulated palladium is similar to that of bulk palladium metal (0.23 eV lower), with the Raman spectrum of Pd@SWNT showing only a negligible difference in the G band position when compared to an empty SWNT.

In contrast to the smaller group 10 elements, the FD-XAS of $Pt(acac)_2$@SWNT shows a slight increase in the platinum L_{III} edge energy relative to that of a $Pt(acac)_2$ control sample, indicating a small reduction of electron density on the Pt centres inside the nanotubes; (figure 3.11 e, table 3.1). However, Raman spectroscopy shows no shift in the G band of the SWNT suggesting little or no charge transfer between the guest and the nanotube upon encapsulation. This suggests that the molecule is becoming more polarised in the nanotube, which implies weakening of the Pt-O bond and will be discussed further in Chapter V.

Heating $Pt(acac)_2$@SWNT under argon at 500 ^oC for one hr resulted in the decomposition of $Pt(acac)_2$ to form Pt@SWNT. The energy of the Pt L_{III} edge in Pt@SWNT is increased significantly relative to bulk metallic Pt which suggests the host SWNT depletes electron density around the metal. This correlates with a small red shift of the G band in the Raman spectrum of the host nanotubes (-4 cm^{-1}), confirming that some electron transfer takes place from platinum to the SWNT in the Pt@SWNT material, leading to platinum in an oxidation state slightly above zero.

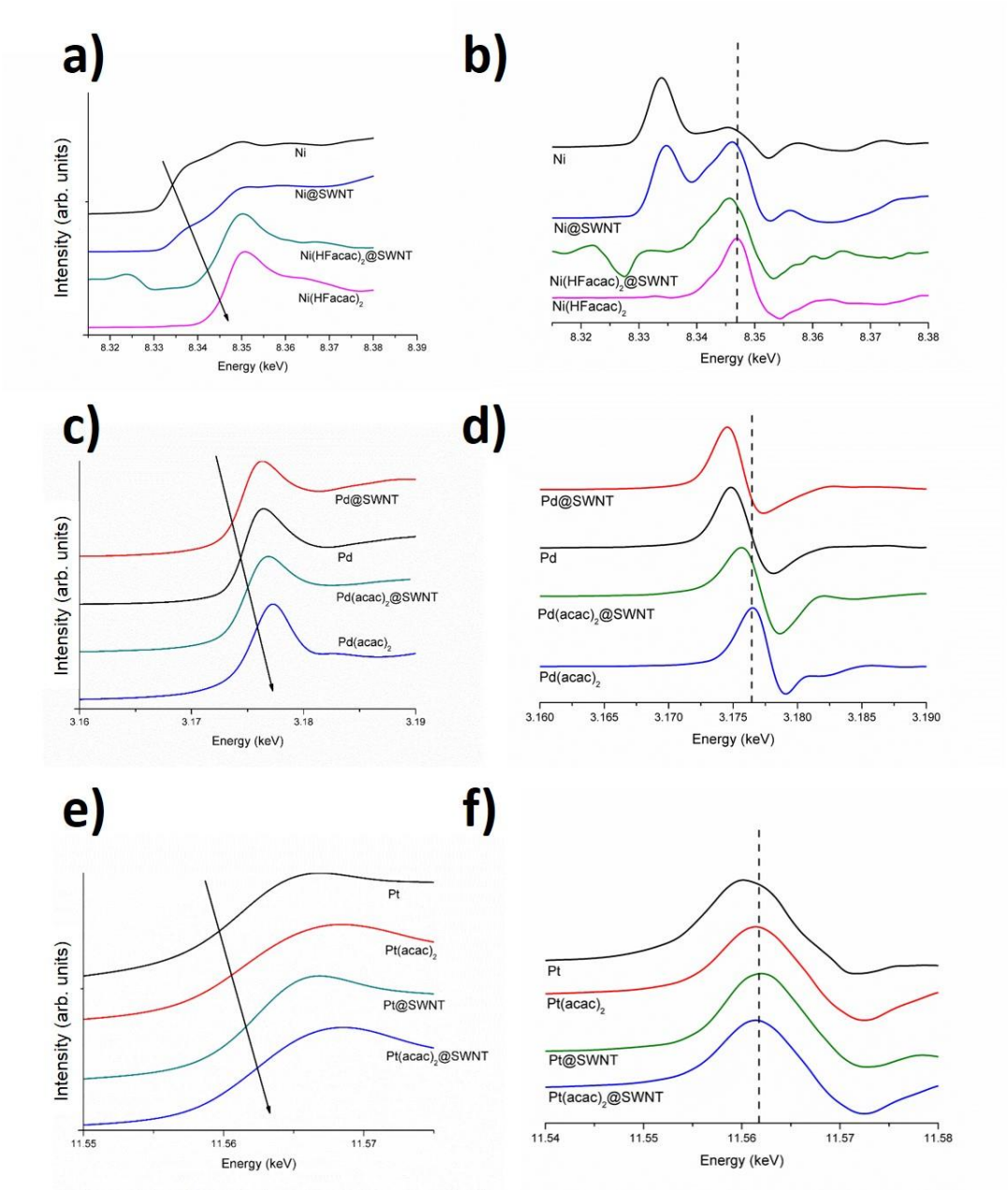


Figure 3.11: Normalised FD-XAS of (a) encapsulated nickel compounds compared to known standards. The encapsulation of $Ni(HFacac)_2$ leads to a decrease in the nickel K edge energy which shows an increase of electron density onto the nickel. Upon formation of NiNPs, the edge decreases even further; b) the first derivative of each smoothed spectrum, to determine the excitation edge position; c) encapsulated palladium compounds compared to known standards. The encapsulation of $Pd(acac)_2$ leads to a decrease in the palladium L_{III} edge energy of the Pd centre which shows an increase of electron density onto the palladium. Upon formation of PdNPs, the edge decreases even further and is similar to that of bulk palladium; d) the first derivative of each smoothed spectrum is shown, to determine the excitation edge position; e) platinum compounds compared to known standards. The encapsulation of $Pt(acac)_2$ leads to an increase in the platinum L_{III} edge energy which shows a decrease of electron density on the Pt. After decomposition to platinum, the edge decreases slightly

but still remains much higher than that of bulk platinum and f) the first derivative of each smoothed spectrum, to determine the excitation edge energy.

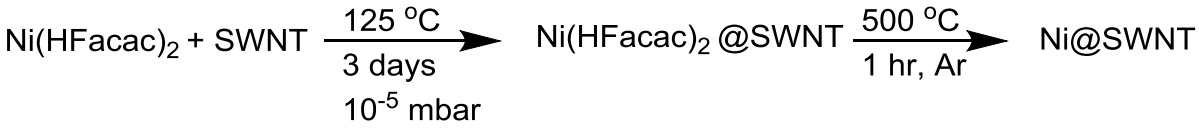
Table 3.1: Shifts in edge energy of the encapsulated group 10 metals with respect to (w.r.t.) M(0) controls. Data for the nickel K edge, palladium L_{III} edge and platinum L_{III} edge energies are shown. Where applicable the G band of materials compared to that of a pristine SWNT have been recorded, and the direction of charge transfer monitored.

Nickel containing materials	**Edge energy (eV) (shift w.r.t. Ni(0), eV)**	**G band position (cm^{-1}) (shift w.r.t. pristine SWNT)**	**Direction of electron transfer (if applicable)**
Ni	8333.89 ± 0.009 (0)	-	
Ni@SWNT	8334.75 ± 0.099 (0.88)	1591 (+1)	No transfer observed
$NiCl_2$	8342.45 ± 0.066 (8.56)	-	
$Ni(HFacac)_2$@SWNT	8345.65 ± 0.584 (11.76)	1591 (+1)	No transfer observed
$Ni(HFacac)_2$	8346.89 ±0.066 (13.00)	-	
Palladium containing materials	**Edge energy (eV) (shift w.r.t. Pd (0), eV)**	**G band position (cm^{-1}) (shift w.r.t. pristine SWNT)**	**Direction of electron transfer (if applicable)**
Pd	3174.86 ± 0.073 (0)	-	
Pd@SWNT	3174.63 ± 0.064 (-0.23)	1590 (0)	No transfer observed
$Pd(acac)_2$@SWNT	3174.89 ± 0.058 (0.03)	1594 (+4)	SWNT → $Pd(acac)_2$
$PdCl_2$	3175.31 ± 0.183 (0.45)	-	
$Pd(acac)_2$	3175.88 ± 0.072 (1.04)	-	
Platinum containing materials	**Edge energy (eV) (shift w.r.t. Pt (0), eV)**	**G band position (cm^{-1}) (shift w.r.t. pristine SWNT)**	**Direction of electron transfer (if applicable)**
Pt	11561.30 ± 0.70 (0)	-	
$Pt(acac)_2$	11562.16 ± 0.74 (0.86)	-	
PtI_2	11562.22 ± 0.39	-	

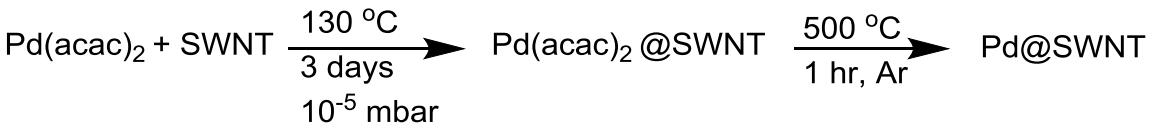
	(0.92)		
Pt@SWNT	11562.30 ± 0.21 (1.00)	1586 (-4)	Pt → SWNT
$Pt(acac)_2$@SWNT	11562.67 ± 0.20 (1.37)	1590 (0)	Pt → O
PtI_4	11563.19 ± 0.26 1.89)	-	
SWNT	-	1590 (0)	-

3.3 Discussion

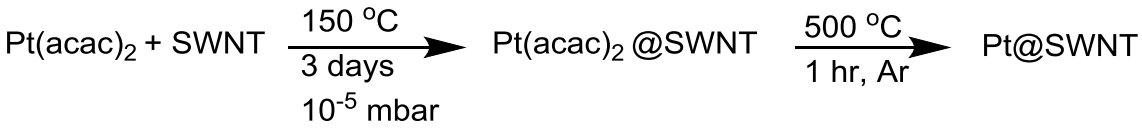
In contrast to the thermal treatment of $Cu(acac)_2$@SWNT (Chapter III), heating the encapsulated group 10 molecules under argon only led to the loss of volatile ligands and the presence of MNPs; no evidence of oxide formation was found (schemes 3.1, 3.2, 3.3)



Scheme 3.1: Formation of Ni@SWNT from a nickel containing precursor.



Scheme 3.2: Formation of Pd@SWNT from a palladium containing precursor.



Scheme 3.3: Formation of Pt@SWNT from a platinum containing precursor.

When observing the dynamics of clusters of the group 10 atoms, nickel clusters appear to have undergone extensive fragmentation, and although a few large clusters were

observed, most were small and highly dynamic under the electron beam. This is of contrast to palladium clusters, which don't appear as dynamic under the electron beam, and there was no evidence of single atoms becoming detached from the main cluster. On the other hand, platinum atoms appear fast moving, and there is evidence of individual atoms getting detached from the small cluster (figure 3.10) but not the large rod.

Analogous to the group 11 metals (Chapter II), the ratio T_{max} *(M)* to E_{coh}(M) can be used as a guide to qualitatively show the amount of kinetic energy an atom receives from the 80 keV electron beam (table 3.2).

Table 3.2: Cohesive energy of metals (E_{coh}) and maximum transferred energy (T_{max}(M)) from the 80 kV electron beam for the group 10 metal atoms. The ratio *T(M)/*E_{coh} represents the energy received from the electron beam as a percentage of metal cohesive energy.

Metal	T_{max}*(M)* (eV)	Cohesive energy, E_{coh} (eV/atom)	[T_{max}(M)/E_{coh}] x 100 (%)
Nickel	3.23	4.44	73
Palladium	1.78	3.89	46
Platinum	0.97	5.84	17

Nickel atoms are shown to receive the highest proportion of energy required for their ejection from the bulk, and so it would be expected that nickel would act more dynamically under the electron beam, followed by palladium and platinum. Nickel clusters are observed to have highly effective interactions with the sidewall of the nanotube, with the extensive formation of multi-vacancy defects, which leads to the rapid breakage of the nanotube sidewall. This is significant as controlled cutting of the SWNT sidewalls is extremely important for the fabrication of nanoscale electronic devices [18, 19]

Conversely no persistent Pd-C interactions are found, which shows a very weak interaction between the cluster and sidewall, whereas PtNPs appear to effectively interact with the sidewall. For both large and small clusters, platinum atoms insert into vacancies in the sidewall and assist in annealing the sidewall by removing defects.

Similarly, there are more single trapped atoms of platinum than palladium or nickel. These are atoms which have formed σ–bonds with the carbon atoms surrounding defects in the nanotube wall. Once single metal atoms become embedded within the nanotube, the C-C bonds of the nanotube wall can become dislodged to an atom specific degree, where they are either ejected from the nanotube, or engage with the MNP and become involved in a process of restructuring to form new carbon structures.

Nickel atoms promote the formation of hemispherical nano-buds by attaching to the sidewall of a SWNT and using the carbon atoms removed from the SWNT sidewall by the electron beam to form small carbon structures. This process happens quite fast, owing to the effectiveness of nickel in removing atoms from the nanotube sidewall, and expediently the nano-bud is formed. Palladium metal clusters effectively catalyse the formation of extended carbon cylinders, but in the case shown previously (figure 3.7) the carbon is from the opposite face of the cluster, and it simply passes through, extruding from the other side. Since palladium has been shown to interact with the sidewall very weakly, this is unsurprising. On the other hand, platinum clusters are shown to effectively catalyse small hemispherical carbon shells, but no extended cylinders were observed. Platinum therefore has been shown to anneal carbon nanostructures most effectively as it forms relatively strong bonds with carbon atoms

but can then easily dissociate, and is the most effective of the three elements, since palladium struggles to bond to carbon and nickel bonds too strongly.

3.4 Conclusion

The group 10 metals have been successfully encapsulated into SWNTs and their interactions with carbon studied, which has allowed for comparisons and trends to be shown throughout the group (figure 3.12). Nickel appears to form the most effective bonds with carbon, as it readily attaches to both the sidewall of the SWNT and adventitious carbon. This is of contrast to palladium, which although readily restructures carbon into cylinders, doesn't seem to engage in any bonding with the nanotube sidewall. Platinum seems the most effective element at entering the sidewall of defective SWNTs and healing them. As a contrast, nickel engages in strong σ-bonding with SWNTs which results in the irreversible destruction of the SWNT sidewall. Similarly, although palladium doesn't engage in bonding with sidewalls, it is very effective at restructuring adventitious carbon inside the SWNT.

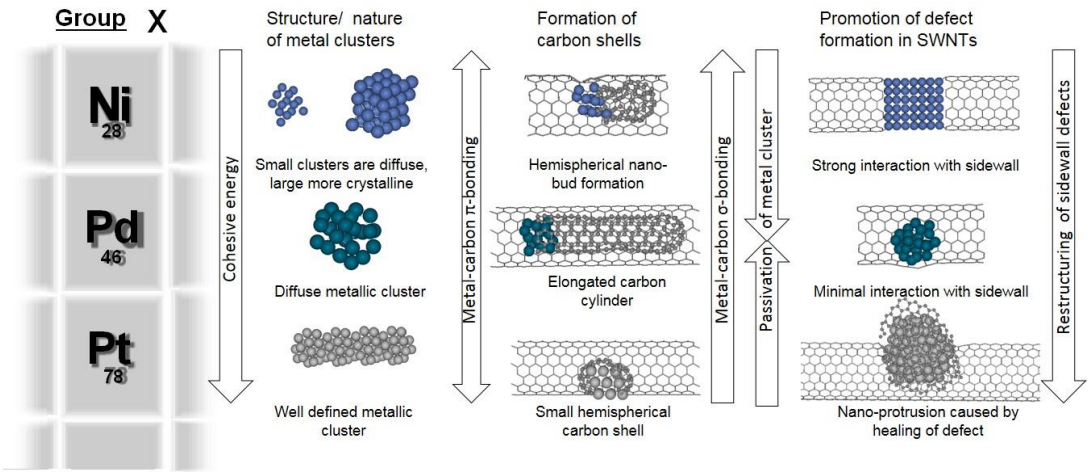


Figure 3.12: Schematic representation of the observed trends of the group 10 metals inside SWNTs, when studied using 80 keV AC-HRTEM.

In order for a metal to be an effective catalyst, it must bind strongly to another material but also readily detach, and this study has shown that platinum atoms would be the

most appropriate catalysis as they form strong bonds with carbon, but readily disengage. This is shown by how effectively nanotube sidewall defects are restructured.

The group 10 metals are widely used for catalytic and detection processes, and the findings from this investigation have very exciting implications as it shows just how effective each metal is relative to the others, and forms the basis of the investigation into the sensing properties of group 10 metals at the nanoscale, Chapter VI.

3.5 Experimental

SWNTs (P2, arc discharge, Carbon Solutions, USA) were annealed at 600 ^{o}C for 15 min to open their termini and remove any residual amorphous carbon from their internal cavities resulting in a 50% mass loss being observed. The metallic precursors, $Ni(HFacac)_2$, $Pd(acac)_2$ and $Pt(acac)_2$ were used as supplied (Sigma Aldrich).

3.5.1 Encapsulation of Complexes

Each metal precursor (10 mg) was sealed under vacuum (10^{-5} bar) in a Pyrex ampoule with freshly opened SWNTs (5 mg) and heated at slightly above their sublimation temperature for 3 days to ensure penetration of the SWNT by the complexes (see table 3.3 below). The samples were cooled rapidly and repetitive washing with dichloromethane (4 x 25 mL) was performed to remove any excess material from the exterior of the SWNTs.

Table 3.3: A summary of conditions required to form each encapsulated metal species.

Initial compound	Amount of compound (mmol)	Sublimation temperature (°C)
$Ni(HFacac)_2$	2.12×10^{-2}	125
$Pd(acac)_2$	3.28×10^{-2}	130
$Pt(acac)_2$	2.54×10^{-2}	150

3.5.2 Formation of MNPs@SWNT

Under atmospheres of argon, $Ni(HFacac)_2$@SWNT (5 mg), $Pd(acac)_2$@SWNT (5 mg), $Pt(acac)_2$@SWNT (5 mg) were heated at 500 °C for 1 hr and allowed to cool down slowly.

3.5.3 Electron Microscopy

SWNTs filled with the encapsulated materials were dispersed in propan-2-ol using an ultrasonic bath and drop cast onto lacey carbon-coated copper TEM grids (Agar). HR-TEM imaging and electron beam irradiation was carried out on a JEOL 2100 FEG-TEM microscope operated at 100 kV. Aberration-corrected TEM was performed at the University of Ulm on a C_s corrected FEI Titan 80-300 TEM operated at 80 kV with information limit enhancement by reduced extraction voltage. All images were processed using Gatan Digital Micrograph, and the quoted distances were measured by drawing a line profile and measuring the electron intensity.

3.5.4 EDX Spectroscopy

Local EDX spectra were acquired for samples mounted on lacey carbon-coated copper TEM grids using an Oxford Instruments INCA X-ray microanalysis system. The electron beam was condensed onto areas of specimens (bulk specimen or nanotube bundles) suspended over holes of the amorphous carbon film.

3.5.5 Raman Spectroscopy

The samples were separately dispersed in propan-2-ol, mounted onto Si(100) supports. Raman spectroscopy was performed using a HORIBA Jobin Yvon LabRAM HR spectrometer equipped with an automated *xyz* stage (Märzhäuser). Spectra were acquired using a 532 nm laser at 0.2mW power, in the range 50 to 4000 cm^{-1}, with 5 seconds and 8 accumulations per spectral window, using a 50× objective and a 300 μm confocal pinhole. To simultaneously scan a range of Raman shifts, a 600 lines/mm rotatable diffraction grating along a path length of 800 mm was employed. Spectra were detected using a SYNAPSE CCD detector (1024 pixels) thermoelectrically cooled to −60 °C. Before the spectra collection, the instrument was calibrated using the Rayleigh line at 0 cm^{-1} and a standard Si(100) reference band at 520.7 cm^{-1}.

3.5.6 Fluorescence-Detected X-ray Absorption Spectroscopy

All FD-XAS measurements were carried out on the XMaS beamline (BM28) at the ESRF. Samples were deposited onto carbon tape, which was then mounted onto a stainless steel sample holder. FD-XAS edge inflection points were obtained by fitting a smoothing spline to the measured spectrum, and taking the first derivative of the fitted spectrum.

3.6 References

1. M. S. Khan, A. Haque, M. K. Al-Suti and P. R. Raithby, *J. Organomet. Chem.*, 2015, **793**, 114.
2. R. Akiyama and S. Kobayashi, *J. Am. Chem. Soc.*, 2003, **125**, 3412.
3. W. Keim, *Angew. Chem. Int. Ed.*, 1990, **29**, 235.
4. G. A. Bhaduri and L. Siller, *Catal. Sci. Tech.*, 2013, **3**, 1234.
5. H. M. Chen, R.-S. Liu, M.-Y. Lo, S.-C. Chang, L.-D. Tsai, Y.-M. Peng and J.-F. Lee, *J. Phys. Chem. C*, 2008, **112**, 7522.
6. X. Batlle and A. Labarta, *J. Phys. D: Appl. Phys.*, 2002, **35**, R15.
7. B. Issa, I. Obaidat, B. Albiss and Y. Haik, *Int. J. Mol. Sci.*, 2013, **14**, 21266.
8. R. Prasad and B. R. Bhat, *Sens. Actuator B-Chem.*, 2015, **220**, 81.
9. B. H. Liu, R. Q. Hu and J. Q. Deng, *Anal. Chem.*, 1997, **69**, 2343.
10. K. E. Toghill and R. G. Compton, *Int. J. Electrochem. Sci.*, 2010, **5**, 1246.
11. M. H. Perez-Temprano, J. A. Casares and P. Espinet, *Chem. Eur. J.*, 2012, **18**, 1864.
12. A. Dumas and P. Couvreur, *Chem. Sci.*, 2015, **6**, 2153.
13. Q. Fu, G. Weinberg and D. S. Su, *New Carbon Mater.*, 2008, **23**, 17.
14. I. V. Lebedeva, T. W. Chamberlain, A. M. Popov, A. A. Knizhnik, T. Zoberbier, J. Biskupek, U. Kaiser and A. N. Khlobystov, *Nanoscale*, 2014, **6**, 14877.
15. A. S. Sinitsa, T. W. Chamberlain, T. Zoberbier, I. V. Lebedeva, A. M. Popov, A. A. Knizhnik, R. L. McSweeney, J. Biskupek, U. Kaiser and A. N. Khlobystov, *Nano Lett.*, 2017, **17**, 1082.
16. T. Zoberbier, T. W. Chamberlain, J. Biskupek, M. Suyetin, A. G. Majouga, E. Besley, U. Kaiser and A. N. Khlobystov, *Small*, 2016, **12**, 1649.
17. T. W. Chamberlain, J. C. Meyer, J. Biskupek, J. Leschner, A. Santana, N. A. Besley, E. Bichoutskaia, U. Kaiser and A. N. Khlobystov, *Nat. Chem.*, 2011, **3**, 732.
18. X. F. Guo, J. P. Small, J. E. Klare, Y. L. Wang, M. S. Purewal, I. W. Tam, B. H. Hong, R. Caldwell, L. M. Huang, S. O'Brien, J. M. Yan, R. Breslow, S. J. Wind, J. Hone, P. Kim and C. Nuckolls, *Science*, 2006, **311**, 356.
19. F. Xiong, A. D. Liao, D. Estrada and E. Pop, *Science*, 2011, **332**, 568.

Chapter IV: A One-Pot-One-Reactant Synthesis of Platinum Compounds at the Nanoscale

4.1 Introduction:

The development of new methodologies for the controlled arrangement of molecules and atoms into highly ordered arrays is vitally important for harnessing the functional properties emerging at the nanoscale due to the effects of confinement, which are essential for catalytic, electronic and biomedical applications. The cylindrical internal cavity of single-walled carbon nanotubes (SWNTs) provides an effective template for control of the exact positions and orientations of molecules and atoms and has been successfully applied to the construction of nanoscale architectures from a variety of metals,[1-3] organic molecules,[4-6] and inorganic compounds.[7-12]

A striking example of the power of this technique was reported by Chuvilin *et al.* who demonstrated that sulfur-terminated graphitised nanoribbons, practically impossible to fabricate by synthetic chemistry routes, can be spontaneously formed from inexpensive, readily available precursors, such as tetrathiafulvalene, in one step within SWNTs.[13, 14] More recently, very narrow double-walled carbon nanotubes have been demonstrated as effective containers for templating the important, but still elusive, allotrope of carbon, carbyne.[15] Shi *et al.* demonstrated that at high temperature the host nanotube can template the formation of this new allotrope of carbon and protect it from undesired side reactions, thus paving the way for the first bulk production of carbyne. These examples clearly demonstrate the intrinsic ability of the SWNTs to direct chemical reactions and control the dimensionality of products

formed inside nanotubes, where the product structure is crucially determined by the internal diameter of the nanotube.

Low-dimensional inorganic materials, including transition metal chalcogenides, are currently of particular interest due to the fact that their semiconducting electronic properties can be precisely tuned by shaping their structures into nanoribbons, in an analogous fashion to graphene.[16] While the host nanotube can control the dimensions of the inorganic structure, control of the stoichiometry is typically achieved by immersing open SWNTs into a molten inorganic compound with the desired, predetermined chemical composition, so that the nanotube becomes filled with cations and anions in the correct ratio due to capillary forces. A now ubiquitous technique, it has led to the encapsulation of many inorganic compounds, such as $LaCl_3$,[17] KI,[18] CoI_2,[19] SnTe,[20] and BaI_2,[9] yielding nanostructures with well-defined composition and morphology, and physical properties often different to those found in the bulk (see Chapter 1, section 1.3). However, the need to melt inorganic compounds in this method imposes severe limitations on the choice of encapsulated materials, as many important inorganic materials, such as metal sulfides, decompose before melting or melt at extremely high temperature, *e.g.* the melting point of MoS_2 is 1185 °C.[21]

The direct synthesis of inorganic compounds inside nanotubes can offer an attractive alternative which may significantly broaden the scope of inorganic compounds that are confined to the nanoscale. The nanotube in this case acts simultaneously as a nanoscale reactor and a template for controlling the dimensions of inorganic structures. As shown in Chapter I, inorganic synthesis inside nanotubes has been successfully applied by Eliseev *et al.* to the synthesis of CdS@SWNT by treating pre-encapsulated CdI_2, inserted into nanotubes from the molten phase, with sulfur at high

temperature.[22] This elegantly avoids the problem that bulk CdS has a melting point of 1750 °C, precluding the molten phase filling of this material. Similarly, the formation of low-dimensional MS_2 (M = Mo,[23] W[24]) in multi-walled carbon nanotubes has been demonstrated by Wang *et al. via* the decomposition of molecular complexes demonstrating the further potential for tailoring bespoke semiconducting inorganic materials with nanoscale precision.

In this study, the use of carbon nanotubes as nanoreactors in stepwise and one-pot inorganic syntheses has been advanced, highlighting the advantages and limitations of the different approaches. Using the compounds of platinum as models, a new strategy for the fabrication of inorganic nanomaterials with controlled structure and composition has been outlined. Conducting the chemical transformations inside the host nanotube allows structural determination of the reaction products with atomic precision by aberration-corrected high resolution transmission electron microscopy (AC-HRTEM) and aberration-corrected scanning transmission electron microscopy (AC-STEM), while a unique approach based on cross-correlation of fluorescence-detected X-ray absorption spectroscopy (FD-XAS) and Raman spectroscopy applied at each stage of inorganic synthesis in carbon nanotubes enables determination of the exact oxidation state of metal in inorganic compounds formed inside nanotubes and the vibrational properties of the host nanotube respectively. This methodology enables changes in host-guest interactions from one stage of inorganic synthesis to another to be monitored by multiple techniques for the first time, providing a systematic understanding of the electron transfer between the nanoreactor and encapsulated compound during all stages of the formation process.

4.2 Results and Discussion:

4.2.1 Stepwise Synthesis

The stepwise formation of inorganic materials in SWNTs can be achieved by selecting an appropriate metal precursor, i.e. small volatile metal complexes consisting of the required metallic element for the desired inorganic material, and inserting them into the nanotube (figure 4.1 a), followed by thermal treatment to remove the volatile ligand from the nanotube cavity (figure 4.1 b), with the sequential addition of a non-metallic element which reacts with the metal to form a desired inorganic compound. If necessary, more reaction steps can be added to convert the inorganic compound to another product (figure 4.1 d).

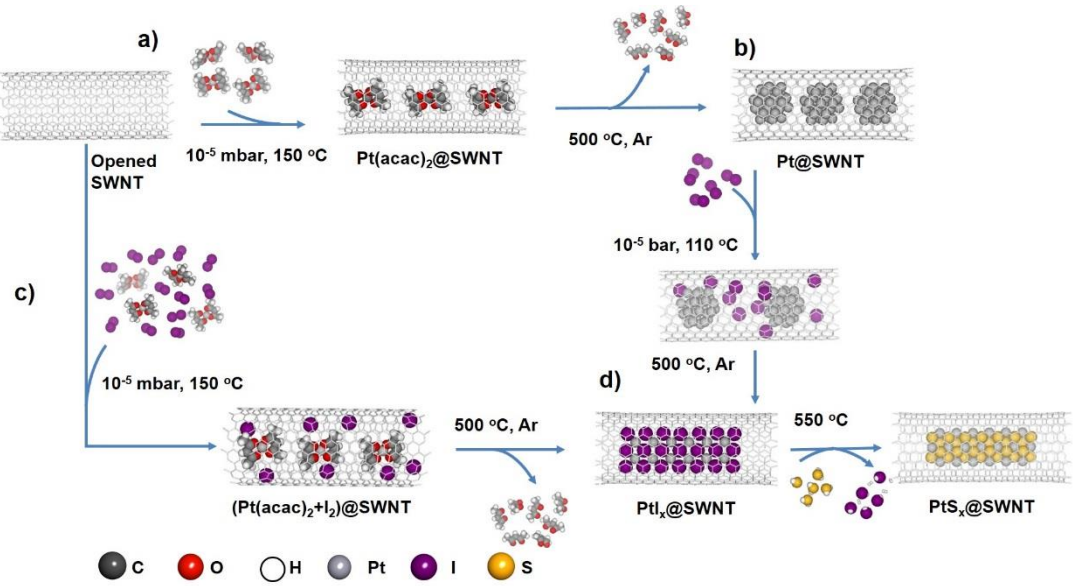


Figure 4.1: Schematic illustration depicting how inorganic materials can be formed using nanotubes as templates; a) the encapsulation of a selected metal precursor for the desired metallic element followed by thermal decomposition to form MNPs@SWNT; b) the addition of the second element by adding a second precursor followed by chemical reaction to form the inorganic material; c) the formation of inorganic materials using a one-step filling process in which both precursors, metallic and non-metallic, are added at the same time followed by chemical reaction; d) the transformation of one encapsulated inorganic material to another by treatment with a suitable reagent inside the nanotube.

To explore and evaluate this approach for inorganic synthesis in SWNTs, platinum acetylacetonate, $Pt(acac)_2$ was inserted into SWNTs from the gas phase, with the excess removed from the exterior of SWNTs by applying a selective dichloromethane washing technique,[25] leaving only $Pt(acac)_2$ molecules that are encapsulated within the nanotube, $Pt(acac)_2$@SWNT. FD-XAS of $Pt(acac)_2$@SWNT shows a slight increase in the platinum L_{III} edge energy relative to that of a $Pt(acac)_2$ control sample (table 4.1) indicating a small reduction of electron density on the metal centre of $Pt(acac)_2$ inside the nanotubes (figure 4.2 a,b); however, Raman spectroscopy (figure 4.2 c) shows no shift in the G band of the SWNT suggesting little or no charge transfer between the guest and the nanotube upon encapsulation (as shown previously in Chapter III, section 3.2.3).[26] Heating $Pt(acac)_2$@SWNT under argon at 500 ^oC for 1 hr resulted in the decomposition of $Pt(acac)_2$ and the release of metallic platinum into the SWNT cavities in the form of cylindrical nanoparticles with an average length of 1.5 nm and diameter of 1.0 nm as confirmed by HR-TEM imaging (figure 4.2 d inset). As shown in Chapter III, and table 4.1 below, the energy of the Pt L_{III} edge in Pt@SWNT is increased significantly relative to bulk metallic platinum which suggests the host SWNT depletes electron density around the metal. This correlates well with a small but measurable red shift of the G band in the Raman spectrum of the host nanotubes, confirming that some electron transfer takes place from metallic platinum to SWNT in the Pt@SWNT material, leading to platinum in an oxidation state slightly above zero (table 4.1)

Table 4.1: A summary of the electron transfers taking place in the materials produced. The energy of the platinum L_{III} edge of the materials produced is compared to known standards, and shown with respect to (w.r.t.) the energy of the platinum L_{III} edge for Pt(0).Where applicable the shift in G band of the SWNT is listed, and the direciton of charge transfer taking place within each material is summarised.

Sample	Original excitation edge (eV) (shift w.r.t. Pt(0) (eV)	G band position (cm^{-1}) (shift w.r.t. pristine SWNTs (cm^{-1}))	Direction of electron transfer (if applicable)
Pt	11561.30 ± 0.70 (0)	-	
$Pt(acac)_2I_2$@SWNT	11561.84 ± 0.03 (0.54)	1595 (+5)	Pt ← SWNT
$Pt(acac)_2$	11562.16 ± 0.74 (0.86)	-	-
PtI_2	11562.22 ± 0.39 (0.92)	-	-
Pt@SWNT	11562.30 ± 0.21 (1.00)	1586 (-4)	Pt → SWNT
PtI_2@SWNT	11562.52 ± 0.24 (1.22)	1590 (0)	No transfer observed
$Pt(acac)_2$@SWNT	11562.67 ± 0.20 (+1.37)	1590 (0)	Pt →O, see chapters III and V
$Pt(acac)_2(SCN)_2$@SWNT	11563.00 ± 0.13	1585 (-5.0)	Pt → SWNT

	(1.70)		
PtI_4	11563.19 ± 0.26	-	-
	(1.89)		
$Pt(acac)_2I_2$	11563.34 ± 0.24	-	-
	(2.04)		
PtS_2@SWNT	11563.58 ± 0.22	1590 (0)	No transfer observed
	(2.28)		
$Pt(acac)_2(SCN)_2$	11563.63 ± 0.12	-	-
	(2.33)		
SWNT	-	1590	-

In the next step, Pt@SWNT was treated with iodine vapour (figure 4.1 b) leading to the direct synthesis of platinum iodide inside nanotubes, PtI_2@SWNT, from the constituent elements (figure 4.2 f, inset). Raman spectroscopy shows that the G band of the host nanotube in PtI_2@SWNT returns to a similar position to that of empty SWNTs, and FD-XAS shows that the energy of the Pt edge of PtI_2@SWNT is similar to that of known Pt (II) complexes, with both methods agreeing that no electron transfer takes place between the nanotube and charge-neutral compound PtI_2, which contrasts with the observed Pt to SWNT electron transfer in Pt@SWNT as described above, or SWNT to iodine electron transfer described for I_2@SWNT in the literature.[26] Addition of H_2S to PtI_2@SWNT led to the transformation of platinum iodide to the platinum sulfide compound PtS_2@SWNT (figure 4.1 d) which in a

similar fashion to the iodide exhibits no electron transfer with the nanotube as the Raman G band position in PtS_2@SWNT coincides with that of empty SWNTs. This is in agreement with FD-XAS showing a Pt excitation edge energy similar to that of known Pt (IV) complexes (table 4.1), thus confirming a charge-neutral PtS_2 material inside the nanotube. This series of chemical transformations inside carbon nanotubes clearly illustrates that stepwise inorganic synthesis involving transformations of a metal complex to metal nanoparticles, to metal iodide and to metal sulfide can be achieved in SWNTs with each stage verified by TEM, as well as FD-XAS and Raman spectroscopy revealing the nature of the interactions between the inorganic compounds and the host nanotube.

In a separate experiment, both $Pt(acac)_2$ and I_2 were encapsulated in SWNT simultaneously, from the gas phase followed by heat treatment of the encapsulated molecules ($Pt(acac)_2$ + I_2)@SWNT that triggers a chemical reaction between $Pt(acac)_2$ and I_2 to form PtI_2@SWNT in one step, which is analogous to a popular one-pot synthetic approach in preparative chemistry in the absence of SWNTs (figure 4.1c). This platinum iodide appears to be identical to the same compound formed in the stepwise process above, which clearly indicates the advantages of the one-pot synthesis in nanotubes, allowing for the bypass of several stages of the stepwise approach, i.e. $Pt(acac)_2$ insertion and thermal decomposition, followed by I_2 insertion into SWNTs. While both of these approaches appear to be effective in controlling the dimensions of inorganic nanostructures, being strictly defined by the diameter of SWNTs, detailed analysis of the elemental composition of the inorganic products reveals a problem of stoichiometry control. Unlike organic molecular compounds, inorganic materials have a capacity for non-stoichiometric ratios of the constituent elements, which is evident from energy dispersive X-ray (EDX) analysis indicating

that the materials synthesised inside nanotubes in both approaches have a non-stoichiometric ratio of metal and halogen/chalcogen. Specifically, the content of iodine in PtI_2@SWNT appears to be consistently higher that predicted for PtI_2 (figure 4.2 e), and traces of iodine still remain present in the nanotubes even after conversion of PtI_2@SWNT to PtS_2@SWNT (figure 4.2 f). This observation clearly highlights the challenge of controlling the correct proportions of reactants in nanotubes; I_2 is more volatile than $Pt(acac)_2$ and has a lower vapour pressure which means that it will always be loaded into the nanotube in excess of the Pt precursor, thus making the removal of extra iodine difficult, even after platinum iodide is transformed into platinum sulfide (figure 4.2 f). As even a small deviation from the exact stoichiometric composition causes drastic effects in the physiochemical properties of inorganic materials, such as in the case of silicon doping with nitrogen or boron; diamond doping with nitrogen; or boron nitride doping with carbon, effective control of the ratios of the elements is of paramount importance in inorganic synthesis at the nanoscale.

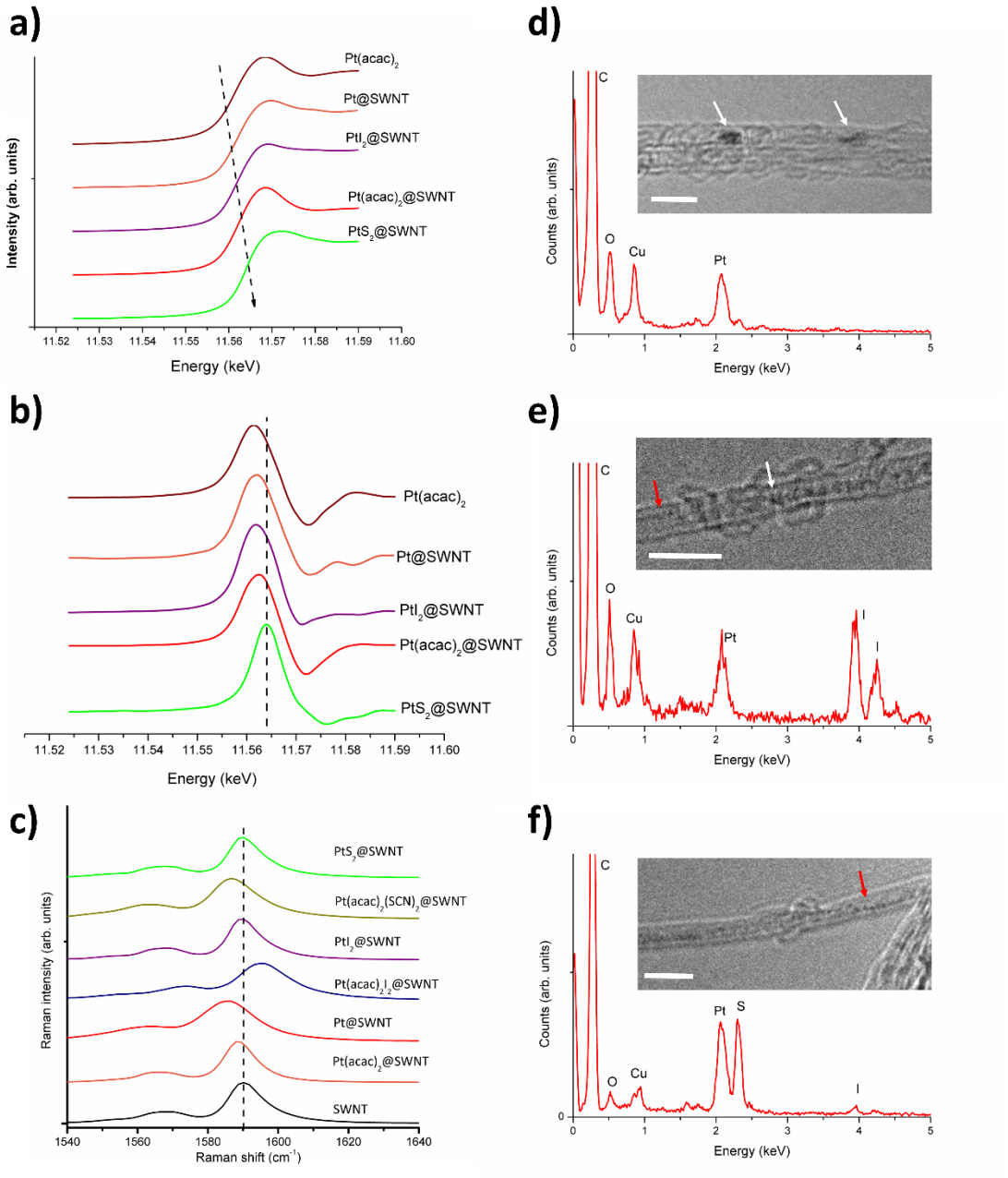


Figure 4.2: a) Normalised FD-XAS showing the platinum L_{III} edge of materials in SWNTs using a stepwise approach compared to that of bulk $Pt(acac)_2$; b) the first derivative of each spectrum is shown, to determine the excitation edge position; c) Normalised Raman spectra showing how the G band of the nanotube shifts depending on the encapsulated material. The encapsulation of molecular species (Pt complexes or I_2) leads to electron transfers between the nanotube and guest; however, the encapsulated PtX (X = I or S) compounds exhibit no change in G band meaning that no charge transfer is taking place; d) an EDX spectrum of Pt@SWNT, a low magnification TEM image (the white arrows showing Pt) of the sample is shown inset; e) an EDX spectrum of PtI_2@SWNT formed using the one-pot method. An excess of iodine is present in the sample. Inset is a TEM image showing clusters of Pt atoms (white arrow) and I atoms (red arrow) within the SWNT; and f) an EDX spectrum of PtS_2@SWNT formed from the treatment of PtI_2@SWNT with H_2S. Traces of iodine are still present in the sample. Inset

is a TEM image of PtS_2@SWNT formed by the transformation of PtI_2@SWNT. In agreement with the EDX spectrum, excess iodine is present (red arrow); (the scale bars are all 2nm, all EDX spectra were recorded at 100 keV primary electron energy and integrated over a small bundle of nanotubes. Copper peaks are due to the TEM specimen grid.

4.2.2 Encapsulation of Precursors

A possible solution to this challenge can be found by designing a molecular precursor where the elements are present in the desired stoichiometric ratio for a specific inorganic product, which can then be encapsulated and converted into inorganic material in SWNTs in a one-pot/one-reactant synthesis (figure 4.3). The advantage of such an approach is that it involves a single step and the stoichiometric ratio of the metal and halogen/chalcogen components in the material formed can be carefully tuned. The use of coordination compounds of transition metals offers excellent possibilities for controlling the composition and stoichiometry of the reactants. For example, the coordination environment of four-coordinate platinum complexes, such as $Pt(acac)_2$, can be expanded to six-coordinate by appending two extra ligands to the axial positions, which can carry the correct amounts of the desired non-metallic element (scheme 4.1). For example, the addition of two iodide or two thiocyanate ligands that occupy the two axial positions in the octahedral complex of platinum allows fixing of the ratio of metal to halogen or chalcogen to 1:2 thus ensuring the correct stoichiometry of the inorganic compound formed inside the nanotubes (figure 4.3).

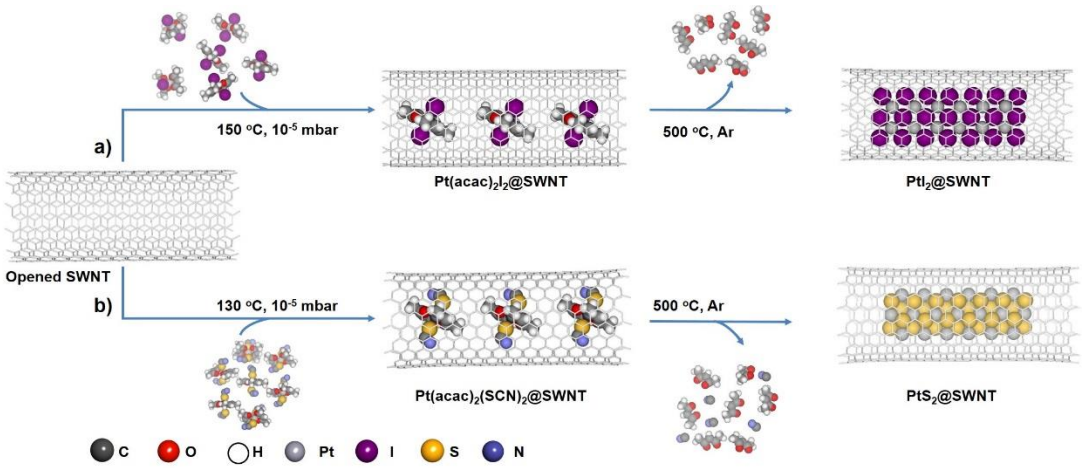
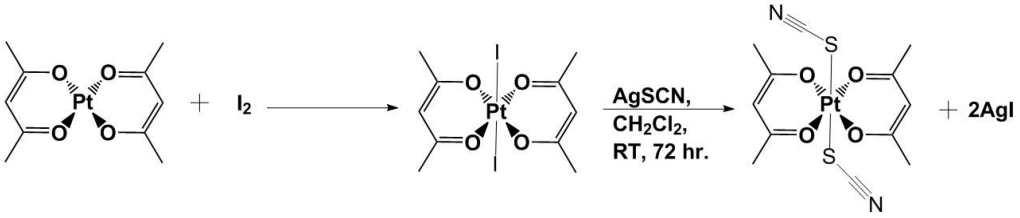


Figure 4.3: Schematic illustration depicting how inorganic materials can be formed using nanotubes as templates. The formation of a) PtI_2@SWNT; and b), PtS_2@SWNT are shown using our methodology. In general a molecular precursor which contains all of the required elements, in the correct stoichiometry for the desired inorganic material, is encapsulated. The thermal treatment of the resultant precursor then leads to decomposition, chemical reaction to form the inorganic material in the nanotubes and expulsion of any volatile by-products into the gas phase.

To illustrate the principle of one-pot/one-reactant synthesis in nanoreactors, the molecular precursors *trans-bis*(acetylacetonato)di-iodoplatinum and *bis*(acetylacetonato)di-thiocyanatoplatinum containing Pt:I (1:2) and Pt:S (1:2) respectively were prepared by reacting $Pt(acac)_2$ with I_2 to give $Pt(acac)_2I_2$, and then reacting $Pt(acac)_2I_2$ with AgSCN to afford $Pt(acac)_2(SCN)_2$, using previously reported methods (scheme 4.1).[27, 28]



Scheme 4.1: The formation of $Pt(acac)_2I_2$ and $Pt(acac)_2(SCN)_2$ from $Pt(acac)_2$.

The resultant $Pt(acac)_2X_2$ (X = I, figure 4.3 a; SCN, figure 4.3 b) compounds were added to SWNTs and sealed in an ampoule under vacuum (10^{-5} bar). Heating at a temperature slightly above the sublimation points of the platinum complexes allowed

the precursor molecules to penetrate the open ends of the nanotubes and become encapsulated. The excess material was removed from the nanotube surface by washing with CH_2Cl_2, leaving only molecules inserted in the nanotubes. Interestingly, the encapsulation of $Pt(acac)_2I_2$@SWNT led to a significant reduction in the absorption energy of the Pt L_{III} edge indicative of an increase of electron density onto the Pt centres as compared to free $Pt(acac)_2I_2$ (figure 4.4 a,b, table 4.1)), which is complimented by a significant blue-shift of the Raman G band of the host SWNT (figure 4.2 b), implying electron transfer from the nanotube to the guest molecule which has not be observed for any other Pt compounds in this study. In contrast, $Pt(acac)_2(SCN)_2$@SWNT showed a decrease in the Pt edge energy in the FD-XAS (figure 4.4 c,d) and a red shift of the nanotube G band (figure 4.2 b), indicating that the electron is transferred in the opposite direction to the previous complex, i.e. from $Pt(acac)_2(SCN)_2$ to SWNTs. A simple thermal treatment led to the facile transformation of the molecular precursors to the desired inorganic structures, PtI_2@SWNT and PtS_2@SWNT (figure 4.3) with the stoichiometric 1:2 metal to halogen/chalcogen composition, as confirmed by EDX spectroscopy (figures 4.4 e, f).

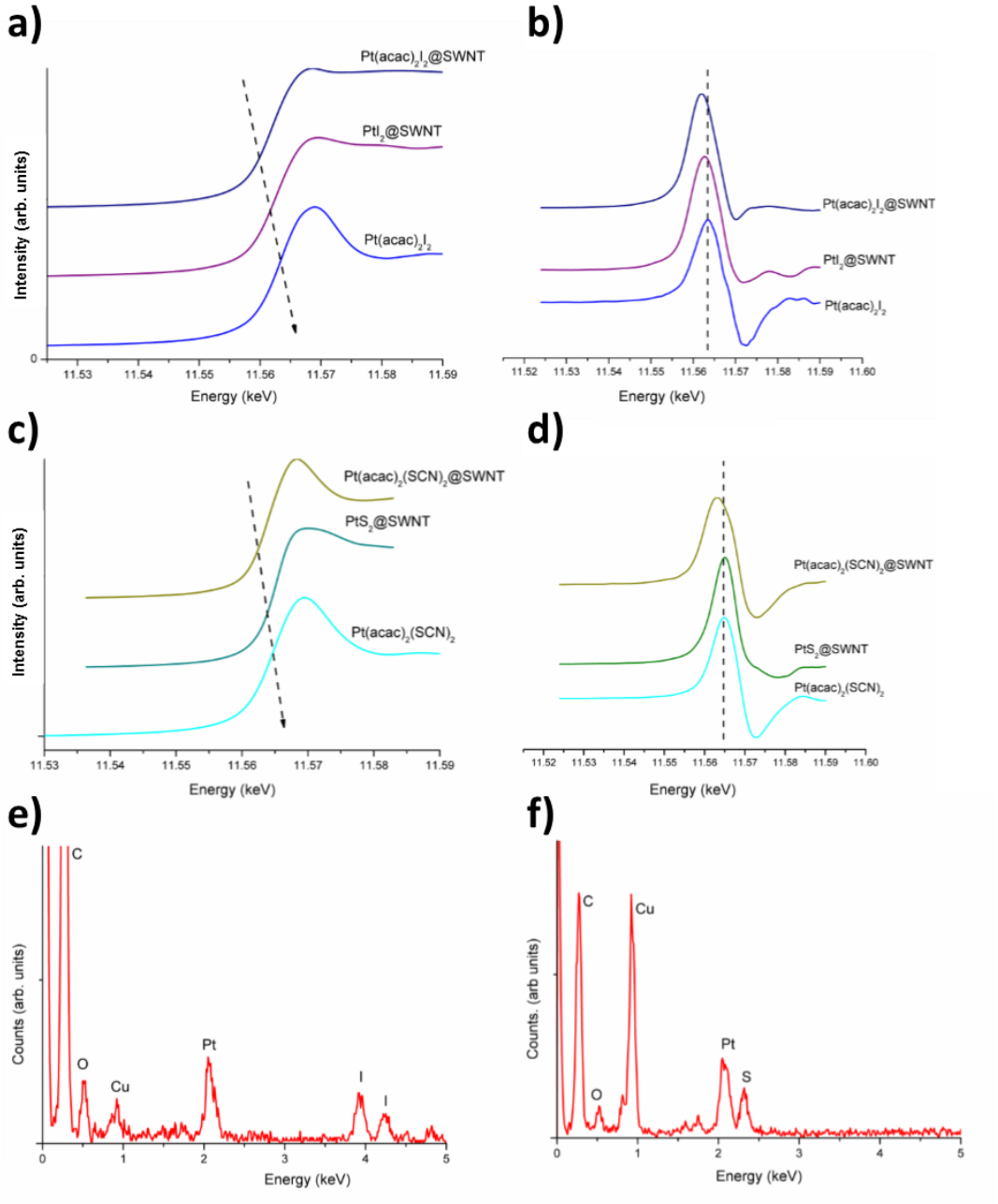


Figure 4.4: a,c) Normalised FD-XAS showing the Pt L_{III} edge of materials formed in SWNTs, using molecular precursors containing suitable amounts of material for the formation of PtI_2@SWNT (a) and PtS_2@SWNT (c); The first derivative of each spectrum is shown to the right of each plot; (b) shows the first derivative of platinum and iodine containing compounds in SWNTs, and (d_ shows the first derivative of Pt and S containing compounds in SWNTs); EDX spectra recorded at 100 keV primary electron energy and integrated over a small bundle of nanotubes showing e), PtI_2@SWNT; and f), PtS_2@SWNT, both formed *via* the thermal decomposition of molecular precursors containing the desired stoichiometric ratios of the two elements inside SWNTs. The spectra confirm the successful formation of the inorganic materials inside the nanotubes in each case. Copper peaks are due to the TEM specimen grid.

4.2.2.1 PtI_2@SWNT

While the new one-pot-one-reactant approach clearly enabled a precise control of the stoichiometry, it is essential to verify the atomic structure of the inorganic compounds formed in this method, to ensure that the new molecular precursors still deliver inorganic materials with well-defined atomic structures. AC-HRTEM is one of the most direct tools for the structural characterisation of inorganic materials formed within SWNTs, as the precise atomic composition and any distortions in the crystal lattice can be clearly visualised to determine the effects of nanoscale confinement.[24, 29, 30] AC-HRTEM of the PtI_2@SWNT sample prepared by the one-pot-one-reactant approach revealed high filling of PtI_2 within the SWNTs (figure 4.5 a) in which the entire channel was filled with the crystalline inorganic material. In a representative example, an individual filled nanotube with a diameter of *ca.* 1.52 nm, similar to that of an (11,11) SWNT (figure 4.5 c), is observed to contain a quasi-one-dimensional PtI_2 crystal characterised by a close-packed cubic lattice (figure 4.5 c). Bulk PtI_2 has a monoclinic unit cell with space group P1 21/C, but due to the confinement effects of the nanotube, a new form of PtI_2 is present, with bond lengths and angles around the platinum atoms derived from the asymmetric unit of the bulk crystal structure of PtI_2.[31] This forms a new cubic plane (figure 4.5 b), with only small lattice distortions observed in the confined nanocrystals compared to spacings in the asymmetric unit in the bulk phase. Lattice measurements in experimental AC-HRTEM images showed regular spacings between atomic positions in the direction parallel to the nanotube of 0.39 nm, compared to a distance of 0.38 nm between iodine atoms in the asymmetric unit of bulk PtI_2. An electron density profile map (figure 4.5 d) generated from the area under the red line (figure 4.5 c) confirms the periodicity of the interatomic spacings. Such a level of distortion in inorganic structures is consistent with the

literature and is a result of the confined lattice adapting to the nanotube channel in order to increase van der Waals interactions with the nanotube sidewalls.[9, 17, 30] A fast Fourier transform (FFT, figure 4.5 e) shows the crystallinity of the material. Similarly, there appears to be a slight increase in the observed diameter of the SWNT due to an elliptic distortion of the nanotube channel to accommodate the PtI_2 species which has also been reported previously for such systems, such as CoI_2@SWNT in Chapter I (section 1.3.2.1).[19] Computational modelling was utilised to generate a 3D model of PtI_2@SWNT (figure 4.5 f) to enable comparison with experimental AC-HRTEM images. Scherzer defocussed AC-HRTEM images were then calculated for a (11,11) SWNT and the derived crystal fragment using QSTEM TEM simulation and are in good agreement with the experimentally obtained image (figure 4.5 c).

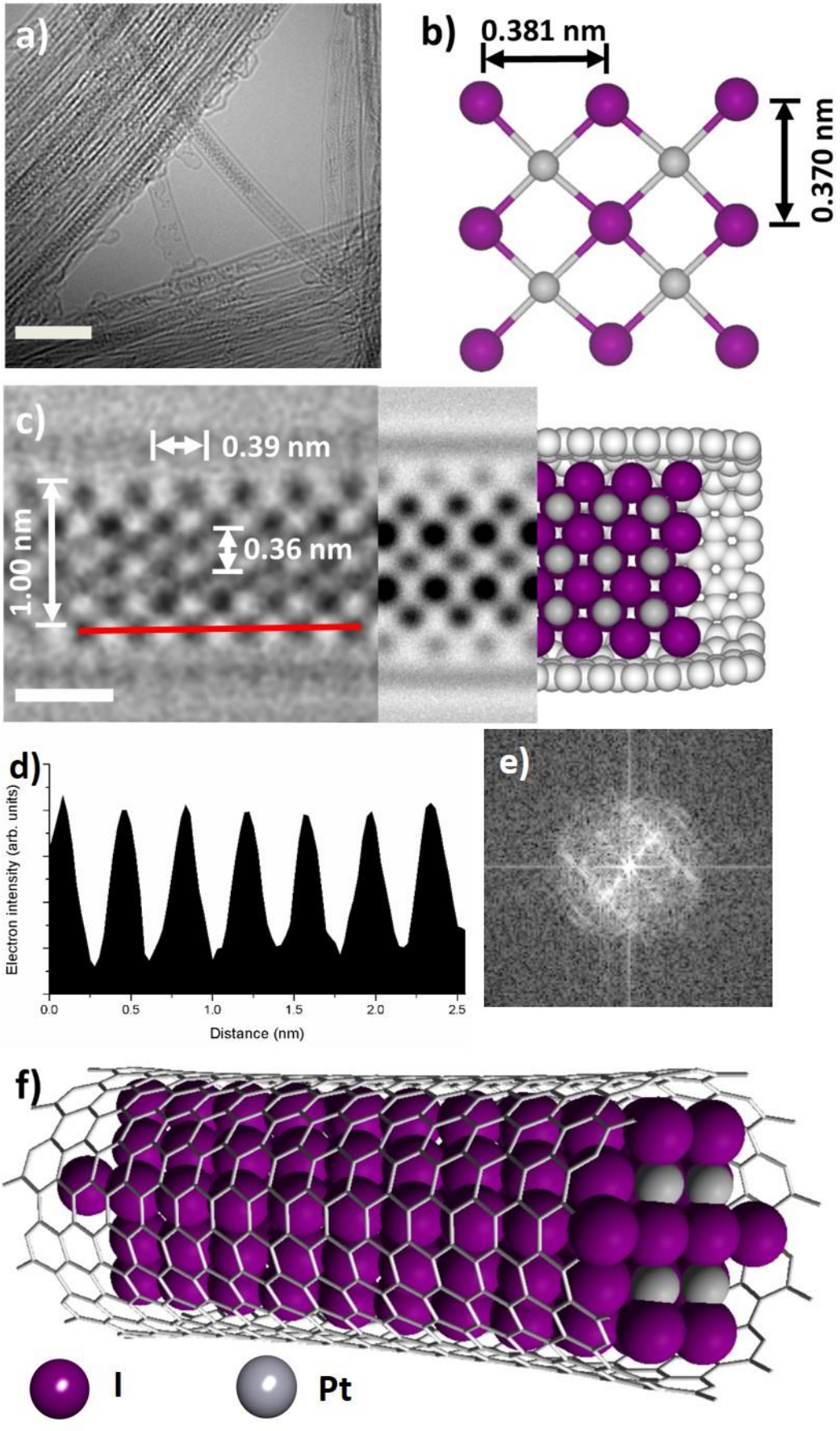

a)
b)
0.381 nm
0.370 nm
c)
0.39 nm
0.36 nm
1.00 nm
d)
Electron intensity (arb. units)
0.0
0.5
1.0
1.5
2.0
2.5
Distance (nm)
e)
f)
I
Pt

Figure 4.5: a) An AC-HRTEM micrograph showing a bundle of PtI_2@SWNT in which the majority of the SWNTs are highly filled with inorganic material, the scale bar is 5 nm; b) An extended portion of the crystal structure of PtI_2 derived from the asymmetric unit of bulk PtI_2 with key atomic distances shown; the grey and purple spheres represent platinum and iodine atoms respectively; c) an AC-HRTEM micrograph showing a small section of a 1.52 nm SWNT containing PtI_2 material and the corresponding atomic distances to the structure in b) are shown. A QSTEM simulation (80 kV) showing a projection of how a portion of the derived PtI_2 structure could fit inside an (11,11) SWNT, complimented by the cross-section of computational simulation to show its shape in the nanotube, the scale bar is 0.5 nm; d) an electron density profile map generated from the red line in (c) confirmed the periodicity of the interatomic distances; e) an FFT showing crystallinity of the material; f) a geometry optimised model showing how the proposed PtI_2 crystal would fit into a (11,11) SWNT.

AC-HRTEM shows many different orientations of PtI_2 inside the SWNT, and it is possible to perform QSTEM simulations on different projections of the geometry optimised model. The resultant simulated TEM images correlate very well with the experimental TEM images which supports the proposed models (figure 4.6).

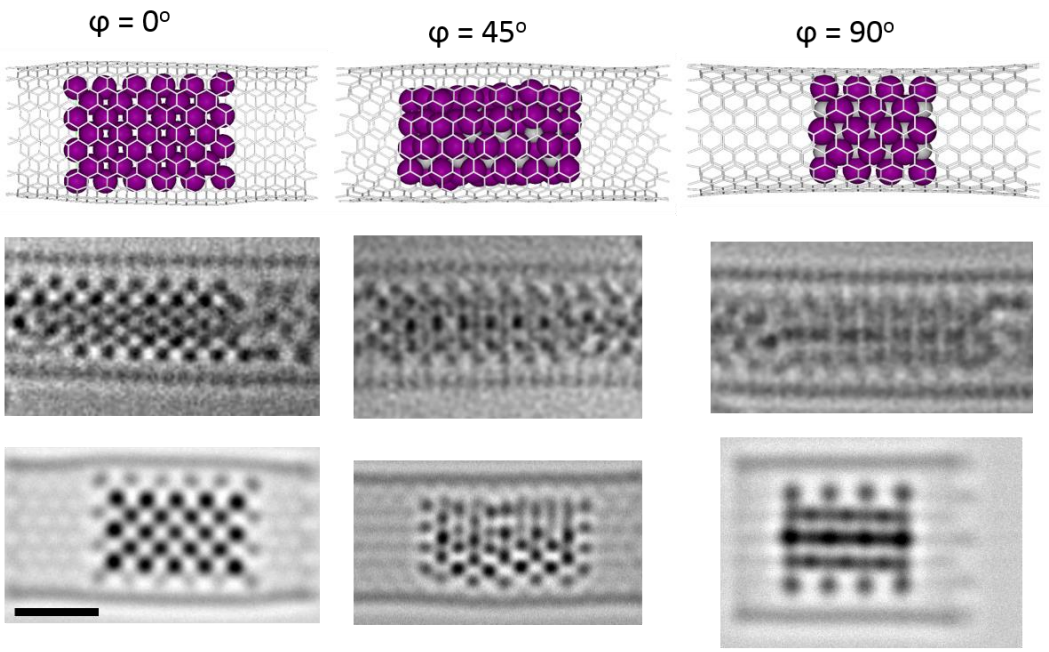


Figure 4.6: Series showing a model of PtI_2@SWNT (top row) with the corresponding AC-HRTEM image (80 kV, middle row) and image simulation (QSTEM, 20 slices per image, bottom row). The model has been tilted by 45° (middle column) and 90° (right column). The corresponding HR-TEM images and subsequent simulations are shown underneath each model.

In bright-field AC-HRTEM images (figures 4.5, 4.6) the observed contrast of atoms is proportional to $Z^{0.5}$, where Z is the atomic number of the element which usually results in large differences in contrast between heavy and light elements making it easy to discriminate between them; however, this technique is less efficient at distinguishing between two heavy elements such as Pt (Z=78) and I (Z=53) present in our material. Consequently, it is important to confirm the identities of the atoms within the lattice using a complimentary technique, aberration-corrected scanning transmission electron microscopy (AC-STEM). With AC-STEM the intensity of contrast is proportional to Z^{α}, where α depends on the detector angle and is typically 1.7-1.8[32] making it easier to distinguish between two heavy atoms within the same structure. AC-STEM images of PtI_2@SWNT clearly show a cubic lattice (figure 4.7 a), similar to that observed with AC-HRTEM and correlates well with the proposed model of encapsulated PtI_2 (figure 4.7 b).

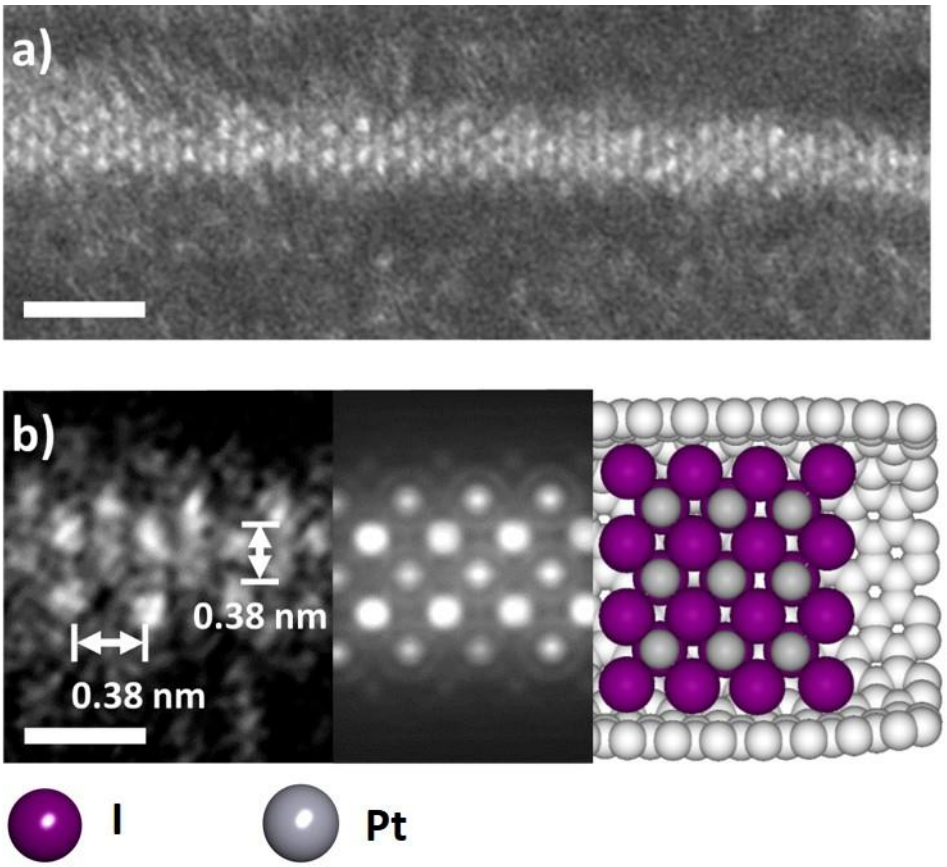


Figure 4.7 a) AC-STEM image showing a SWNT containing PtI_2 in which the SWNT is highly filled with the inorganic material, the scale bar is 1 nm; b) AC-STEM micrograph showing a small section of a SWNT containing PtI_2 material and the corresponding atomic distances to the derived structure of PtI_2. The material adopts a cubic configuration analogous to that observed in the bright field images in figure 4.5, the scale bar is 0.5 nm.

4.2.2.2 PtS_2@SWNT

AC-HRTEM images of PtS_2@SWNT material prepared in the one-pot/one-reactant synthesis clearly show extended inorganic nanostructures within the channels of SWNTs (figure 4.8 a). In contrast to the encapsulated PtI_2@SWNT, only platinum atoms can be visualised by AC-HRTEM in this sample due to the significant difference between the atomic numbers of sulfur and platinum. The encapsulated material in PtS_2@SWNT is characterised by a hexagonal lattice analogous to that of bulk PtS_2 (figure 4.8 b). The edge of the encapsulated PtS_2 adopts a zigzag conformation, with only sulfur atoms in contact with the nanotube sidewall (Figure

4.8 c,d) and the Pt-Pt separations of the encapsulated PtS_2 matching those in the bulk PtS_2.

An AC-STEM image of PtS_2@SWNT (figure 4.8 e) clearly shows a hexagonal lattice of platinum atoms matching that in AC-HRTEM images for this material (figure 4.8 c). The Pt-Pt interatomic distances appear to be in much closer agreement with bulk PtS_2 with only a small increase in the direction parallel to the principal SWNT axis. Although the nanotube sidewall cannot be observed in AC-STEM, in contrast to the images obtained using bright field AC-HRTEM, only three layers of platinum atoms are present in this sample suggesting that the host nanotube is narrower (figure 4.8 f).

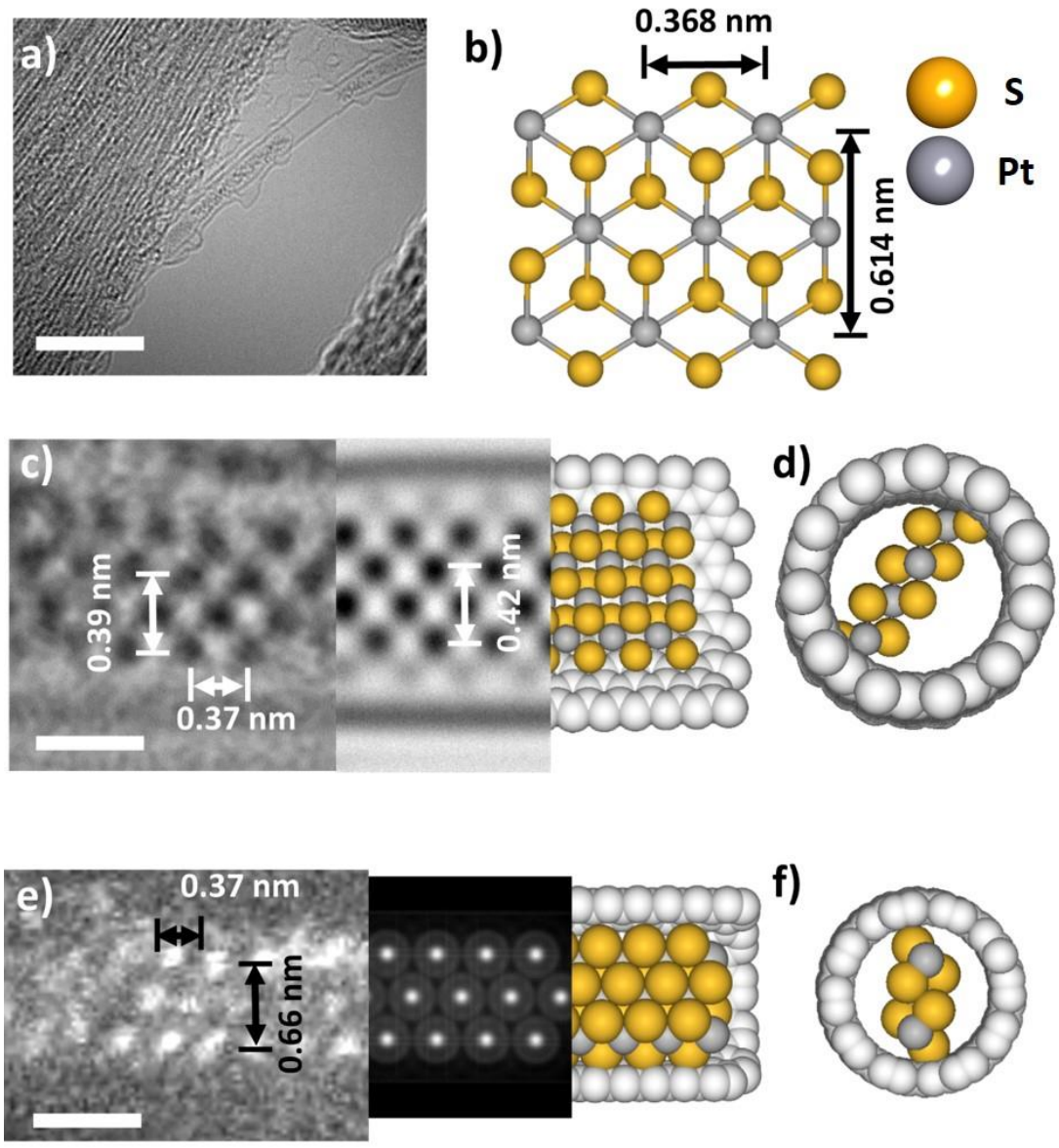


Figure 4.8: a) An AC-HRTEM micrograph showing a bundle of nanotubes containing PtS_2 material. The majority of SWNTs appear to be highly filled, and a single standing tube is visible, the scale bar is 5 nm; b) a portion of the crystal structure of bulk PtS_2, with key atomic distances shown; the grey and yellow spheres represent platinum and sulfur atoms respectively; c) an AC-HRTEM micrograph showing a small section of a 1.32 nm SWNT containing PtS_2 and Pt-Pt interatomic distances corresponding to PtS_2 structure tilted by 45º are shown; a QSTEM simulation (80 kV) showing how PtS_2 could fit inside a SWNT, complimented by a computational simulation to show its morphology in the nanotube; d) a geometry-optimised model depicting the cross section of PtS_2@SWNT; e) an AC-STEM image showing what appears to be a single strand of PtS_2 in a SWNT, the material adopts a hexagonal configuration analogous to that shown in c); however, there are only three layers of atoms present suggesting that the nanotube is narrower; furthermore, a STEM simulation (200 kV)

showing how PtS_2 could fit inside a (11,11) SWNT, complimented by a simulation to show its morphology in the nanotube; f) a geometry-optimised model depicting the cross section of PtS_2@SWNT.

4.3 Conclusion

Inorganic synthesis at the nanoscale is an important, but challenging task because of the need for simultaneous control of the dimensionality and stoichiometry of nanostructures. Carbon nanotubes, acting as nanocontainers effectively provide strict control of the size and shape of nanostructures, as has been demonstrated in this study by employing SWNTs as reaction vessels for the direct inorganic synthesis of a series of platinum containing compounds at the nanoscale. A detailed comparison of the stepwise and one-pot synthetic approaches clearly illustrates the advantages of the latter in terms of efficiency. However, the stepwise approach offers an excellent opportunity for studying the mechanisms of host-guest interactions between the SWNT and encapsulated compounds. It has been shown that a combination of FD-XAS and Raman spectroscopy can probe both the inorganic compound and the nanotube properties, and shed light on the direction and magnitude of electron transfer between the nanotube and compound inside. For example, two structurally related platinum complexes $Pt(acac)_2I_2$ and $Pt(acac)_2(SCN)_2$ have shown opposing electronic interactions with SWNTs, withdrawing or donating electron density from/to the host nanotube, which alters both the oxidation state of the Pt and the vibrational properties of the SWNT. However, neither one-pot nor stepwise approaches appeared to be able to provide sufficient control of the stoichiometry in the inorganic products formed inside the nanotube.

A solution to this problem was found by exploiting the diversity of the coordination chemistry of platinum complexes acting as precursors for the inorganic nanostructures. The coordination environment of the platinum atom in the precursor

complex was expanded by appending extra ligands bearing the necessary elements (I or S) in a correct and precise proportion to platinum, thus paving the way to stoichiometrically controlled synthesis inside nanotubes, as demonstrated by the synthesis of novel PtI_2@SWNT and PtS_2@SWNT nanostructures in the new one-pot-one-reactant approach with the specifically designed multi-element containing precursors. The new strategy for inorganic synthesis at the nanoscale was shown to be versatile and universal, enabling the formation of previously inaccessible quasi-one-dimensional platinum containing nanomaterials suitable for a variety of technological applications. These range from electronic devices where electronic doping of the nanotube is precisely modulated by electron transfer between the SWNT and encapsulated compound, to new catalytic platforms exploiting the unique chemical properties of platinum compounds, where the shape of the crystal and oxidation state of the metal are controlled by steric and electron interactions with the host nanotube.

4.4 Experimental

4.4.1 Materials

SWNTs (P2-SWNTs, arc discharge, Carbon Solutions, USA) were annealed at 600 ^{o}C for 15 min to open their termini and remove any residual amorphous carbon from their internal cavities resulting in a 50% weight loss being observed. The platinum precursor, $Pt(acac)_2$ was used as supplied (Sigma Aldrich). The substituted platinum precursors $Pt(acac)_2I_2$[27] and $Pt(acac)_2(SCN)_2$[28] were synthesised in accordance with published procedures.

4.4.1.1 PtI_2@SWNT

$Pt(acac)_2$ (90 mg, 0.229 mmol) and freshly opened SWNTs (25 mg) were sealed together under vacuum (10^{-5} bar) in a Pyrex ampoule and heated at 150 ^oC for 3 days to ensure penetration of the SWNT by the $Pt(acac)_2$. The ampoule was cooled rapidly in ice-water and repetitive washing with dichloromethane (4 x 25 mL) was performed, followed by filtration to remove any excess material from the exterior of the SWNTs, forming $Pt(acac)_2$@SWNT. Under at atmosphere of argon, $Pt(acac)_2$@SWNT (10 mg, 0.0196 mmol) was heated at 500 ^oC for 1 hr and allowed to cool down slowly forming Pt@SWNT. This sample was sealed in a Pyrex ampoule with an excess of I_2 and heated at 110 ^oC for 3 days to give PtI_2@SWNT.

Alternatively, $Pt(acac)_2I_2$ (10 mg) was sealed in a Pyrex ampoule under vacuum (10^{-5} bar) with freshly opened SWNTs (5 mg) and heated for 3 days at 150 ^oC. The ampoule was cooled rapidly in ice water and then heated under argon at 500 ^oC for 1 hr to give PtI_2@SWNT

4.4.1.2PtS_2@SWNT

Argon was passed over PtI_2@SWNT (5.7 mg) in a tube furnace for 1 h. The sample was then heated in the presence of a moderate H_2S gas flow (*ca.* 15mL/min) at 550 ^oC for 2 h. The sample was then allowed to cool by 5 ^oC/min under argon.

Alternatively, $Pt(acac)_2(SCN)_2$ (10 mg, 0.0196 mmol) was sealed under vacuum (10^{-5} bar) in a Pyrex ampoule with SWNTs (5 mg) and heated at 130 ^oC for 3 days. After rapidly cooling in ampoule in ice water, the sample was washed with chloroform (4 x 10 mL), then heated under argon at 500 ^oC for 1 hr to give PtS_2@SWNT.

4.4.2 Electron Microscopy

SWNTs filled with the encapsulated materials were dispersed in propan-2-ol using an ultrasonic bath and drop cast onto lacey carbon-coated copper TEM grids (Agar). HR-TEM imaging was carried out on a JEOL 2100 FEG-TEM microscope operated at 200 kV. AC-HRTEM was performed at the University of Ulm on a C_s corrected FEI Titan 80-300 TEM operated at 80 kV with information limit enhancement using reduced extraction voltage. AC-STEM was performed at the University of Birmingham using a 200 kV JEOL 2100F microscope fitted with a high angle annular dark field (HAADF) detector. All images were processed using Gatan Digital Micrograph, and the quoted distances were measured by drawing a line profile and measuring the electron intensity.

4.4.3 EDX Spectroscopy

Local EDX spectra were acquired for samples mounted on TEM grids using an Oxford Instruments INCA X-ray microanalysis system. The electron beam was condensed onto areas of specimens (bulk specimen or nanotube bundles) suspended over holes of the amorphous carbon film.

4.4.4 Raman Spectroscopy

Raman spectroscopy was performed using a HORIBA Jobin Yvon LabRAM HR spectrometer equipped with an automated *xyz* stage (Märzhäuser). Spectra were acquired using a 532 nm laser at 0.2 mW power, in the range 50 to 4000 cm^{-1}, with 5 seconds and 8 accumulations per spectral window, using a 50× objective and a 300 μm confocal pinhole. To simultaneously scan a range of Raman shifts, a 600 lines/mm rotatable diffraction grating along a path length of 800 mm was employed. Spectra were detected using a SYNAPSE CCD detector (1024 pixels) thermoelectrically

cooled to −60 °C. Before the spectra collection, the instrument was calibrated using the Rayleigh line at 0 cm^{-1} and a standard Si(100) reference band at 520.7 cm^{-1}.

4.4.5 Image Simulation

TEM image simulation was carried out using the multislice program QSTEM. QSTEM uses the Dirac-Fock scattering potential of Rez *et al.*[33] A fixed number of 20 slices per nanotube was chosen and images were calculated with a sampling of 0.05 nm per pixel. The aberration coefficients and defocus parameters *df, C*S, *A1*, and *B*2 were set according to the imaging conditions in the specific experiment. The convergence angle was fixed at 0.5 mrad. The effect of limited electron dose was emulated by applying noise to the calculated images using a custom-made Monte-Carlo program exploiting the Poisson statistics of electrons. Atomic models of SWNTs were built using a custom-made program taking into account different nanotube chiralities, if determinable in the experimental images. The structural models of the inorganic nanomaterials are based on scaled bulk structures and the complex models (PtX@SWNT) are rendered and iteratively fitted to the experimental results.

STEM image simulation was performed using both a kinetic approach (for speed) and frozen phonon multislice method to check for dynamical scattering effect. [34, 35] The simulation was performed at 200keV, with a Cs of 10 μm, convergence angle of 25 mrad, inner collection angles 60 mrad, outer collection angle of 160 mrad, and a mechanical vibration factor of 0.1A.

4.4.6 Fluorescence-Detected X-ray Absorption Spectroscopy (FD-XAS)

All FD-XAS measurements were carried out on the XMaS beamline (BM28) at the ESRF. Samples were deposited onto carbon tape, which was then mounted onto a stainless steel sample holder. FD-XAS edge inflection points were obtained by fitting

a smoothing spline to the measured spectrum, and taking the first derivative of the fitted spectrum.

4.5 References

1. A. Govindaraj, B. C. Satishkumar, M. Nath and C. N. R. Rao, *Chem. Mater.*, 2000, **12**, 202.
2. C. H. Kiang, J. S. Choi, T. T. Tran and A. D. Bacher, *J. Phys. Chem. B*, 1999, **103**, 7449.
3. R. Nakanishi, R. Kitaura, P. Ayala, H. Shiozawa, K. de Blauwe, P. Hoffmann, D. Choi, Y. Miyata, T. Pichler and H. Shinohara, *Phys. Rev. B*, 2012, **86**.
4. K. Yanagi, Y. Miyata and H. Kataura, *Adv. Mater.*, 2006, **18**, 437.
5. T. Takenobu, T. Takano, M. Shiraishi, Y. Murakami, M. Ata, H. Kataura, Y. Achiba and Y. Iwasa, *Nat. Mater.*, 2003, **2**, 683.
6. Y. Ren and G. Pastorin, *Adv. Mater.*, 2008, **20**, 2031.
7. N. A. Kiselev, A. S. Kumskov, V. G. Zhigalina, N. I. Verbitskiy, L. V. Yashina, A. L. Chuvilin, A. L. Vasiliev, A. A. Eliseev and Iop, in *18th Microscopy of Semiconducting Materials Conference*, eds. T. Walther and J. L. Hutchison, 2013, vol. 471.
8. R. R. Meyer, J. Sloan, R. E. Dunin-Borkowski, A. I. Kirkland, M. C. Novotny, S. R. Bailey, J. L. Hutchison and M. L. H. Green, *Science*, 2000, **289**, 1324.
9. J. Sloan, S. J. Grosvenor, S. Friedrichs, A. I. Kirkland, J. L. Hutchison and M. L. H. Green, *Angew. Chem.-Int. Edit.*, 2002, **41**, 1156.
10. M. Hulman, P. Costa, M. L. H. Green, S. Friedrichs and H. Kuzmany, in *Electronic Properties of Synthetic Nanostructures*, eds. H. Kuzmany, J. Fink, M. Mehring and S. Roth, Amer Inst Physics, Melville, 2004, vol. 723, pp. 278.
11. E. Flahaut, J. Sloan, S. Friedrichs, A. I. Kirkland, K. S. Coleman, V. C. Williams, N. Hanson, J. L. Hutchison and M. L. H. Green, *Chem. Mater.*, 2006, **18**, 2059.
12. B. C. Satishkumar, A. Taubert and D. E. Luzzi, *J. Nanosci. Nanotechnol.*, 2003, **3**, 159.
13. A. Chuvilin, E. Bichoutskaia, M. C. Gimenez-Lopez, T. W. Chamberlain, G. A. Rance, N. Kuganathan, J. Biskupek, U. Kaiser and A. N. Khlobystov, *Nat. Mater.*, 2011, **10**, 687.
14. T. W. Chamberlain, J. Biskupek, G. A. Rance, A. Chuvilin, T. J. Alexander, E. Bichoutskaia, U. Kaiser and A. N. Khlobystov, *ACS Nano*, 2012, **6**, 3943.
15. L. Shi, P. Rohringer, K. Suenaga, Y. Niimi, J. Kotakoski, J. C. Meyer, H. Peterlik, M. Wanko, S. Cahangirov, A. Rubio, Z. J. Lapin, L. Novotny, P. Ayala and T. Pichler, *Nat. Mater.*, 2016, **15**, 634.
16. A. K. Geim and I. V. Grigorieva, *Nature*, 2013, **499**, 419.
17. C. G. Xu, J. Sloan, G. Brown, S. Bailey, V. C. Williams, S. Friedrichs, K. S. Coleman, E. Flahaut, J. L. Hutchison, R. E. Dunin-Borkowski and M. L. H. Green, *Chem. Commun.*, 2000, 2427.
18. J. Sloan, M. C. Novotny, S. R. Bailey, G. Brown, C. Xu, V. C. Williams, S. Friedrichs, E. Flahaut, R. L. Callender, A. P. E. York, K. S. Coleman, M. L. H. Green, R. E. Dunin-Borkowski and J. L. Hutchison, *Chem. Phys. Lett.*, 2000, **329**, 61.

19. E. Philp, J. Sloan, A. I. Kirkland, R. R. Meyer, S. Friedrichs, J. L. Hutchison and M. L. H. Green, *Nat. Mater.*, 2003, **2**, 788.
20. L. V. Yashina, A. A. Eliseev, M. V. Kharlamova, A. A. Volykhov, A. V. Egorov, S. V. Savilov, A. V. Lukashin, R. Puttner and A. I. Belogorokhov, *J. Phys. Chem. C*, 2011, **115**, 3578.
21. R. Cusak, *Proc. Roy. Irish. Acad.*, 1897, **4**, 399.
22. A. A. Eliseev, M. V. Chernysheva, N. I. Verbitskii, E. A. Kiseleva, A. V. Lukashin, Y. D. Tretyakov, N. A. Kiselev, O. M. Zhigalina, R. M. Zakalyukin, A. L. Vasiliev, A. V. Krestinin, J. L. Hutchison and B. Freitag, *Chem. Mater.*, 2009, **21**, 5001.
23. Z. Wang, H. Li, Z. Liu, Z. Shi, J. Lu, K. Suenaga, S.-K. Joung, T. Okazaki, Z. Gu, J. Zhou, Z. Gao, G. Li, S. Sanvito, E. Wang and S. Iijima, *J. Am. Chem. Soc.*, 2010, **132**, 13840.
24. Z. Wang, K. Zhao, H. Li, Z. Liu, Z. Shi, J. Lu, K. Suenaga, S.-K. Joung, T. Okazaki, Z. Jin, Z. Gu, Z. Gao and S. Iijima, *J. Mater. Chem.*, 2011, **21**, 171.
25. Q. Fu, G. Weinberg and D. S. Su, *New Carbon Mater.*, 2008, **23**, 17.
26. L. Grigorian, K. A. Williams, S. Fang, G. U. Sumanasekera, A. L. Loper, E. C. Dickey, S. J. Pennycook and P. C. Eklund, *Phys. Rev. Lett.*, 1998, **80**, 5560.
27. P. M. Cook, L. F. Dahl, D. Hopgood and R. A. Jenkins, *J. Chem. Soc., Dalton Trans.*, 1973, 294.
28. A. Grabowski and W. Preetz, *Z. Anorg. Allg. Chem.*, 1987, **544**, 95.
29. A. A. Eliseev, L. V. Yashina, N. I. Verbitskiy, M. M. Brzhezinskaya, M. V. Kharlamova, M. V. Chernysheva, A. V. Lukashin, N. A. Kiselev, A. S. Kumskov, B. Freitag, A. V. Generalov, A. S. Vinogradov, Y. V. Zubavichus, E. Kleimenov and M. Nachtegaal, *Carbon*, 2012, **50**, 4021.
30. N. A. Kiselev, R. M. Zakalyukin, O. M. Zhigalina, N. Grobert, A. S. Kumskov, Y. V. Grigoriev, M. V. Chernysheva, A. A. Eliseev, A. V. Krestinin, Y. D. Tretyakov, B. Freitag and J. L. Hutchison, *J. Microsc.*, 2008, **232**, 335.
31. G. Thiele, W. Weigl and H. Wochner, *Z. Anorg. Allg. Chem.*, 1986, **539**, 141.
32. Z. W. Wang, Z. Y. Li, S. J. Park, A. Abdela, D. Tang and R. E. Palmer, *Phys. Rev. B*, 2011, **84**, 073408.
33. D. Rez, P. Rez and I. Grant, *Acta Crystallogr. Sect. A*, 1994, **50**, 481.
34. D. S. He, Z. Y. Li and J. Yuan, *Micron*, 2015, **74**, 47.
35. R. Aveyard, R. Ferrando, R. L. Johnston and J. Yuan, *Phys. Rev. Lett.*, 2014, **113**, 075501.

Chapter V: Monitoring Nanoscale Transformations using Fluorescence-Detected X-ray Absorption Spectroscopy

5.1 Introduction

Metal nanoparticles (MNPs) have attracted considerable interest recently due to their applications in catalysis and sensing.[1-4] In order to comprehensively unlock the potential of these materials, it is important to fully understand how they form. As shown in Chapters II and III, due to advances in aberration-corrected high resolution transmission electron microscopy (AC-HRTEM), it is possible to not only view nano-sized materials in direct space and real time, but also apply energy and initiate chemical transformations, such as the formation of highly crystalline platinum nanoparticles from amorphous platinum, or the breakage of a SWNT sidewall catalysed by encapsulated nickel nanoparticles (Chapter III). Prolonged irradiation of a sample by electron beam irradiation results in the displacement of carbon atoms and bond dissociations, leading to the gradual destruction of the sample being analysed which is a generally undesirable process.[5-7] Therefore, whilst it is possible to monitor inorganic transformations using AC-HRTEM, electron microscopy is an invasive analytical technique which can perturb the intrinsic structures of materials and mask chemical transformations.

As shown in previous chapters, fluorescence-detected X-ray absorption spectroscopy (FD-XAS) can be employed as a technique to characterise nanomaterials by probing amongst other qualities, the oxidation state of materials, and so can be used as a

method of discriminating between the encapsulated precursors and the product formed upon their heating.[8, 9] This is possible since the shape and magnitude of the spectral features from each compound are different, which corresponds to variations in the oxidation states of the materials.[10] Notably, unlike AC-HRTEM, it is a bulk technique which involves exposing a sample to X-rays, over an area typically on the order of mm^2, and so is also non-destructive at the conditions required for obtaining data. This is advantageous as it allows the material to then be retained for further analysis.

As well as using this technique to characterise materials statically, it is also possible to form a material, apply an external stimulus such as heat, and perform FD-XAS *in-situ*. Subsequently, time resolved FD-XAS is an appropriate technique for obtaining information on the formation mechanisms of MNPs. For example, the nucleation process of AuNPs has been investigated by Wai *et al.* using *in-situ* XAS and allowed for the proposal of a detailed reaction mechanism, as intermediates were detected.[11] Additionally, Ohyama *et al*. showed how the formation of AuNPs is affected by the presence of dodecanethiol and a catalytic activity dependence on the size of AuNPs was observed.[12] More recently, Jiang *et al*. have demonstrated that the reduction of Pt^{4+} ions can be investigated using the same technique,[13] and so observing how the edge energies of each material change as a function of temperature should allow for a detailed explanation of the properties of each transformation.

Carbon nanostructures such as single-walled carbon nanotubes (SWNTs), are extremely interesting as they contain distinctive nanoscale channels which can be filled with a variety of different materials including inorganic salts,[14-16] organic molecules,[17, 18] and metallic nanoparticles.[19-21] The mechanical, chemical and physical properties of MNPs can be altered upon encapsulation into SWNTs which

can lead to changes in catalytic activity, as is observed for the synthesis of ammonia catalysed by ruthenium nanoparticles.[22] Furthermore, the stability of platinum nanoparticles can be improved upon encapsulation into carbon nanostructures which in turn could lead to a decrease in platinum consumption for catalytic processes.[23] Not only can SWNTs act as sheaths to improve the efficiency of MNPs, their unique one-dimensional channel allows them to act as nano test tubes which ensures that the analysis and reaction of encapsulated molecules can be done with ease.

As shown previously, the thermal treatment of $Cu(acac)_2$@SWNT leads to the formation of Cu_2O_x@SWNT (Chapter II), whereas the thermal treatment of $Pt(acac)_2$@SWNT leads to the formation of Pt@SWNT (Chapter III). When observed at static temperatures, the $M(acac)_2$@SWNT (M= Cu, Pt) precursors have many noticeable differences to their respective products, with changes in their electronic properties, physical morphology and chemical properties all being observed. Herein, the formation of Cu_2O_x@SWNT from $Cu(acac)_2$@SWNT, and Pt@SWNT from $Pt(acac)_2$@SWNT has been investigated using FD-XAS, and this has allowed for the precise temperature of each respective transformation to be determined.

5.2 Results and Discussion

5.2.1 *Ex-situ* Decomposition of $Cu(acac)_2$@SWNT to Cu_2O_x@SWNT

As shown in Chapter II, $Cu(acac)_2$@SWNT (figure 5.1 a) can be heated under an inert atmosphere at 500 °C to form Cu_2O_x@SWNT (figure 5.1 b, scheme 5.1), where x > 1.

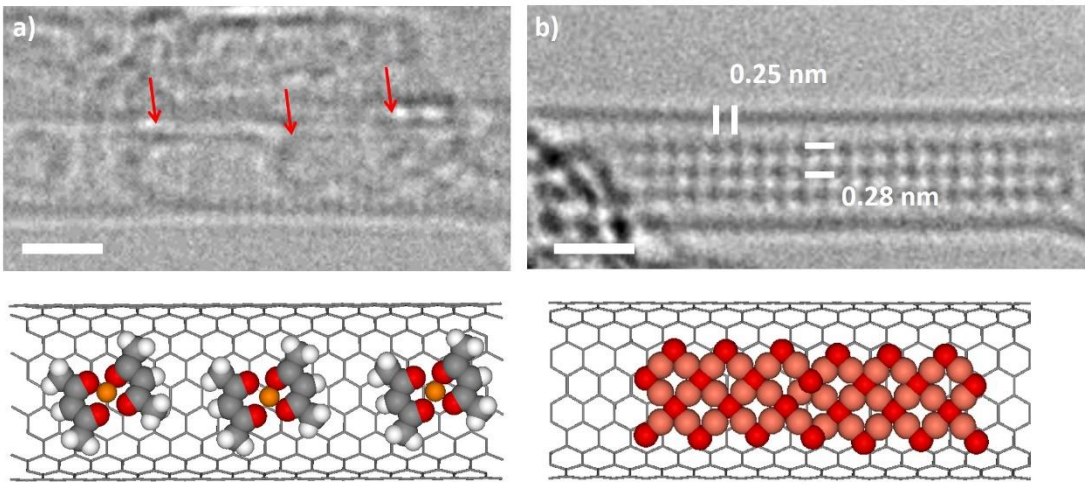


Figure 5.1: AC-HRTEM images showing a) $Cu(acac)_2$@SWNT, the darker contrast features (red arrows) are copper, whereas the lighter contrast material is a mixture of adventitious carbon and remnants of the acetylacetonate ligand which is decomposing under the electron beam; b), Cu_2O_x@SWNT. The structure adopts a highly crystalline cubic arrangement. The scale bars are 0.5 nm and below each AC-HRTEM image is a geometry optimised model of the structures in a (10,10) SWNT.

$$Cu(acac)_2 + SWNT \xrightarrow[3\ days,\ 10^{-5}\ mbar]{110\ ^oC} Cu(acac)_2@SWNT \xrightarrow[1\ hr,\ Ar]{500\ ^oC} [Cu_2O_x]^{((x-1).2)-}@SWNT^{((x-1).2)+}$$

Scheme 5.1: The formation of Cu_2O_x@SWNT, by first encapsulating $Cu(acac)_2$ into SWNTs and then heating.

Raman spectroscopy reveals a large blue shift in the position of the G band of Cu_2O_x@SWNT relative to an empty SWNT and $Cu(acac)_2$@SWNT (+11 cm^{-1}), (figure 5.2), indicating charge transfer from the SWNT to the encapsulated material.[24] The model of Cu_2O@SWNT (figure 5.1 b) shows an excess of oxygen atoms in the material, and so it is probable that the resultant structure has a slight negative charge,

which results in a transfer of electron density being observed from the nanotube and hence the blue shift of the G band, as described in Chapter II.[25]

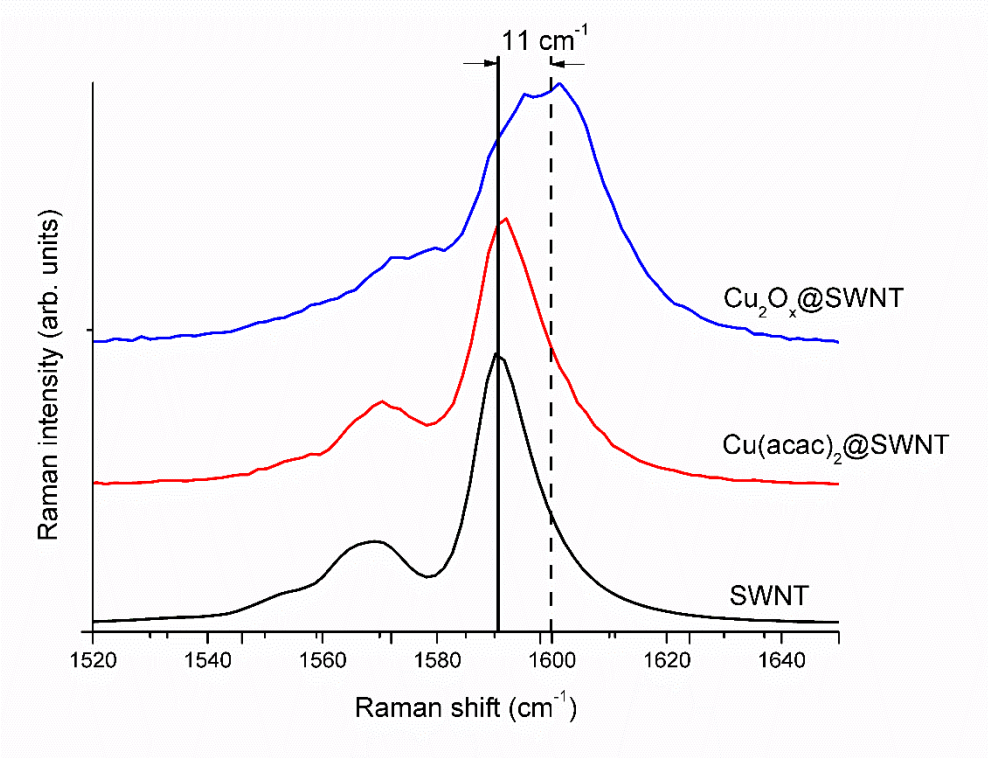


Figure 5.2: Normalised Raman spectra focussing on the G band of Cu_2O_x@SWNT (blue) and $Cu(acac)_2$@SWNT (red) compared to an empty SWNT (back). Whilst there is a negligible shift in the G band spectra of $Cu(acac)_2$@SWNT relative to empty SWNTs, the position of the G band of Cu_2O_x@SWNT sample increases significantly (+11 cm^{-1}).

FD-XAS was recorded for both materials. The energy of the copper K edge of both materials was taken, and compared to the copper K edge of a variety of standards (table 5.1).

Table 5.1: Copper K edge energy of $Cu(acac)_2$@SWNT, Cu_2O_x@SWNT, and known standards relative to copper metal.

Material	Formal Cu oxidation state	Cu K edge (eV)	Difference from Cu K edge of Cu(0) (eV)
Cu	0	8975.53 ± 0.079	**0**
Cu_2O_x@SWNT	1	8980.42 ± 0.037	**4.89**
$Cu(CO_2CH_3)$	1	8982.18 ±0.061	**6.65**
$Cu(acac)_2$	2	8984.76 ± 0.370	**9.23**
$Cu(acac)_2$@SWNT	2	8986.76 ± 0.093	**11.23**

An increase in the K edge energy of copper in $Cu(acac)_2$@SWNT is observed relative to the unencapsulated material which suggests a decrease of electron density on the copper centre when the complex is encapsulated. As the Raman data does not show any significant change in the G band of the SWNT for $Cu(acac)_2$@SWNT, this demonstrates that any charge transfer that takes place in this material occurs only in the complex itself, and does not involve the SWNT. Since FD-XAS shows a decrease of electron density on the copper atom upon encapsulation, it is proposed that the nanotube has acted to polarise the Cu-O bonds, resulting in greater shift of electron density from the Cu atom to O atoms, such that the Cu-O bond becomes more ionic (figure 5.3 a).

Upon heating to 500 ^oC a significant decrease in the energy of the copper K edge from $Cu(acac)_2$@SWNT to Cu_2O_x@SWNT occurs which indicates that the copper centre has gained electron density. The energy is similar to that of a known Cu(I) complex, copper (I) acetate, but is slightly lower, and is therefore is consistent with the

formation of a Cu(I) species, but with electron density being transferred from the nanotube to the guest compound (figure 5.3 b).

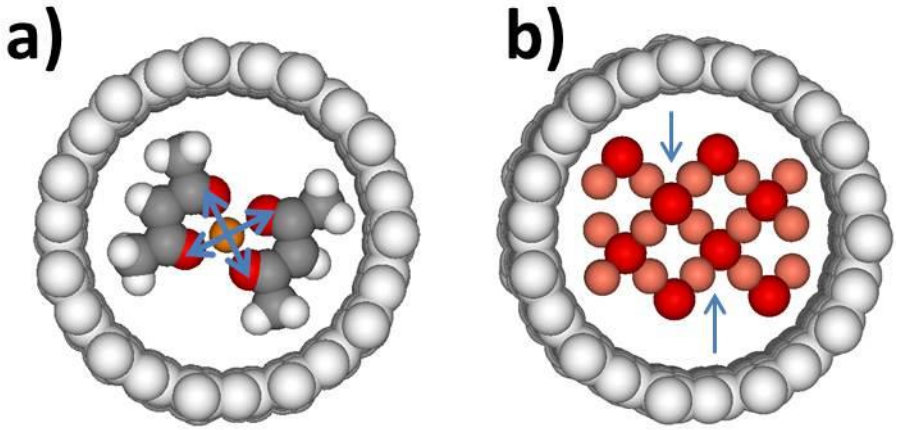


Figure 5.3: Models of (a) $Cu(acac)_2$@SWNT and (b) Cu_2O_x@SWNT showing charge transfers taking place within the guest species (blue arrows depict the flow of negative charge). With $Cu(acac)_2$@SWNT electron density is shifted further from the copper atom to oxygen atoms resulting in the polarisation of the bonds, whereas for Cu_2O_x@SWNT, negative charge is transferred from the nanotube wall to the guest material.

Not only are the positions of the copper K edge of $Cu(acac)_2$@SWNT and Cu_2O_x@SWNT significantly different, their shapes also vary. While the FD-XAS of $Cu(acac)_2$@SWNT shows a sharp transition between 8.972 to 8.993 keV (figure 5.4 a), the spectrum for Cu_2O_x@SWNT has a slightly broader range (8.969 to 8.992 keV) with a distinct feature at 8.98k eV (figure 5.4 b). All of the spectra were smoothed using Matlab, and figure 5.4 gives an example of how accurate the smoothing was. The points represent the raw data, and the black line shows the curves produced as a result of the smoothing.

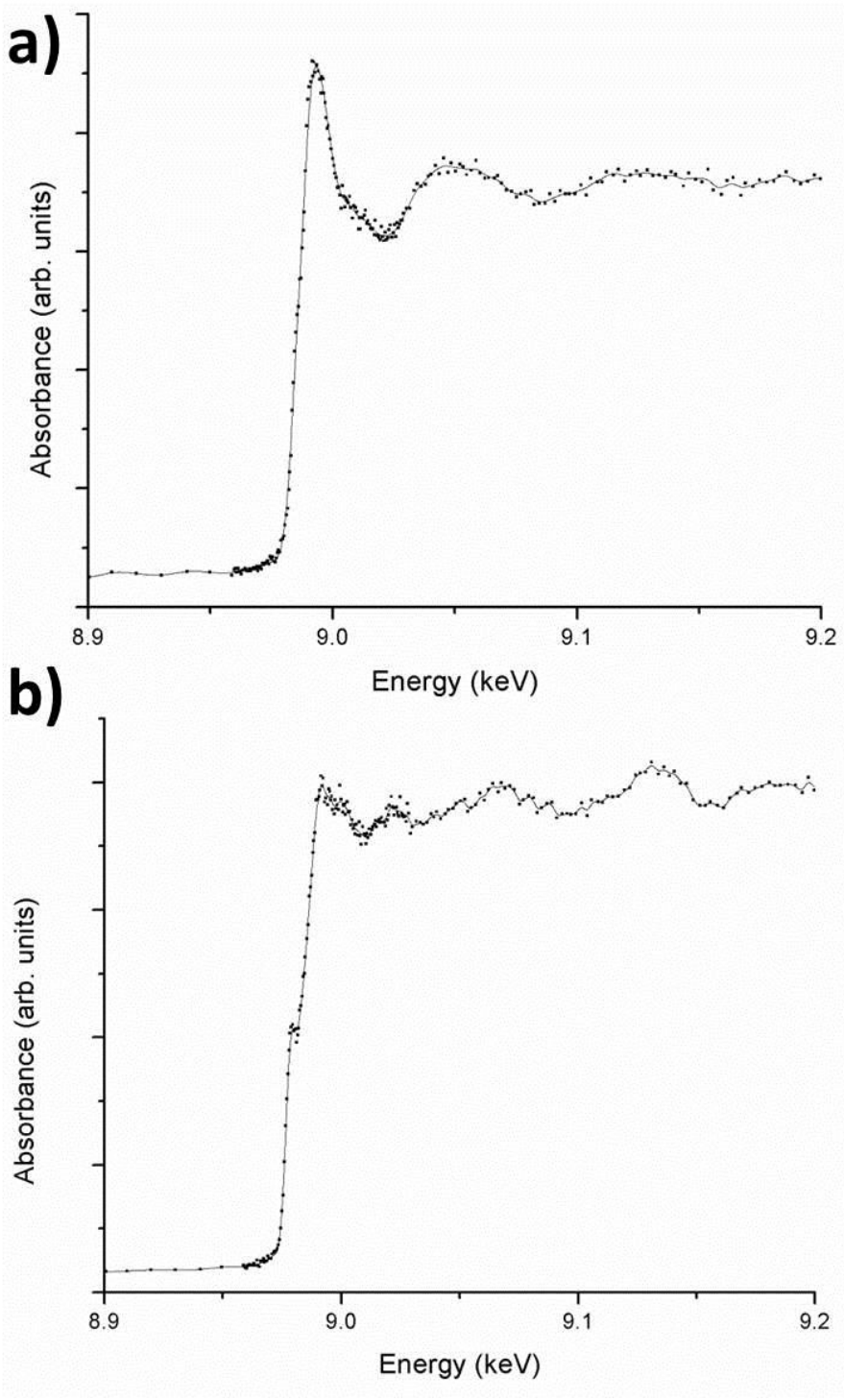


Figure 5.4: Normalised FD-XAS of (a) $Cu(acac)_2$@SWNT and (b) Cu_2O_x@SWNT. The Cu_2O_x@SWNT was formed *ex-situ* and both spectra were recorded at room temperature. The shape of the two spectra are noticeably different, with an extra feature observed at 8.98 keV for the spectrum of Cu_2O_x@SWNT.

5.2.1.1 Attempted Monitoring of the Shift with *in-situ* Heating

Clearly, the AC-HRTEM images of $Cu(acac)_2$@SWNT before and after heat treatment demonstrate that different materials are present inside the nanotube, and this is supported by both the Raman and FD-XAS data which show changes in electronic states of the SWNT and guest compound upon heating. Therefore the sample was heated slowly, and systematically monitored using FD-XAS to investigate whether the precise transition could be observed.

The encapsulated metallic precursor $Cu(acac)_2$@SWNT (5 mg) was placed in a glass capillary tube and held in position with glass wool (figure 5.5 a.1). The tube was placed within an aluminium frame, and sealed in place using wax, to ensure no air could enter the system. The frame was then placed in position above a heater (figure 5.5 a.4) and attached to a helium source (in figure 5.5 a.2, out figure 5.5 a.3, flow rate *ca.* 30 mL/min), and the system was purged with helium for 15 min to ensure all air was removed from the capillary tube. Finally, the system was heated rapidly (at a rate of 50 ^{o}C/s) which allowed for precise control of temperature when needed.

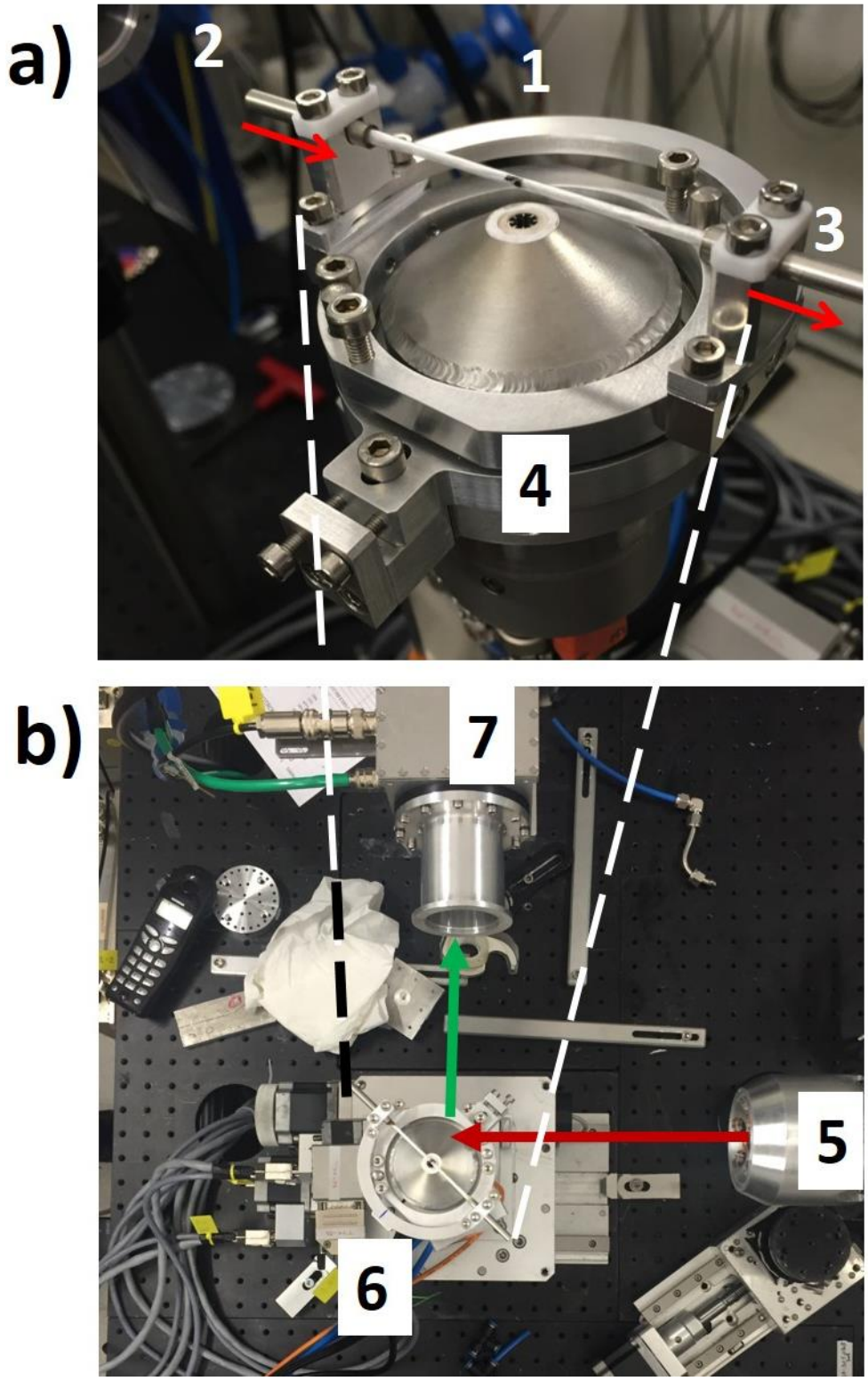


Figure 5.5: Photographs from the ESRF showing a) how the sample of $Cu(acac)_2$@SWNT was prepared for the heating experiment. A small amount of $Cu(acac)_2$@SWNT was placed in a glass capillary tube (1), which was placed in a steel frame and mounted above a heat source (4). A helium gas flow was attached (2), to purge the system of air and provide an inert atmosphere; b) the position of the X-ray source (5) relative to the sample (6) and fluorescence

detector, (7). The red arrow represents the flow of X-rays, and the green arrow shows the fluorescence signal, which is detected perpendicular to the X-ray source.

Initially, a spectrum of $Cu(acac)_2$@SWNT was recorded at room temperature and the sample was heated to 100 ^oC (at a rate of 50 $^oC/s$), held at this temperature for 5 min and another spectrum was recorded. X-rays (figure 5.5 b.5, red arrow) were tuned to the required energy for the copper K edge (8.988 keV) and travelled through the sample (figure 5.5 b.6) and X-ray fluorescence (green arrow) was detected perpendicularly (figure 5.5 b.7).

After obtaining a spectrum of the sample at 100 ^oC, which took approximately 8 min, the temperature of the arrangement was increased from 100 ^oC to 125 ^oC, held for 5 min and a subsequent spectra recorded, the scan took approximately 8 min and this process continued in 25 ^oC steps until there was no further change in the energy of the edge position. $Cu(acac)_2$@SWNT was consequently heated to 300 ^oC over *ca.* 120 min. Each spectrum was smoothed using a Matlab function, and all spectra were collated and compared with that of Cu_2O_x@SWNT formed *ex-situ* (figure 5.6)

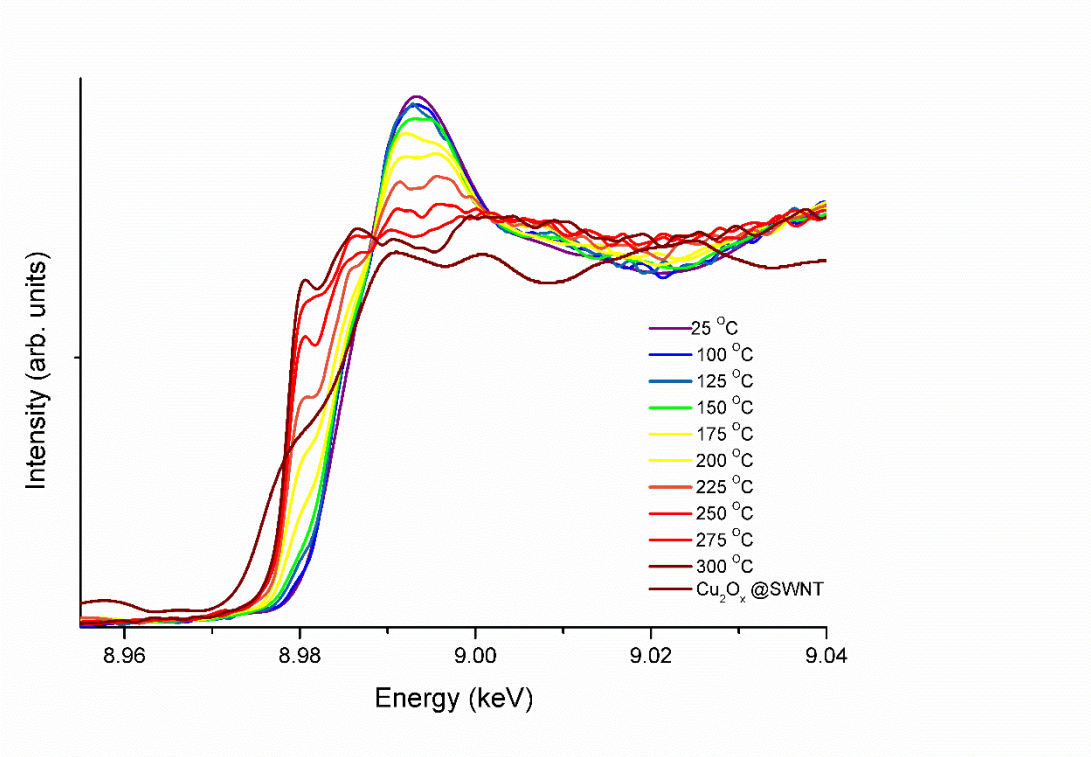


Figure 5.6: FD-XAS obtained for Cu(acac)$_2$@SWNT at 25 ºC (purple line), then heated to 100 ºC (blue) followed by subsequent heating at 25 ºC increments. As the temperature increases, the shape of each spectrum changes, and gradually appears to resemble that of Cu$_2$O$_x$@SWNT formed *ex-situ*.

When the edge region of all the spectra are closely examined (figure 5.7), it is clear that the energy of the edge decreases as a function of temperature (figure 5.7 a). The first derivative of the edge position at each temperature has been shown which allows for the exact position of the energy to be recorded (figure 5.7 b), and at temperatures below 175 ^{o}C, the edge occurs at around 8.9889 keV; however, when heated to 175 ^{o}C, there is a decrease of around 5 eV to 8.9838 keV. After further heating to 200 ^{o}C the edge decreases by another 5 eV to 8.9787 keV.

The sample was further heated to 300 ^{o}C, but no additional shift in the energy of the edge was observed. Since the energy of the copper K edge of Cu(acac)$_2$@SWNT (8.9867 keV) has a standard deviation of 0.0183 eV, and the copper K edge of Cu$_2$O$_x$@SWNT (8.9763 keV) has a standard deviation of 0.0933 eV, a change of 10 eV is clearly significant. This experiment has shown that the edge energy of

$Cu(acac)_2$@SWNT decreases as a function of temperature and is only 2eV greater than the edge position of Cu_2O_x@SWNT formed *ex-situ*.

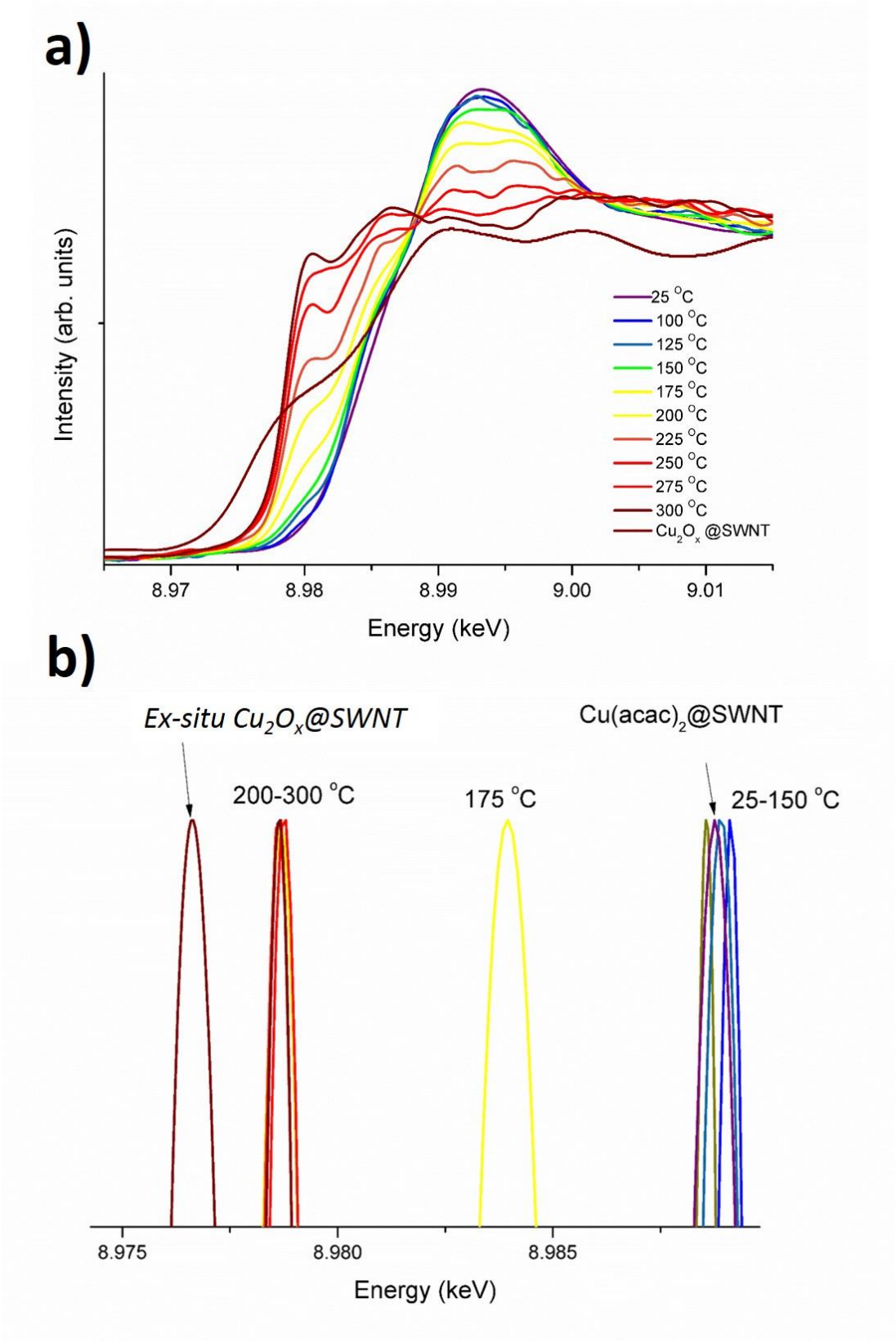


Figure 5.7: The specta from figure 5.6, zoomed in to show how the position of the edge changes as a function of temperature. There is a significant decrease in the position of the edge (*ca.* 5 eV) at 175 ºC, which is depicted by the first derivatives of each edge (b).

As shown by the first derivative plots of each spectrum (figure 5.7 b), the position of the edge decreased after 175 ^{o}C. The values before 175 ^{o}C are typical of that of Cu(acac)$_2$@SWNT, whereas the data obtained at higher temperatures is more indicative of the formation of a reduced copper species, and is similar to that of Cu-$_2$O$_x$@SWNT formed *ex-situ*. Figure 5.8 shows how the energy of the Cu edge varies as a function of temperature, with the energy positions of Cu$_2$O$_x$@SWNT formed *ex-situ* and monitored at 25 ^{o}C and 300 ^{o}C shown for reference (red squares).

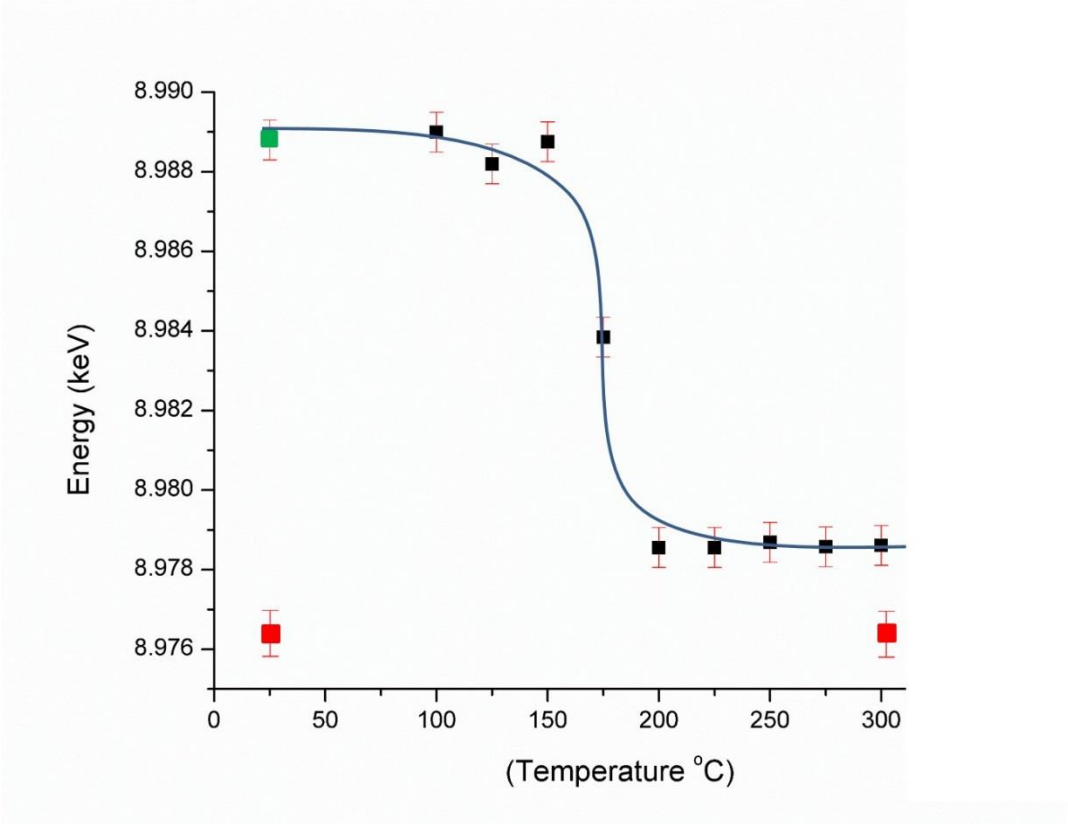


Figure 5.8: A plot showing how the energy of the copper K edge in Cu(acac)$_2$@SWNT changes as a function of temperature. Between the starting temperature of 25 ^{o}C (green square) and 150 ^{o}C the edge energy remains around 8.988 keV, followed by a significant decrease in the edge energy around 175 ^{o}C. After 200 ^{o}C the position of the edge stabilises at around 8.9784 keV, which is a similar energy to the edge positions of Cu$_2$O$_x$@SWNT formed *ex-situ* (red squares).

Since the heat dependent FD-XAS showed that a significant decrease in the edge energy occurs around 175 ^{o}C, an additional sample of Cu(acac)$_2$@SWNT was

prepared and heated at 175 ^{o}C for 1 hr and the edge energy constantly monitored (figure 5.9 a). The energy the edges were compared to the edge of $Cu(acac)_2$ at 25 ^{o}C (green square) and Cu_2O_x@SWNT formed *ex-situ* (red line figure 5.9 a). It is important to note that as a control, Cu_2O_x@SWNT formed *ex-situ* was monitored at both 25 ^{o}C and 300 ^{o}C to ascertain whether the edge is affected by temperature change, and no change was observed, and consequently is assumed to remain constant with temperature. It was envisaged that holding the sample at a temperature around the experimentally obtained transition point should allow for a very gradual change to be observed. After the first spectrum was recorded at 175 ^{o}C, a process which took 8 min, a decrease of 8 eV in the edge energy was observed, and after prolonged heating no further change was observed.

Monitoring how the edge energy changes when held around the temperature of formation allowed for detailed kinetic behaviour to be observed. By comparing how close the values obtained were when $Cu(acac)_2$@SWNT was held at 175 ^{o}C, to $Cu(acac)_2$ at 25 ^{o}C and Cu_2O_x@SWNT formed *ex-situ*, it is possible to evaluate how far the reaction has completed. If the edge obtained for Cu_2O_x@SWNT (8.9763 keV) represents 100% conversion, and the values for the edge of $Cu(acac)_2$@SWNT obtained at 25 ^{o}C represents 0% conversion, the first value obtained from heating $Cu(acac)_2$@SWNT to 175 ^{o}C (*ca.* 8.9784 keV) represents 80% conversion, and the subsequent energies also hover around this point, implying no further reaction at 175 ^{o}C (figure 5.9 b). Therefore the rate of transformation is too fast and takes place on a time scale quicker than FD-XAS measurements.

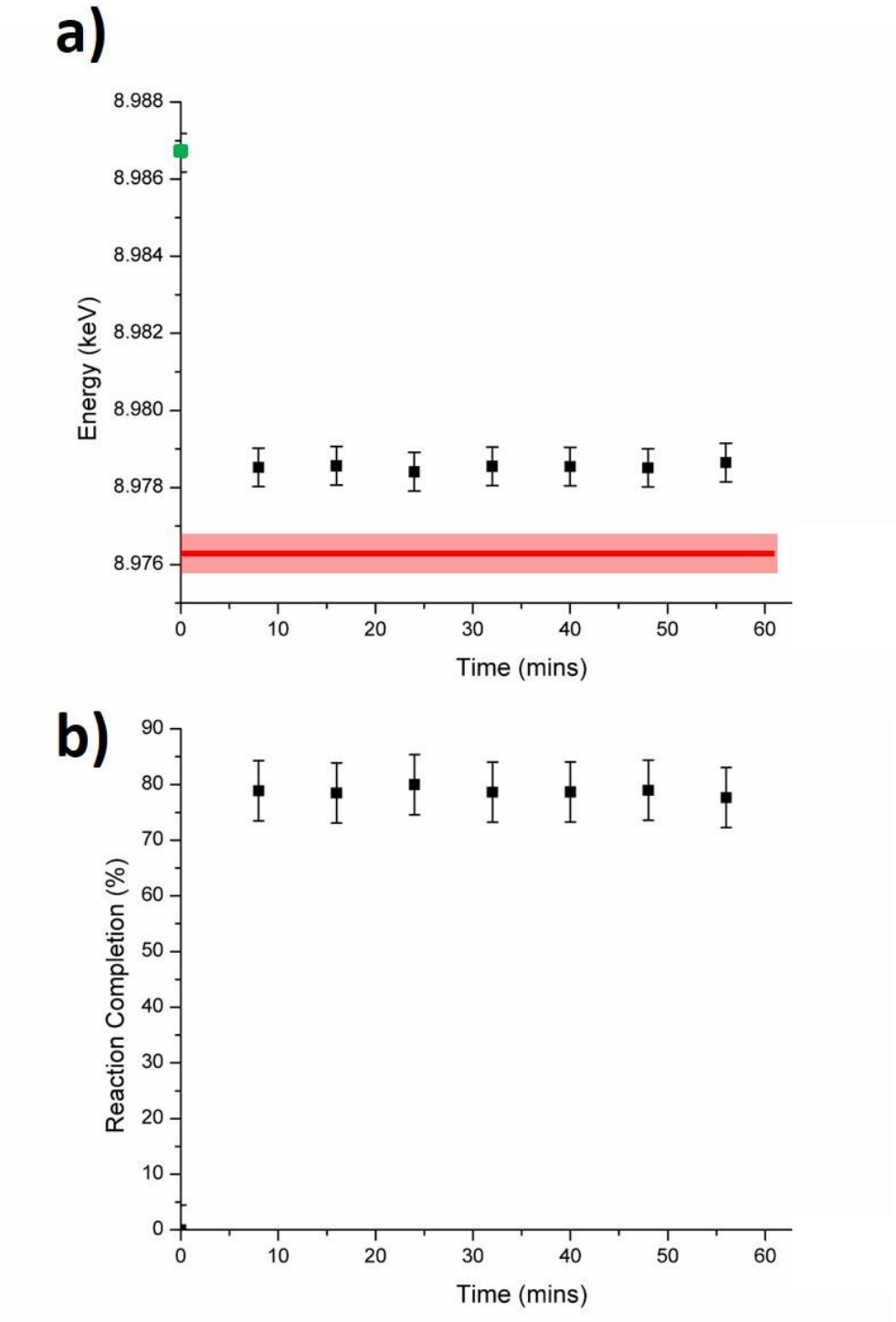


Figure 5.9: a) A plot showing how the edge energy changes when $Cu(acac)_2$@SWNT is heated at 175 ºC for 1 hr. Initially there is a decrease (8 eV) from that of $Cu(acac)_2$@SWNT at 25 ºC (green square), but over time, there is no significant difference at 175 ºC, and all values remain within 0.3 eV of each other. The edge energy of Cu_2O_x@SWNT formed *ex-situ* is shown for comparison (red line); b) A plot showing the reaction completion of $Cu(acac)_2$@SWNT to Cu_2O_x@SWNT as a function of time. After heating

$Cu(acac)_2$@SWNT from 25 ºC to 175 ºC, the reaction rapidly takes place and a rate of 80% conversion to Cu_2O_x@SWNT is observed.

$Cu(acac)_2$@SWNT has been heated to form Cu_2O_x@SWNT, and the changes monitored using FD-XAS. It has been shown that the transition occurs rapidly at around 175 ^oC which is a significantly lower temperature than that for bulk $Cu(acac)_2$ which shows that encapsulation within the hollow channel of the SWNT lowers the activation energy (E_a) needed for the reaction.[26] By comparing data obtained from the FD-XAS of $Cu(acac)_2$@SWNT with bulk $Cu(acac)_2$, a decrease of electron density on the copper is observed upon encapsulation which is caused by the Cu-O bonds being polarised which weakens the bonding and subsequently lowers the energy required. Confinement into a SWNT lowers the activation barrier of transformations since van der Waals interactions polarising the bonds reduce the bond enthalpy (figure 5.10), and so less energy is required to transform $Cu(acac)_2$@SWNT into Cu_2O_x@SWNT.[27]

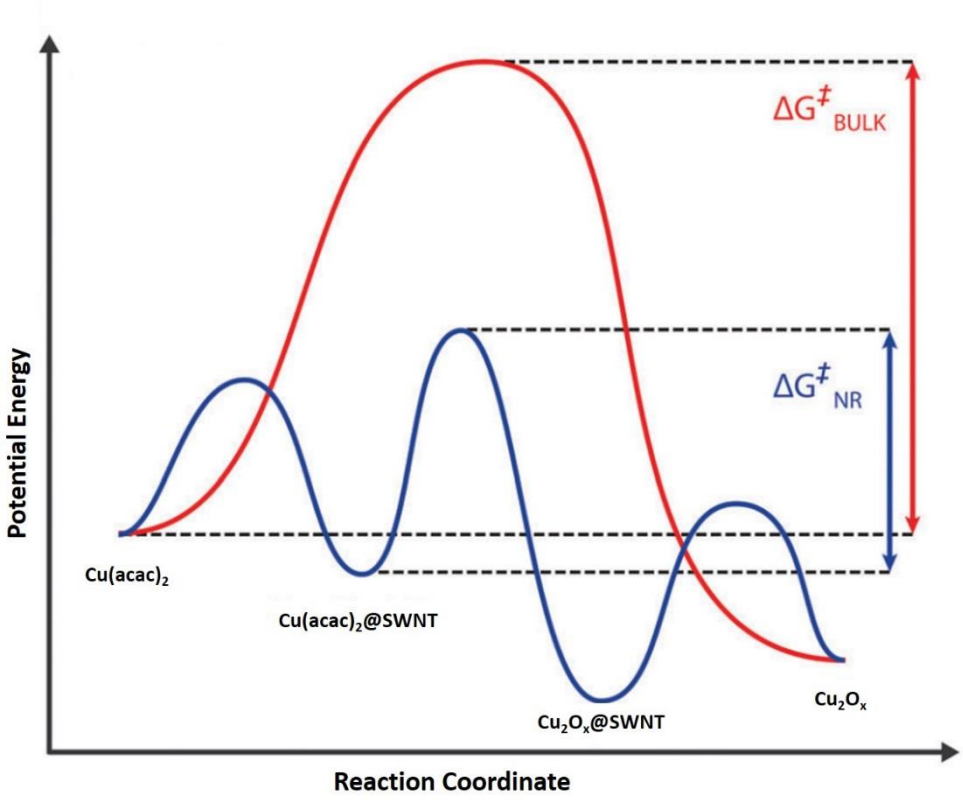
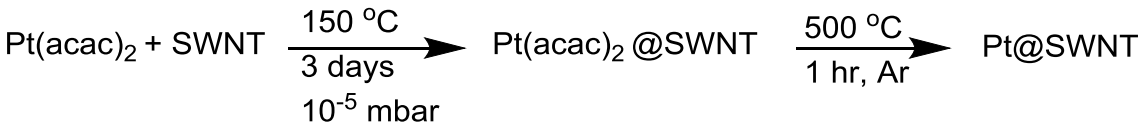


Figure 5.10: A reaction energy profile hypothetically comparing the formation of Cu_2O_x@SWNT from $Cu(acac)_2$@SWNT. Although there are more stages due to the necessary encapsulation and release of products, the stabilisation of the transition state *via* van der Waals forces can reduce the activation energy necessary for the reaction to proceed. Adapted from Miners *et al.*, 2016.[28]

$Cu(acac)_2$@SWNT was further heated to 500 ^oC to completely replicate the *ex-situ* experiment, and the position of the copper K edge was monitored; however, no further change in the shape of the edge, or position was found to occur, and so the energy of the edge and shape of the spectrum never fully reaches the position for Cu_2O_x@SWNT formed *ex-situ*. This could be caused by the ability of the nanotube to stabilise the charge of the formed species, *i.e.* it is possible that this sample has a higher loading of material that the sample formed *ex-situ*, and so the nanotube is physically unable to transfer anymore charge, therefore this needs to be investigated further.

5.2.2 Transformation of $Pt(acac)_2$@SWNT to Pt@SWNT

In addition to copper, platinum has attracted significant interest due to its applications in catalysis and sensing.[4, 29-31] However, unlike $Cu(acac)_2$@SWNT, when $Pt(acac)_2$@SWNT is heated to 500 ^oC in an inert atmosphere, platinum nanoparticles form, with no oxide present (Chapter III, Scheme 5.2).



Scheme 5.2: The formation of Pt@SWNT from the encapsulation and subsequent heating of $Pt(acac)_2$.

AC-HRTEM analysis of $Pt(acac)_2$@SWNT shows discrete clusters of complex (figure 5.11 a). Upon heating the sample at 500 ^oC, the volatile acetylacetonate ligands are removed from the platinum, leading to the formation of a metallic structure (figure 5.11 b).

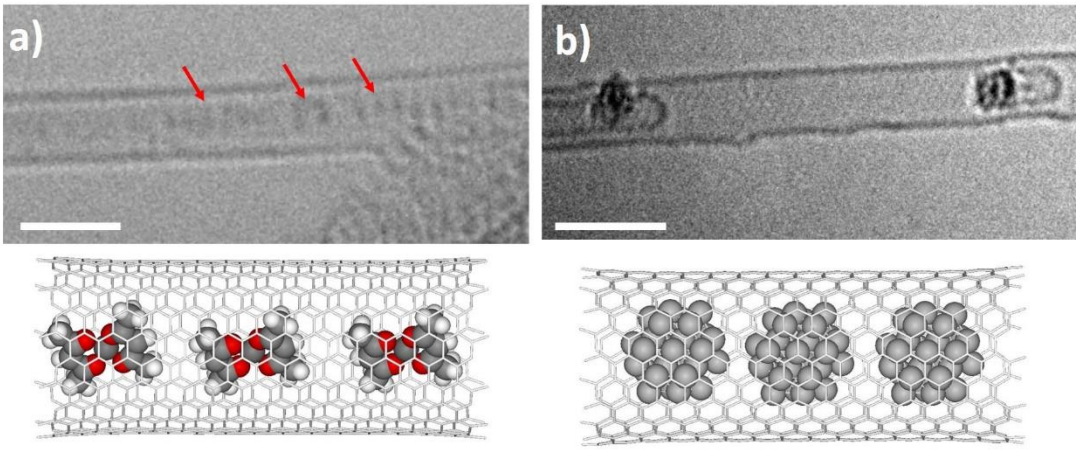


Figure 5.11: AC-HRTEM images of a) $Pt(acac)_2$@SWNT, the red arrows show the platinum atoms, and b) Pt@SWNT. The scale bars are 2 nm. Below each AC-HRTEM image is a geometry optimised model of each structure in a (10,10) SWNT.

Raman spectroscopy has been performed on $Pt(acac)_2$@SWNTs and Pt@SWNT (figure 5.12), with attention being placed on the G band of the structures, relative to

empty SWNTs. Whilst there is only a negligible change in the position of the G band upon the encapsulation of $Pt(acac)_2$, upon thermal decomposition to Pt@SWNT, the G band red shifts by 4 cm^{-1} which is indicative of an electron transfer from the Pt to the SWNT, which is opposite to the shift observed for Cu_2O_x@SWNT.

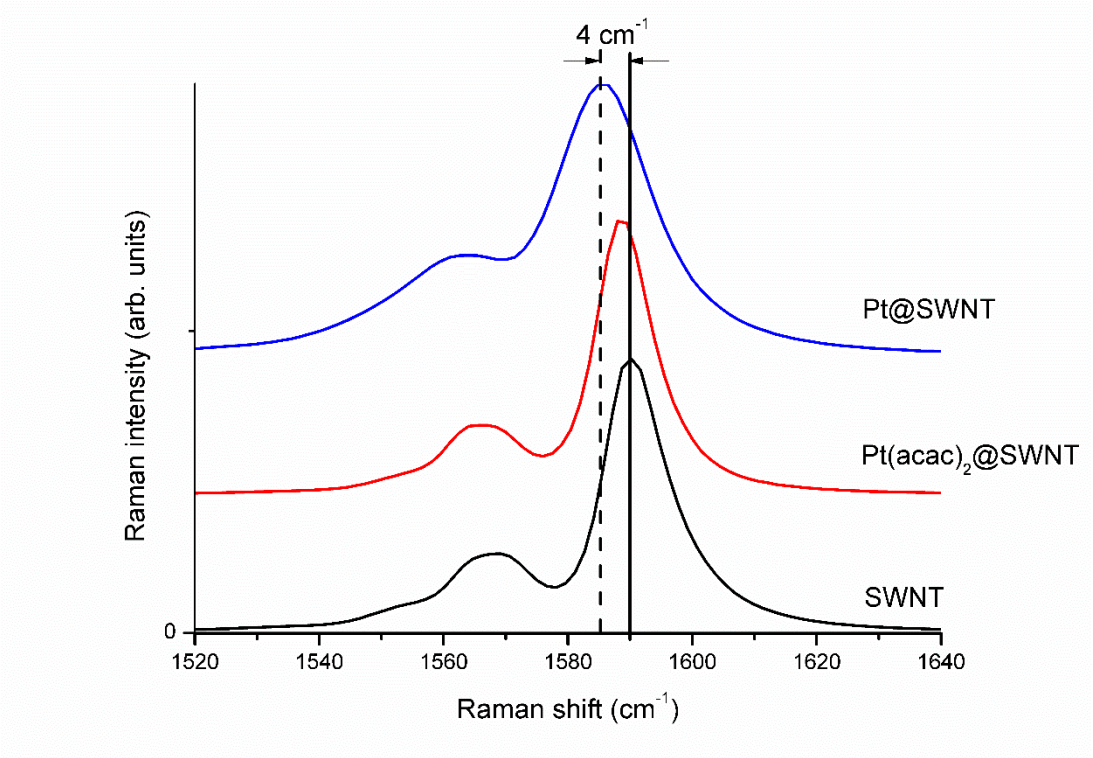


Figure 5.12: Normalised Raman spectra showing how the G band of the nanotube shifts depending on the encapsulated material. The encapsulation of $Pt(acac)_2$@SWNT leads to a negligible change in the position in the G band of the SWNT compared to empty SWNTs, and upon thermal decomposition the position of the G band decreases more significantly (4 cm^{-1}).

There is an increase in the energy of the platinum L_{III} edge of $Pt(acac)_2$ upon its encapsulation into SWNTs which is similar to the increase in the copper K edge observed upon encapsulation of $Cu(acac)_2$@SWNT. An increase of 1.48 eV occurs (table 5.2), which although seems small is significant given the small standard deviations of each sample. Again, this increase in edge energy, complimented by no

change in the G band of the SWNT being observed in Raman, is attributed to the SWNT polarising the Pt-O bonds in the $Pt(acac)_2$ complex (figure 5.13).

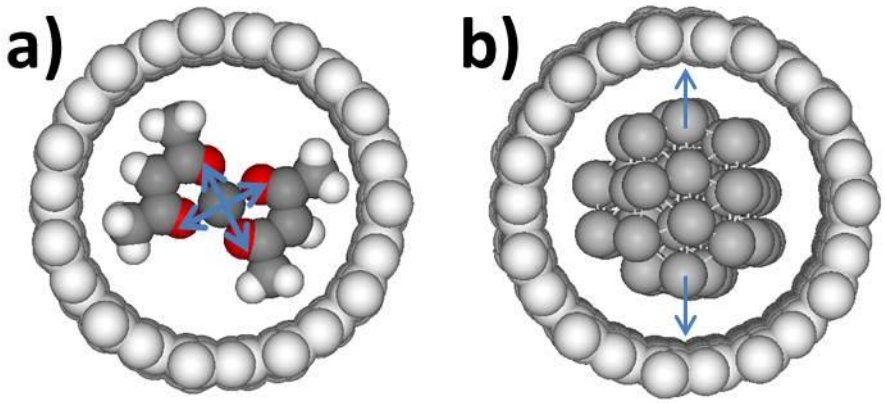


Figure 5.13: models of $Pt(acac)_2$@SWNT (a) and Pt@SWNT (b) showing electron transfers taking place within the materials (blue arrow depicts flow of electron charge). For $Pt(acac)_2$@SWNT electron density is being shifted from the platinum atom to oxygen atoms which results in the polarisation of the bonds, whereas for Pt@SWNT, electron density is being transferred from the platinum to the carbon atoms of the nanotube wall.

Table 5.2: Platinum L_{III} edge energy of $Pt(acac)_2$, $Pt(acac)_2$@SWNT and Pt@SWNT, compared to known standards and relative to Pt metal.

Sample	Formal Pt oxidation state	Pt L_{III} edge (eV)	Energy difference from Pt (eV)
Pt	0	11554.98 ± 0.239	0
$Pt(acac)_2$	2	11556.08 ± 0.045	1.10
Pt@SWNT	0	11556.24 ± 0.002	1.26
PtI_2	2	11556.99 ± 0.050	2.01
$Pt(acac)_2$@SWNT	2	11557.56 ± 0.021	2.58

Upon thermal decomposition to form Pt@SWNT, the edge energy decreases by *ca.* 1.32 eV to 11556.24 eV (figure 5.14), which, again, although much smaller than the change which occurred for the copper K edge, is significant given the standard deviation for each material. Although the formation of platinum leads to a decrease in the edge energy, it is still significantly higher (1.26 eV) than the edge of bulk platinum which suggests a decrease of electron density on the platinum. This is complimented by the Raman data which shows a decrease in the G band suggesting charge has been transferred from platinum to the SWNT. Such electron transfers from encapsulated MNPs to SWNT are not uncommon, and have been reported for many encapsulated metal nanoparticles such as europium and erbium.[32, 33]

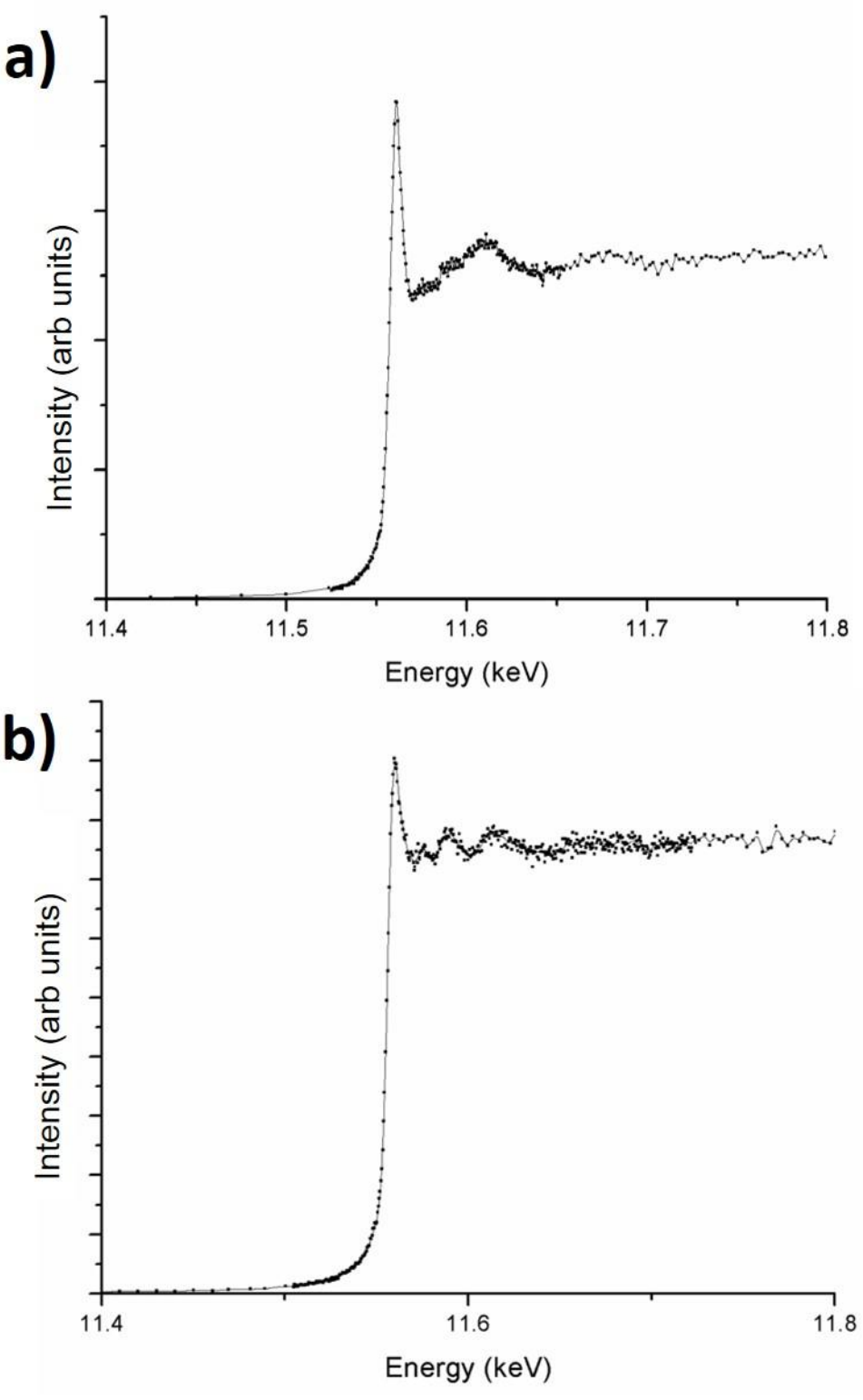


Figure 5.14: Normalised FD-XAS of (a) $Pt(acac)_2$@SWNT and Pt@SWNT (b). Both samples were recorded at room temperature, and there is a decrease in the position of the platinum L_{III} edge after thermal decomposition

5.2.2.1 Attempted Monitoring of the Shift with *in-situ* Heating

In a similar method to the investigation of $Cu(acac)_2$@SWNT, $Pt(acac)_2$@SWNT was heated up from 100 ^oC to 350 ^oC in an inert atmosphere. An FD-XAS was recorded at 25 ^oC intervals, and the platinum edge energy monitored at these temperatures, with the whole heating taking approximately 2 hr (figure 5.15). Similarly to the *in-situ* heating of $Cu(acac)_2$@SWNT, the edge generally decreases; however, not as sharply.

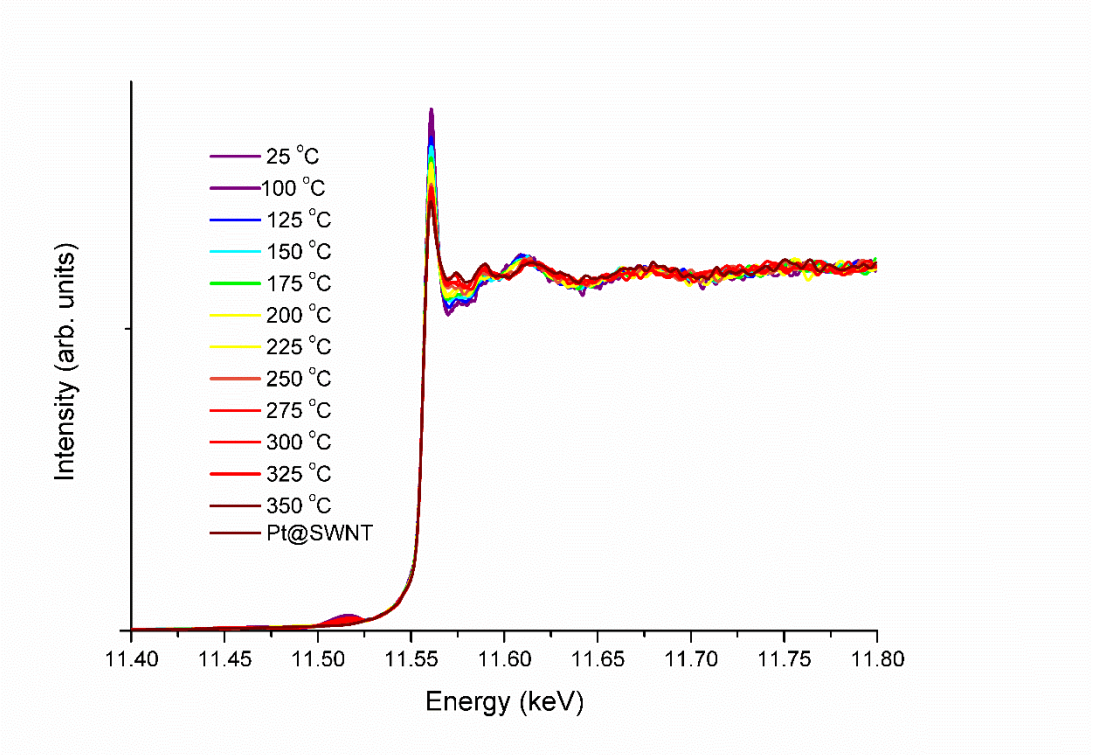


Figure 5.15: FD-XAS obtained for $Pt(acac)_2$@SWNT at 25 ^oC (purple line), then heated to 100 ^oC (blue) followed by subsequent heating at 25 ^oC intervals. As the temperature increases, the morphology of each spectra changes, and gradually appears to resemble that of Pt@SWNT formed *ex-situ*.

Although the position of the edge inflections are all quite similar in value (figure 5.16 a), the first derivative has been taken of each edge (figure 5.16 b) and these show a gradual decrease in the position of the edge.

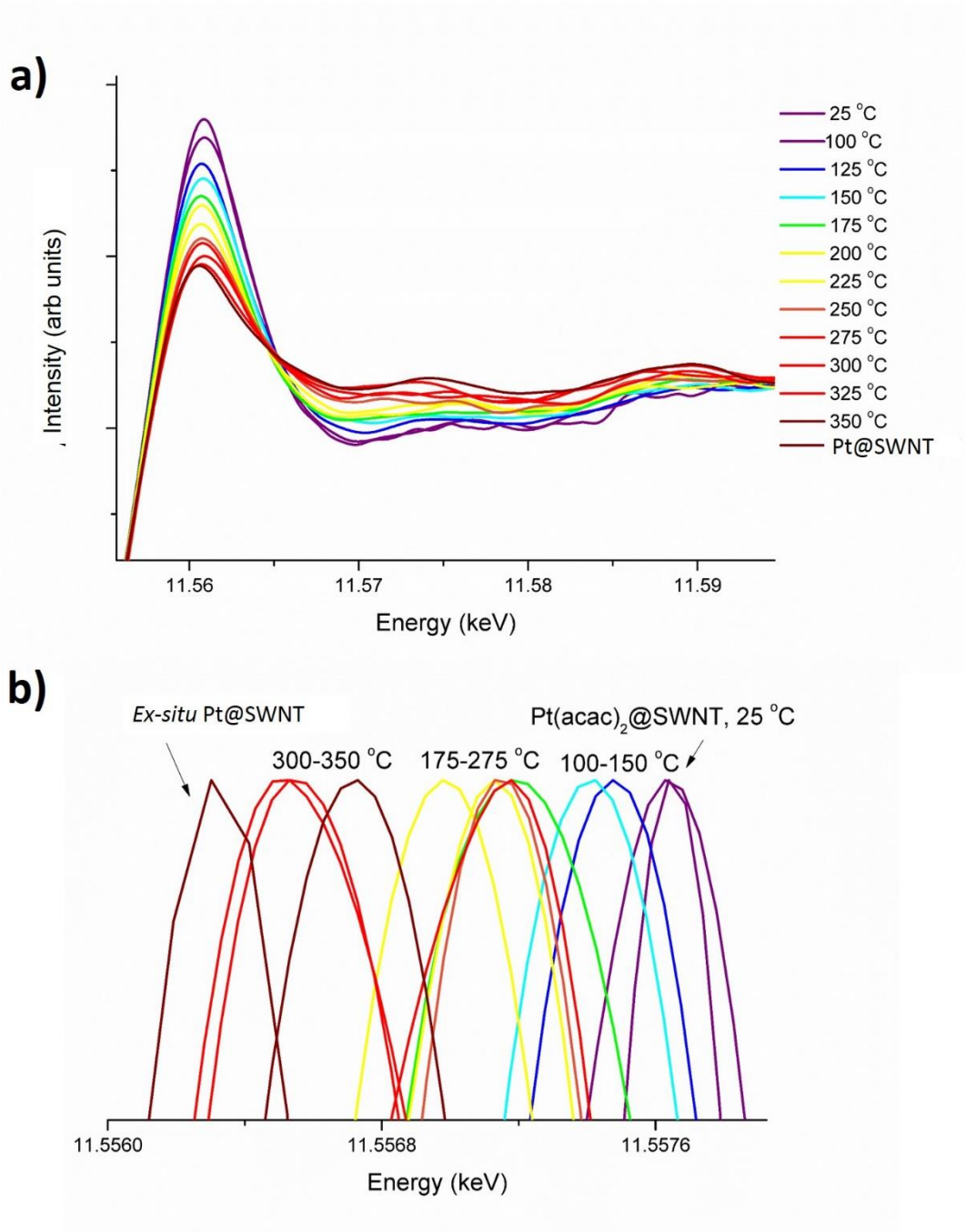


Figure 5.16: The Pt L_{III} edge of FD-XAS spectra of $Pt(acac)_2$@SWNT heated from 100 °C to 350 °C at 25 °C intervals. $Pt(acac)_2$@SWNT at room temperature and Pt@SWNT formed *ex-situ* are shown for comparison. There is a decrease of *ca.* 1 eV in the edge of $Pt(acac)_2$@SWNT upon heating, as shown in the first derivatives of each spectrum (b).

In contrast to the heating of $Cu(acac)_2$@SWNT, the change in the edge energy as a function of temperature is much more gradual (figure 5.17). The energy remains constant at 100 °C, decreases linearly between 100 and 175 °C, then remains

constantly around 11557.0 keV before decreasing further after 275 ºC. Eventually, the edge approaches that of Pt@SWNT formed *ex-situ*, 11556.24 eV, as shown by the red squares.

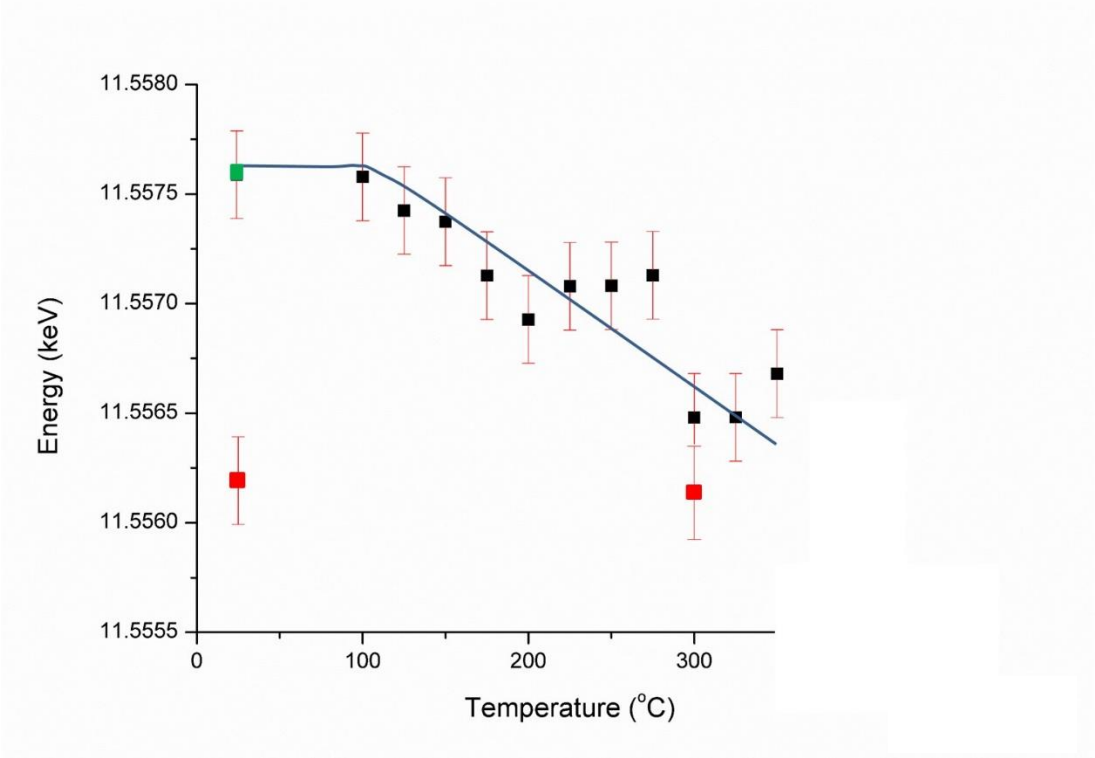


Figure 5.17: A plot showing how the Pt L_{III} edge of $Pt(acac)_2$@SWNT decreases as a function of temperature. At 100 ºC the edge is similar to that of $Pt(acac)_2$@SWNT at room temperature, however with heating the edge decreases. Overall there is a decrease of *ca.* 1.3 eV which is indicative of the platinum L_{III} edge of Pt@SWNT formed *ex-situ*. The edge energies of Pt@SWNT obtained statically at 25 ºC and 350 ºC are shown for reference (red squares).

Similarly to the decomposition of $Cu(acac)_2$@SWNT, there is a decrease in the edge energy position (1.4 eV) upon heating, which is comparable to the difference observed between $Pt(acac)_2$@SWNT and Pt@SWNT measured statically. In the same way as the investigation into $Cu(acac)_2$@SWNT, a new sample of $Pt(acac)_2$@SWNT was prepared and held at 175 ºC for 1 hr. FD-XAS measurements each took 10 min to complete, and were constantly obtained throughout, with the edge energy monitored as a function of time (figure 5.18 a). In contrast to $Cu(acac)_2$@SWNT where there was a sharp decrease in the edge energy during the first 10 min, with

Pt(acac)$_2$@SWNT, there is a slight decrease in the edge energy over time when held at 175 ^{o}C. Additionally, kinetic behaviour can be monitored by examining the value of the edge at 175 ^{o}C compared to Pt(acac)$_2$@SWNT at 25 ^{o}C and Pt@SWNT formed *ex-situ*. After initially heating the sample, the edge energy suggests a conversion of *ca.* 50%, which slowly increases over time (figure 5.18 b).

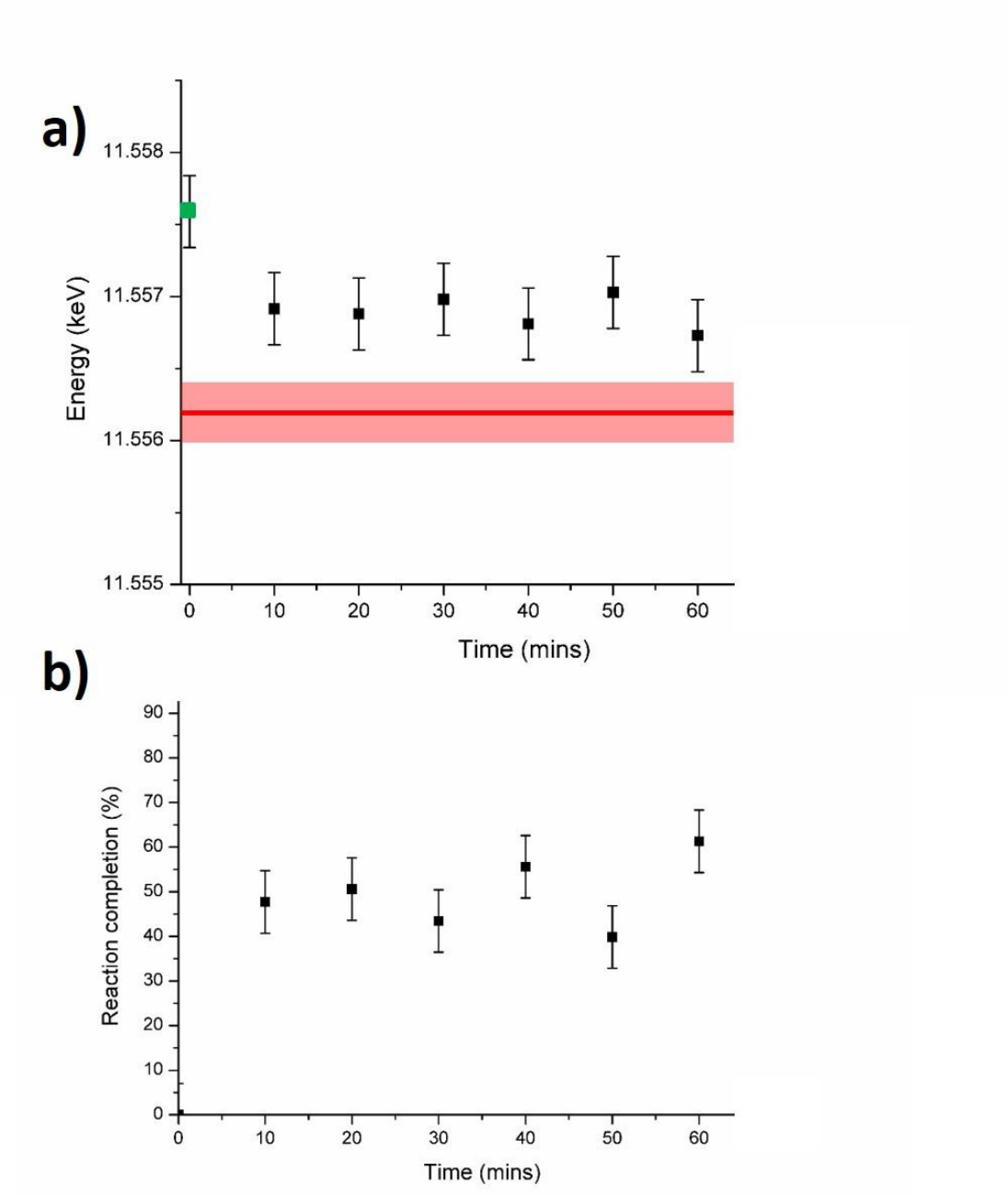


Figure 5.18: a) A plot showing how the edge energy changes when held at 175 ^{o}C for a set amount of time, and compared to Pt(acac)$_2$@SWNT at 25 ^{o}C (green

square) and Pt@SWNT (red line). There is a slight decrease in the edge energy over time; b) A plot showing how Pt(acac)$_2$@SWNT to Pt@SWNT as a function of time, as calculated by monitoring the position of the Pt L_{III} edge of the sample at 175 ^oC.

Similarly to the transformation of Cu(acac)$_2$@SWNT, it has been demonstrated that Pt(acac)$_2$@SWNT can be heated to form a new material, with FD-XAS being an appropriate method to analyse the system *in-situ*. In the same way to copper, the transformation has been showed to occur at a much lower temperature than observed in bulk Pt(acac)$_2$, as free Pt(acac)$_2$ decomposes at around 280 ^oC.[34] Again, this can be attributed to the polarisation of the Pt-O bond as caused by the nanotube. Unlike the transformation of Cu(acac)$_2$@SWNT to Cu_2O_x@SWNT, the formation of Pt@SWNT from Pt(acac)$_2$@SWNT has a few significant differences, the most striking being that there is only 1.32 eV difference between the edges of encapsulated Pt and Pt(acac)$_2$, compared to 12 eV between Cu(acac)$_2$@SWNT and Cu_2O_x@SWNT but this can be attributed to the nature of the platinum L_{III} edge compared to the copper K edge. Additionally, the transition appears much less defined as there is only a gradual decrease in the edge energy and not a sharp drop around 175 ^oC which was observed with copper. Unlike the transformation of Cu(acac)$_2$@SWNT, heating Pt(acac)$_2$@SWNT at 175 ^oC only leads to *ca.* 50% transformation, and even after heating for 1 hr no significant change was observed which shows that a higher temperature is needed to achieve full decomposition.

5.3 Conclusion

FD-XAS has been used to monitor how the oxidation state of the metals in both Pt(acac)$_2$@SWNT and Cu(acac)$_2$@SWNT change upon heating. Whilst only preliminary, the results of this investigation provide a solid basis for investigating transformations inside SWNTs, since clear quantifiable trends are shown

spectroscopically. The changes in edge energy, and therefore oxidation states of the metal centres occur rapidly, and a majority of both of the materials was converted within the first 10 min at 175 ^{o}C. This shows a dramatic decrease in the decomposition temperatures of both the acetylacetonate complexes when confined into SWNTs, and can be attributed to polarisation of the M-O bonds which lowers the E_a for bond dissociation. Complimentary use of Raman spectroscopy and FD-XAS supports this hypothesis, as polarisation of the encapsulated complexes upon encapsulation is shown, but no electron transfers to the host nanotube is observed.

In order to fully ascertain whether Cu(acac)$_2$@SWNT heated gradually up to 500 ^{o}C produces the same material as produced *ex-situ*, detailed AC-HRTEM images of the products formed from *in-situ* heating are required, and monitoring the transformation *in-situ* by Raman could also prove to be enthralling in revealing what has occurred to the sample. Additionally, since the edge energy of Pt(acac)$_2$@SWNT never fully reached the position of Pt@SWNTs, further analysis of this is also required.

It has been shown that the temperature for MNP formation from metallic precursors is much lower than previously thought, which has profound implications on the conditions required to transform materials in nanotubes and could possibly lead to a paradigm shift in the field of nanomaterials synthesis within carbon nanoreactors.

5.4 Experimental

Pt(acac)$_2$@SWNT (M = Pt, Cu) were prepared as previously explained in Chapters II and III.

5.4.1 Fluorescence-Detected X-ray Absorption Spectroscopy (FD-XAS)

All static-temperature FD-XAS measurements were carried out on the XMaS beamline (BM28) and SpLine (BM25a) at the ESRF. Samples were deposited onto carbon tape, which was then mounted onto a stainless steel sample holder. FD-XAS edge inflection points were obtained by fitting a smoothing spline to the measured spectrum, using Matlab, and taking the first derivative of the fitted spectrum.

In-situ experiments were performed on the SpLine (BM25a) at the ESRF. $M(acac)_2$@SWNT (5 mg) was placed in a glass capillary tube and held in position (figure 5.5 a.1). The tube was placed within an aluminium frame, sealed, placed in position above a heater (figure 5.5 a.4) and attached to a helium source (in figure 5.5 a2, out figure 5.5 a3, flow rate *ca.* 30 mL/min). Prior to all experiments, the system was purged with helium for 15 min to ensure all air was removed from the capillary tube. Finally, the system was heated rapidly (at a rate of 50 ^{o}C/s) and spectra recorded.

5.4.2 Electron Microscopy

SWNTs filled with the encapsulated materials were dispersed in propan-2-ol using an ultrasonic bath and drop cast onto lacey carbon-coated copper TEM grids (Agar). HR-TEM imaging was carried out on a JEOL 2100 FEG-TEM microscope operated at 200 kV. Aberration-corrected HR-TEM was performed at the University of Ulm on a C_s corrected FEI Titan 80-300 TEM operated at 80 kV with information limit enhancement using reduced extraction voltage. All images were processed using Gatan Digital Micrograph, and the quoted distances were measured by drawing a line profile and measuring the electron intensity.

5.4.3 Raman Spectroscopy

Raman spectroscopy was performed using a HORIBA Jobin Yvon LabRAM HR spectrometer equipped with an automated *xyz* stage (Märzhäuser). Spectra were acquired using a 532 nm laser at 0.2mW power, in the range 50 to 4000 cm^{-1}, with 5 seconds and 8 accumulations per spectral window, using a 50× objective and a 300 μm confocal pinhole. To simultaneously scan a range of Raman shifts, a 600 lines/mm rotatable diffraction grating along a path length of 800 mm was employed. Spectra were detected using a SYNAPSE CCD detector (1024 pixels) thermoelectrically cooled to −60 °C. Before the spectra collection, the instrument was calibrated using the Rayleigh line at 0 cm^{-1} and a standard Si(100) reference band at 520.7 cm^{-1}.

5.5 References

1. L. M. de la Rosa-Romo, M. T. Oropeza-Guzman, A. Olivas-Sarabia and G. Pina-Luis, *Sens. Actuator B-Chem.*, 2016, **233**, 459.
2. Y. Y. Liang, H. L. Wang, P. Diao, W. Chang, G. S. Hong, Y. G. Li, M. Gong, L. M. Xie, J. G. Zhou, J. Wang, T. Z. Regier, F. Wei and H. J. Dai, *J. Am. Chem. Soc.*, 2012, **134**, 15849.
3. V. M. Aroutiounian, *Lith. J. Phys.*, 2015, **55**, 319.
4. S. Palanisamy, H. F. Lee, S. M. Chen and B. Thirumalraj, *RSC Adv.*, 2015, **5**, 105567.
5. V. H. Crespi, N. G. Chopra, M. L. Cohen, A. Zettl and S. G. Louie, *Phys. Rev. B*, 1996, **54**, 5927.
6. T. Susi, J. Kotakoski, R. Arenal, S. Kurasch, H. Jiang, V. Skakalova, O. Stephan, A. V. Krasheninnikov, E. I. Kauppinen, U. Kaiser and J. C. Meyer, *ACS Nano*, 2012, **6**, 8837.
7. J. C. Meyer, F. Eder, S. Kurasch, V. Skakalova, J. Kotakoski, H. J. Park, S. Roth, A. Chuvilin, S. Eyhusen, G. Benner, A. V. Krasheninnikov and U. Kaiser, *Phys. Rev. Lett.*, 2012, **108**.
8. F. Zhang, F. Jiao, X. L. Pan, K. Gao, J. P. Xiao, S. Zhang and X. H. Bao, *ACS Catal.*, 2015, **5**, 1381.
9. D. Friebel, V. Viswanathan, D. J. Miller, T. Anniyev, H. Ogasawara, A. H. Larsen, C. P. O'Grady, J. K. Norskov and A. Nilsson, *J. Am. Chem. Soc.*, 2012, **134**, 9664.
10. H. G. Manyar, R. Morgan, K. Morgan, B. Yang, P. Hu, J. Szlachetko, J. Sa and C. Hardacre, *Catal. Sci. Tech.*, 2013, **3**, 1497.
11. T. Yao, Z. H. Sun, Y. Y. Li, Z. Y. Pan, H. Wei, Y. Xie, M. Nomura, Y. Niwa, W. S. Yan, Z. Y. Wu, Y. Jiang, Q. H. Liu and S. Q. Wei, *J. Am. Chem. Soc.*, 2010, **132**, 7696.

12. J. Ohyama, K. Teramura, T. Shishido, Y. Hitomi, K. Kato, H. Tanida, T. Uruga and T. Tanaka, *Chem. Phys. Lett.*, 2011, **507**, 105.
13. F. L. Jiang, C. Li, H. Y. Fu, X. J. Guo, G. Z. Wu and S. M. Chen, *PCCP*, 2016, **18**, 19259.
14. A. A. Eliseev, L. V. Yashina, N. I. Verbitskiy, M. M. Brzhezinskaya, M. V. Kharlamova, M. V. Chernysheva, A. V. Lukashin, N. A. Kiselev, A. S. Kumskov, B. Freitag, A. V. Generalov, A. S. Vinogradov, Y. V. Zubavichus, E. Kleimenov and M. Nachtegaal, *Carbon*, 2012, **50**, 4021.
15. M. V. Kharlamova, M. M. Brzhezinskay, A. S. Vinogradov, I. P. Suzdalev, Y. V. Maksimov, V. K. Imshennik, S. V. Novichikhin, A. V. Krestinin, L. V. Yashina, A. V. Lukashin, Y. D. Tret'yakov and A. A. Eliseev, *Nanotechnol. Russ.*, 2009, **4**, 634.
16. N. Thamavaranukup, H. A. Hoppe, L. Ruiz-Gonzalez, P. Costa, J. Sloan, A. Kirkland and M. L. H. Green, *Chem. Commun.*, 2004, 1686.
17. K. Yanagi, Y. Miyata and H. Kataura, *Adv. Mater.*, 2006, **18**, 437.
18. A. Chuvilin, E. Bichoutskaia, M. C. Gimenez-Lopez, T. W. Chamberlain, G. A. Rance, N. Kuganathan, J. Biskupek, U. Kaiser and A. N. Khlobystov, *Nat. Mater.*, 2011, **10**, 687.
19. T. W. Chamberlain, T. Zoberbier, J. Biskupek, A. Botos, U. Kaiser and A. N. Khlobystov, *Chem. Sci.*, 2012, **3**, 1919.
20. T. Zoberbier, T. W. Chamberlain, J. Biskupek, N. Kuganathan, S. Eyhusen, E. Bichoutskaia, U. Kaiser and A. N. Khlobystov, *J. Am. Chem. Soc.*, 2012, **134**, 3073.
21. I. V. Lebedeva, T. W. Chamberlain, A. M. Popov, A. A. Knizhnik, T. Zoberbier, J. Biskupek, U. Kaiser and A. N. Khlobystov, *Nanoscale*, 2014, **6**, 14877.
22. S. J. Guo, X. L. Pan, H. L. Gao, Z. Q. Yang, J. J. Zhao and X. H. Bao, *Chem. Eur. J.*, 2010, **16**, 5379.
23. L. M. Zhang, Z. B. Wang, J. J. Zhang, X. L. Sui, L. Zhao and D. M. Gu, *Carbon*, 2015, **93**, 1050.
24. L. Grigorian, K. A. Williams, S. Fang, G. U. Sumanasekera, A. L. Loper, E. C. Dickey, S. J. Pennycook and P. C. Eklund, *Phys. Rev. Lett.*, 1998, **80**, 5560.
25. A. Botos, J. Biskupek, T. W. Chamberlain, G. A. Rance, C. T. Stoppiello, J. Sloan, Z. Liu, K. Suenaga, U. Kaiser and A. N. Khlobystov, *J. Am. Chem. Soc.*, 2016, **138**, 8175.
26. A. G. Nasibulin, P. P. Ahonen, O. Richard, E. I. Kauppinen and I. S. Altman, *J. Nanopart. Res.*, 2001, **3**, 385.
27. T. S. Koblenz, J. Wassenaar and J. N. H. Reek, *Chem. Soc. Rev.*, 2008, **37**, 247.
28. S. A. Miners, G. A. Rance and A. N. Khlobystov, *Chem. Soc. Rev.*, 2016, **45**, 4727.
29. J. B. Raoof, S. R. Hosseini and S. Rezaee, *J. Mol. Liq.*, 2015, **212**, 767.
30. Z. L. Liu, L. M. Gan, L. Hong, W. X. Chen and J. Y. Lee, *J. Power Sources*, 2005, **139**, 73.
31. D. Zhai, B. Liu, Y. Shi, L. Pan, Y. Wang, W. Li, R. Zhang and G. Yu, *ACS Nano*, 2013, **7**, 3540.
32. R. Nakanishi, R. Kitaura, P. Ayala, H. Shiozawa, K. de Blauwe, P. Hoffmann, D. Choi, Y. Miyata, T. Pichler and H. Shinohara, *Phys. Rev. B*, 2012, **86**.
33. P. Ayala, R. Kitaura, R. Nakanishi, H. Shiozawa, D. Ogawa, P. Hoffmann, H. Shinohara and T. Pichler, *Phys. Rev. B*, 2011, **83**, 085407.

34. S. Flanagan, E. Hall, W. Bowie, J. W. Fuhs, R. Logan, F. Maniei and A. Hunt, *Green Chem.*, 2005, **7**, 333.

Chapter VI: Applications of Metal containing Carbon Nanostructures

6.1 Introduction

Metal nanoparticles (MNPs) have many industrial and biological applications, in areas such as magnetic separation,[1] targeted drug delivery,[2] and data storage.[3, 4] It is becoming vitally important to sense small molecules, especially from a biological perspective, and in a society where diabetes mellitus type II is becoming increasingly prevalent, the attraction of a highly selective and sensitive glucose sensor is clear.[5] This is especially true given that contemporary methods of monitoring blood glucose levels involve disposable strips which contain enzymes that have to be produced by cultivating bacteria, and therefore a more sustainable approach is desired.[6]

Electrochemistry can be employed as a method of sensing small molecules, and is a technique that works by delivering electrons needed for a redox process to proceed in the presence of a catalyst, which are traditionally enzymes. At present, enzymatic based electrochemical sensors are ubiquitous and these dominate the field due to the high selectivity of the enzymes which enables the manufacturing of sensors that can detect infinitesimal quantities of specific molecules.[7] For example, the enzyme glucose oxidase is widely used for the biological sensing of glucose,[8] but unfortunately the lack of enzymatic performance in sub-optimal conditions (such as an extreme pH or temperature) and problems surrounding competitive inhibition remain their biggest disadvantage.[9]

On the other hand, MNPs supported on a surface can be used as an alternative to enzymes for the sensing of small molecules electrocatalytically. Although the action

of each individual electrochemical sensor is unique to the molecule being probed (analyte) and the sensor, a metal centre is present and the sensing mechanism is provided by a catalytic process usually involving a redox couple.[10] Applying a specific potential to a metal containing material can lead to it being oxidised or reduced, which causes a significant change in the current at that particular potential. Metal organic frameworks,[11] and zeolites,[12] are among nanoporous materials which can be employed in the sensing of small molecules and gases, as their intrinsic morphologies enable them to be tailored for the sensing of particular analytes through the tuning of their internal cavity dimensions; although there are drawbacks surrounding the syntheses of such structures, such as low synthetic yield, and thermal instability.[13]

Due to their ability to confine molecules and size selectivity, carbon nanostructures (CNs) may hold the key to producing a highly selective and sensitive non-enzymatic glucose sensor. The nano-sized channels which CNs possess can encapsulate MNPs and protect them from external conditions which would otherwise decrease their efficiency.[14, 15] The deposition of MNPs on CNs for catalytic and sensing applications is highly documented,[16-20] but there are few examples of sensing with materials encapsulated within CNs. The group 10 metals and their oxides were shown to be highly effective for the electrochemical probing of glucose,[21, 22] and so throughout this section, the ability of group 10 metal and metal oxide nanoparticles encapsulated into CNs to detect glucose will be investigated.

The diameter of SWNTs are *ca.* 0.7 – 2 nm and upon encapsulation of molecules and formation of MNPs they act as templates, with the MNPs occupying almost the full width of the SWNT, with a gap of *ca.* 0.3 nm accounting for the van der Waals radii of both host and guest (figure 6.1). This tight fit results in a relatively low surface-

area of interaction between the encapsulated MNPs and a prospective analyte (such as glucose which is shown below as an example), and therefore MNPs@SWNT are not the most suitable material for small molecule sensing, and a wider CN is required.

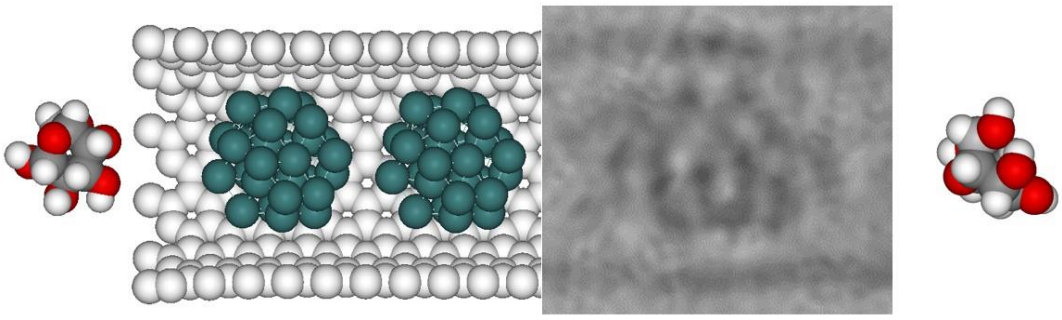


Figure 6.1: Schematic diagram with accompanying AC-HRTEM image showing the size of glucose compared to MNPs@SWNT. In this example, the MNPs are PdNPs, and these effectively block the internal cavity of the SWNT from glucose which restricts contact with PdNPs beyond the first PdNP.

Hollow graphitised carbon nanofibres (GNFs, figure 6.2) are carbon structures which consist of a smooth outer surface but internally contain step-edges of rolled up layers of graphene 2-3 nm high. The internal diameters of GNFs range from 20-150 nm which is significantly wider than SWNTs, and so these step-edges provide favourable, stabilised environments for MNPs to bind, due to an increase in surface area, and therefore increased van der Waals interactions.[15]

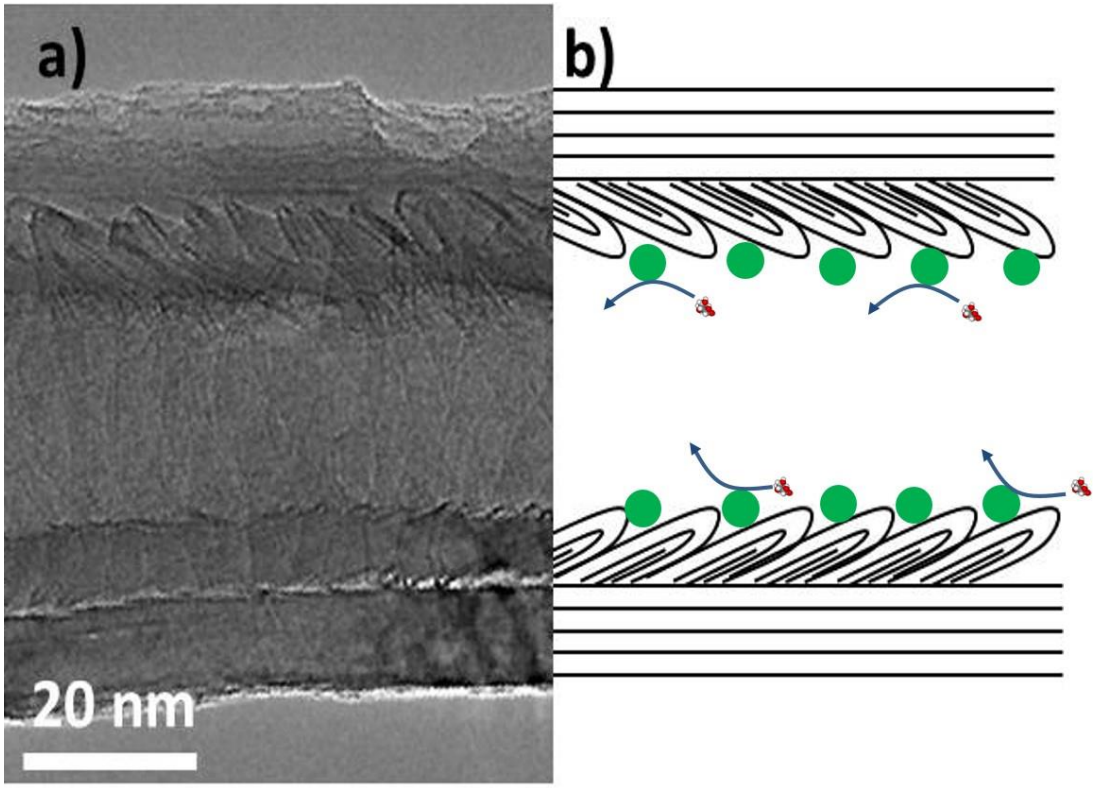


Figure 6.2: A HR-TEM image (a) and model (b) of a hollow graphitised carbon nanofibre (GNF). The hollow cavity with a diameter of *ca.* 50 nm contains step-edges on which small particles can reside (as demonstrated by the green circles). Due to the large diameter of the GNF, glucose molecules (pictured) can readily enter the GNF channel and access many MNPs which are deeper inside the nanostructure.

Herein, the synthesis of group 10 metal nanoparticles and their oxides encapsulated inside GNFs has been reported. All materials have been fully structurally characterised and their sensitivity towards glucose at a range of concentrations has been monitored. This investigation demonstrates an important application for MNPs encapsulated within CNs and could eventually lead to the development of more stable, accurate, ergonomic blood glucose sensors.

6.2 Results and Discussion

6.2.1 MNPs Encapsulated within GNFs

In order to encapsulate MNPs into GNFs, appropriate precursor metal complexes were identified. As an adaptation of the encapsulation of group 10 metal complexes

into SWNTs, (Chapter III), $M(acac)_2$ (M = Pt, Pd) and $Ni(HFacac)_2$, (HFacac = $((F_3CCO)_2CH)^-$) were heated in the presence of GNFs at slightly above their sublimation temperatures under vacuum (see Experimental, section 6.4 for the exact temperatures). The quantity of metal complex used was chosen by calculating the amount of compound required for a 2% metal loading by weight.

Each encapsulated complex was then heated at 500 ^oC under argon for 1 hr, resulting in the loss of the volatile organic ligands and aggregation of metal atoms to form metal nanoparticles in GNFs.

6.2.1.1 Materials Characterisation

High resolution transmission electron microscopy (HR-TEM) has been used to analyse the materials produced (figure 6.3). NiNPs appear as a low contrast material (figure 6.3 a) compared to platinum and palladium which will be discussed later, and have a mean particle size of 4.10 nm. Closer inspection of individual particles (figure 6.3 b) reveals lattice spacing of 0.19 nm, which is consistent with the spacing between the (111) planes of bulk nickel.[23] Additionally, the encapsulation of palladium (figure 6.3 c) led to the formation of slightly larger nanoparticles (mean diameter of 6.63 nm). Furthermore, closer inspection of individual PdNPs revealed a lattice spacing of 0.23 nm (figure 6.3 d) which is consistent of the spacing between the (111) planes of bulk palladium.[24]

As shown previously (Chapter IV), in bright field TEM, the contrast of each material is directly proportional to the square root of the atomic number, Z, which leads to the elements with a larger atomic number having a higher contrast, and consequently, PtNPs appear with very high contrast (figure 6.4 e), and a mean particle size of 5.32 nm is observed.[25] As stated earlier, the step-edges provide a favourable environment

for PtNPs to form on (figure 6.4 f). The particles near the step edge appear to have a lattice spacing of 0.20 nm, which is consistent with the (200) plane spacing observed in bulk platinum.

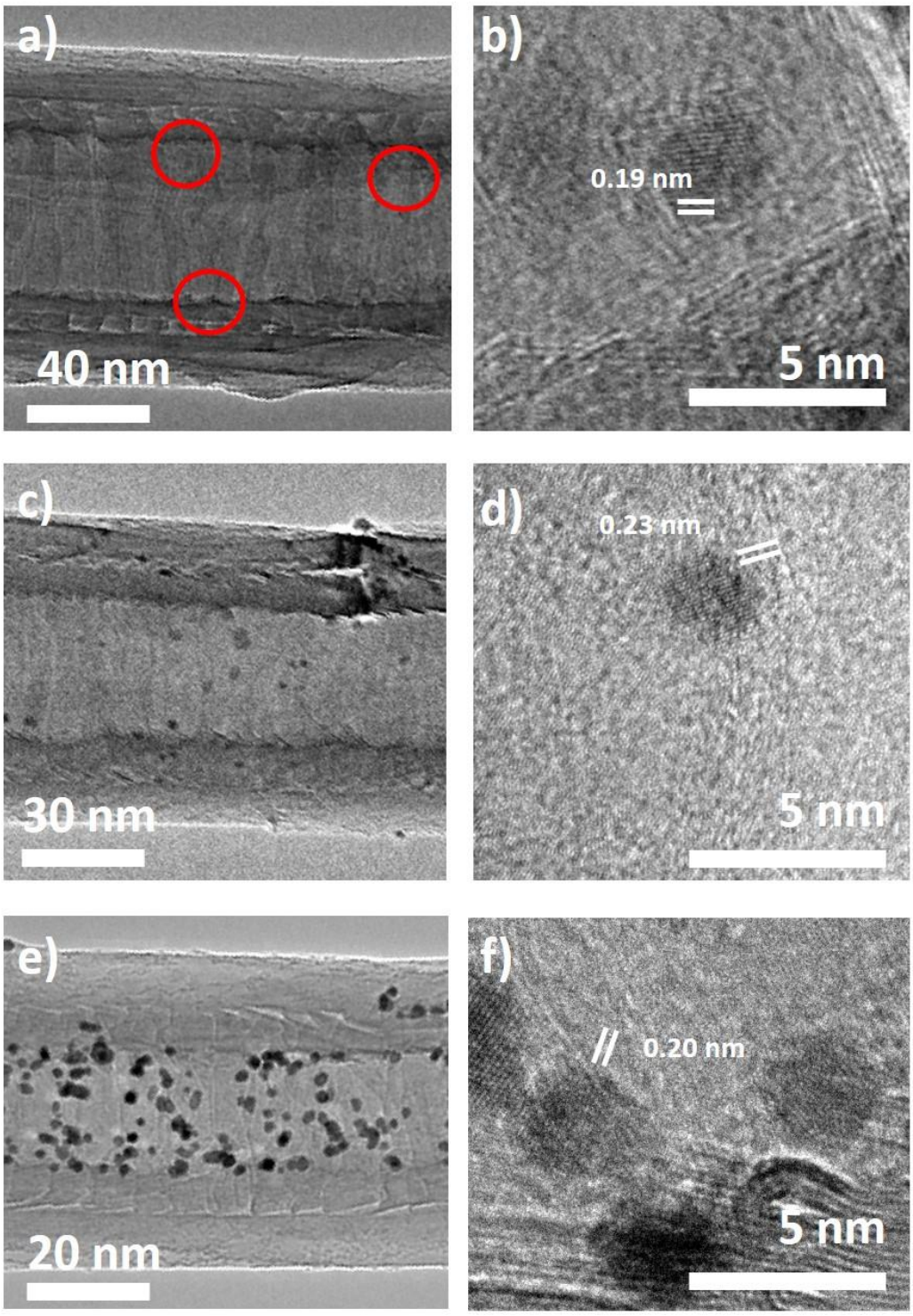


Figure 6.3: HR-TEM images showing (a,b) nickel; (c,d) palladium; and (e,f) platinum encapsulated within GNFs. The contrast of the nanoparticles depends

on the atomic number of the elements present, with platinum appearing the darkest, followed by palladium and nickel. Although each sample was prepared to give a 2% metal loading by weight, a larger amount of platinum appears to have been encapsulated than palladium or nickel.

Despite the quantity of metallic precursor being calculated to allow for precisely 2% loading for each metal into GNFs, it is clear from the TEM images that there is a higher loading of platinum inside the GNFs compared to palladium and nickel in each of their respective samples. Thermogravimetric analysis (TGA, figure 6.4) confirms that the filling rate was higher for platinum (1.9%), than palladium (1.1 %) and nickel (0.9 %).[26]

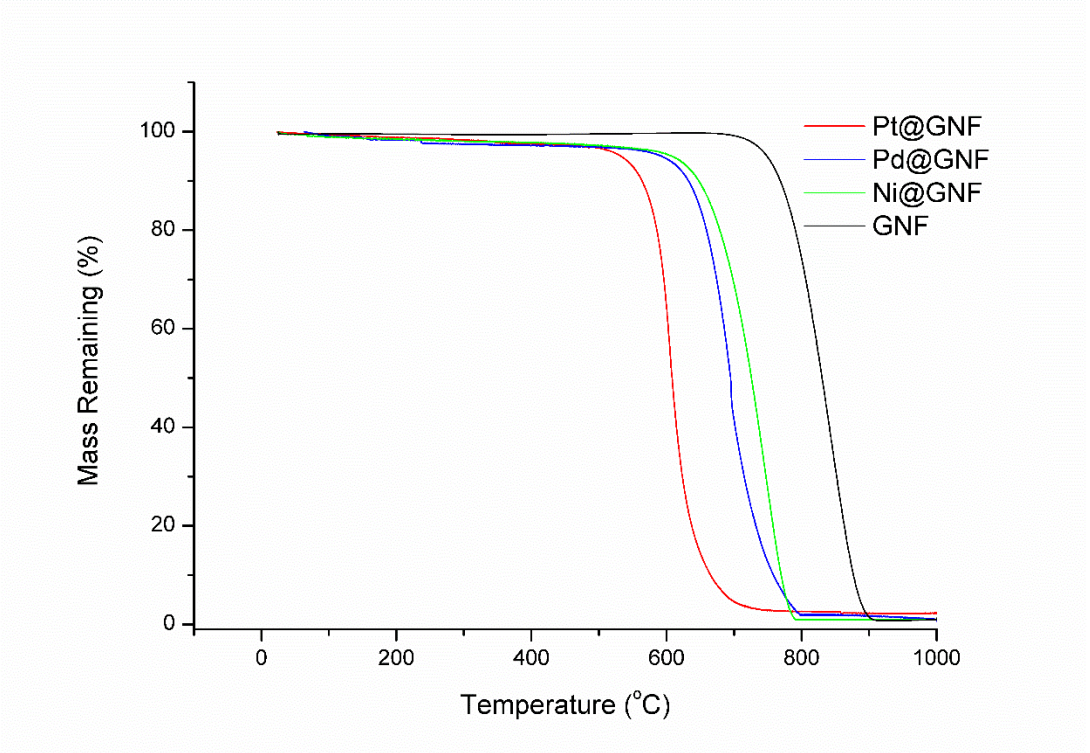


Figure 6.4: TGA of Pt@GNF (red), Pd@GNF (blue) and Ni@GNF (green) compared to an empty GNF (black). TGA confirms the mass of each metal inside GNFs; 0.9% for nickel, 1.1% for palladium and 2% for platinum.

EDX spectroscopy was employed to characterise the materials (figure 6.5 a-c) and confirmed the presence of nickel, palladium and platinum in each of the respective samples. Additionally, powder X-ray diffraction (XRD) proved to be an effective method for characterisation of the samples, as the nature of the GNFs, being highly

ordered, defined structures, yielded characteristic diffraction patterns and the encapsulation of different MNPs leads to the appearance of other peaks corresponding to a particular crystal lattice. The powder XRD data obtained for Ni@GNF (red line, figure 6.5 d) shows no noticeable differences when compared with that of an empty GNF (black line, figure 6.5 d), but this can be attributed to the small size of the NiNPs making them undetectable using powder XRD.[27]

The powder XRD obtained for Pd@GNF also appears very similar to that of empty GNFs, although there is a small peak at 39^{o} which can be attributed to the (111) lattice of palladium (figure 6.5 e),[24] and the weakness of the signal could be due to the small size of the nanoparticles formed. Conversely, the powder XRD of Pt@GNF shows a variety of strong peaks at 40^{o}, 46^{o} and 68^{o} which can be attributed to the (111), (200) and (220) planes of platinum respectively (figure 6.5 f).[26]

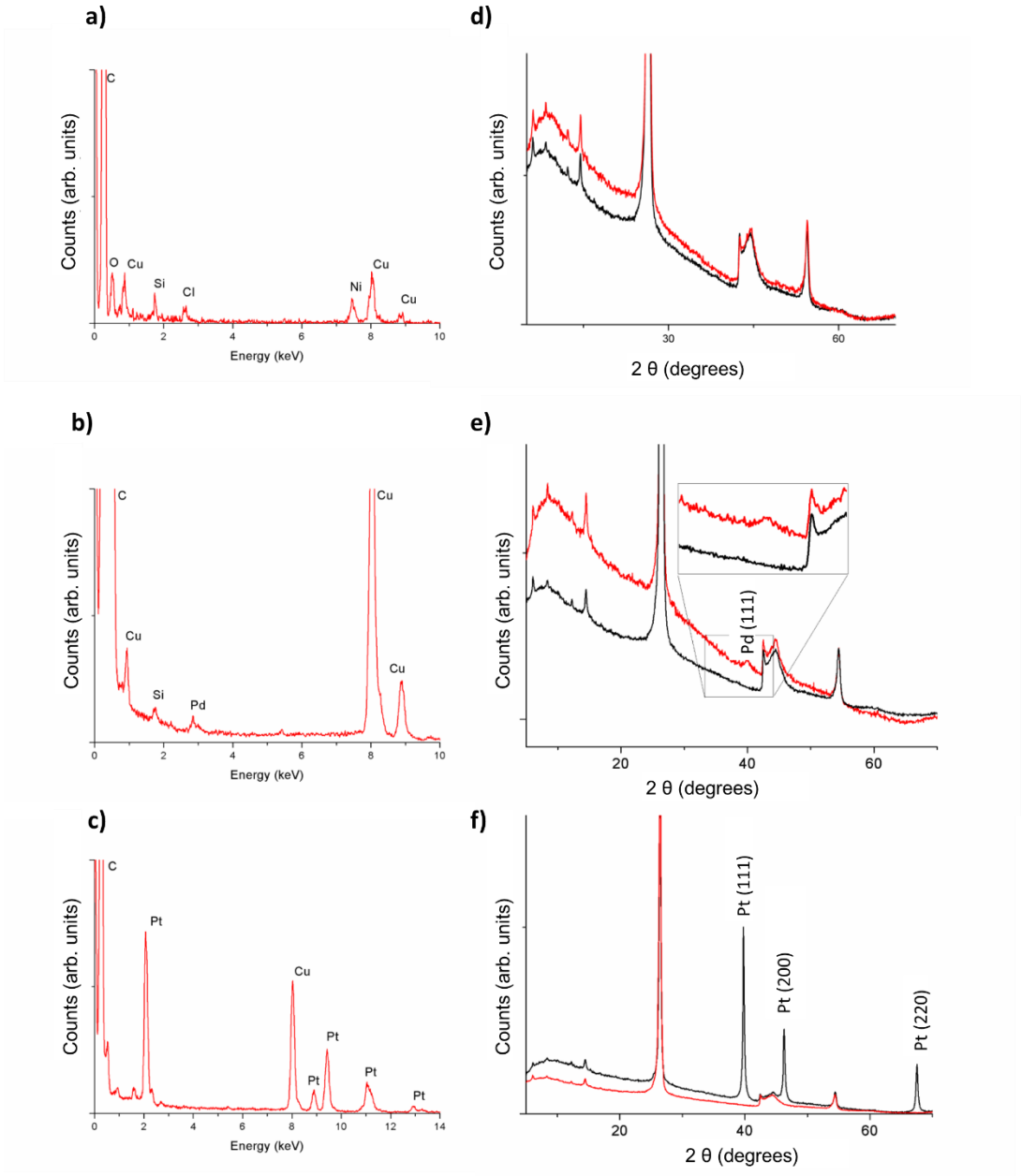


Figure 6.5: (a-c) EDX spectra of Ni@GNF (a), Pd@GNF (b) and Pt@GNF (c). Copper and silicon signals originate from the grid used for analysis, powder XRD of (d) Ni@GNF, (e) Pd@GNF and (f) Pt@GNF (red line), each compared to that of an empty GNF, back line. Characteristic crystal planes of each sample are present which proves the occurrence of each MNP in each sample (where applicable).

6.2.1.2 Sensing Glucose

Initially, as a control experiment to ascertain the characteristics of glucose sensing, bulk platinum was used as the sensor. A three electrode cell was prepared, with a platinum working electrode, vitreous carbon counter electrode, Ag/AgCl reference

electrode, and 0.1 M NaOH as the electrolyte. Cyclic voltammograms (CVs) were performed with potential sweeps between -0.1 V and 1.0 V, and to investigate the glucose sensing abilities of bulk platinum, 10 mM of glucose was added to the solution and a CV was performed.

Upon addition of glucose, an anodic wave at -0.6 V is observed (figure 6.6) which is attributed to the chemisorption and oxidation of glucose to the Pt (scheme 6.1).[28]

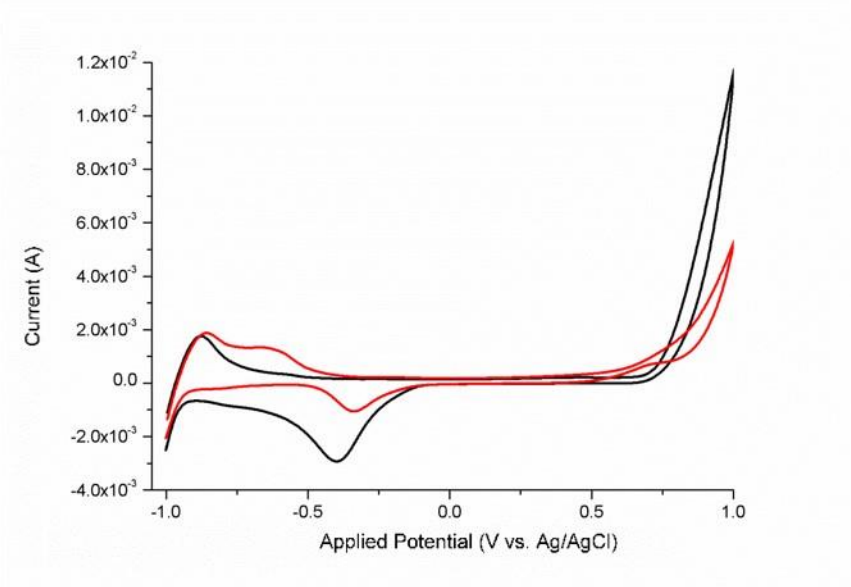
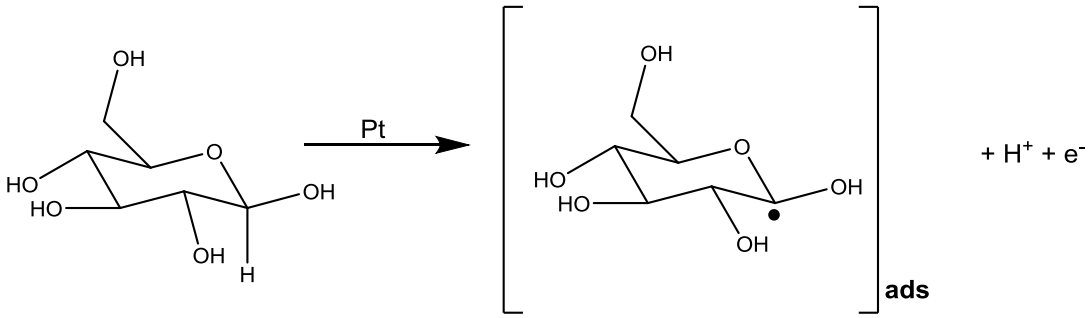


Figure 6.6: Cyclic voltammogram of a platinum wire working electrode without glucose (black) and with 10 mM glucose (red). A cyclic potential sweep was performed between -1.0 V and 1.0 V, a Ag/AgCl reference electrode and a platinum wire counter electrode were used and all CVs were performed in NaOH (0.1 M) as the supporting electrolyte at 293 K, at a scan rate of 100 mVs^{-1}. The anodic wave at -0.6 V is attributed to the chemisorption and oxidation of glucose.

Following the adsorption and oxidation of glucose onto the Pt surface at -0.6 V,[29] (scheme 6.1) electrochemical dissociation of the NaOH electrolyte takes place and OH^- anions adsorb onto the surface of the Pt, creating PtOH (scheme 6.2).

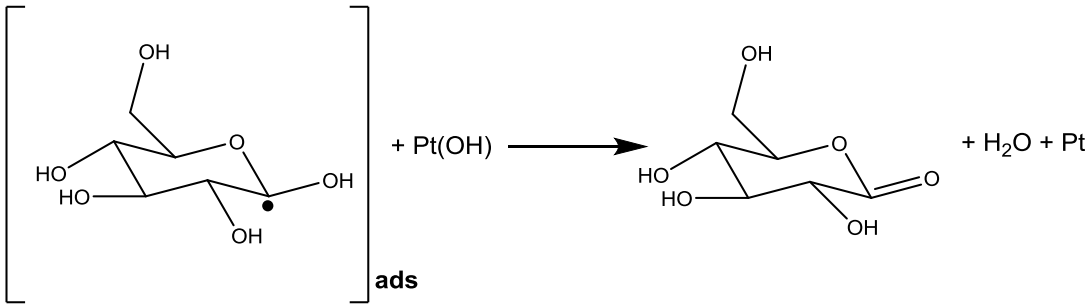
The PtOH then oxidises the adsorbed glucose to glucolactoate which in turn reduces the PtOH to Pt, resulting in a decreased current being observed at the electrode for platinum reduction on the reverse sweep at -0.4 V (scheme 6.3).



Scheme 6.1



Scheme 6.2



Scheme 6.3

This demonstrates that bulk platinum can be used for sensing glucose and provides a viable mechanism for the oxidation. A system was devised whereby the three nanomaterials could be used to compare and contrast their ability to sense glucose. Each MNP@GNF sample was dispersed in propan-2-ol alcohol and Nafion, to form a concentrated suspension which was then drop-cast onto glassy carbon electrodes (GCEs) and left to dry (figure 6.7). Nafion was included to adhere the materials to GCEs more efficiently, which in turn improved the durability of the sensors.[30]

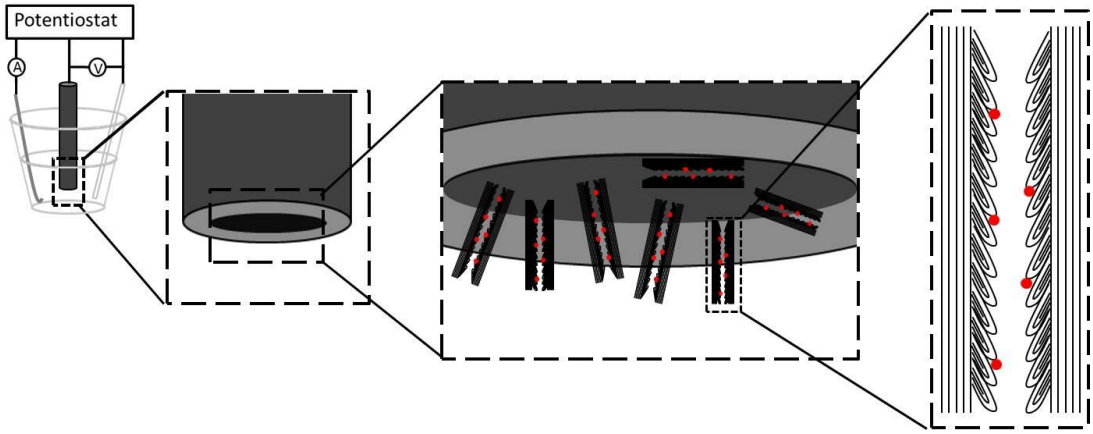


Figure 6.7: A three electrode set-up is used, with a platinum counter electrode, Ag/AgCl reference electrode and the MNP@GNF deposited on a GCE working electrode.[31]

For healthy humans, the concentration of glucose in blood is usually between 4-7 mM; however, for an individual with diabetes mellitus, these levels constantly rise above 10 mM and so for any of these materials to be considered as viable alternatives to current glucose sensors, it is important that they detect glucose in a wide range.[32] The first material to be investigated was Pt@GNF. This was drop-cast to the GCE and systematically added to solutions of NaOH with increasing concentrations of glucose (0 mM to 12.5 mM, in 2.5 mM increments), and CVs were performed at each concentration (figure 6.8 b) and compared to that of a GCE (figure 6.8 a).

Upon addition of 2.5 mM glucose, a cathodic wave appears at -0.47 V (figure 6.8 b, orange line) which can be attributed to the formation of glucolactone. Upon subsequently increasing the glucose concentration, the cathodic wave gets larger and the current decreases linearly for concentrations of glucose below 10 mM, but then rises linearly for concentrations above this (figure 6.8 e). This result shows that the material is sensitive to glucose, and for concentrations of glucose below 10 mM, the concentration is directly proportional to the current. An increase in current at higher concentrations makes this material unsuitable for use as a glucose sensor as it would

be impossible to distinguish between high and low concentration materials, and so other materials need to be investigated.

The CVs of Pd@GNF (figure 6.8 c) and Ni@GNF (figure 6.8 d) were recorded using the same concentrations of glucose. Both nanomaterials show sensitivity towards glucose when compared with GCE. Pd@GNF showed a linear dependence on current for glucose concentrations of between 2.5 mM and 10 mM (figure 6.8 f). The gradient of the linear region ($2.963 \times 10^{-7} AmM^{-1}$), can be used to show how sensitive the material is to glucose, but is lower than that observed for many other non-enzymatic glucose sensors,[29] and so whilst this result is encouraging, the small linear range and low sensitivity suggest that this is not practical for monitoring changes in blood glucose concentration, and no substantial trend was also observed between the glucose concentration and current for the NiNP@GNF sensor (figure 6.8 d,g)

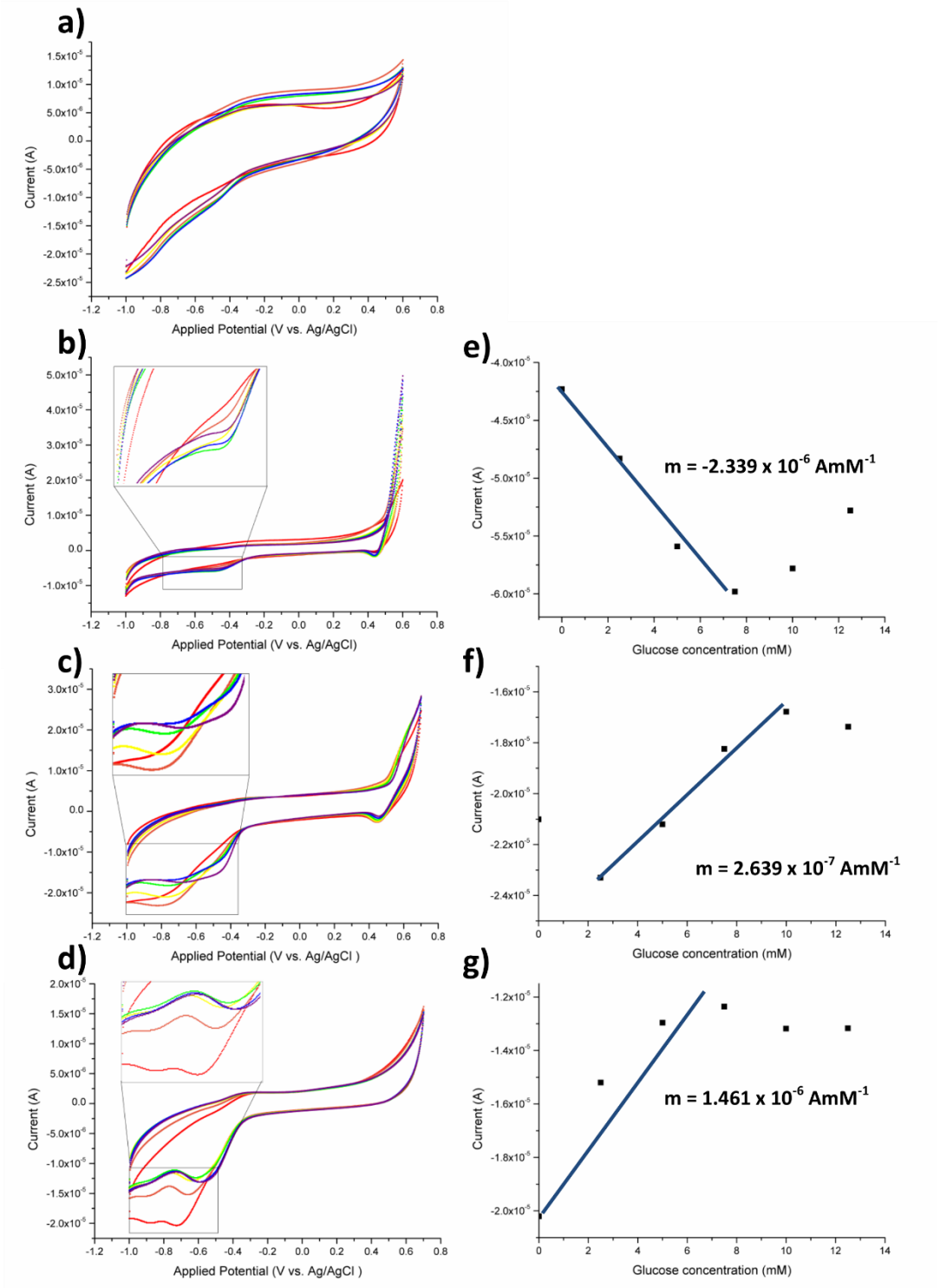


Figure 6.8: Cyclic voltammograms of (a) a GNF electrode, (b), a Pt@GNF electrode (c) a Pd@GNF electrode and (d) a Ni@GNF electrode with various concentrations of glucose; 0 mM (red), 2.5 mM (orange), 5.0 mM (yellow), 7.5 mM (green), 10 mM (blue) and 12.5 mM (purple). A cyclic potential sweep was performed between -1.0 V and 0.6 V for (a), -1.0 V and 0.7 V for (b), (c) and (d). A Ag/AgCl reference electrode and a platinum wire counter electrode were used and all CVs were performed in NaOH (0.1 M) as the supporting electrolyte at 293 K and at a scan rate of 100 mVs^{-1}; e) A plot showing how the concentration

of glucose affects the current of the cathodic wave of Pt@GNF ((b) inset); f) how the concentration of glucose affects the cathode wave of Pd@GNF ((c) inset) and f), a plot showing how glucose concentration affects the current of the cathodic of Ni@GNF ((d) inset).

6.2.2 Metal Oxides Encapsulated within GNFs

MNPs@GNF have shown promising results for the sensing of glucose, but lack a wide ranging linear current response to the analyte. Examples in the literature have shown that multi-walled carbon nanotubes decorated with nickel oxide act as an effective glucose sensor,[10] and so to ascertain whether the encapsulated group 10 metal oxides were effective glucose sensors with improved efficiency, the three encapsulated MNP species were oxidised to form M_xO_y@GNF.

The group 10 MNPs were oxidised by heating in air at elevated temperatures for 5 hr. It has been established that MNPs can act catalytically to oxidise GNFs,[15] and so TGA of the MNPs@GNFs was used to determine the precise oxidation temperatures of GNFs in the presence of MNPs, to avoid inadvertently oxidising the GNFs in the process. TGA proved to be a valuable tool to quantitatively ascertain the precise amount of encapsulated metal (figure 6.4) and can also be used to qualitatively demonstrate how different metal nanoparticles catalyse the oxidation. The sample is heated, its mass is constantly monitored, with decreases in mass caused by the formation of volatile compounds such as CO_2 which are formed upon oxidation of the GNF.

6.2.2.1 Materials Characterisation

6.2.2.1.1 Nickel Oxide Formation

As shown by the TGA, in the presence of nickel, GNFs begin to oxidise in air at around 600 ^oC, and so heating Ni@GNF in air at 550 ^oC for 4 hr led to the formation of Ni_2O_3 without oxidising the GNF, as determined by powder XRD and HR-TEM.

Ni_2O_3 is present in the GNFs as small particles with a mean size of 4.70 nm (figure 6.9 a). Closer inspection of one the nanoparticles reveals a lattice spacing of 0.25 nm, (figure 6.9 b). Powder XRD of Ni_2O_3@GNF (figure 6.9 c, blue line) shows a peak at 32^o which can be attributed to the (002) plane of Ni_2O_3, but also a peak at 45^o is present which is due to the (111) plane of Ni. Upon heating Ni@GNF, the average particle size increased from 4.10 nm to 4.70 nm, and so this supports the assignment that NiNPs were too small to be detected before heating (figure 6.5 d) and that Ni_2O_3 and NiNPs of increased diameter are present in this new sample.[27, 33]

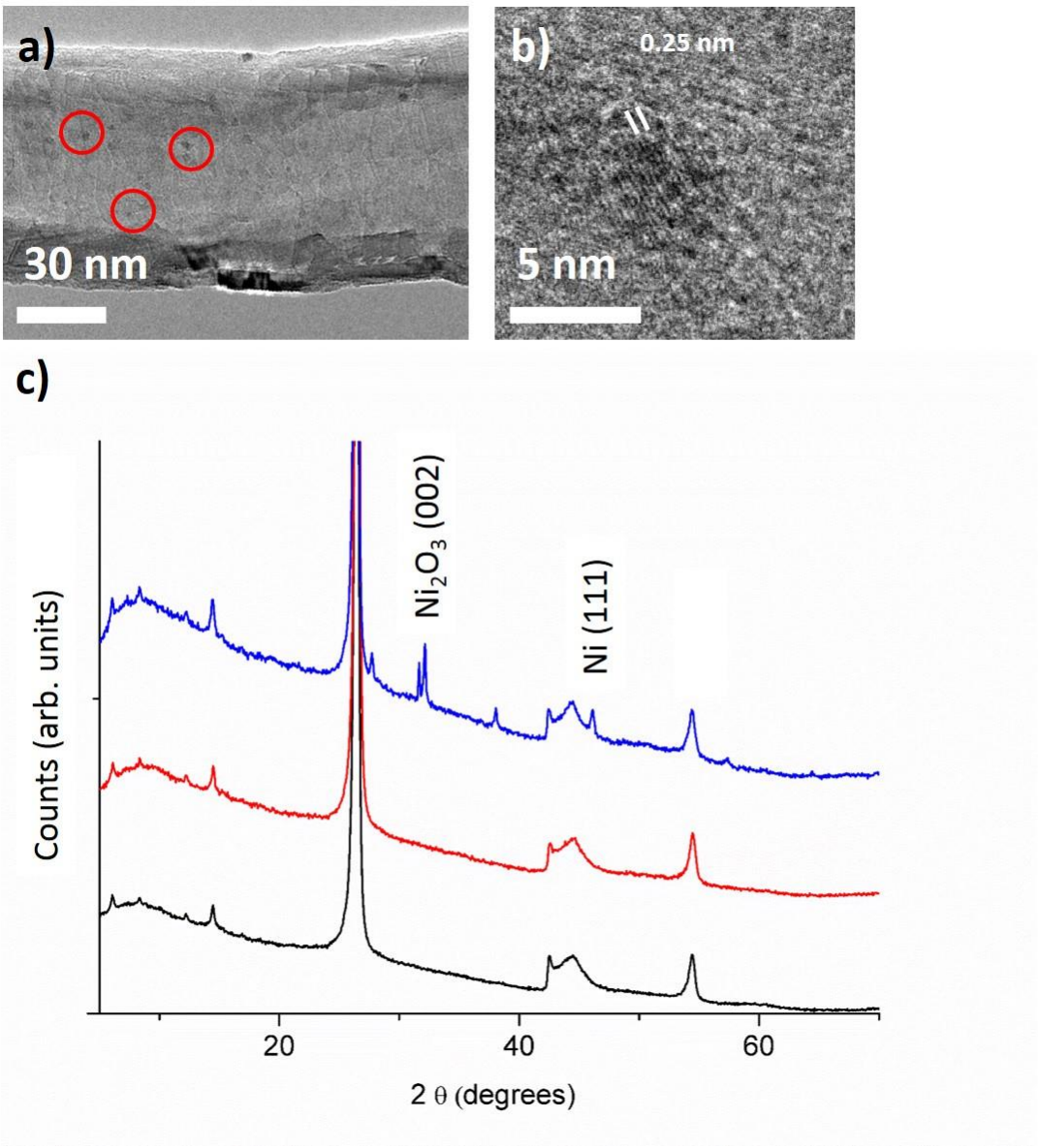


Figure 6.9 (a,b) HR-TEM images of Ni_2O_3@GNF. The metal particles (circled) are slightly larger than those of nickel, and this is reflected in (c), the powder XRD (blue line) which shows peaks for the formation of Ni_2O_3 and NiNPs, when compared to that previously obtained for Ni@GNF before heating (red line).

6.2.2.1.2 Palladium Oxide Formation

Heating Pd@GNF in air at 500 ^{o}C for 4 hr led to the formation of PdO@GNF, as determined by powder XRD and HR-TEM (figure 6.10 a). Similarly to the formation of Ni_2O_3 from Ni, heating Pd to form PdO has led to an increase in nanoparticle size, with a mean size of 8.95 nm being observed. The observed particles have a lattice spacing of 0.26 nm, which corresponds to spacings between the (101) planes of PdO (figure 6.10 b). Powder XRD confirms the formation of PdO@GNF (6.10 c), with peaks at 39^{o}, 60^{o} and 71^{o} corresponding to the (101), (200) and (220) planes respectively.[34]

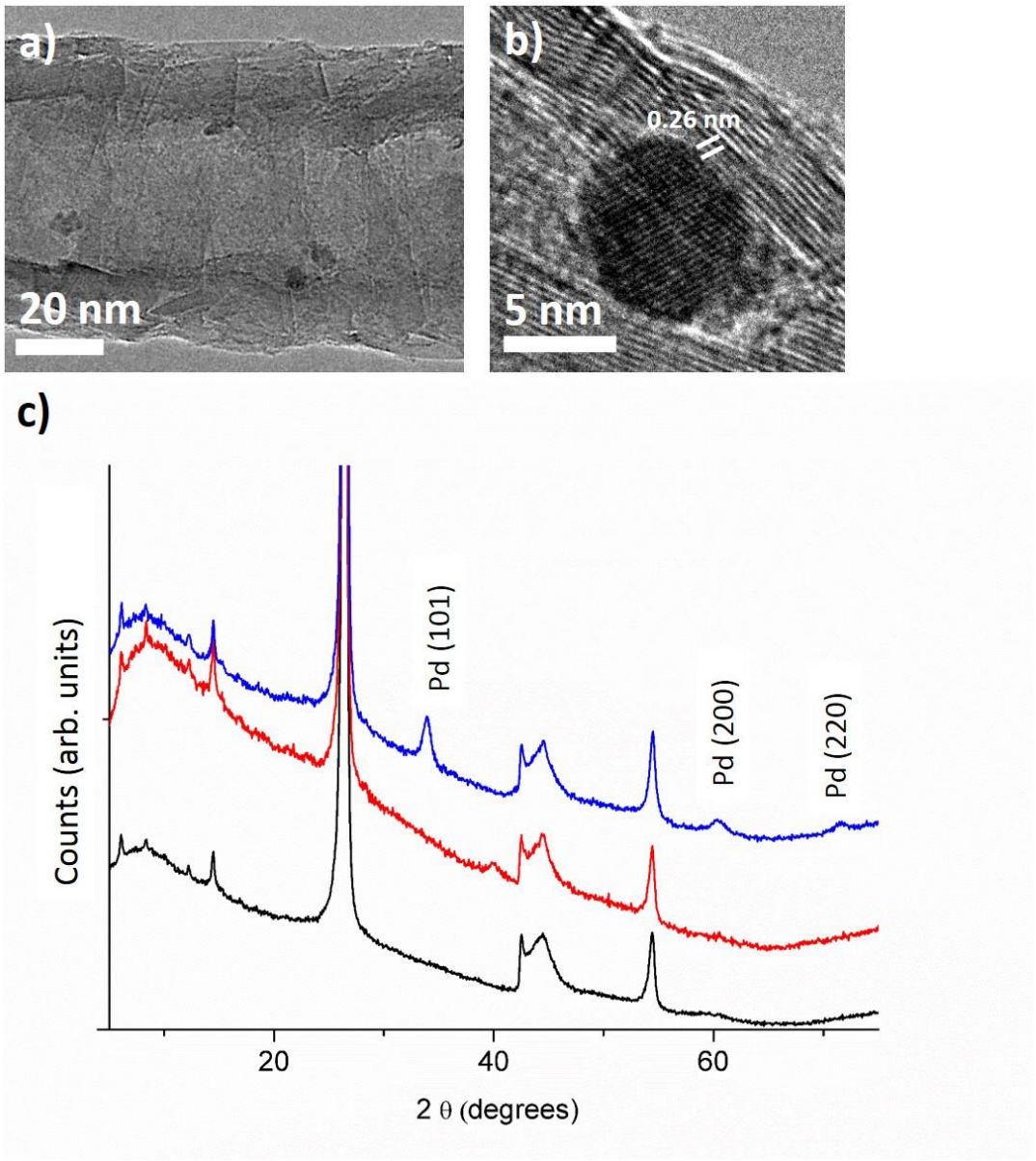


Figure 6.10: (a,b) HR-TEM images of PdO@GNF. The particles are slightly larger than those of Pd. The PdO nanoparticle has a lattice spacing of 0.26 nm which corresponds to the (101) plane spacing of bulk PdO. This is present in (c), the powder XRD spectra (blue line) as a peak at 39º, along with the (200) and (220) planes at 60º and 71º respectively, which don't appear in the spectra of Pd@GNF (red line).

6.2.2.1.3 Platinum Oxide Formation

As shown by the TGA (figure 6.4) PtNPs readily catalysed the oxidation of GNFs at 500 ºC, and so a much lower temperature than for the two previous MNPs, 400 ºC, was chosen. Heating Pt@GNF in air at 400 ºC for 5 hr led to the formation of PtO_2@GNF as confirmed by powder XRD and HR-TEM (figure 6.11).

Upon oxidation, the mean particle size has increased (from 6.63 nm to 8.95 nm) and HR-TEM reveals a lattice spacing of 0.17 nm which is consistent with the (110) plane spacing of PtO_2. The powder XRD peaks at 33^o, 39^o and 58^o are consistent with the respective (111), (101) and (110) planes of PtO_2, which confirms the presence of the oxide (figure 6.11 c).[35]

The powder XRD also shows peaks at 40^o, 46^o and 68^o which are consistent with PtNPs still being present, although the considerable decrease in intensity of these peaks relative to the diffractogram of only Pt@GNF suggests that either there are fewer PtNPs, their crystallinity has decreased or they have become smaller.

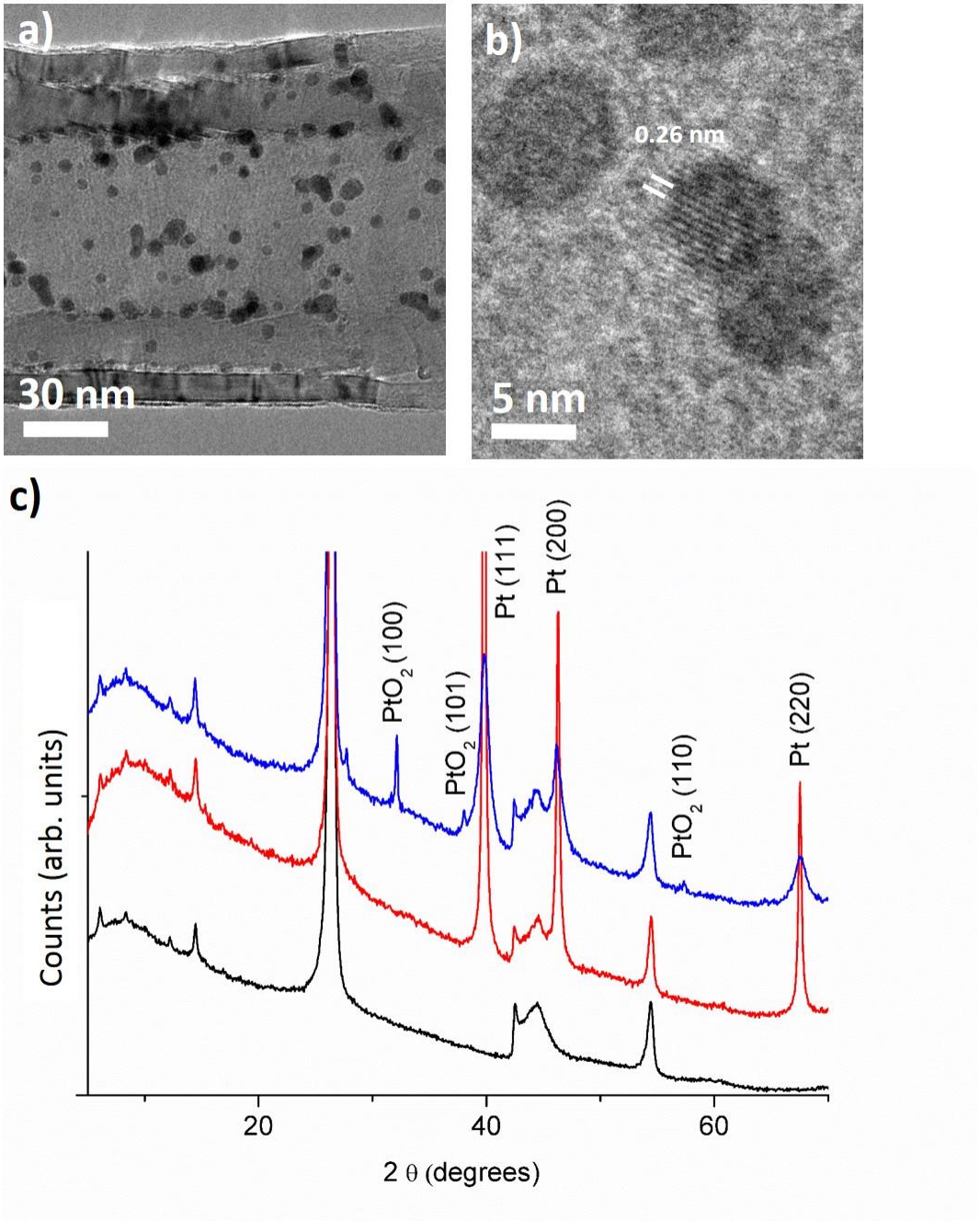


Figure 6.11: (a,b) HR-TEM images of PtO_2@GNF. The particles are slightly larger than those of PtNPs. Closer inspection of the PtO_2 nanoparticle shows a lattice spacing of 0.26 nm which corresponds to the (110) plane spacings of bulk Pt. This is present in (c), the powder XRD spectra (blue line) as a peak at 58º, along with the (100) and (101) planes at 33º and 39 respectively, which don't appear in the spectra of Pt@GNF (red line).

6.2.2.2 Glucose Sensing using MO_x@GNF

CVs of NiO_x@GNF were performed in varying concentrations of glucose (figure 6.12 a). Upon addition of glucose to the system, a redox couple occurs at around -0.4 V

which suggests that the system is sensitive to glucose, but no trend is observed upon increasing the glucose concentration (figure 6.12 d). The CVs of Ni_2O_3@GNF at varying concentrations of glucose appear different to those of Ni@GNF (figure 6.8 d). This is interesting as although this sample also contains NiNPs, the response to glucose is different to that of just Ni@GNF and so the response can be attributed to the formation of Ni_2O_3.

CVs of PdO@GNF were performed at varying concentrations (figure 6.12 b). Prior to the addition of glucose, there is a broad anodic wave at -0.6 V, and a sharp cathodic wave at -0.45 V (red line). Systematically increasing the glucose concentration not only results in a slight positive shift in the position of these waves, but also a change in the wave current. Monitoring both the cathodic and anodic currents as a function of concentration reveals that the currents increase linearly in the range 2.5 mM to 12.5 mM glucose (figure 6.12 e), which is within the ideal range for anthropological blood glucose sensing.

Similarly, CVs of PtO_2@GNF with varying concentrations of glucose reveal an anodic wave at -0.7 V which linearly increased in current upon further addition of glucose (figure 6.12 c).

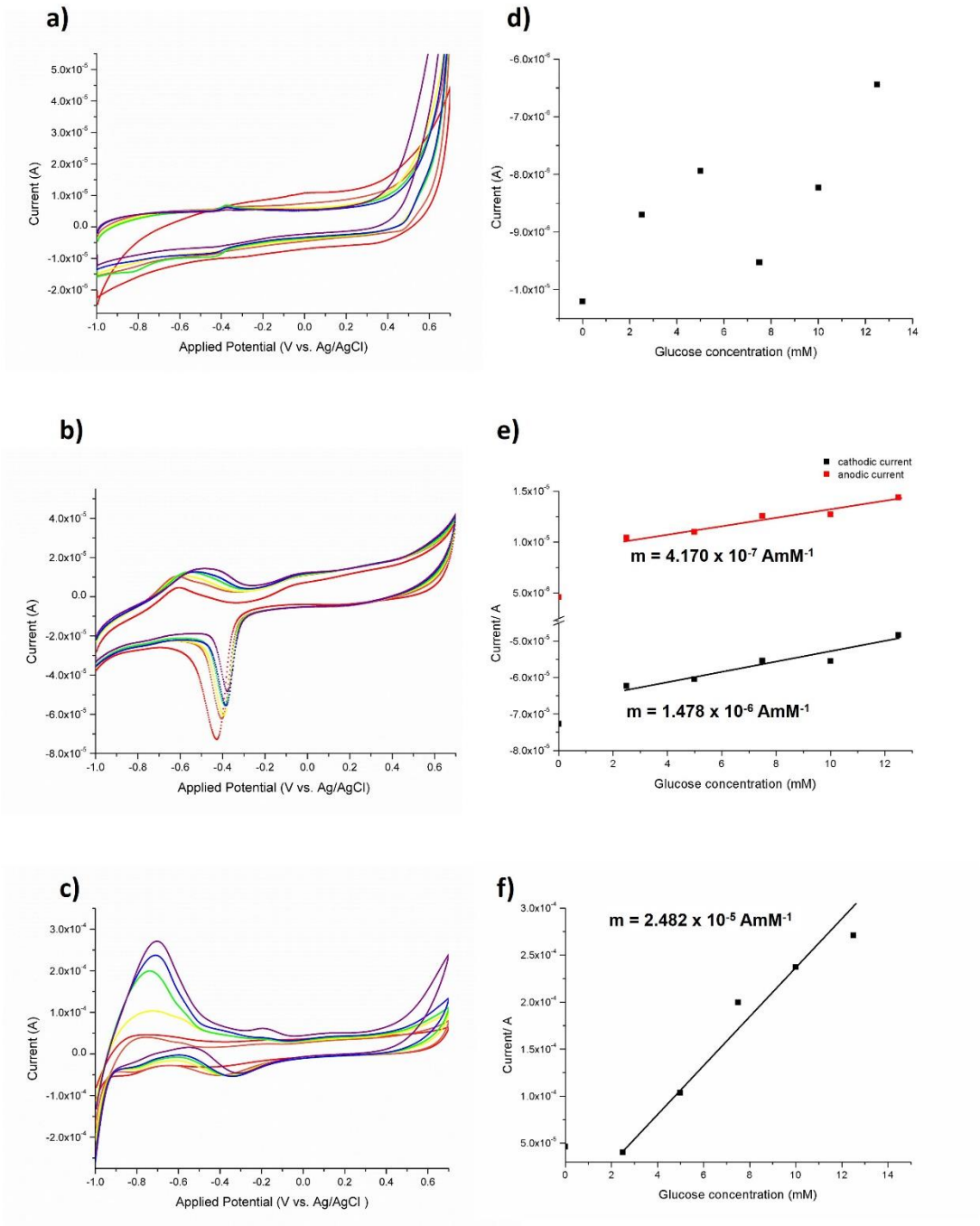


Figure 6.12: CVs of (a) a Ni_2O_3@GNF electrode, (b) a PdO@GNF electrode, (c) a PtO_2@GNF electrode with various concentrations of glucose; 0 mM (red), 2.5 mM (orange), 5.0 mM (yellow), 7.5 mM (green), 10 mM (blue) and 12.5 mM (purple). A cyclic potential sweep was performed between -1.0 V and 0.7 V, a Ag/AgCl reference electrode and a Pt wire counter electrode were used and all CVs were performed in NaOH (0.1 M) as the supporting electrolyte at 293 K and at a scan rate of 100 mVs^{-1}; d) A plot of how the cathodic wave at -0.42 V for the NiO_x@GNF electrode changes as a function of concentration, and no trend is observed; e) Plots showing how the anodic (red line) and cathodic (black line) wave currents change for the PdO@GNF electrode as a function of glucose concentration, and f) a plot showing how the anodic wave at -0.7 V for the

PtO_2@GNF electrode increases linearly with glucose concentration between 2.5 mm and 7.5 mM, before increasing more gradually.

By considering the gradient of the current responses to concentration graphs (figures 6.8 e-g and 6.12 d-f) it is possible to determine which materials are most sensitive to glucose, as a larger current response across a given concentration range enables intermediate concentrations to be determined more accurately. PtO_2@GNF has therefore been shown to be the most effective glucose sensor, followed by PdO@GNF.

As shown by TGA and HR-TEM analysis, although the mass of molecular precursors was precisely calculated to give a 2% metal loading by weight for each, more platinum was encapsulated than nickel or palladium. Since more platinum was present inside the GNFs, a large current was observed, as defined by the Cottrell relation.[36] The main forces responsible for stabilising MNPs inside GNFs are van der Waals forces, and since platinum has a higher atomic number than palladium and nickel, PtNPs can be held more stably inside GNFs.[15, 37] Conversely, very little nickel was observed inside the GNFs.

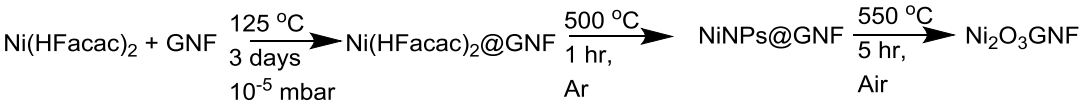
Furthermore, the Sabatier principle is a concept which defines an effective catalytic surface to be one that both effectively binds to reactants but readily dissociates, and therefore is neither too reactive nor too inert.[38] The AC-HRTEM measurements performed on group 10 metals in SWNTS (Chapter III) demonstrate that nickel binds very effectively to carbon, followed by platinum and then palladium, and so it is possible that PtO_2 nanoparticles are able to both bind and dissociate from glucose molecules most effectively.

In addition, the MO_x@GNF samples were found to perform better than their encapsulated MNP precursors. This can be attributed to an increase in Lewis acidity

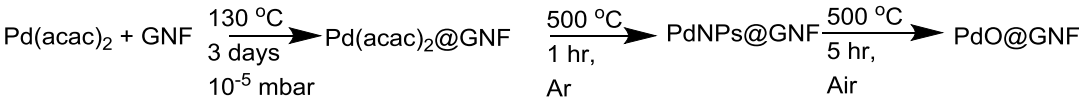
of the metal atoms upon oxide formation, which would increase their affinity towards hydroxide groups, facilitating the electrochemical reaction

6.3 Conclusions

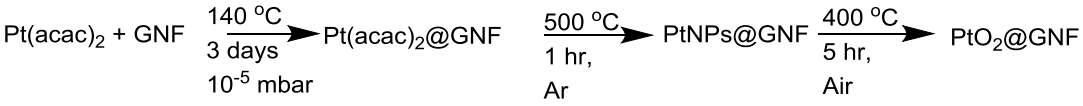
The syntheses of MNPs@GNF (M= Ni, Pd, and Pt) and their subsequent oxides has been performed, and the materials fully structurally characterised (Schemes 6.5-6.7).



Scheme 6.5: The formation of nickel oxide nanoparticles inside GNFs.



Scheme 6.6: The formation of palladium oxide nanoparticles inside GNFs.



Scheme 6.7: The formation of platinum oxide nanoparticles inside GNFs.

A three electrode cell was implemented to probe the sensing capabilities of all synthesised nanomaterials, and whilst all materials were shown to be sensitive to glucose, PdO@GNF and PtO_2@GNF proved to be the most effective, with noticeable trends in the CVs upon varying the concentration of glucose (table 6.1)

Table 6.1: A summary of materials synthesised, and their response to glucose concentration

Material	Redox wave (V)	Linear range (mM)	Gradient (AmM^{-1})
Ni@GNF	Cathodic -0.7	0-5	1.461×10^{-6}
Pd@GNF	Cathodic -0.7	2 - 10	2.693×10^{-7}
Pt@GNF	Cathodic -0.5	0 – 7.5	-2.339×10^{-6}
Ni_2O_3@GNF	Anodic/Cathodic -0.4	-	-
PdO@GNF	Cathodic -0.4	2-12	1.478×10^{-5}
	Anodic -0.6	2-12	4.170×10^{-7}
PtO_2@GNF	Anodic -0.7	2-12	2.482×10^{-5}

For these materials to become commercially viable it is necessary to investigate their electrochemistry at a much wider range of glucose concentrations, and to examine the durability of the catalysts over longer periods of time. Additionally, in the blood there are many electroactive compounds which could interfere and produce an electrical response themselves, such as Bilirubin, a component of bile, and a variety of proteins.[39] In order to validate the efficiency of these materials to sensing glucose in the blood, the sensitivity of MNPs@GNF towards these other components would need to be investigated, although a benefit of using encapsulated MNPs is that molecules above a particular size won't be able to enter the GNFs.

The results of this investigation provide a basis for future development of non-enzymatic glucose sensors from encapsulated metal oxide nanoparticles.

6.4 Experimental

All chemicals, unless otherwise stated were purchased from Sigma Aldrich chemical company, and used as purchased.

6.4.1 Synthesis of MNPs@GNF

Group 10 metal-containing complexes (x mg) were sealed under high vacuum (10^{-5} mbar) with dried (500 ^{o}C for 1 hr) PR19 GNFs (10 mg) in a Pyrex ampoule. Each system was heated to slightly above the temperature of the initial compound's sublimation (table 6.2) for 3 days, and then cooled rapidly. Each product was then sealed in Pyrex ampoule under argon and heated at 500 ^{o}C for 1 hr to form MNPs@GNF (M= Ni, Pt, Pd).

Table 6.2: Experimental parameters for the formation of each MNPs@GNF (M= Ni, Pt, Pd).

Material	Initial compound	Mass of compound (mg)	Encapsulation temperature (^{o}C)	Oxidation temperature (^{o}C)
Ni@GNF	$Ni(HFacac)_2$	1.610	125	550
Pd@GNF	$Pd(acac)_2$	0.573	130	500
Pt@GNF	$Pt(acac)_2$	0.403	150	400

6.4.1.1 Synthesis of M_xO_y@GNF

MNPs@GNF (5 mg) (M= Ni, Pt, Pd) were each heated at a specified temperature (see Table 6.2) for 5 hr and then left to cool to room temperature.

6.4.2 HR-TEM Analysis

GNFs filled with the encapsulated materials were dispersed in propan-2-ol using an ultrasonic bath and drop cast onto lacey carbon-coated copper TEM grids (Agar). HR-TEM imaging and electron beam irradiation was carried out on a JEOL 2100 FEG-TEM microscope operated at 200 kV.

6.4.3 EDX Spectroscopy

Local EDX spectra were acquired for samples mounted on TEM grids using an Oxford Instruments INCA X-ray microanalysis system. The electron beam was condensed onto areas of specimens (bulk specimen or nanotube bundles) suspended over holes of the amorphous carbon film.

6.4.4 Powder XRD Analysis

Powder X-ray measurements were performed using a PANalytical X'Pert Pro diffractometer with a Cu K (α) radiation source (λ= 1.5432 nm, 40 kV, 40 mA) in Bragg-Bretano geometry using a Si zero background holder. All samples were moistened with propan-2-ol to aid GNF adhesion and parameters for a typical experiment were:

Start angle: 5°

Stop angle: 80°

Step size: 0.0525°

Time/step: 6080 s

Scan speed: 0.0020°/s

6.4.5 Thermogravimetric Analysis

Thermogravimetric measurements were performed using a TA Q500 thermogravimetric analyser. All samples were performed in air on platinum pans. The parameters for all experiments were:

Ramp: 10 °C/min from 20-1000 °C

Isotherm: 10 min @ 1000 °C

Air flow: 60 mL/min

6.4.6 Electrochemical Experiments

All electrochemistry was carried out using an Autolab PGSTAT302N pontentiostat. For the electrochemical experiments using the synthesised materials, a three-electrode cell was set up with a GCE covered with the sample as the working electrode, platinum wire as the counter electrode and a Ag/AgCl (sat. KCl) reference electrode. The electrolyte was made up of 25 mL 0.1 M NaOH, diluted with deionised water. The modified GCE was produced by spotting 10 - 15 µL of a solution containing HPLC grade propan-2-ol (10 µL), the sample material (0.5 mg) and Nafion 5 % perfluorinated resin solution (10 µL) which had been sonicated for 15 min onto a polished (microfibre cloth) GCE and leaving to dry at room temperature. Before measurements were taken, the electrolyte was degassed with argon for *ca.* 20 min and stirred magnetically and briefly degassed again between additions of glucose solution. Glucose concentrations, potential ranges, step potentials and scan rates have been quoted in the Results and Discussion section where applicable.

6.5 References

1. J. Dobson, *Gene Therapy*, 2006, **13**, 283.
2. S. Rudge, C. Peterson, C. Vessely, J. Koda, S. Stevens and L. Catterall, *J. Controlled Release*, 2001, **74**, 335.
3. Y. S. Kang, S. Risbud, J. F. Rabolt and P. Stroeve, *Chem. Mater.*, 1996, **8**, 2209.
4. V. Mody, R. Siwale, A. Singh and H. Mody, *J. Pharm. Bioall. Sci.*, 2010, **2**, 282.
5. I. Torjesen, *BMJ*, 2016, **352**.
6. A. Heller and B. Feldman, *Chem. Rev.*, 2008, **108**, 2482.
7. S. Ferri, K. Kojima and K. Sode, *J. Diabetes Sci. Tech.*, 2011, **5**, 1068.
8. C. Malitesta, F. Palmisano, L. Torsi and P. G. Zambonin, *Anal. Chem.*, 1990, **62**, 2735.
9. J. Bao, K. Furumoto, M. Yoshimoto, K. Fukunaga and K. Nakao, *Biochem. Eng. J.*, 2003, **13**, 69.
10. R. Prasad and B. R. Bhat, *Sens. Actuator B-Chem.*, 2015, **220**, 81.
11. Z. H. Wang, H. P. Liu, S. Y. Wang, Z. L. Rao and Y. Y. Yang, *Sens. Actuator B-Chem.*, 2015, **220**, 779.
12. B. H. Liu, R. Q. Hu and J. Q. Deng, *Anal. Chem.*, 1997, **69**, 2343.

13. J. M. Falkowski, S. Liu and W. Lin, *Isr. J. Chem.*, 2012, **52**, 591.
14. T. T. Nguyen and P. Serp, *ChemCatChem*, 2013, **5**, 3595.
15. A. La Torre, M. d. C. Giménez-López, M. W. Fay, G. A. Rance, W. A. Solomonsz, T. W. Chamberlain, P. D. Brown and A. N. Khlobystov, *ACS Nano*, 2012, **6**, 2000.
16. E. Ramirez-Meneses, V. Montiel-Palma, V. H. Chavez-Herrera and J. Reyes-Gasga, *J. Mater. Sci.*, 2011, **46**, 3597.
17. Y. Y. Zhou, C. H. Liu, J. Liu, X. L. Cai, Y. Lu, H. Zhang, X. H. Sun and S. D. Wang, *Nano Micro Lett.*, 2016, **8**, 371.
18. T. van Haasterecht, C. C. I. Ludding, K. P. de Jong and J. H. Bitter, *J. Energy Chem.*, 2013, **22**, 257.
19. B. I. Kharisov, O. V. Kharissova, U. O. Mendez and I. G. De La Fuente, *Synth. React. Inorg. Met.-Org. Nano-Met. Chem.*, 2016, **46**, 55.
20. F. Tan, X. Fan, G. Zhang and F. Zhang, *Mater. Lett.*, 2007, **61**, 1805.
21. L. T. Hoa, K. G. Sun and S. H. Hur, *Sens. Actuator B-Chem.*, 2015, **210**, 618.
22. D. Zhai, B. Liu, Y. Shi, L. Pan, Y. Wang, W. Li, R. Zhang and G. Yu, *ACS Nano*, 2013, **7**, 3540.
23. A. Ul-Hamid, A. Quddus, H. Saricimen and H. Dafalla, *Mater. Res.*, 2015, **18**, 20.
24. R. Wojcieszak, M. J. Genet, P. Eloy, P. Ruiz and E. M. Gaigneaux, *J. Phys. Chem. C*, 2010, **114**, 16677.
25. Z. W. Wang, Z. Y. Li, S. J. Park, A. Abdela, D. Tang and R. E. Palmer, *Phys. Rev. B*, 2011, **84**, 073408.
26. V. Gnutzmann and W. Vogel, *Z. Phys. D-Atoms Mol. Clusters*, 1989, **12**, 597.
27. W. F. Yan, V. Petkov, S. M. Mahurin, S. H. Overbury and S. Dai, *Catal. Commun.*, 2005, **6**, 404.
28. C. P. Wilde and M. J. Zhang, *J. Chem. Soc., Faraday Trans.*, 1993, **89**, 385.
29. K. E. Toghill and R. G. Compton, *Int. J. Electrochem. Sci.*, 2010, **5**, 1246.
30. S. Litster and G. McLean, *J. Power Sources*, 2004, **130**, 61.
31. R. L. McSweeney, T. W. Chamberlain, E. S. Davies and A. N. Khlobystov, *Chem. Commun.*, 2014, **50**, 14338.
32. K. S. Polonsky, B. D. Given and E. Vancauter, *J. Clin. Invest.*, 1988, **81**, 442.
33. A. K. Sharma, D. Sameerah, D. Charu, V. Utkarshaa and S. Ankur, *Int. J. Chem. Eng. Appl.*, 2015, **6**, 156.
34. A. Baylet, P. Marecot, D. Duprez, P. Castellazzi, G. Groppi and P. Forzatti, *PCCP*, 2011, **13**, 4607.
35. J. R. McBride, G. W. Graham, C. R. Peters and W. H. Weber, *J. Appl. Phys.*, 1991, **69**, 1596.
36. A. B. L. Faulkner, *Electrochemical Methods*, John Wiley & Sons, Phoenix, 2 edn., 2001.
37. G. A. Rance, D. H. Marsh, S. J. Bourne, T. J. Reade and A. N. Khlobystov, *ACS Nano*, 2010, **4**, 4920.
38. P. Sabatier, *Ber. Dtsch. Chem. Ges.*, 1911, **44**, 1984.
39. M. H. Beers and A. J. Fletcher, *The Merck Manual of Medical Information*, Merck Research Laboratories, Whitehouse Station, NJ, 2003.

Concluding Remarks

The production of inorganic nanostructures and controlled methods for their fabrication have never been more important, especially since it is becoming increasingly necessary to encroach the frontiers of material synthesis and delve into the nanoscale realm. This thesis, which demonstrates the formation of novel compounds and hybrid architectures; an innovative synthetic approach for their formation; and subsequently suggests future applications of the synthesised nanomaterials, contributes to this ever growing and essential area of research in a variety of different aspects.

It is crucial to explore how metal nanoparticles (MNPs) act on the atomic scale, not only to harness their potential for future applications, but also to gain a fundamental appreciation for the role of metals in catalysis, and thus their interactions with carbon comprehensively need to be studied. Single-walled carbon nanotubes (SWNTs) have proved to be excellent candidates as nano-sized test tubes, and two different groups of metals have been methodically investigated. In Chapter II, the group 11 metals were encapsulated into SWNTs, and this represents the first systematic study of the interactions between the coinage metals with carbon on the atomic scale. Although the three metals were found to promote the formation of different carbon nanostructures on the nanoscale such as the formation of fullerene type structures by copper nanoparticles; extended carbon cylinders by silver nanoparticles; and a metal carbide with gold nanoparticles; neither of these three metals extensively damaged the SWNT sidewall and so all transformations were easily viewed using aberration-corrected high resolution transmission electron microscopy (AC-HRTEM).

This is of contrast to the group 10 metals which were systematically investigated in Chapter III, where profound differences in the interactions between each MNP and carbon, both from the SWNT sidewall and also adventitious carbon in the nanotube were observed. While small clusters of nickel nanoparticles (NiNPs) promoted the formation of small hemispherical nanobuds, palladium nanoparticles (PdNPs) were found to stimulate the growth of elongated carbon cylinders, and platinum nanoparticles (PtNPs) led to the formation of small hemispherical carbon shells. Additionally, it was found that NiNPs readily engaged in bonding with the nanotube sidewall, rapidly leading to its demise, whereas PdNPs had a very minimal interaction with the sidewall. On the other hand, PtNPs were shown to readily enter defects in the sidewall of SWNTs and heal them, which demonstrates the striking differences in reactivity between the three metals in this particular group of the periodic table.

In addition to the encapsulation of MNPs into SWNTs, a novel methodology to synthesise inorganic compounds in SWNTs has been developed, resulting in the fabrication of new, low-dimensional forms of PtX_2@SWNT (X = I, S). Both stepwise and one-pot synthetic approaches for the formation of the platinum compounds have been implemented, with each having their own merits. The stepwise approach provides an excellent opportunity to both spectroscopically and microscopically probe the mechanisms of inorganic material formation, and it has been shown that by the complimentary use of fluorescence-detected X-ray absorption spectroscopy (FD-XAS) and Raman spectroscopy, a full understanding of electron transfers between the host nanotube and guest inorganic nanomaterial can be achieved. However, when using a stepwise approach, the stoichiometry of products cannot be guaranteed, as each of the atomic precursors have different physical and chemical properties leading to differing encapsulation rates inside the SWNT channel. To combat this, the

coordination environment of the metal centre was expanded to append new ligands, leading to the stoichiometrically controlled syntheses of PtI_2@SWNT and PtS_2@SWNT, which were both fully structurally characterised using a variety of different techniques. QSTEM TEM simulation and aberration-corrected scanning transmission electron microscopy (AC-STEM) imaging proved invaluable tools for both confirming the structural information observed by AC-HRTEM and discriminating between the different metal and non-metal components inside the SWNT. Although the encapsulated PtS_2 was found to have the same crystal structure as in the bulk, PtI_2 was found to have a different structure which is a result of confinement inside the SWNT.

The simultaneous necessity to control both stoichiometry and morphology of nanostructures represents the most challenging task for the synthesis of materials at the nanoscale, but the use of SWNTs provides a solution to this, and it is envisaged that once an all-encompassing understanding of the mechanisms of inorganic syntheses at the nanoscale has been obtained, both the metal centre and ligands could be systematically changed which could lead to the intelligent design of a whole new range of bespoke nanoscale materials.

Motivated by the desire to master inorganic chemistry at the nanoscale, attempts have been made to comprehensively understand the mechanisms of formation of such materials, and this has involved both microscopically monitoring reactions using AC-HRTEM to probe reactions in direct space and real time, and also spectroscopically by using FD-XAS. Advancements in AC-HRTEM imaging have allowed not only for the observation of nanostructures with atomic precision, but also for the electron beam to be used as a source of controlled energy to drive chemical transformations, and once the intricate process of electron beam interactions with materials are fully

understood, mechanisms of reactions on the single molecular level can be uncovered. The invasive nature of the electron beam can unfortunately pose a problem when trying determine intrinsic structure of materials inside the nanotube, but recent advancements in AC-HRTEM imaging have led to the development of an AC-HRTEM which uses an electron beam with the energy as low as 20 keV, allowing for atomic resolution imaging with vastly diminished sample degradation.[1] This will have profound implications on the structural analysis of materials, especially beam sensitive samples such as cell tissues and proteins, making it possible to study organic reactions on the atomic scale.

As part of the quest to probe transformations at the nanoscale, FD-XAS has been used to monitor transformations of encapsulated coordination complexes M(acac)$_2$@SWNT (M = Cu, Pt) to inorganic materials during heating. A unique methodology was developed to probe the oxidation states of each of the metal centres, and it was found that transformations occur at a much lower temperature than observed for the bulk materials, which has profound consequences for using the nanotubes as nanoreactors and could lead to the development of a new set of synthetic procedures for nanomaterials.

In addition to synthesising nanomaterials to gain a fundamental understanding of their structures, it is also important to investigate avenues for potential applications for such structures. As demonstrated in Chapter VI, MNPs (M = Ni, Pd, Pt) have been prepared inside hollow graphitised carbon nanofibres (GNFs) and transformed to their corresponding oxides where their ability to sense glucose has been examined. It was found that although all materials were sensitive to glucose, the metal oxides were more effective than just their corresponding metals, and this could potentially be harnessed for the development of more efficient blood glucose sensors.

As well as mono-metallic nanoparticles attracting a lot of interest due to potential industrial applications, there is a growing interest surrounding alloyed nanoparticles, so-called 'nanoalloys'. These materials are of significant interest as catalysts, for example Au-Ag nanoparticles attached to the surface of SWNTs have been used to capture CO.[2] Furthermore, platinum containing nanoalloys were synthesised on a flat surface and have shown to be effective catalysts for the oxidation of methanol,[3] therefore the synthesis of such materials inside SWNTs could prove to be beneficial. The feasibility of doing this has been demonstrated by Li *et al.* who described the formation of bimetallic CoPt and FePt nanostructures inside multi-walled carbon nanotubes,[4] and so as an extension it would be interesting to investigate the syntheses of such structures in SWNTs.

Overall, the use of AC-HRTEM to visualise individual atoms inside the quasi-one-dimensional SWNTs has proved invaluable, as it has allowed the synthesised materials to be viewed in direct space and real time, and the unique methodology of cross correlating both FD-XAS and Raman spectroscopy has allowed the electronic properties of the systems to be studied. Further spectroscopic techniques such as electron energy loss spectroscopy (EELs) could prove beneficial to probing the materials, as it is more sensitive to elements with a lower atomic number and therefore be used to resolve the lighter elements present in this study.

In conclusion, this work has determined the metal-carbon bonding characteristics of the late transition metals; synthesised novel, bespoke inorganic nanomaterials using a variety of newly developed reaction pathways; established a new method for monitoring transformations at the nanoscale both microscopically and spectroscopically; and tested new hybrid nanomaterials for potential uses as glucose sensors. The research represented in this thesis significantly contributes to the field of

studying materials in SWNTs. For most of the previous millennium, chemists have relied on the use of laboratory glassware to investigate the chemical properties of materials, but SWNTs have proven to be a revolutionary new piece of apparatus for studying materials on the atomic scale, as demonstrated by both the encapsulation of late transition metals into SWNTs and the formation of innovative low-dimensional inorganic structures. Thus, this thesis opens a new chapter in the chemistry of inorganic materials, not only by providing an analytical tool for viewing atomic level chemical processes, but also advancing the synthetic methodologies for inorganic materials, right at a time when the world needs them the most.

7.1 References

1. M. Linck, P. Hartel, S. Uhlemann, F. Kahl, H. Muller, J. Zach, M. Haider, M. Niestadt, M. Bischoff, J. Biskupek, Z. Lee, T. Lehnert, F. Borrnert, H. Rose and U. Kaiser, *Phys. Rev. Lett.*, 2016, **117**, 5.
2. H. Akbarzadeh, M. Abbaspour and S. Salemi, *New J. Chem.*, 2016, **40**, 310.
3. X. F. Yu, D. S. Wang, Q. Peng and Y. D. Li, *Chem. Eur. J.*, 2013, **19**, 233.
4. X. Li, T. Hungria, C. Garcia Marcelot, M. R. Axet, P. F. Fazzini, R. P. Tan, P. Serp and K. Soulantica, *Chem. Commun.*, 2016, **52**, 2362.